

**GAS-PHASE REACTIVITY STUDIES OF ORGANIC POLYRADICALS,
AND STUDIES OF C-H BOND ACTIVATION OF HYDROCARBONS BY
ION-MOLECULE REACTIONS WITH *closo*-[B₁₂Br₁₁]⁻ IONS USING MASS
SPECTROMETRY**

by
Xin Ma

A Dissertation

Submitted to the Faculty of Purdue University

In Partial Fulfillment of the Requirements for the degree of

Doctor of Philosophy



Department of Chemistry
West Lafayette, Indiana
December 2020

**THE PURDUE UNIVERSITY GRADUATE SCHOOL
STATEMENT OF COMMITTEE APPROVAL**

Dr. Hilikka I. Kenttämä, Chair

Department of Chemistry

Dr. Scott A. McLuckey

Department of Chemistry

Dr. Mingji Dai

Department of Chemistry

Dr. Jianguo Mei

Department of Chemistry

Approved by:

Dr. Christine A. Hrycyna

*To my parents,
for their unconditional love and support*

ACKNOWLEDGMENTS

First of all, I would like to thank my PhD thesis advisor, Professor Hilkka I. Kenttamaa, for her guidance and help throughout the entire six years of my PhD studies. She is a mentor who not only cares about research work but makes any efforts to help students become a real professional scientist. I would also like to express my thanks to my thesis committee members, Dr Scott A. McLuckey, Dr Mingji Dai, and Dr Jianguo Mei, for their help and support. Also, Dr. John J. Nash is acknowledged for his help in quantum chemical calculations in almost all my research work, and Mark Carlson from Jonathan Amy Facility for Chemical Instrumentation of Purdue University, for his help and useful discussion on modification, troubleshooting and installment of different mass spectrometers.

Special thanks to Dr Jonas Warneke, my collaborator at Universität Leipzig in Germany, for his inspiration and useful discussion. I am always impressed by his enthusiastic, passionate and rigorous attitude toward science. His critical thinking on scientific challenges is invaluable to me.

I would like to thank past and current group members of Kenttamaa labs, for their mentorship, help and discussion. In particular, I would like to express my thanks to the friends I made at Purdue University, Dr Chunfen Jin, Dr Hanyu Zhu, Dr Joann Max, Dr Xueming Dong, Erlu Feng, Judy Kuan-Yu Liu, Victoria M. Boulos, Wanru Li, Hanning Jiang, Jie Wang, Shunyu Liu, and Bin Zhang for making my life at Purdue meaningful and memorable.

I would also like to express my gratitude to my family, especially my parents, for their unconditional love and endless support. I would never become who I am today without their love and support.

TABLE OF CONTENTS

LIST OF TABLES	9
LIST OF FIGURES	10
LIST OF SCHEMES.....	15
ABSTRACT.....	17
CHAPTER 1. INTRODUCTION AND OVERVIEW.....	18
1.1 Introduction.....	18
1.2 Thesis Overview	19
1.3 References.....	21
CHAPTER 2. INSTRUMENTATION AND PRINCIPLES OF LINEAR QUADRUPOLE ION TRAP MASS SPECTROMETRY AND HIGH-RESOLUTION ORBITRAP MASS SPECTROMETRY.....	23
2.1 Introduction.....	23
2.2 Ionization Methods	24
2.2.1 Electrospray Ionization.....	24
2.2.2 Atmospheric Pressure Chemical Ionization.....	26
2.3 Linear Quadrupole Ion Trap (LQIT) Mass Spectrometry.....	27
2.3.1 Overview.....	27
2.3.2 Ion motion in LQIT	30
2.3.3 Mass Analysis and Detection.....	34
2.3.4 Tandem Mass Spectrometry	36
2.4 Basic Principles of High-resolution Orbitrap Mass Spectrometry	37
2.4.1 Overview.....	38
2.4.2 Ion Transfer and Motion in the Orbitrap Mass Analyzer	38
2.5 Gas-phase Ion-molecule Reactions.....	39
2.5.1 Instrument Modifications for Ion-molecule Reactions in LQITs	40
2.5.2 Brauman's Double-well Potential Energy Surface.....	41
2.5.3 Kinetics of Gas-phase Ion-molecule Reactions.....	43
2.6 References.....	45

CHAPTER 3. SYNTHESIS OF RADICAL PRECURSORS AND LIGNIN MODEL COMPOUNDS.....	48
3.1 General Experimental Conditions.....	48
3.2 Synthesis of Quinoline-based <i>para</i> -Benzyne Precursors.....	48
3.2.1 Synthesis of 5-Iodo-8-nitroquinoline.....	48
3.2.2 Synthesis of 8-Iodo-5-nitroquinoline.....	49
3.2.3 Synthesis of 5,8-Diiodoquinoline	50
3.2.4 Synthesis of 5-Iodo-8-nitroisoquinoline	51
3.2.5 Synthesis of 5,8-Dithiomethylquinoline	52
3.3 Synthesis of Substituted Pyridine-based <i>meta</i> -Benzyne Precursors.....	53
3.3.1 Synthesis of 3-Hydroxy-2,6-diiodopyridine	53
3.3.2 Synthesis of 3-Cyano-2,6-diiodopyridine.....	54
3.3.3 Synthesis of 3-Amino-2,6-diiodopyridine	54
3.3.4 Synthesis of 3-Methoxy-2,6-diiodopyridine.....	55
3.4 Synthesis of Cyano-substituted Pyridine-based <i>para</i> -Benzyne Precursors	56
3.4.1 Synthesis of 2-Cyano-3,6-diiodopyridine.....	56
3.4.2 Synthesis of 4-Cyano-2,5-diiodopyridine.....	57
3.5 Synthesis of an H-lignin Model Compound	58
3.6 NMR Spectra	65
3.7 X-ray Crystallography	109
3.8 References.....	112
CHAPTER 4. GROUND-STATE SINGLET <i>META</i> -BENZYNE CATIONS REACT FROM AN EXCITED TRIPLET STATE	113
4.1 Introduction.....	113
4.2 Experimental Section	114
4.3 Results and Discussion	118
4.3.1 Reactions of Allyl Iodide.....	119
4.3.2 Reactions of <i>N</i> -Methylformamide	124
4.3.3 Reactions of Ethanol.....	125
4.3.4 Reactions of Tetrahydrofuran	126
4.3.5 Triplet-state Reactivity	129

4.3.6	Theroretical Disquisition	130
4.4	Conclusions.....	131
4.5	References.....	133
CHAPTER 5. POLAR EFFECTS CONTROL THE REACTIVITY OF THREE BIRADICALS WITH A 1,4-TOPOLOGY		136
5.1	Introduction.....	136
5.2	Experimental Section.....	136
5.3	Results and Discussion	139
5.3.1	Reactivity of the Biradicals Generated upon Ion Trap Collision-activated Dissociation.....	139
5.3.2	Reactivity of Biradicals Generated upon In-source Collison-activated Dissociation..	143
5.3.3	Structural Elucidation of the Highly Reactive Biradical Generated upon Two Consecutive ITCAD Steps of 1	144
5.3.4	Reactivity-controlling Factors for <i>para</i> -Benzynes 5 , 6 and 7	151
5.4	Conclusions.....	151
5.5	References.....	152
CHAPTER 6. REACTIVITY OF CYANO-SUBSTITUTED PYRIDINIUM-BASED <i>PARA</i> -BENZYNES ARE CONTROLLED BY POLAR EFFECTS.....		156
6.1	Introduction.....	156
6.2	Experimental Section	157
6.3	Results and Discussion	159
6.4	Conclusions.....	165
6.5	References.....	165
CHAPTER 7. GENERATION AND REACTIVITY STUDIES OF QUINOLINE-BASED OXENIUM CATIONS IN A LINEAR QUADRUPOLE ION TRAP MASS SPECTROMETER.....		168
7.1	Introduction.....	168
7.2	Experimental Section.....	169
7.3	Results and Discussion	170
7.3.1	Generation and Structure Characterization of the Oxenium Ions.....	170
7.3.2	Reactions with Dimethyl Disulfide, Allyl Iodide, and Cyclohexane	172

7.3.3	Reactions with Water, Methanol and Acetonitrile	179
7.3.4	Comparison to a Naphthalene-based Oxenium Ion	181
7.4	Conclusions.....	182
7.5	Future Work	183
7.6	References.....	183
CHAPTER 8. REACTIONS OF ELECTROPHILIC ANIONS $[B_{12}X_{11}]^-$ (X = Cl, Br) WITH HYDROCARBON MOLECULES: A SYSTEMATIC STUDY		185
8.1	Introduction.....	185
8.2	Experimental Section	186
8.3	Results and Discussion	187
8.3.1	Reactions with Acyclic Alkanes	187
8.3.2	Reactions with Cyclic Hydrocarbons	194
8.3.3	Reactions with Alkenes	197
8.3.4	Reactions with Aromatic Hydrocarbons.....	198
8.4	Conclusions.....	200
8.5	Future Work	201
8.6	References.....	201
VITA.....		203
PUBLICATIONS.....		204

LIST OF TABLES

Table 4.1 Reactions, total reaction efficiencies and branching ratios for primary products of biradicals 1 – 8 for reactions with allyl iodide and the calculated ΔE_{S-T} values (kcal mol ⁻¹) and PAs (kcal mol ⁻¹) of the conjugate bases of the biradicals in their singlet (S) and triplet (T) states. The experimental PAs of 1 and 2 were obtained previously by bracketing experiments ³⁶ and the calculated PA of allyl iodide was obtained from literature. ³⁵ Reactions that appear to occur from triplet states are bolded and underlined and the relevant PAs are bolded	121
Table 4.2 Reactions, reaction efficiencies and branching ratios for primary products of biradicals 1 – 8 upon interactions with tetrahydrofuran and their calculated ΔE_{S-T} values (kcal mol ⁻¹) and the PAs (kcal mol ⁻¹) of the conjugate bases of the biradicals in their singlet (S) and triplet (T) electronic states. The experimental PA of tetrahydrofuran was obtained from literature. ³⁷ The PA values in bold indicate which state is proposed to transfer a proton to tetrahydrofuran.	128
Table 5.1 Reactions, their efficiencies and primary product branching ratios for gas-phase reactions of dimethyl disulfide, cyclohexane and allyl iodide with the biradicals generated from 1 – 4 upon ITCAD and their calculated EA_{vs} and S-T splittings	141
Table 5.2 Reactions, their efficiencies, and the primary product branching ratios upon reactions with dimethyl disulfide, cyclohexane and allyl iodide for the unknown biradical generated from 1 and for biradicals 7 and 8 , together with their calculated EA_{vs} and S-T splittings.	150
Table 6.1 Reaction efficiencies ^a and product branching ratios for reactions of biradicals 1 – 4 ^b with dimethyl disulfide and cyclohexane, and their calculated ^c vertical electron affinities (EA_v) and S-T splittings (ΔE_{S-T}), as well as the proton affinities (PA) of their conjugate bases.	161
Table 6.2 Reaction efficiencies ^a and product branching ratios for reactions of monoradicals 5 – 12 ^b with dimethyl disulfide and cyclohexane and their calculated ^c vertical electron affinities (EA_v)	162
Table 7.1 Calculated relative enthalpies (H_{rel} , kcal mol ⁻¹) for 1 – 4 at their $1^3A''$, $1^3A'$, $1^1A'$ and $1^1A''$ states, and their corresponding vertical electron affinities (EA_v , eV), and the vertical electron affinity for quinoline radical cation	171
Table 7.2 Reactions, total reaction efficiencies and branching ratios for primary products of biradicals 1 – 4 for reactions with dimethyl disulfide, allyl iodide and cyclohexane, and their calculated EA_{vs} ^a (eV) and ΔE_{S-T} ^b values (kcal mol ⁻¹).....	178
Table 7.3 Reactions, total reaction efficiencies and branching ratios for primary products of biradicals 1 – 4 for reactions with dimethyl disulfide, allyl iodide and cyclohexane, and their calculated EA_{vs} ^a (eV) and ΔE_{S-T} ^b values (kcal mol ⁻¹).....	181
Table 7.4 Reactions, total reaction efficiencies and branching ratios for primary products of biradicals 5 for reactions with dimethyl disulfide and allyl iodide.....	182

LIST OF FIGURES

Figure 2.1 Illustration of the ionization process via ESI	24
Figure 2.2 Illustrations of (a) ion evaporation model (IEM) and (b) charge residue model (CRM) of a positively charged ion cluster	25
Figure 2.3 Illustration of an APCI source	27
Figure 2.4 Schematic drawing of an LQIT mass spectrometer and the typical operational pressures of each region.....	28
Figure 2.5 A typical DC potential gradient for the ion transmission in the API and ion optics region of an LQIT mass spectrometer.....	29
Figure 2.6 Schematic drawing of an LQIT mass analyzer.....	30
Figure 2.7 The Mathieu stability diagram for a linear quadrupole ion trap. Ions have stable trajectories are in the center region (line-crossed region) of the diagram, with proper a_u and q_u values.	32
Figure 2.8 Demonstration of the ions' axial trapping in z direction by a potential well generated by applying a DC potential gradient to the front, center and back section of the ion trap. Typically, the relative magnitude of the DC potentials is $DC\ 3 > DC\ 1 > DC\ 2$	33
Figure 2.9 Illustration of ions' ejection using resonance ejection approach in Mathieu stability diagram	34
Figure 2.10 Schematic drawing of the ion detection system	35
Figure 2.11 Tailored isolation RF waveform applied to x-rods of a linear quadrupole ion trap ..	36
Figure 2.12 Schematic drawing of an LQIT-orbitrap mass spectrometer	38
Figure 2.13 Schematic drawing of the external reagent mixing manifold.....	41
Figure 2.14 Potential energy surfaces for (a) reactions in solution and (b) reactions in gas-phase	42
Figure 2.15 The tightness of the TS energy level and the separated reactant energy level of a gas-phase ion-molecule reaction in a Brauman's double-well potential energy surface	43
Figure 3.1 ^1H NMR spectrum for 5-iodo-8-nitroquinoline.....	65
Figure 3.2 ^{13}C NMR spectrum for 5-iodo-8-nitroquinoline.....	66
Figure 3.3 ^1H NMR spectrum for 8-iodo-5-nitroquinoline.....	67
Figure 3.4 ^{13}C NMR spectrum for 8-iodo-5-nitroquinoline.....	68
Figure 3.5 ^1H NMR spectrum for 5,8-diiodoquinoline.....	69
Figure 3.6 ^{13}C NMR spectrum for 5,8-diiodoquinoline.....	70

Figure 3.7 ^1H NMR spectrum for 5-iodo-8-nitroisoquinoline	71
Figure 3.8 ^{13}C NMR spectrum for 5-iodo-8-nitroisoquinoline	72
Figure 3.9 ^1H NMR spectrum for 5,8-dithiomethylquinoline.....	73
Figure 3.10 ^{13}C NMR spectrum for 5,8-dithiomethylquinoline	74
Figure 3.11 ^1H NMR spectrum for 3-hydroxy-2,6-diiodopyridine.....	75
Figure 3.12 ^{13}C NMR spectrum for 3-hydroxy-2,6-diiodopyridine	76
Figure 3.13 ^1H NMR spectrum for 3-cyano-2,6-diiodopyridine	77
Figure 3.14 ^{13}C NMR spectrum for 3-cyano-2,6-diiodopyridine	78
Figure 3.15 ^1H NMR spectrum for 3-amino-2,6-diiodopyridine.....	79
Figure 3.16 ^{13}C NMR spectrum for 3-amino-2,6-diiodopyridine.....	80
Figure 3.17 ^1H NMR spectrum for 2,6-diiodo-3-methoxypyridine	81
Figure 3.18 ^{13}C NMR spectrum for 2,6-diiodo-3-methoxypyridine.....	82
Figure 3.19 ^1H NMR spectrum for 2-cyano-3,6-diiodopyridine	83
Figure 3.20 ^{13}C NMR spectrum for 2-cyano-3,6-diiodopyridine	84
Figure 3.21 ^1H NMR spectrum for 4-cyano-2,5-diiodopyridine	85
Figure 3.22 ^{13}C NMR spectrum for 4-cyano-2,5-diiodopyridine	86
Figure 3.23 ^1H NMR spectrum for 4-(benzyloxy)benzaldehyde.....	87
Figure 3.24 ^{13}C NMR spectrum for 4-(benzyloxy)benzaldehyde.....	88
Figure 3.25 ^1H NMR spectrum for methyl 2-phenoxyacetate	89
Figure 3.26 ^{13}C NMR spectrum for methyl 2-phenoxyacetate.....	90
Figure 3.27 ^1H NMR spectrum for methyl 3-(4-(benzyloxy)phenyl)-3-hydroxy-2-phenoxypropanoate.....	91
Figure 3.28 ^{13}C NMR spectrum for methyl 3-(4-(benzyloxy)phenyl)-3-hydroxy-2-phenoxypropanoate.....	92
Figure 3.29 ^1H NMR spectrum for 1-(4-(benzyloxy)phenyl)-2-phenoxypropane-1,3-diol.....	93
Figure 3.30 ^{13}C NMR spectrum for 1-(4-(benzyloxy)phenyl)-2-phenoxypropane-1,3-diol.....	94
Figure 3.31 ^1H NMR spectrum for 4-(4-(benzyloxy)phenyl)-2,2-dimethyl-5-phenoxy-1,3-dioxane	95
Figure 3.32 ^{13}C NMR spectrum for 4-(4-(benzyloxy)phenyl)-2,2-dimethyl-5-phenoxy-1,3-dioxane	96
Figure 3.33 ^1H NMR spectrum for 4-(2,2-dimethyl-5-phenoxy-1,3-dioxan-4-yl)phenol	97

Figure 3.34 ^{13}C NMR spectrum for 4-(2,2-dimethyl-5-phenoxy-1,3-dioxan-4-yl)phenol	98
Figure 3.35 ^1H NMR spectrum for methyl 2-(4-(2,2-dimethyl-5-phenoxy-1,3-dioxan-4-yl)phenoxy)acetate	99
Figure 3.36 ^{13}C NMR spectrum for methyl 2-(4-(2,2-dimethyl-5-phenoxy-1,3-dioxan-4-yl)phenoxy)acetate	100
Figure 3.37 ^1H NMR spectrum for methyl 3-(4-(benzyloxy)phenyl)-2-(4-(2,2-dimethyl-5-phenoxy-1,3-dioxan-4-yl)phenoxy)-3-hydroxypropanoate	101
Figure 3.38 ^{13}C NMR spectrum for methyl 3-(4-(benzyloxy)phenyl)-2-(4-(2,2-dimethyl-5-phenoxy-1,3-dioxan-4-yl)phenoxy)-3-hydroxypropanoate	102
Figure 3.39 ^1H NMR spectrum for 1-(4-(benzyloxy)phenyl)-2-(4-(2,2-dimethyl-5-phenoxy-1,3-dioxan-4-yl)phenoxy)propane-1,3-diol	103
Figure 3.40 ^{13}C NMR spectrum for 1-(4-(benzyloxy)phenyl)-2-(4-(2,2-dimethyl-5-phenoxy-1,3-dioxan-4-yl)phenoxy)propane-1,3-diol	104
Figure 3.41 ^1H NMR spectrum for 2-(4-(2,2-dimethyl-5-phenoxy-1,3-dioxan-4-yl)phenoxy)-1-(4-hydroxyphenyl)propane-1,3-diol	105
Figure 3.42 ^{13}C NMR spectrum for 2-(4-(2,2-dimethyl-5-phenoxy-1,3-dioxan-4-yl)phenoxy)-1-(4-hydroxyphenyl)propane-1,3-diol	106
Figure 3.43 ^1H NMR spectrum for 1-(4-((1,3-dihydroxy-1-(4-hydroxyphenyl)propan-2-yl)oxy)phenyl)-2-phenoxypropane-1,3-diol	107
Figure 3.44 ^{13}C NMR spectrum for 1-(4-((1,3-dihydroxy-1-(4-hydroxyphenyl)propan-2-yl)oxy)phenyl)-2-phenoxypropane-1,3-diol	108
Figure 3.45 5-Iodo-8-nitroquinoline	109
Figure 3.46 3-Hydroxy-2,6-diiodopyridine	109
Figure 3.47 3-Cyano-2,6-diiodopyridine	110
Figure 3.48 3-Amino-2,6-diiodopyridine	110
Figure 3.49 2,6-Diiodo-3-methoxypyridine	110
Figure 3.50 2-Cyano-3,6-diiodopyridine	111
Figure 3.51 4-Cyano-2,5-diiodopyridine	111
Figure 4.1 Studied biradicals	114
Figure 4.2 Mass spectra measured after 300 ms reactions with allyl iodide for (a) 3 , (b) 5 (zoomed area near m/z 169), and (c) 7 . The proton transfer product ions (m/z 169) are labelled in red. The ions of m/z of 81 and 295 are secondary product ions formed upon reactions of the ions of m/z 169 with allyl iodide (see Table 1 for their identities). The ion of m/z 96 is a water adduct formed from 1 upon reactions with adventitious water in the ion trap.	124

Figure 4.3 (a) Mass spectrum measured after 300 ms of reactions of **8** with *N*-methylformamide. The proton transfer product ion (m/z 60) is labelled in red. The ion of m/z 119 is the protonated *N*-methylformamide dimer generated upon reactions of the ion of m/z 60 with *N*-methylformamide. The ion of m/z 146 is a water adduct formed upon reactions of **8** with adventitious water in the ion trap. The ion of m/z 187 is an adduct of **8** with *N*-methylformamide and the ion of m/z 205 is a water adduct of this ion. The ions of m/z 159 and m/z 170 are fragment ions of the ion of m/z 187 formed via loss of CO and NH₃, respectively. (b) Mass spectrum measured after 3000 ms reactions of **1** with *N*-methylformamide. The ion of m/z 96 is an adduct formed upon reactions of **1** with adventitious water in the ion trap..... 125

Figure 4.4 Mass spectra measured after 300 ms reactions with ethanol for (a) **4** and (b) **6**. The proton transfer product ions (m/z 47) are labelled in red. The ions of m/z 75 and 93 are secondary product ions formed upon reactions of the ions of m/z 47 with ethanol; the ion of m/z 93 is a protonated ethanol dimer and the ion of m/z 75 is the product formed from the ion of m/z 93 upon elimination of a water molecule. The ions of m/z 121 and 131 are formed upon dissociation of the ethanol adduct (m/z 149) via elimination of ethylene and water, respectively..... 126

Figure 5.1 Four protonated biradical precursors..... 139

Figure 5.2 Mass spectra measured after 1,000 ms reaction with dimethyl disulfide for the biradicals generated from precursors **1** – **4** (a – d). 140

Figure 5.3 ITCAD mass spectra obtained using the same collision energy (20, arbitrary units) for (a) the product ion of m/z 222 formed upon abstraction of two SCH₃ groups from dimethyl disulfide by the biradical generated from **1** and (b) the authentic 5,8-dithiomethylquinolinium cation. .. 143

Figure 5.4 Reaction product mass spectra measured for the unknown biradical generated from **1** by using (a) ITCAD and (b) ISCAD after 1,000 ms reaction with dimethyl disulfide..... 144

Figure 5.5 ITCAD mass spectra obtained using the same collision energy (40 arbitrary units) for (a) **1** and (b) **2** (ions of m/z 301). **9** has a higher relative abundance than **10** in part a because the C-NO₂ bond is easier to break than the C-I bond in a cation..... 145

Figure 5.6 The product ion mass spectra measured for (a) the unknown reactive biradical generated from **9** upon ITCAD and (b) the biradical generated from **10** upon ITCAD after reactions with dimethyl disulfide for 1,000 ms. 146

Figure 5.7 ITCAD mass spectra for the product ions of m/z of 222 generated upon abstraction of two SCH₃ groups from dimethyl disulfide by (a) the unknown biradical generated from **1** and (b) biradical **7**..... 149

Figure 6.1 *para*-Benzyne analogs studied 157

Figure 7.1 Generation of the studied oxenium ions in LQIT and studied oxenium ions..... 169

Figure 7.2 Important resonance structures of **1** – **4** 172

Figure 7.3 Mass spectra measured after 100 ms reactions with dimethyl disulfide for **1** – **4**, the ion of m/z 162 is an adduct formed upon reactions with adventitious water in the ion trap..... 173

Figure 7.4 CAD mass spectra of the adduct ions (m/z 238) formed upon reactions of **1** – **3** with dimethyl disulfide (collision energy 15, arbitrary unit). 174

Figure 7.5 Mass spectra measured after 100 ms reactions with allyl iodide for 1 – 4 , the ion of m/z 162 is an adduct formed upon reactions with adventitious water in the ion trap.....	176
Figure 7.6 Mass spectra measured after 1000 ms reactions with cyclohexane for 1 – 4 , the ion of m/z 162 is an adduct formed upon reactions with adventitious water in the ion trap.	176
Figure 7.7 Mass spectra measured after 100 ms reactions with water for 1 – 4	179
Figure 7.8 Mass spectra measured after 100 ms reactions with methanol for 1 – 4 , the ion of m/z 162 is an adduct formed upon reactions with adventitious water in the ion trap.....	180
Figure 7.9 Mass spectra measured after 100 ms reactions with acetonitrile for 1 – 4 , the ion of m/z 162 is an adduct formed upon reactions with adventitious water in the ion trap.....	180
Figure 8.1 Illustration of the electrophilic $[B_{12}X_{11}]^-$ anion	185
Figure 8.2 CAD Fragmentation spectra of the $[B_{12}Br_{11}]^-$ adducts with five different isomers of C_6H_{14} . The color code is explained in the text.....	190
Figure 8.3 Reaction mass spectrum of $[B_{12}Br_{11}]^-$ with cyclohexane after 30 ms of reaction.	194
Figure 8.4 CAD mass spectra of the adduct ions upon the reactions of $[B_{12}Br_{11}]^-$ with (a) cyclohexane, (b) cyclohexene, and (c) 1,3-cyclohexadiene (Collision energies 25, 30, and 30, arbitrary units, respectively).	195
Figure 8.5 CAD mass spectra of the adduct ions upon the reactions of $[B_{12}Br_{11}]^-$ with (a) cyclohexane, and (b) cyclohexane- d_{12}	196
Figure 8.6 Reaction mass spectrum of $[B_{12}Br_{11}]^-$ with 1-hexene after 30 ms of reaction.....	197
Figure 8.7 CAD mass spectrum of the adduct ion formed upon the reaction of $[B_{12}Br_{11}]^-$ with 1-hexene.	198
Figure 8.8 CAD mass spectra of the adduct ions formed upon reactions of $[B_{12}Br_{11}]^-$ with (a) benzene, (b) styrene, and (c) <i>trans</i> - β -Methylstyrene. (Collision energy 30, arbitrary units, the ion of m/z 1129: unidentified peak)	199

LIST OF SCHEMES

Scheme 2.1 One possible ionization (protonation) mechanism for APCI using N ₂ as the reagent gas, "A" refers to the analyte molecule	26
Scheme 3.1 Synthetic route to 5-iodo-8-nitroquinoline.....	48
Scheme 3.2 Synthetic route to 8-iodo-5-nitroquinoline.....	49
Scheme 3.3 Synthetic route to 5,8-diiodoquinoline.....	50
Scheme 3.4 Synthetic route to 5-iodo-8-nitroisoquinoline	51
Scheme 3.5 Synthesis of 5,8-Dithiomethylquinoline	52
Scheme 3.6 Synthetic route to 3-hydroxy-2,6-diiodopyridine.....	53
Scheme 3.7 Synthetic route to 3-cyano-2,6-diiodopyridine	54
Scheme 3.8 Synthetic route to 3-amino-2,6-diiodopyridine.....	54
Scheme 3.9 Synthetic route to 3-methoxy-2,6-diiodopyridine.....	55
Scheme 3.10 Synthetic route to 2-cyano-3,6-diiodopyridine	56
Scheme 3.11 Synthetic route to 4-cyano-2,5-diiodopyridine	57
Scheme 3.12 Synthetic route to an H-lignin trimer with β -O-4 linkages	59
Scheme 5.1 Attempted generation of the 5,8-didehydroisoquinolinium cation.	136
Scheme 5.2 Proposed mechanism for the formation of 7 from 1 upon ITCAD	146
Scheme 5.3 Calculated enthalpy changes for two possible iodine atom loss reactions from 3 to generate 5 (all numbers are in kcal/mol and relative to the protonated radical precursor; M062X-6-311++(d,p) level of theory)	147
Scheme 5.4 Generation of authentic biradical 7	148
Scheme 5.5 Two competing reaction pathways after the first ITCAD event of 3 . Top: <i>retro</i> -Bergman cyclization; bottom: <i>para</i> -benzyne (5) formation. The same applies to generation of biradical 6	148
Scheme 6.1 Proposed mechanisms for two H atom abstractions, ¹⁴ H atom abstraction followed by electron transfer, ³⁰ and H atom abstraction followed by radical-radical recombination for biradical 2 upon reactions with cyclohexane.	163
Scheme 6.2 Proposed mechanisms for two SCH ₃ abstractions by biradical 1 upon reaction with two dimethyl disulfide molecules.	164
Scheme 6.3 Proposed zwitterionic resonance structures for the transition state of the H atom abstraction reaction by biradical 3	165

Scheme 7.1 Possible addition and fragmentation mechanism for reactions of 2 and dimethyl disulfide.....	174
Scheme 7.2 Proposed mechanism for CH ₂ abstraction (<i>m/z</i> 158) by 4 from dimethyl disulfide	175
Scheme 7.3 Proposed mechanism for the formation of the ion of <i>m/z</i> 146 (“2 × H abstraction”) upon reactions of 1 with cyclohexane.....	175
Scheme 8.1 Three possible elementary mechanisms for the reaction between the electrophilic [B ₁₂ Br ₁₁] ⁻ anion and alkane molecule	188
Scheme 8.2 Fragmentation reaction leading to the [B ₁₂ Br ₁₁ CH ₂] ⁻ adduct (blue-marked signals in Figure 8.2). α-R denotes fragmentation of the C-C bond next to the α-carbon of the alkyl residue.	191
Scheme 8.3 Fragmentation reaction leading to the [B ₁₂ Br ₁₁ C ₂ H ₄] ⁻ adduct (yellow-marked signals in Figure 8.2). β-R denotes fragmentation of the C-C bond next to the β-carbon of the alkyl residue.	192
Scheme 8.4 Possible mechanism for the formation of homologous ions with a variable number of CH ₂ units [B ₁₂ Br ₁₁ C _{<i>n</i>} H _{2<i>n</i>}] ⁻ (<i>n</i> = 3–5, yellow-marked signals in Figure 8.2) in the case of <i>n</i> -hexane. β-R denotes fragmentation of the C-C bond next to the β-carbon of the alkyl residue.	192
Scheme 8.5 Fragmentation reaction leading to the [B ₁₂ Br ₁₁ H ₂] ⁻ adduct (purple-marked signals in Figure 8.2).....	193
Scheme 8.6 Reaction of an alkene with a quaternary center with [B ₁₂ Br ₁₁] ⁻ , leading to [B ₁₂ Br ₁₁ CH ₃] ⁻ adduct (red-marked signals in Figure 8.2) upon the fragmentation of the reaction intermediate.....	193
Scheme 8.7 Proposed addition mechanism of [B ₁₂ Br ₁₁] ⁻ to alkenes (a) and proposed mechanism for the formation of the ion of <i>m/z</i> 1011 upon reactions of [B ₁₂ Br ₁₁] ⁻ and alkenes.....	198
Scheme 8.8 Proposed addition mechanism of [B ₁₂ Br ₁₁] ⁻ to benzene.....	199

ABSTRACT

Mass spectrometry (MS) is a powerful and versatile analytical tool, especially for identification and analysis of complex mixtures. Coupling to high-performance liquid chromatography (HPLC) or gas chromatography (GC) provides additional dimension for mixture analysis. MS manipulates ionized analytes and separates them based on their *mass-to-charge* (m/z) ratios. MS is capable of providing molecular weight (MW) information by generating pseudo-molecular ions of the analytes. Detailed elemental compositions can be also obtained if high resolution MS is used. MS can also provide extensive structural information of the analyte ions. One of the most commonly used technique is tandem mass spectrometry (MS^n). Ions of interest are isolated and subject to sequential reactions (reactions with other molecules or dissociation reactions) to generate product ions that can provide structural information. MS is also a powerful tool for generating and studying highly reactive reaction intermediates, such as organic polyradicals.

The research described in this dissertation mainly focuses on the generation and gas-phase reactivity studies of different organic biradicals. Their reactions with various organic reagents are studied, and the reactivity-controlling factors are discussed. For example, the reactivity of several substituted pyridine-based biradical cations with 2,6-topology are discussed (all with singlet ground states), and their special reactivity from their excited triplet states are illustrated. Besides, several quinoline-based biradicals and cyano-substituted pyridine-based *para*-benzyne cations are also discussed. Some of the radicals (or ions) described in this dissertation are generated for the first time, i.e. the quinoline-based oxenium cations. Their structural characterization and gas-phase reactivity toward some organic molecules are discussed in the dissertation. Further, an electrophilic anion, *closo*- $[B_{12}X_{11}]^-$ ($X = Cl, Br$) and its application in the activation of C-H and C-C bonds in hydrocarbon molecules are described in the dissertation.

CHAPTER 1. INTRODUCTION AND OVERVIEW

1.1 Introduction

Mass spectrometry (MS) is a powerful analytical tool that has been flourishing for more than a century since its first introduction by J. J. Thomson in 1913.¹ Currently, MS has extensive applications in many different areas such as pharmaceutical industry,² petroleum industry,³ environmental science,⁴ and materials science.⁵ Further, with the continuous development of more powerful MS instruments, MS technique keeps gaining more sensitivity, accuracy, specificity and versatility to resolve various new analytical challenges.⁶

Despite the many variations in MS instrumentation, the core of most MS experiments includes the following four steps. The first step is analyte introduction/evaporation into the gas phase, followed by the second step, which is the ionization of the gas-phase molecules for MS manipulation under vacuum. In the third step, the ionized analytes are separated from each other based on their *mass-to-charge* (m/z) ratios. Finally, in the fourth step, the ions are detected. In tandem mass spectrometry (MS/MS) experiments, the ionized analytes can be isolated from all other ions and subjected to reactions followed by further MS analysis and detection. A typical mass spectrum shows the relative abundances of the detected ions as a function of their m/z -ratio.

A desirable mass spectrum provides information on the molecular weight (MW) of the analyte via generation of a stable molecular ion or pseudo-molecular ion structural information for the analyte ion via reactions. If very accurate mass measurements can be performed, then the mass spectrum can also provide the elemental composition of the analyte.⁷

Sometimes, structural information is obtained for the ionized analyte ions by measuring a simple mass spectrum.⁸ However, more often, this is accomplished via tandem mass spectrometry (MSⁿ) experiments.⁹ In a typical MSⁿ experiment, the ions of interest are isolated from the other ions and subjected to reactions. The product ions usually contain characteristic structural motifs that are present in the precursor ions and therefore provide structural information. Fragmentation reactions are commonly used, and collision-activated dissociation (CAD) is one of the most widely

used fragmentation techniques.¹⁰ In a typical CAD experiment, the isolated precursor ions are accelerated and allowed to collide with inert gas molecules to convert part of their kinetic energy into their internal energy. When enough internal energy has been accumulated in the ion, fragmentation occurs,¹¹ and structural information is often obtained.

Nonetheless, CAD cannot always provide adequate structural information, e.g., structural isomeric ions often fragment in the same manner.¹² Therefore, ion-molecule reactions have been explored and used as an alternative means of providing extra dimension(s) of structural information for analyte ions.¹³ Instead of accelerating the analyte ions and allowing them to undergo collisions with inert gas molecules, in ion-molecule reactions, the analyte ions (that are not accelerated) are enabled to react with neutral reagent molecules to generate diagnostic product ions. By proper selection of the reagent molecules, structural information can be obtained, which may enable the differentiation of isomeric ions.^{14,15} Furthermore, the product ions formed upon ion-molecule reactions can be subjected to CAD to obtain more structural information.^{14,15} Therefore, multistep tandem mass spectrometric (MS^n) techniques based on CAD and ion-molecule reactions are desirable in complex mixture analysis, such as analysis of pharmaceutical products and biofuels.^{15,16} Additionally, coupling of such techniques to chromatography, such as liquid chromatography, can further improve the applicability of the method.^{14,15}

Ion trap mass spectrometers are exceptionally useful for studies of charged reactive reaction intermediates that cannot be readily studied in the condensed phases due to the difficulty in either generating pure intermediates or due to their high reactivities under these conditions.¹⁷ Therefore, studies of charged reaction intermediates, such as charged organic radicals, have been extensively conducted using tandem mass spectrometry, including studies of the generation, reactions and reaction kinetics of charged mono- and polyradicals.^{18,19} Many novel charged radicals have been generated in mass spectrometers over the past decades.²⁰

1.2 Thesis Overview

The basic principles of ionization techniques, linear quadrupole ion trap mass spectrometry, orbitrap mass spectrometry, tandem mass spectrometry techniques, and fundamental aspects of collision-activated dissociation in a linear quadrupole ion trap mass spectrometer, and fundamental

aspects of gas-phase ion-molecule reactions are discussed in Chapter 2 of the dissertation. Chapter 3 lists all the synthetic procedures for radical precursors and H-lignin model compounds, with their NMR spectra and some X-ray crystallography images. The rest of the dissertation mainly focuses on the discovery and reactivity studies of different organic biradicals, the reactivity studies of fragment ions of a *closo*-borate anion $[\text{B}_{12}\text{X}_{12}]^{2-}$ ($\text{X} = \text{Cl}, \text{Br}$), and the development of functional-group selective ion-molecule reactions, described as below.

1) Studies of the reactivity of different organic biradicals. Chapter 4 introduces the discovery that several protonated *meta*-benzynes react from an excited triplet state although they all have singlet ground states. The reactivity of the *meta*-benzynes toward four different reagents are discussed, and one unique product, formed via transfer of a proton from the protonated *meta*-benzynes to the reagents, is emphasized as it is indicative of the triplet reactivity of the *meta*-benzynes. Chapter 5 discusses the formation of a novel, highly reactive biradical while attempting to generate a quinoline-based *para*-benzyne. This chapter focuses on attempts of the generation of a *para*-benzyne analog by using different radical precursors and different fragmentation techniques. Factors that control the reactivity of the biradicals are also discussed. Chapter 6 focuses on the study of the reactivity-controlling factors of three isomeric cyano-substituted *para*-benzyne analogs. Chapter 7 introduces the discovery of four quinoline-based oxenium cations and their reactivity toward different reagents. They were proved as carbocations instead of biradicals based on reactions with organic molecules that typically show diagnostic radical reaction products, and reactions with nucleophiles. The structures of these newly discovered cations based on quantum chemical calculations are also discussed.

2) Chapter 8 mainly focuses on ion-molecule reactions of fragment ions of a *closo*-borate anion $[\text{B}_{12}\text{X}_{12}]^{2-}$ ($\text{X} = \text{Cl}, \text{Br}$). This chapter discusses the activation of C-H and C-C bonds in hydrocarbons by using ion-molecule reactions with *closo*- $[\text{B}_{12}\text{X}_{11}]^-$ ions (formed upon elimination of an X^- ion from $[\text{B}_{12}\text{X}_{12}]^{2-}$). The reaction patterns of *closo*- $[\text{B}_{12}\text{X}_{11}]^-$ ions with different classes of hydrocarbon molecules and studies of the possible reaction mechanisms are also discussed in detail in this chapter.

1.3 References

1. Thomson, J. J. *Rays of Positive Electricity and Their Application to Chemical Analyses*; Longmans, Green and Co.: London, 1913.
2. Leurs, U.; Mistarz, U. H.; Rand, K. D. *Eur. J. Pharm. Biopharm.* **2015**, *93*, 95–109.
3. Rodgers, R. P.; McKenna, A. M. *Anal. Chem.* **2011**, *83* (12), 4665–4687.
4. Petras, D.; Nothias, L.-F.; Quinn, R. A.; Alexandrov, T.; Bandeira, N.; Bouslimani, A.; Castro-Falcón, G.; Chen, L.; Dang, T.; Floros, D. J.; Hook, V.; Garg, N.; Hoffner, N.; Jiang, Y.; Kapono, C. A.; Koester, I.; Knight, R.; Leber, C. A.; Ling, T.-J.; Luzzatto-Knaan, T.; McCall, L.-I.; McGrath, A. P.; Meehan, M. J.; Merritt, J. K.; Mills, R. H.; Morton, J.; Podvin, S.; Protsyuk, I.; Purdy, T.; Satterfield, K.; Searles, S.; Shah, S.; Shires, S.; Steffen, D.; White, M.; Todoric, J.; Tuttle, R.; Wojnicz, A.; Sapp, V.; Vargas, F.; Yang, J.; Zhang, C.; Dorrestein, P. C. *Anal. Chem.* **2016**, *88* (22), 10775–10784.
5. Schudel, G.; Lai, V.; Gordon, K.; Weis, D. *Chem. Geol.* **2015**, *410*, 223–236.
6. McLuckey, S. A.; Wells, J. M. *Chem. Rev.* **2001**, *101* (2), 571–606.
7. Hernández, F.; Sancho, J. V.; Ibáñez, M.; Abad, E.; Portolés, T.; Mattioli, L. *Anal. Bioanal. Chem.* **2012**, *403* (5), 1251–1264.
8. Griffiths, J. *Anal. Chem.* **2008**, *80*(15), 5678–5683.
9. Louris, J. N.; Brodbelt-Lustig, J. S.; Graham Cooks, R.; Glish, G. L.; van Berkel, G. J.; McLuckey, S. A. *Int. J. Mass Spectrom. Ion Processes* **1990**, *96* (2), 117–137.
10. Sleno, L.; Volmer, D. A. *J. Mass Spectrom.* **2004**, *39*(10), 1091–1112.
11. Cooks, R. G. *J. Mass Spectrom.* **1995**, *30* (9), 1215–1221.
12. Castro-Perez, J. M. *Drug Discov. Today* **2007**, *12* (5–6), 249–256.
13. Osburn, S.; Ryzhov, V. *Anal. Chem.* **2013**, *85*(2), 769–778.
14. Kong, J. Y.; Yu, Z.; Easton, M. W.; Niyonsaba, E.; Ma, X.; Yerabolu, R.; Sheng, H.; Jarrell, T. M.; Zhang, Z.; Ghosh, A. K.; Kenttämaa, H. I. *Anal. Chem.* **2018**, *90*(15), 9426–9433.
15. Zhu, H.; Ma, X.; Kong, J. Y.; Zhang, M.; Kenttämaa, H. I. *J. Am. Soc. Mass Spectrom.* **2017**, *28* (10), 2189–2200.
16. Sheng, H.; Tang, W.; Gao, J.; Riedeman, J. S.; Li, G.; Jarrell, T. M.; Hurt, M. R.; Yang, L.; Murria, P.; Ma, X.; Nash, J. J.; Kenttämaa, H. I. *Anal. Chem.* **2017**, *89* (24), 13089–13096.
17. Williams, P. E.; Jankiewicz, B. J.; Yang, L.; Kenttämaa, H. I. *Chem. Rev.* **2013**, *113* (9), 6949–6985.

18. Kotha, R. R.; Nash, J. J.; Kentt ämaa, Hilikka I. *Eur. J. Org. Chem.* **2017**, 2017(11), 1407–1412.
19. Ma, X.; Jin, C.; Wang, D.; Nash, J. J.; Kentt ämaa, H. I. *Chem. Eur. J.* **2019**, 25 (25), 6355–6361.
20. Max, J.; Ma, X.; Kotha, R.; Ding, D.; Milton, J.; Nash, J. J.; Kentt ämaa, H. I. *Int. J. Mass Spectrom.* **2019**, 435, 280–290.

CHAPTER 2. INSTRUMENTATION AND PRINCIPLES OF LINEAR QUADRUPOLE ION TRAP MASS SPECTROMETRY AND HIGH-RESOLUTION ORBITRAP MASS SPECTROMETRY

2.1 Introduction

Mass spectrometry (MS) has become one of the most powerful analytical techniques throughout the development of decades.¹ Many challenging problems related to environment, energy and pharmaceutical industry have been successfully solved, and accordingly, MS techniques and instrumentations have been continuously and largely improved to tackle more demanding analytical challenges.²⁻⁶

Typical MS analysis involves three basic steps. 1) Ion generation. Analytes in solutions must undergo solvent evaporation followed by ionization for MS manipulations. Therefore, various types of ionization techniques have been developed for different analytes and experimental conditions, such as electron ionization (EI),⁷ chemical ionization (CI),⁸ electrospray ionization (ESI),^{9,10} desorption electrospray ionization (DESI),¹¹ direct analysis in real time (DART),¹² atmospheric pressure chemical ionization (APCI),^{13,14} atmospheric pressure photoionization (APPI), field desorption/field ionization (FD/FI),^{15,16} matrix-assisted laser desorption ionization (MALDI),¹⁷ laser desorption/ionization (LDI),¹⁸ and many other ionization techniques. In the context of this dissertation, ESI and APCI are the two ionization techniques used for all the experiments and will be introduced in detail in the following sections. 2) Separation of ions based on their mass-to-charge (m/z) ratios. Different mass analyzers can separate ions in different ways based on various principles. This dissertation will mainly focus on the principles of trapping instruments, where ions are confined in a certain space for manipulation and separation. Linear quadrupole ion trap (LQIT) mass spectrometer and high-resolution orbitrap mass spectrometer are two types of trapping instruments used for the research in this dissertation. Trapping instruments are excellent in gas-phase ion-molecule reaction kinetics studies. The theoretical and experimental aspects of these two types of instruments will be described in detail. 3) Detection of ions. Ions after separation will be ejected to detectors and their relative abundances will be measured as a function of m/z values. Basic principles for detection of ions will be introduced in this dissertation.

2.2 Ionization Methods

Evaporation and ionization of analytes are the essential first steps for MS analysis. A wide range of ionization techniques have been developed for different experimental conditions and different physical and chemical properties of analytes. In particular, two atmospheric pressure ionization techniques, electrospray ionization (ESI) and atmospheric pressure chemical ionization (APCI) will be introduced in this section.

2.2.1 Electrospray Ionization

Electrospray ionization (ESI) was invented in 1989 as a “soft” ionization technique¹⁸ compared to electron ionization (EI) as it does not cause extensive fragmentations of analytes upon ionization. It is especially good for ionizing polar and thermally labile analytes.¹⁹⁻²¹ Additionally, ESI is good for analyzing macromolecules as it tends to generate multiply charged ions. Therefore, mass spectrometric analysis of proteins and other biomolecules has become a crucial research topic. For ESI operated at positive ion mode, analytes tend to form protonated molecules with one (singly charged) or more protons (multiply charged) attached to the analyte molecules. In negative ion mode, analyte molecules are usually deprotonated.

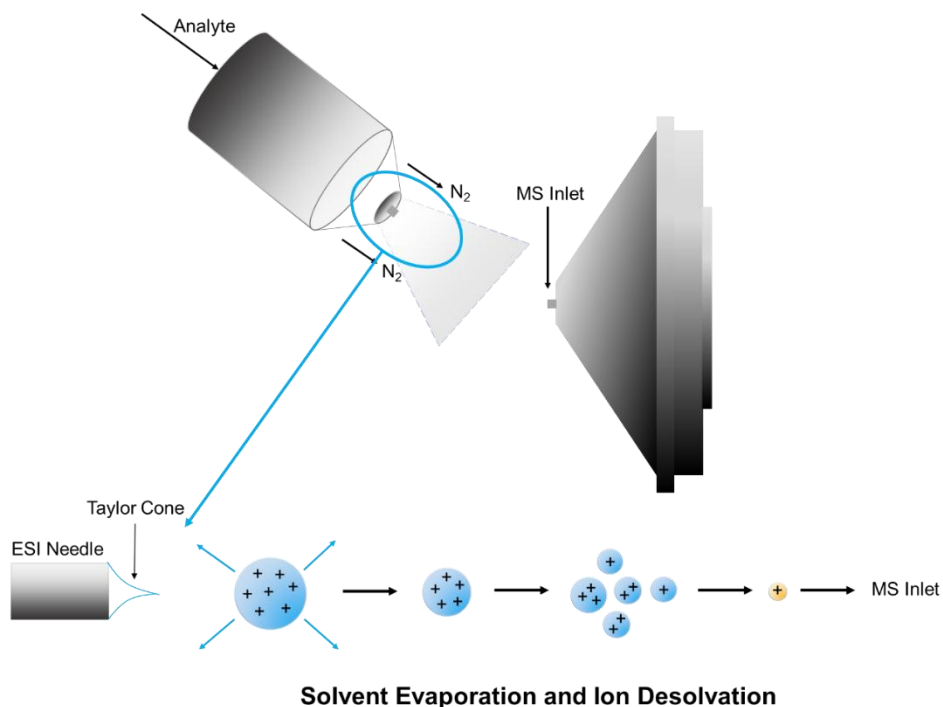


Figure 2.1 Illustration of the ionization process via ESI

As shown in Figure 2.1, the solution containing analytes gets charged at the tip of the ESI capillary (the “needle”) by a high voltage ($\pm 2 - 5$ kV),²⁰ and a fine mist of multiply charged droplets are formed.² The charged droplets are then evaporated, and the analytes are desolvated with the help of a drying gas (usually N₂).²² As the evaporation of the solvents, smaller droplets with prominently larger electrostatic repulsion will eventually overcome the surface tension of the droplet. At this critical point (so-called “Rayleigh instability limit”), the droplets further break into even smaller droplets, and the process repeats till all solvent molecules are removed.

Two models were proposed to describe the solvent evaporation and analyte ionization processes in ESI, the ion evaporation model (IEM, Figure 2.2 (a))^{23,24} and the charge residue model (CRM, Figure 2.2 (b)).²⁵ In IEM, an individual ion is ejected rapidly from a large charged droplet near the Rayleigh instability limit, till all the ions are ejected into the gas phase. In CRM, larger charged droplets shrink into smaller droplets due to solvent evaporation and a tiny droplet is emitted from the tip of the “Taylor cone” formed due to the large electrostatic repulsion interactions. The process repeats until all the analytes are evaporated and ionized.²⁶

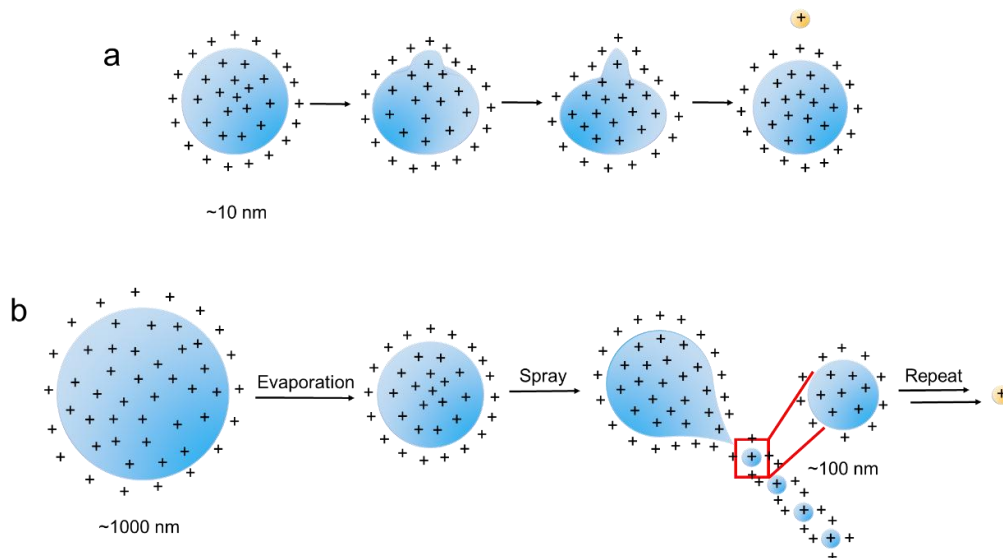
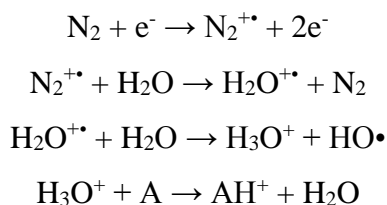


Figure 2.2 Illustrations of (a) ion evaporation model (IEM) and (b) charge residue model (CRM) of a positively charged ion cluster

2.2.2 Atmospheric Pressure Chemical Ionization

Atmospheric pressure chemical ionization (APCI) is another relatively “soft” ionization technique that is good for low polarity analytes.²⁷ Similar to chemical ionization (CI), the analyte molecules get ionized via a series of charge transfer reactions initiated by the ionization of a reagent molecule. A typical APCI reagent molecule used in a linear quadrupole ion trap (LQIT) mass spectrometer is N₂ (Scheme 2.1).



Scheme 2.1 One possible ionization (protonation) mechanism for APCI using N₂ as the reagent gas, “A” refers to the analyte molecule

The solution containing analyte molecules are heated to evaporation in the APCI source and formed a mist of analyte and solvent vapor together with the nitrogen sheath gas. Nitrogen molecular ions are generated by the Corona discharge ionization of the N₂ gas.² The nitrogen molecular ions, known as the primary ions, then ionize other molecules such as solvent molecules and molecules in the vapor. The produced secondary ions, such as molecular ions of water and hydronium ion, react with nitrogen molecular ions or themselves to generate protonated secondary ions. Eventually the protonated secondary ions will transfer the protons to the analyte molecules (Figure 2.3).

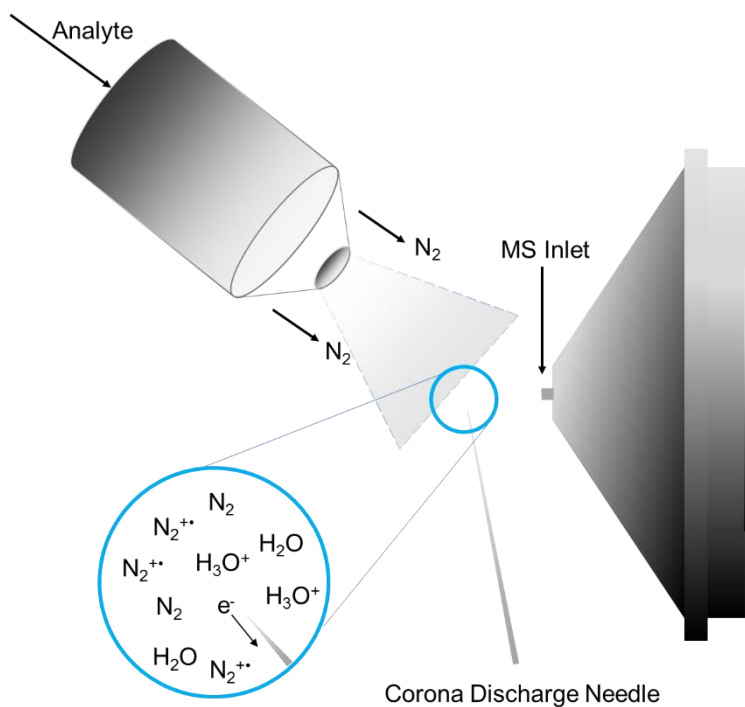


Figure 2.3 Illustration of an APCI source

2.3 Linear Quadrupole Ion Trap (LQIT) Mass Spectrometry

2.3.1 Overview

LQIT experiments in this dissertation were performed in Thermo LTQ linear quadrupole ion trap mass spectrometers equipped with an ESI or APCI source.^{28,29} A schematic drawing of the LQIT is shown in Figure 2.4. The LQIT consists of three basic sections: the atmospheric-pressure ionization (API) region, the ion optics region and the ion trap and detector region. A Leybold T220/150/15S triple-inlet turbomolecular pump is used to maintain the pressure of each region. An Edwards E2M30 rotary-vane mechanical pump evacuates the turbomolecular pump.

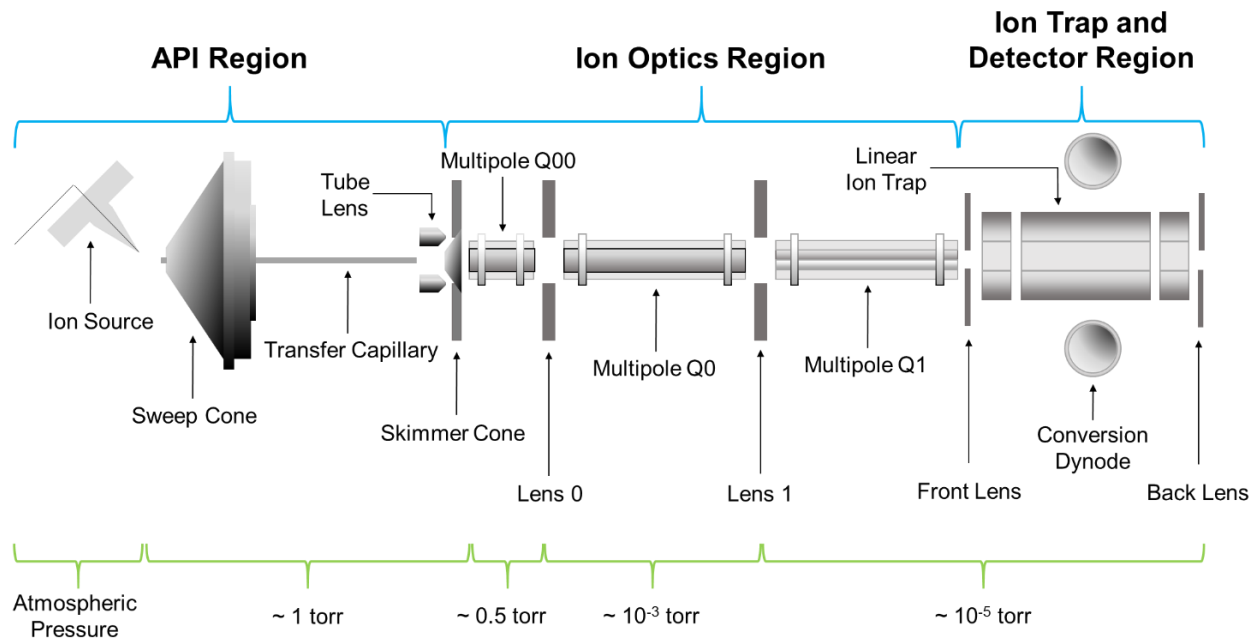


Figure 2.4 Schematic drawing of an LQIT mass spectrometer and the typical operational pressures of each region

2.3.1.1 The API Region

The API region consists of the ion source box, which operates at the atmospheric pressure, and the low-pressure API stack operating at ~ 1 torr, which is maintained by the mechanical pumps. The ion source box holds the ionization sources (ESI, APCI or APPI) at the operational position, it also sets a corona discharge needle and a sweep cone. The API stack consists of an ion transfer capillary, a tube lens and a skimmer cone. The ions generated in the ESI or APCI source are drawn into the API stack due to the pressure gradient and a direct current (DC) voltage gradient (2 – 5 kV to ~ 20 V). The ion beam is guided through the heated transfer capillary, directed by the tube lens to the skimmer cone. The skimmer cone is placed off center of the capillary to prevent neutral molecules from entering the lower-pressure region.²⁹

2.3.1.2 The Ion Optics Region

The ion optics focuses and directs the ion beam toward the ion trap along the axial (z) direction. It consists of two square quadrupoles, Q00 and Q0, and a cylindrical octupole, Q1. Two lenses, Lens 0 and Lens 1 are positioned between Q00, Q0 and Q0, Q1, serving as vacuum baffles. The pressures of Q00, Q0 and Q1 are maintained at ~ 0.5 torr, $\sim 10^{-3}$ torr and $\sim 10^{-5}$ torr, respectively,

by the turbomolecular pump. When ions enter Q00 through the skimmer cone, a radio frequency (RF) voltage with the same amplitude and phase is applied on the opposing rods of the quadrupole. The same voltage with 180° out of phase is applied to the other pair of the opposing rods. Therefore, the ions are moving in a stable circular trajectory in the radial (x and y) direction.²⁹ An attractive DC offset potential is also applied to the quadrupoles to focus the ions to the center of the multipoles and guide the ion beam along the z direction from Q00 toward the ion trap (Figure 2.5).

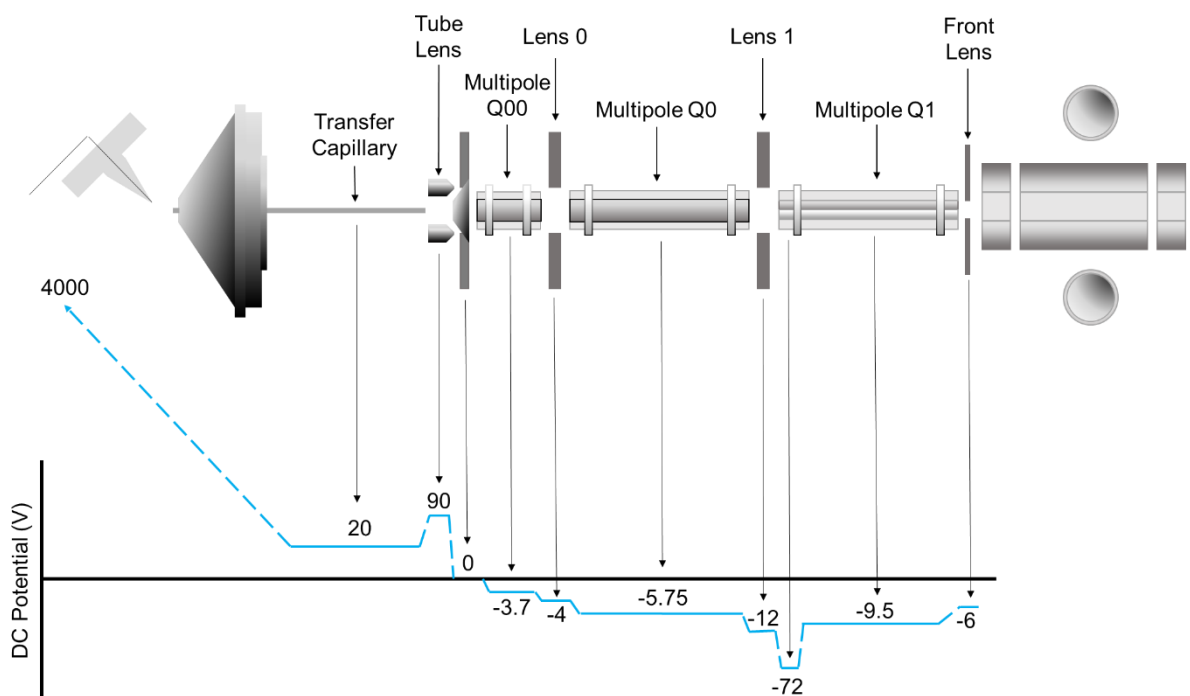


Figure 2.5 A typical DC potential gradient for the ion transmission in the API and ion optics region of an LQIT mass spectrometer

2.3.1.3 The Ion Trap and Detector Region

The linear quadrupole ion trap consists of four parallel hyperbolic rods and are divided into front, center and back sections (Figure 2.6).²⁹ In the radial directions, ions are trapped by the RF potential applied to the rods. Potentials with opposite phases are applied on adjacent rods.³⁰ In the axial direction, DC potentials are applied to each rod to generate a potential well for ion trapping. The DC potential applied to the center section is lower than that applied to the front and back sections. An additional RF potential is applied to the x-rods, for ejecting the ions through the slits on the x-rods for detection. The ions get detected in the ion detection system located on opposite

sides of the x-rods. The detailed description of the ions' motion in the ion trap and the principles of ions' detection will be introduced in the following sections.

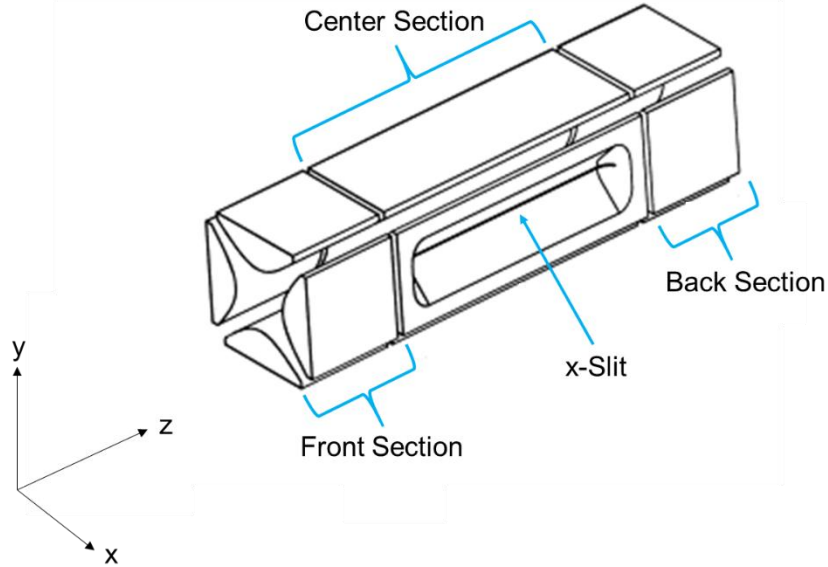


Figure 2.6 Schematic drawing of an LQIT mass analyzer

2.3.2 Ion motion in LQIT

2.3.2.1 Radial Motion

A combination of RF and DC potential is applied to the four rods to generate a quadrupolar electric field for axial trapping of the ions.²⁹ The potentials Φ_0 applied to the rods are expressed as

$$\pm\Phi_0 = \pm(U - V \cos \Omega t) \quad \text{Equation 2.1}$$

where U is the amplitude of the DC potential, V is the peak-to-peak RF amplitude, Ω is the angular frequency applied to the x-rods and t is time. In the x-y direction, the potential Φ_{xy} is described as

$$\Phi_{xy} = \frac{\Phi_0(x^2 - y^2)}{r_0^2} = \frac{(U - V \cos \Omega t)(x^2 - y^2)}{r_0^2} \quad \text{Equation 2.2}$$

where r_0 is the radius of the circle inscribed within the quadrupole rods.^{31,32} As a result, the forces that the ions are subjected to in the x and y directions can be described as Equations 2.3 (F_x) and 2.4 (F_y), respectively

$$F_x = m \frac{d^2x}{dt^2} = -ze \frac{d\Phi}{dx} \quad \text{Equation 2.3}$$

$$F_y = m \frac{d^2y}{dt^2} = -ze \frac{d\Phi}{dy} \quad \text{Equation 2.4}$$

where m is the mass of the ion, z is the number of the charges in the ion and e is the elementary charge. Equations 2.3 and 2.4 can be further rearranged to Equations 2.5 and 2.6 as follows.^{31,32}

$$\frac{d^2x}{dt^2} + \frac{2ze}{mr_0^2} (U - V \cos \Omega t)x = 0 \quad \text{Equation 2.5}$$

$$\frac{d^2y}{dt^2} + \frac{2ze}{mr_0^2} (U - V \cos \Omega t)y = 0 \quad \text{Equation 2.6}$$

These equations indicate that ions with x and y values smaller than r_0 will have stable trajectories in the ion trap. The equations are similar to the Mathieu equation (Equation 2.7)³³

$$\frac{d^2u}{d\xi^2} + (a_u - 2q_u \cos 2\xi)u = 0 \quad \text{Equation 2.7}$$

where a_u and q_u are Mathieu stability parameters. If let $\xi = \frac{\Omega t}{2}$, the equation can be rearranged to

$$\frac{d^2u}{dt^2} + \frac{\Omega^2}{4} (a_u - q_u \cos \Omega t)u = 0 \quad \text{Equation 2.8}$$

therefore, Equations 2.5 and 2.6 can be expressed as Mathieu equations³³

$$a_u = a_x = -a_y = \frac{8zeU}{mr_0^2\Omega^2} \quad \text{Equation 2.9}$$

$$q_u = q_x = -q_y = \frac{4zeU}{mr_0^2\Omega^2} \quad \text{Equation 2.10}$$

An ion with a stable trajectory in the ion trap must meet the criteria where the Mathieu stability parameters of the ion are in the stability region of the Mathieu stability diagram (Figure 2.7). Ions have stable trajectories in the overlapping region. LQIT usually is operated with $a_u = 0$ to trap ions with large range of m/z values. For ions with $a_u = 0$, the larger the ions, the smaller q_u they have at a given RF potential. The q_u value increases as the RF amplitude V increases. The ion becomes unstable in the x-y direction and will be ejected from the ion trap when the q_u value reaches 0.908. Ions with smaller m/z values will be ejected first as they have larger q_u values.

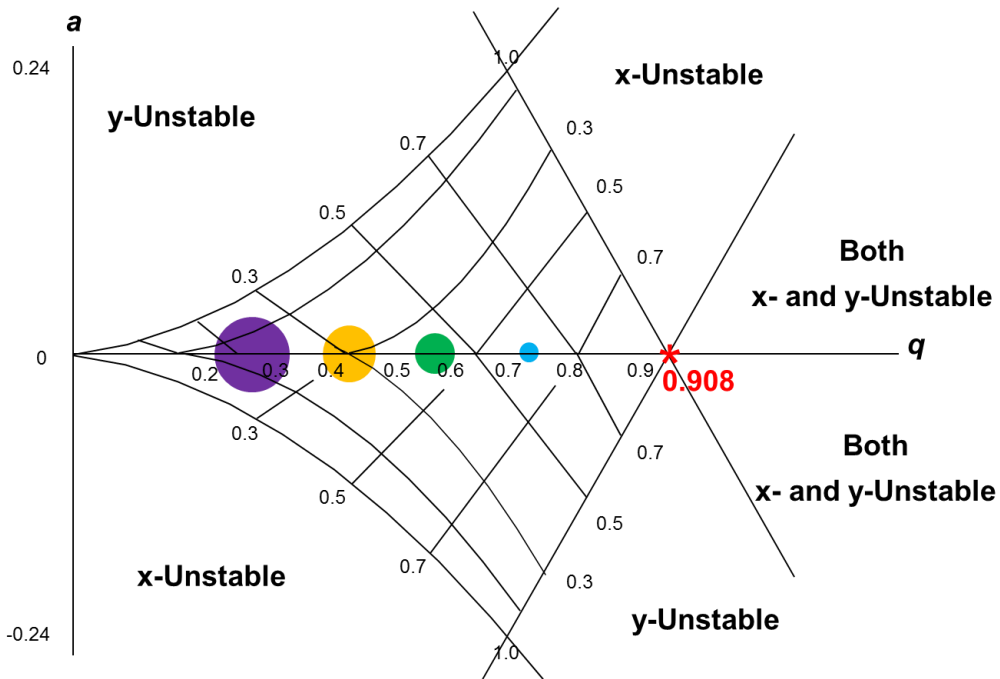


Figure 2.7 The Mathieu stability diagram for a linear quadrupole ion trap. Ions have stable trajectories are in the center region (line-crossed region) of the diagram, with proper a_u and q_u values.

Each ion has a specific secular frequency at a given RF potential which can be described as

$$\omega_u = \frac{\beta_u \Omega}{2} \quad \text{Equation 2.11}$$

where β_u is the approximation for a q_u value less than 0.4.³³ It is defined as

$$\beta_u = \sqrt{\left(a_u + \frac{q_u^2}{2}\right)} \quad \text{Equation 2.12}$$

The maximum value of β_u is 1,³³ therefore, the maximum secular frequency of an ion is one half of the RF frequency.

2.3.2.2 Axial Motion

DC potentials are applied to the four rods of the ion trap to trap the ions axially in the z direction (Figure 2.8). In front and back sections of the ion trap, higher DC potential is applied, so that a potential well is formed to confine the ions to the center section.

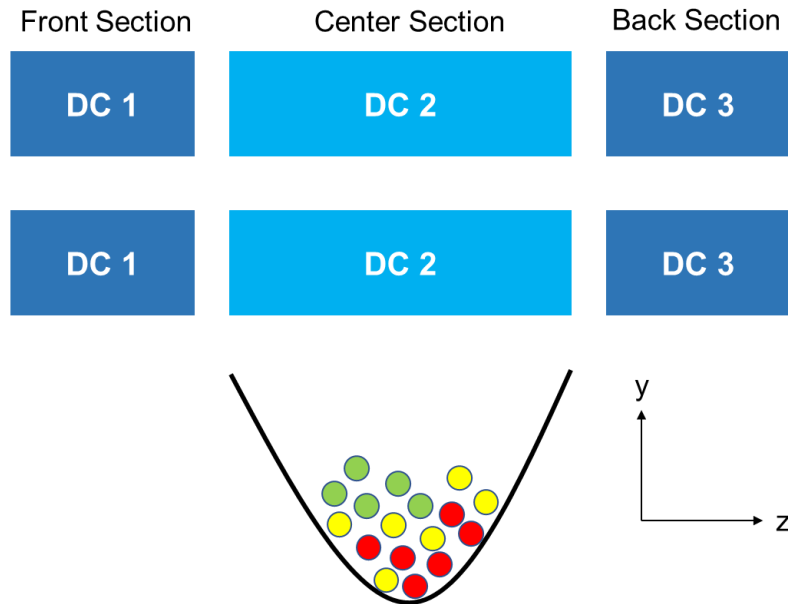


Figure 2.8 Demonstration of the ions' axial trapping in z direction by a potential well generated by applying a DC potential gradient to the front, center and back section of the ion trap.

Typically, the relative magnitude of the DC potentials is $DC\ 3 > DC\ 1 > DC\ 2$.

To increase the efficiency of ion trapping, helium is used as a buffer gas in the ion trap.²⁹ Helium in the ion trap collides with the ions entering the ion trap multiple times to cool down the ions. Ions' kinetic energy is converted to the internal energy of the helium buffer gas so that the

oscillation amplitudes of the ions are decreased. Therefore, the ions can be ejected more efficiently through the slits in the x-rods for detection.

2.3.3 Mass Analysis and Detection

The ions are ejected from the ion trap by resonance ejection.^{34,35} Unlike axial instability scan for ion ejection where q is set to 0.908 (Figure 2.7) by ramping up the RF amplitude, in resonance ejection mode, q value is increased to 0.880 for ion ejection (Figure 2.9).³⁵ In this mode, mass analysis is achieved by linear scanning of the RF amplitude accompanied by applying a supplemental RF voltage to the x-rods.³⁶ Some ions' secular frequency becomes in resonance with the supplemental RF voltage as the main RF voltage increases. Therefore, additional kinetic energy is gained by the ions, an increased amplitude of the ion oscillation eventually leads to ion ejection from the x-slits. Compared to the axial instability scan method, resonance ejection observably increased sensitivity and resolution.^{37,38}

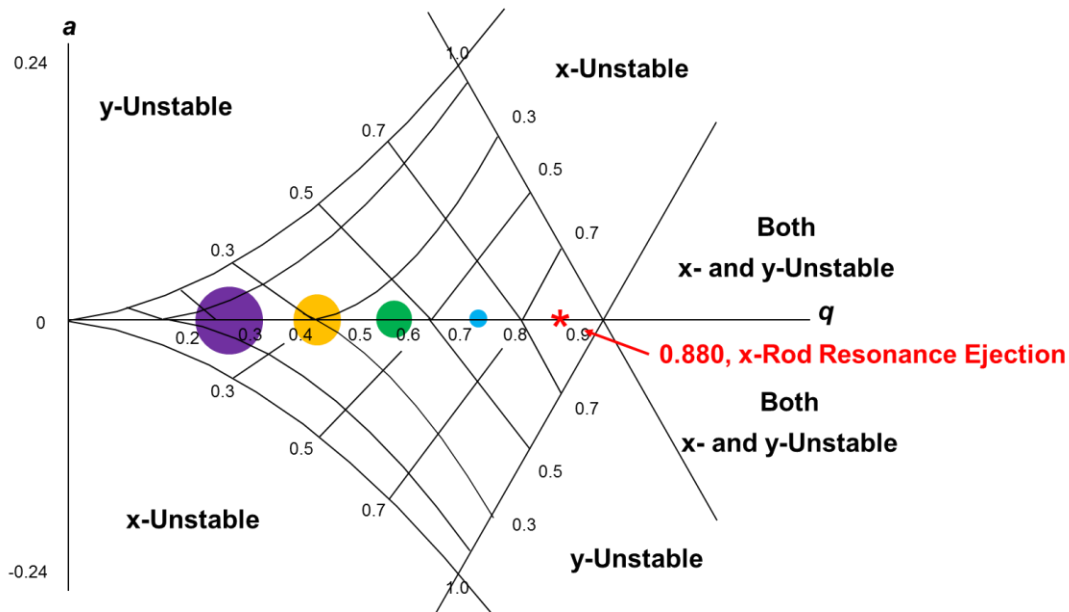


Figure 2.9 Illustration of ions' ejection using resonance ejection approach in Mathieu stability diagram

As described earlier, ions exiting from the x-slits will enter the detection system located on the opposite sides of the x-rods.²⁹ The detection system is composed of two components, a charged conversion dynode and a funnel-shaped electron multiplier (Figure 2.10).²⁹ A large DC potential

(~15 kV) with an opposite phase with the ions is applied to the dynode (-15 kV for positive ions, +15 kV for negative ions). The ions enter the conversion dynode and collide with the surface of the dynode to produce secondary particles. For instance, positive ions generate negatively charged secondary particles such as negative ions and electrons. The secondary electrons are further directed into the electron multiplier by an increasingly positive potential gradient. The electrons repeatedly hit the walls of the electron multiplier as they travel along inside the funnel. A cascade of electrons is thus emitted. Eventually, an ion current is generated and collected at the anode of the multiplier. The m/z values of the ions by scanning the RF voltage, whereas the abundance of the ions is proportional to the amplitude of the ion current. Therefore, a mass spectrum is produced, with m/z value being the x-axis and relative abundance being the y-axis.

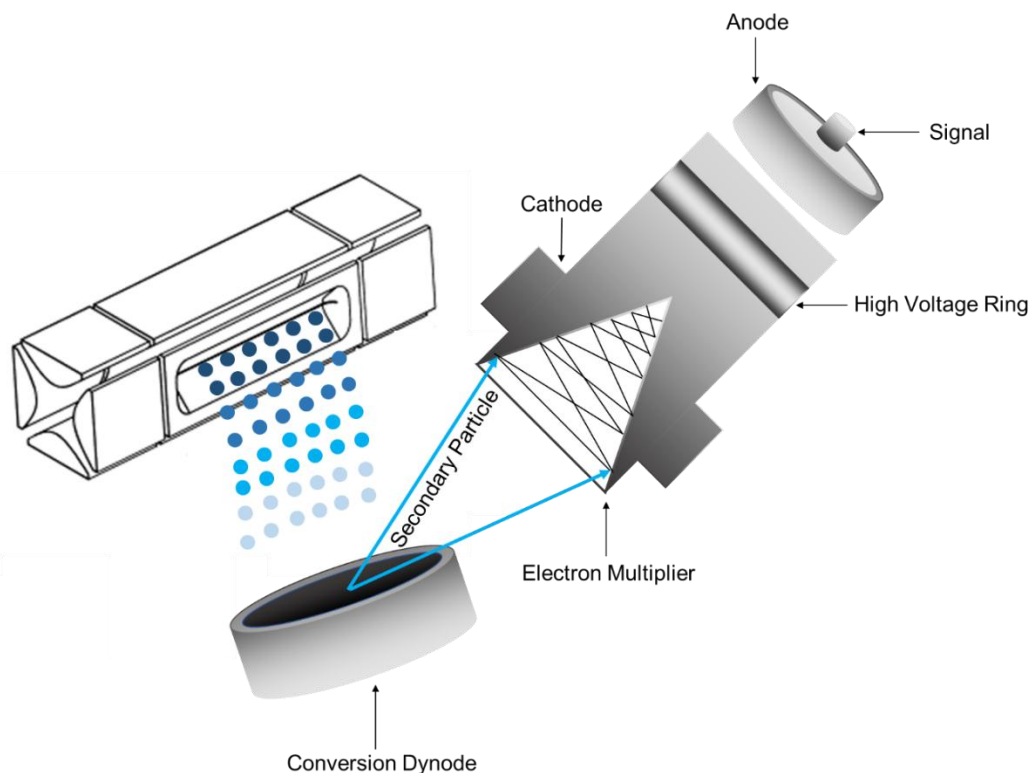


Figure 2.10 Schematic drawing of the ion detection system

2.3.4 Tandem Mass Spectrometry

In LQIT MS, tandem mass spectrometry (MS^n) is achieved in time, i.e. ion isolation and activation are accomplished in the same place (the ion trap), and the multiple isolation steps take place over time.

2.3.4.1 Ion Isolation

Isolation of ions with one specific m/z value in an ion trap can be accomplished by ejecting all the other unwanted ions out of the trap. To achieve this, the q value of the ions of interest is set to 0.830 by ramping the RF voltage. During the ramping of the RF voltage, unwanted ions with m/z values lower than the ions of interest become unstable in trajectory and will be ejected. The rest of the unwanted ions are excited by a tailored broadband waveform ranging from 5 – 500 kHz. A notch at $q = 0.830$ in the waveform assures the stable trajectory of the ions of interest in the ion trap (Figure 2.11).²⁹ The waveform is calculated by the instrument automatically and applied properly at the correct time point.

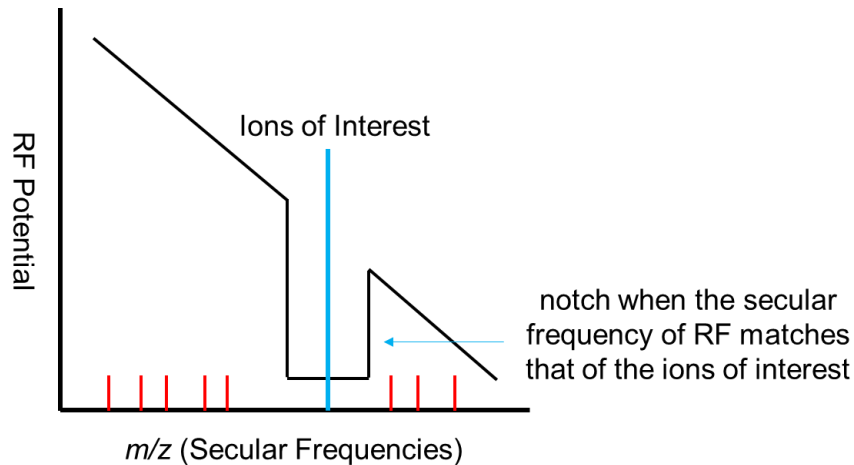


Figure 2.11 Tailored isolation RF waveform applied to x-roads of a linear quadrupole ion trap

2.3.4.2 Collision-activated Dissociation in the LQIT

Collision-activated dissociation (CAD) is one of the most commonly used technique in MS^n for obtaining structural information of analytes. CAD in LQIT is a slow heating process that is achieved by multiple collisions of the analyte ions with the helium buffer gas.^{39,40} The ions are

subjected to dipolar excitation at $q = 0.25$ to gain more kinetic energy for collision.⁴¹ A supplemental RF potential applied to the x-roads with the same secular frequency of the ions of interest result in the acceleration of the ions. Multiple collisions with helium will eventually accumulate enough internal energy to overcome the barrier for the ions to dissociate. The fragment ions obtained can be subjected to the same process for further dissociation in order to gain more structural information. Only the selected precursor ions will be excited during CAD, to prevent the activation of the fragment ions.

The magnitude of q values influences the efficiency of activation of ions. Higher q values lead to higher oscillation frequencies of ions; thus, a higher kinetic energy can be obtained by the ions to cause more fragmentation. The tradeoff is a decrease in the mass range observed when higher q value is applied. Therefore, fragment ions with lower m/z values may not be observed as they are not trapped at this q value. The default q value for the Thermo LTQ and LTQ XL instruments is 0.25.

2.3.4.3 In-source Collision-activated Dissociation

Another commonly used dissociation technique in LQITs is the in-source collision-activated dissociation (ISCAD). It's a technique to cause fragmentation of ions indistinguishably at the medium-pressure free-jet expansion region immediately after the MS orifice (mainly the ion optics region).⁴² An accelerating DC potential is applied to the ion optics region, all the ions entering this region are accelerated and collide with neutral molecules from the air (mostly N_2). Thus, fragmentations can be induced once enough internal energy is restored by the ions. All the fragment ions will then be transferred to the ion trap for further analysis, any fragment ions of interest can be isolated and subjected to further CAD in the ion trap for more fragmentations.

2.4 Basic Principles of High-resolution Orbitrap Mass Spectrometry

A Thermo LQIT Orbitrap mass spectrometer was used to generate all the high-resolution exact masses for the synthesized compounds described in Chapter 3. In this section, the basic principles of the orbitrap mass analyzer are briefly described.

2.4.1 Overview

A schematic illustration of an LQIT-orbitrap is shown in Figure 2.12. In addition to the three components in LQIT, an orbitrap region is connected to the back section of the LQIT. The orbitrap region consists of a transferring octupole, a C-trap, an orbitrap analyzer, and a medium-energy collision-activated dissociation (MCAD) cell. The orbitrap mass analyzer is composed of an inner spindle electrode and an outer barrel electrode. The motions of ions in the orbitrap mass analyzer will be described in the following section. The principles of MCAD will not be discussed in this dissertation.

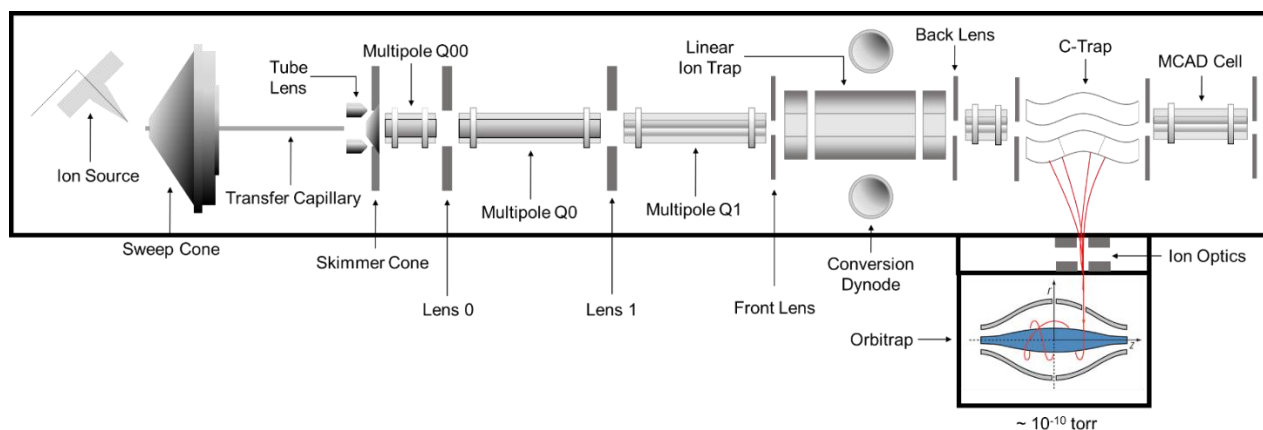


Figure 2.12 Schematic drawing of an LQIT-orbitrap mass spectrometer

2.4.2 Ion Transfer and Motion in the Orbitrap Mass Analyzer

The ions in the LQIT are ejected axially to the transferring octupole and get focused in the C-trap. The C-trap focuses the ion beam by applying a high DC voltage so that the ions can be stored in the center as a tight package.⁴³ The ions are then ejected into the orbitrap off center and moving axially and radially around the spindle electrode of the orbitrap. By measuring the frequency of the axial motion of the ions, m/z values can be obtained. Since frequency of the ions' motion is measured in the orbitrap, high-resolution results with ions' exact masses can be collected.⁴³ The basic principles of the measurements are described as follows.

Axial frequencies of the ions in the orbitrap can be obtained by measuring the image current caused by the motion. The image current measured will be amplified and Fourier transformed so that m/z values of ions can be obtained.

A three-dimensional electrostatic field is generated when a DC potential is applied between the two electrodes of the orbitrap, and can be described as⁴⁴

$$U(r, z) = \frac{k}{2}(z^2 - r^2) + \frac{k}{2}(R_m)^2 \ln\left(\frac{r}{R_m}\right) + C \quad \text{Equation 2.13}$$

where z and r are the axial and angular coordinates of the electrostatic field, k is a field curvature-related constant, R_m is the characteristic radius of the ion motion, and C is a constant. Three types of motions are experienced by the ions in the orbitrap: rotational motion ω_ϕ , radial motion ω_r and oscillation motion ω_z . They can be described as equations in terms of ion's mass m and charge q .^{43,44} Among them, the axial oscillation motion ω_z can be expressed as

$$\frac{\partial^2 z}{\partial t^2} = -kz \frac{q}{m} \quad \text{Equation 2.14}$$

Notably, the axial motion of ions is independent of the energy and position of the ions. Therefore, it is used to determine the m/z values of ions using the following equation

$$\omega_z = \sqrt{\left(\frac{q}{m}\right)k} \quad \text{Equation 2.15}$$

The axial frequency of the ions in the orbitrap is inversely proportional to their m/z values.⁴³

2.5 Gas-phase Ion-molecule Reactions

Gas-phase ion-molecule reactions have been extensively used for structural elucidation, for example, functional-group selective ion-molecule reactions enable the identification of different functional groups and differentiation of analytes containing different functional groups. This approach has been successfully coupled to HPLC analysis and has been applied to drug metabolites

identification, drug impurities identification, and degraded biomass analysis.^{5,45-47} Moreover, gas-phase ion-molecule reactions are widely used to study the reaction kinetics of highly reactive reaction intermediates, such as organic bi- and polyradicals. Some reagents can also be used for activation of chemically inert bonds via gas-phase ion-molecule reactions. In this dissertation, reactivity studies of several substituted pyridine-based biradical cations, quinoline-based *para*-benzyne cations, cyano-substituted pyridine-based biradical cations, and quinoline-based oxenium cations will be discussed. A method using *closo*-[B₁₂X₁₁]⁻ (X = Cl, Br) for C-H and C-C bond activation in hydrocarbons will be introduced, and the reactivity of the [B₁₂X₁₁]^{2•-} radical anion will also be discussed. In addition, the differentiation of protonated sulfites and sulfonate esters will be introduced.

2.5.1 Instrument Modifications for Ion-molecule Reactions in LQITs

The Thermo LTQ and LTQ XL linear quadrupole ion trap instruments have been modified for controlled reagent introduction into the ion trap for the purpose of conducting gas-phase ion-molecule reactions. A home-built external reagent mixing manifold was designed for continuous neutral reagent introduction (Figure 2.13).^{48,49} The manifold consists of two inlets; one is connected to a helium cylinder and the other is sealed with a rubber septum for reagent injection. The reagents are injected via a syringe pump at a flow rate of 5 – 20 $\mu\text{L h}^{-1}$, depending on the volatility of the reagents. The reagents are mixed and diluted with helium with a flow rate of $\sim 500 \text{ mL min}^{-1}$. Part of the diluted reagents are directed to the ion trap via a variable leak valve and the rest go to the exhaust line. The entire manifold set up is bypassed when not in service by a three-way valve connecting the ion trap to the instrument helium and the manifold helium cylinder.

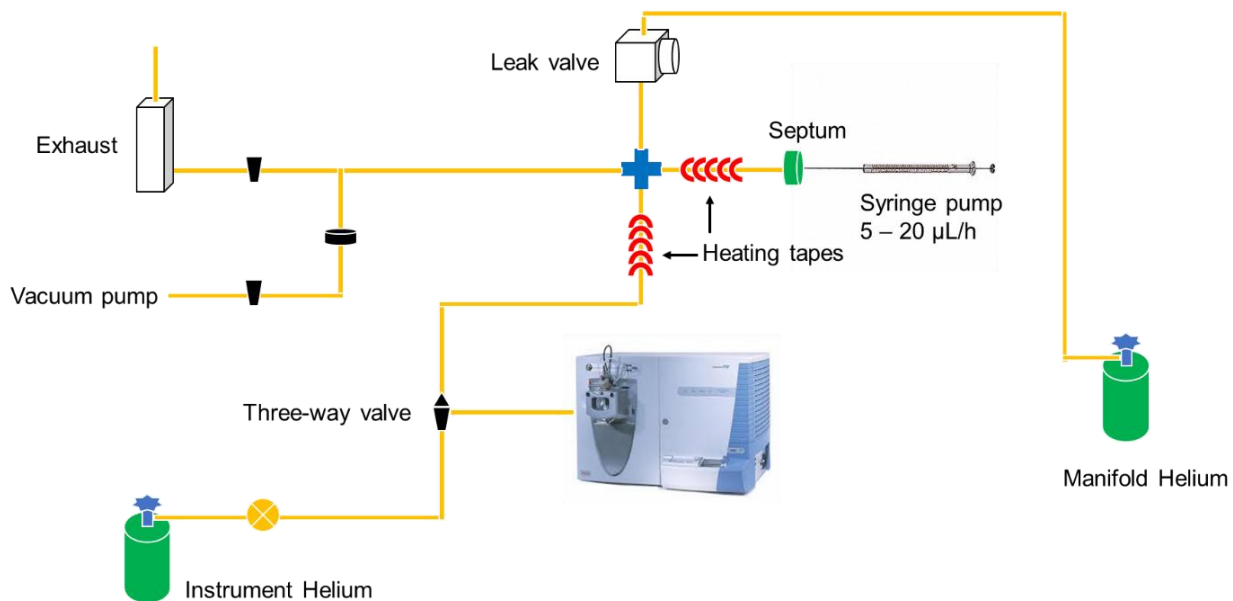


Figure 2.13 Schematic drawing of the external reagent mixing manifold

2.5.2 Brauman's Double-well Potential Energy Surface

Unlike the reactions in solution (Figure 2.14(a)), a double-well potential energy surface was proposed to describe the energetics of gas-phase ion-molecule reactions.^{50,51} In solution, the reaction system must overcome an energy barrier to proceed to the products. The energy barrier is referred as the transition state (TS), an intermediate state that is higher in energy than both the separated reactants and products, as the TS is not as well solvated as the reactants. While in the gas phase, as the ion and the neutral molecule approach and collide to become a reaction complex because of Coulombic attractions, energy will be restored because of the “solvation” of the ion by the molecule.^{50,51} The solvation energy obtained is the total energy that the reaction can utilize to overcome the follow-up reaction barriers. Therefore, exothermic reactions are much more favorable in the gas phase than endothermic reactions as the total energy of the system is conserved. The solvation energy obtained is dependent on the neutral molecule's dipole moment and polarizability.

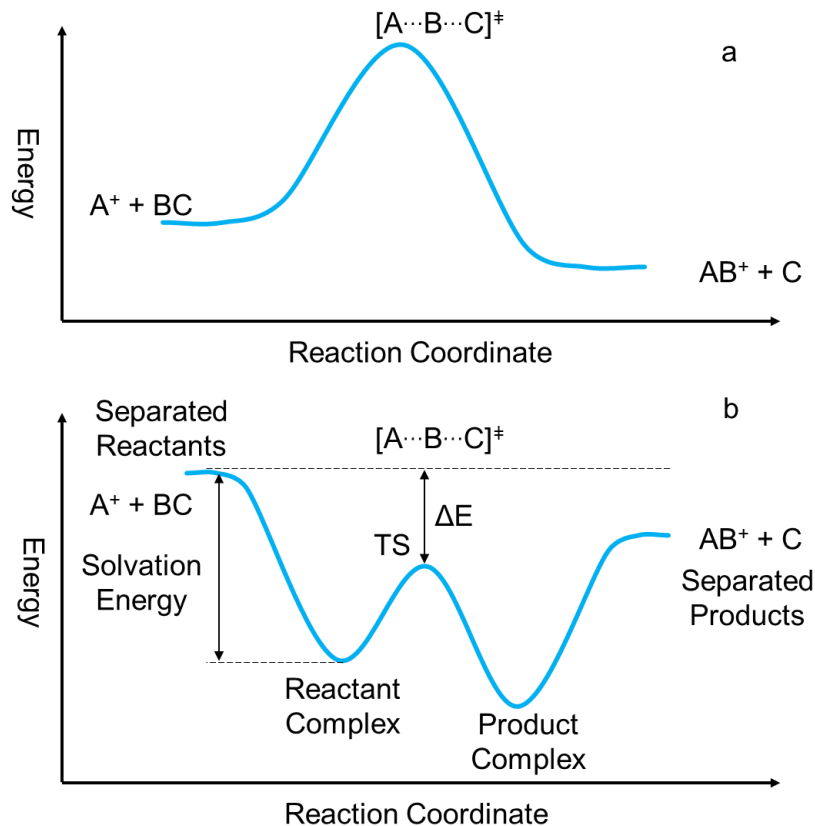


Figure 2.14 Potential energy surfaces for (a) reactions in solution and (b) reactions in gas-phase

In many cases the reaction complexes of gas-phase ion-molecule reactions tend to dissociate back to separated reactants as it's more entropically favored than proceeding to the products through the TS. Usually, the TS proceeding to the products is more rigid compared to the dissociation back to the reactants (Figure 2.15). Therefore, the smaller entropy of the TS compared to the separated reactants leads to a net reaction that does not happen at collision rate though the reaction is exothermic.⁵⁰

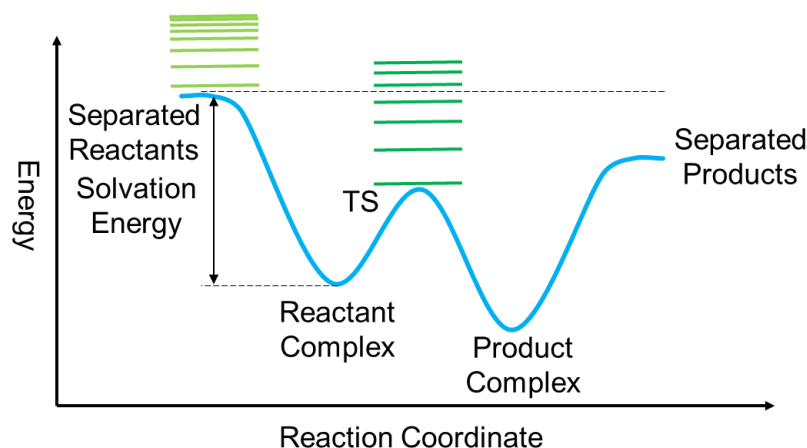


Figure 2.15 The tightness of the TS energy level and the separated reactant energy level of a gas-phase ion-molecule reaction in a Brauman's double-well potential energy surface

2.5.3 Kinetics of Gas-phase Ion-molecule Reactions

Reaction kinetics of the gas-phase ion-molecule reactions are one of the most important intrinsic properties to study, especially for the studies of highly reactive reaction intermediates. Gas-phase reactions usually obey second-order reaction kinetics described as Equation 2.16,

$$r = k[I][R] \quad \text{Equation 2.16}$$

where r is the reaction rate, k is the second-order reaction rate constant, $[I]$ and $[R]$ are the concentrations of the ions and the neutral molecules, separately. For the reaction conditions in the LQITs described in this dissertation, the amount of the neutral molecules injected into the ion trap is in large excess, compared to that of the ions. Therefore, the concentration of the neutral molecule, $[R]$, can be regarded as a constant. The reaction rate of such reaction can be simplified as a pseudo-first reaction and described in Equation 2.17

$$r = k_{obs}[I] \quad \text{Equation 2.17}$$

where

$$k = \frac{k_{obs}}{[R]} \quad \text{Equation 2.18}$$

where k_{obs} can be derived from the slope of a semi-logarithmic rate plot. The concentration of the neutral molecule $[R]$ can be obtained from the pressure p of the molecules measured by the ion gauge. The pressure p measured can be converted to concentration by a conversion factor $1 \text{ torr} = 3.239 \times 10^{16} \text{ molecules cm}^{-3}$, as given in Equation 2.19.

$$k = \frac{k_{obs}}{p(3.239 \times 10^{16})} \quad \text{Equation 2.19}$$

Further, a constant, the Baratron factor B/I was used to correct the sensitivity of the ion gauge toward different molecules, and the sensitivity is affected by the polarizability of the molecule. Ion gauge correction factor ($IGCF$) is used to correct the distance of the ion gauge and the ion trap, and is usually determined by a highly exothermic reaction, i.e. electron transfer reaction or proton transfer reaction. These reactions are assumed to occur at collision rate. The reaction rate constant k can then be determined by Equation 2.20.

$$k = \frac{-k_{obs}}{\left(\frac{B}{I}\right) \times IGCF \times p \times 3.239 \times 10^{16}} \quad \text{Equation 2.20}$$

The reaction efficiency can be calculated by Equation 2.21 once k is determined. It is defined as the percentage of the collisions that lead to a reaction.

$$\%Efficiency = \frac{k}{k_{coll}} \times 100 \quad \text{Equation 2.21}$$

k_{coll} is the theoretical collision rate constant calculated by a parameterized trajectory theory,⁵² which is dependent on the dipole moment, polarizability, molecular weight of the neutral molecule, and the m/z value of the ion.

Additionally, the branching ratios of the primary products are also calculated by taking the ratio of the abundance of each primary product and the sum of the abundances of all product ions at short reaction times. The primary products are the products formed upon reactions of the ion with one neutral molecule, whereas the secondary products are products formed upon reactions with two neutral molecules. The primary products are usually generated as the reactions begin and

may be consumed in longer reaction times if any secondary products present. It can be recognized from the rate plots where the plots for primary products grow in immediately and plateau or even drop eventually. The secondary products accumulate slowly at the beginning of the reaction and increase fast as the reactions proceed, reflected by a crossing over the plot for the primary product. Secondary products can usually be identified by isolating the possible primary products in the ion trap and allowing them to further react with the neutral molecules.

2.6 References

1. McLuckey, S. A.; Wells, J. M. *Chem. Rev.* **2001**, *101*, 571–606.
2. de Hoffmann, E.; Stroobant, V. *Mass Spectrometry Principles and Applications*; John Wiley & Sons, Ltd.: West Sussex, 2007.
3. Bogdal, C.; Alsberg, T.; Diefenbacher, P. S.; MacLeod, M.; Berger, U. *Anal. Chem.* **2015**, *87*, 2852–2860.
4. Dong, X.; Zhang, Y.; Milton, J.; Yerabolu, R.; Easterling, L.; Kenttämaa, H. I. *Fuel*, **2019**, *246*, 126–132.
5. Zhu, H.; Ma, X.; Kong, J. Y.; Zhang, M.; Kenttämaa, H. I. *J. Am. Soc. Mass Spectrom.* **2017**, *28*, 2189–2200.
6. Wu, Q.; Wang, J.-Y.; Han, D.-Qi; Yao, Z.-P. *Trac-trend Anal. Chem.* **2020**, *124*, 1–7.
7. Dempster, A. *Phys. Rev.* **1918**, *11*, 316–325.
8. Munson, M.; Field, F. *J. Am. Chem. Soc.* **1966**, *88*, 2621–2630.
9. Whitehouse, C.; Dreyer, R.; Yamashita, M.; Fenn, J. *Anal. Chem.* **1985**, *57*, 675–679.
10. Yamashita, M.; Fenn, J. *J. Phys. Chem.* **1984**, *88*, 4451.
11. Takács, Z.; Wiseman, J.; Gologan, B.; Cooks, R. *Science* **2004**, *306*, 471.
12. Cody, R.; Laramée, J.; Durst, H. *Anal. Chem.* **2005**, *77*, 2297–2302.
13. Carroll, D.; Dzidic, I.; Stillwell, R.; Haegele, K.; Horning, E. *Anal. Chem.* **1975**, *47*, 2369–2373.
14. Carroll, D.; Dzidic, I.; Stillwell, R.; Horning, M.; Horning, E. *Anal. Chem.* **1974**, *46*, 706–710.
15. Beckey, H. *Int. J. Mass Spectrom. Ion Phys.* **1969**, *2*, 500–503.

16. Beckey, H. *Principles of Field Ionization and Field Desorption Mass Spectrometry*. 1st Ed.; Pergamon Press: Oxford, 1977.
17. Karas, M.; Bahr, U.; Gießmann, U., *Mass Spectrom. Rev.* **1991**, *10*, 335–357.
18. Fenn, J. B.; Mann, M.; Meng, C. K.; Wong, S. F.; Whitehouse, C. M. *Science*. **1989**, *246*, 64–71.
19. Veenstra, T. D. *Biophys. Chem.* **1999**, *79*, 63–79.
20. Cech, N. B.; Enke, C. G. *Mass Spectrom. Rev.* **2001**, *20*, 362–387.
21. Smith, R. D.; Loo, J. A.; Edmonds, C. G.; Barinaga, C. J.; Udseth, H. R. *Anal. Chem.* **1990**, *62*, 882–899.
22. Fenn, J. B.; Mann, M.; Meng, C. K.; Wong, S. F.; Whitehouse, C. M. *Mass Spectrom. Rev.* **1990**, *9*, 37–70.
23. Iribarne, J. V.; Thomson, B. A. *J. Chem. Phys.* **1976**, *64*, 2287–2294.
24. Thomson, B. A.; Iribarne, J. V. *J. Chem. Phys.* **1979**, *71*, 4451–4463.
25. Kebarle, P.; Verkerk, U. H. *Mass Spectrom. Rev.* **2009**, *28*, 898–917.
26. Wilm, M. *Mol. Cell. Proteomics*, **2011**, *10*, M111.009407.
27. Carroll, D. I.; Dzidic, I.; Stillwell, R.N.; Haegele, K. D.; Horning, E. C. *Anal. Chem.* **1975**, *47*, 2369–2372.
28. Bier, M. E.; Syka, J. E. P. *Ion Trap Mass Spectrometer System and Method*, 1995.
29. Schwartz, J. C.; Senko, M. W.; Syka, J. E. P. *J. Am. Soc. Mass Spectrom.* **2002**, *13*, 659–669.
30. March, R. E. *Ion Trap Mass Spectrometry*. *Int. J. Mass Spectrom. Ion Process.* **1992**, *118*, 71–135.
31. Douglas, D. J. *Mass Spectrom. Rev.* **2009**, *28*, 937–960.
32. Douglas, D. J.; Frank, A. J.; Mao, D. *Mass Spectrom. Rev.* **2005**, *24*, 1–29.
33. March, R. E.; Todd, J. F. J.; Todd, J. F. J. *Quadrupole Ion Trap Mass Spectrometry*; John Wiley & Sons, Inc.: Hoboken, 2005.
34. Xu, W.; Song, Q.; Smith, S. A.; Chappell, W. J.; Ouyang, Z. *J. Am. Soc. Mass Spectrom.* **2009**, *20*, 2144–2153.
35. Kaiser, R. E.; Cooks, R. G.; Stafford, G. C.; Syka, J. E. P.; Hamburger, P. H. *Int. J. Mass Spectrom. Ion Process.* **1991**, *106*, 79–115.

36. Stafford Jr, G. C.; Kelley, P. E.; Syka, J. E. P.; Reynolds, W. E.; Todd, J. F. J. *Int. J. Mass Spectrom. Ion Process.* **1984**, *60*, 85–98.
37. Busch, K. L.; Glish, G. L.; McLuckey, S. A. *Mass Spectrometry/Mass Spectrometry: Techniques and Applications of Tandem Mass Spectrometry*; VCH Publishers: New York, 1988.
38. Schwartz, J. C.; Syka, J. E. P.; Jardine, I. *J. Am. Soc. Mass Spectrom.* **1991**, *2*, 198–204.
39. McLuckey, S. A. *J. Am. Soc. Mass Spectrom.* **1992**, *3*, 599–614.
40. Mayer, P. M.; Poon, C. *Mass Spectrom. Rev.* **2009**, *28*, 608–639.
41. Louri, J. N.; Cooks, R. G.; Syka, J. E. P.; Kelley, P. E.; Stafford, G. C.; Todd, J. F. J. *Anal. Chem.* **1987**, *59*, 1677–1685.
42. B. Pramanik, *Applied Electrospray Mass Spectrometry*, CRC, New York, 2002.
43. Makarov, A.; Denisov, E.; Kholomeev, A.; Balschun, W.; Lange, O.; Strupat, K.; Horning, S. *Anal. Chem.* **2006**, *78*, 2113–2120.
44. Kingdon, K. H. *Phys. Rev.* **1923**, *21*, 408–418.
45. Sheng, H.; Tang, W.; Yerabolu, R.; Kong, J. Y.; Williams, P. E.; Zhang, M.; Kenttämaa, H. I. *Rapid Commun. Mass Spectrom.* **2015**, *29*, 730–734.
46. Kong, J. Y.; Yu, Z.; Easton, M. W.; Niyonsaba, E.; Ma, X.; Yerabolu, R.; Sheng, H.; Jarrell, T. M.; Zhang, Z.; Ghosh, A. K.; Kenttämaa, H. I. *Anal. Chem.* **2018**, *90*, 9426–9433.
47. Zhu, H.; Max, J. P.; Marcum, C. L.; Luo, H.; Abu-Omar, M. M.; Kenttämaa, H. I. *J. Am. Soc. Mass Spectrom.* **2016**, *27*, 1813–1823.
48. Gronert, S. *J. Am. Soc. Mass Spectrom.* **1998**, *9*, 845–848.
49. Gronert, S. *Chem. Rev.* **2001**, *101* (2), 329–360.
50. Olmstead, W. N.; Brauman, J. I. *J. Am. Chem. Soc.* **1977**, *99*, 4219–4228.
51. Pellerite, M. J.; Brauman, J. I. *J. Am. Chem. Soc.* **1980**, *102*, 5993–5999.
52. Su, T.; Chesnavich, W. J. *J. Chem. Phys.* **1982**, *76*, 5183–5185.

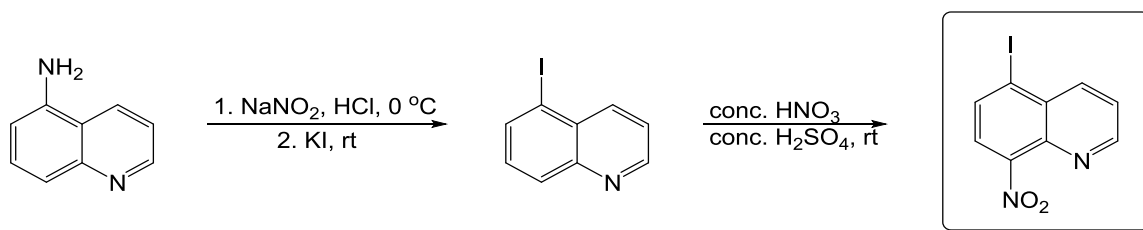
CHAPTER 3. SYNTHESIS OF RADICAL PRECURSORS AND LIGNIN MODEL COMPOUNDS

3.1 General Experimental Conditions

All the starting materials for synthesis were purchased from the following commercial sources: Sigma Aldrich (St Louis, MO), Alfa Aesar, and TCI America. They were used as received. The products were purified by a Teledyne-ISCO CombiFlash automatic flash column by using silica columns as the stationary phase. The H-lignin model compound was generated as a mixture of diastereomers. The solvents used were either provided anhydrous by the commercial source or were pre-dried if necessary. Some reactions were conducted under an inert atmosphere of nitrogen or argon as necessary. All synthesized compounds were characterized by ^1H and ^{13}C NMR, HRMS, and some of them were further confirmed by X-ray crystallography. Chloroform- d , methanol- d_4 and DMSO- d_6 were used as the solvents for NMR experiments. All NMR spectra were collected on a Bruker Avance-III-800 instrument. Data in the NMR spectra were reported as chemical shifts δ (multiplicity, coupling constant J in Hz, integration). The abbreviations for peak multiplicity are s = singlet, d = doublet, t = triplet, q = quartet, and m = multiplet. The chemical shifts were reported in ppm relative to the standard solvent peak. HRMS data were obtained on a Thermo Scientific Orbitrap LTQ XL instrument. The compounds were ionized via either electrospray ionization (ESI) or atmospheric pressure chemical ionization (APCI) in either positive or negative ion mode. The exact masses of the protonated or deprotonated molecules are reported in the units of m/z .

3.2 Synthesis of Quinoline-based *para*-Benzyne Precursors

3.2.1 Synthesis of 5-Iodo-8-nitroquinoline



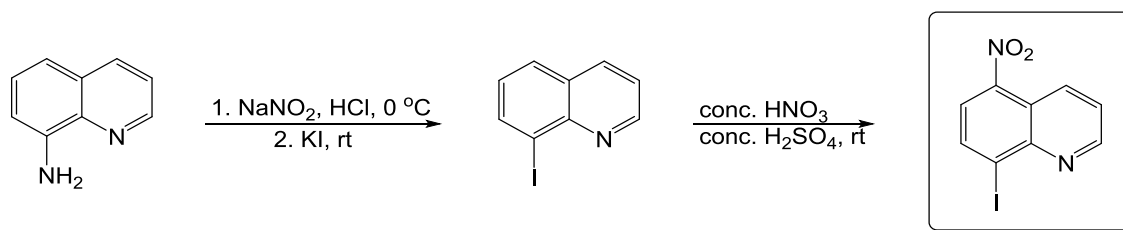
Scheme 3.1 Synthetic route to 5-iodo-8-nitroquinoline

To a solution of 5-aminoquinoline (1.44 g, 10 mmol) in 3 M aq. HCl (20 mL) at 0 °C, aq. NaNO₂ (1.04 g, 15 mmol) was added dropwise. Upon completion of the addition of NaNO₂, aq. KI (3.32 g, 20 mmol) was then added dropwise under the same temperature. Acetone was added to prevent foaming. The temperature was slowly raised to room temperature and the reaction mixture was stirred for 16 hours.¹ Upon completion of the reaction (monitored by TLC), saturated Na₂S₂O₃ solution (20 mL) was added. The reaction mixture was then extracted with ethyl acetate (3 × 10 mL). The organic layers were combined and dried over Na₂SO₄. The crude product was purified by using an auto-flash column to obtain a brown solid (silica, hexanes : EtOAc 2:1 v/v).

The 5-iodoquinoline was dissolved in a mixture of conc. H₂SO₄ and conc. HNO₃ (3:2 v/v) and was stirred at room temperature overnight. The reaction mixture was then neutralized to pH 7 with saturated Na₂CO₃ solution. The aqueous phase was extracted by EtOAc (3 × 10 mL) and the combined organic layers were dried over Na₂SO₄ and purified by chromatography. 5-iodo-8-nitroquinoline was obtained as a yellow solid.

¹H NMR (800 MHz, Chloroform-*d*) δ 9.11 – 9.01 (m, 1H), 8.52 (d, *J* = 8.5 Hz, 1H), 8.29 – 8.22 (m, 1H), 7.78 (dd, *J* = 7.9, 1.7 Hz, 1H), 7.28 (s, 1H). ¹³C NMR (201 MHz, Chloroform-*d*) δ 153.33, 142.95, 140.75, 139.57, 136.38, 131.01, 124.47, 124.08, 103.26. HRMS (+)APCI, calculated for: C₉H₆N₂O₂I [M+H]⁺ 300.9474, found: 301.0028.

3.2.2 Synthesis of 8-Iodo-5-nitroquinoline



Scheme 3.2 Synthetic route to 8-iodo-5-nitroquinoline

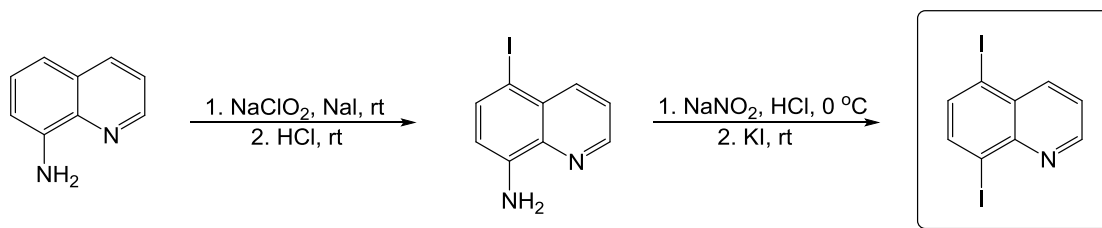
To a solution of 8-aminoquinoline (1.44 g, 10 mmol) in 3 M aq. HCl (20 mL) at 0 °C, aq. NaNO₂ (1.04 g, 15 mmol) was added dropwise. Upon completion of the addition of NaNO₂, aq. KI (3.32 g, 20 mmol) was then added dropwise at the same temperature. Acetone was added to

prevent foaming. The temperature was slowly raised to room temperature and the reaction mixture was stirred for 16 hours.¹ Upon completion of the reaction (monitored by TLC), 5% Na₂S₂O₃ solution (20 mL) was added. The reaction mixture was then extracted with ethyl acetate (3 × 10 mL). The organic layers were combined and dried over Na₂SO₄. The crude product was purified by using an auto-flash column to obtain a brown solid (silica, hexanes : EtOAc 2:1 v/v).

The 8-iodoquinoline was dissolved in a mixture of conc. H₂SO₄ and conc. HNO₃ (3:2 v:v) and was stirred at room temperature overnight. The reaction mixture was then neutralized to pH 7 with saturated Na₂CO₃ solution. The aqueous phase was extracted by EtOAc (3 × 10 mL) and the combined organic layers were dried over Na₂SO₄ and purified by liquid chromatography. 8-Iodo-5-nitroquinoline was obtained as a yellow solid.

¹H NMR (800 MHz, Chloroform-*d*) δ 9.14 (dt, *J* = 4.1, 1.1 Hz, 1H), 9.02 (ddd, *J* = 8.7, 1.5, 0.8 Hz, 1H), 8.54 (dd, *J* = 8.2, 0.8 Hz, 1H), 8.11 (dd, *J* = 8.1, 0.8 Hz, 1H), 7.73 (ddd, *J* = 8.7, 4.1, 0.8 Hz, 1H). ¹³C NMR (201 MHz, Chloroform-*d*) δ 152.47, 147.00, 138.25, 132.77, 131.54, 124.88, 124.74, 121.15, 113.43, 108.54. HRMS (+)APCI, calculated for: C₉H₆N₂O₂I [M+H]⁺ 300.9474, found: 301.0214.

3.2.3 Synthesis of 5,8-Diiodoquinoline



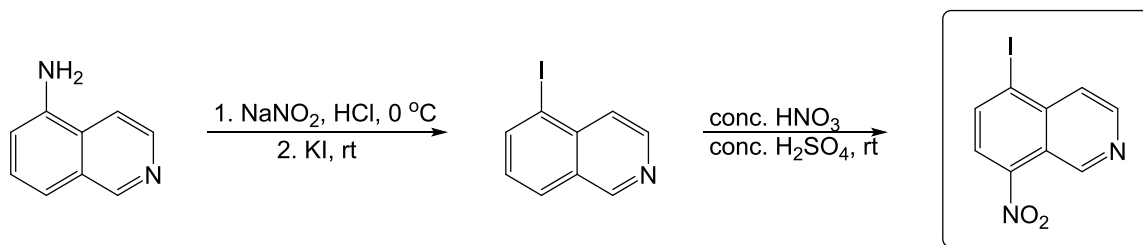
Scheme 3.3 Synthetic route to 5,8-diiodoquinoline

To a solution of 8-aminoquinoline (0.721 g, 5 mmol) in methanol (20 mL), NaClO₂ (0.226 g, 2.5 mmol) and NaI (0.750 g, 5 mmol) were added at room temperature. 1 M HCl solution (~10 mL) was then added dropwise. The reaction mixture was stirred at room temperature for 24 hours and 5% Na₂S₂O₃ solution (20 mL) was added. The aqueous layer was extracted by CH₂Cl₂ (3 × 20 mL), dried and purified via liquid chromatography.

The 8-amino-5-iodoquinoline (0.81 g, 3 mmol) was dissolved in 3 M HCl at 0 °C and aq. NaNO₂ (0.31 g, 4.5 mmol) was added dropwise. Upon completion of the addition of NaNO₂, aq. KI (0.99 g, 6 mmol) was then added dropwise at the same temperature. The reaction mixture was stirred overnight, and the temperature was gradually raised to room temperature.¹ Upon completion of the reaction, saturated Na₂S₂O₃ solution (20 mL) was added. The reaction mixture was then extracted with ethyl acetate (3 × 10 mL). The organic layers were combined and dried over Na₂SO₄. The 5,8-diiodoquinoline was obtained upon purification via liquid chromatography as a brown solid.

¹H NMR (800 MHz, Chloroform-*d*) δ 8.98 (dt, *J* = 3.9, 1.8 Hz, 1H), 8.36 (dt, *J* = 8.5, 1.8 Hz, 1H), 8.07 (dd, *J* = 7.8, 2.0 Hz, 1H), 7.85 (dd, *J* = 7.7, 2.1 Hz, 1H), 7.54 (ddd, *J* = 8.6, 4.3, 2.1 Hz, 1H). ¹³C NMR (201 MHz, Chloroform-*d*) δ 152.19, 147.46, 141.26, 140.71, 138.58, 130.62, 123.70, 104.91, 99.37. HRMS (+)APCI, calculated for: C₉H₆NI₂ [M+H]⁺ 381.8590, found: 382.0804.

3.2.4 Synthesis of 5-Iodo-8-nitroisoquinoline



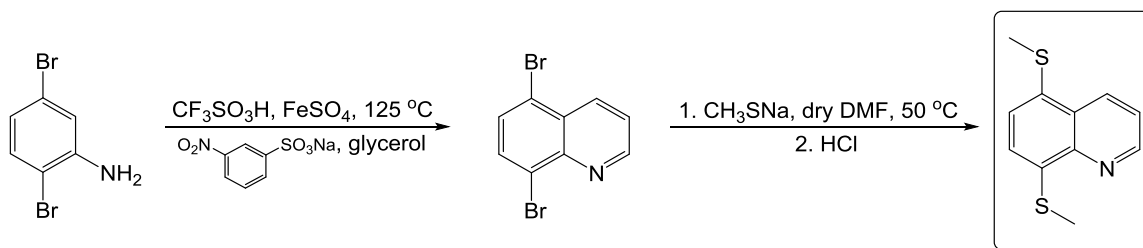
Scheme 3.4 Synthetic route to 5-iodo-8-nitroisoquinoline

To a solution of 5-aminoisoquinoline (1.44 g, 10 mmol) in 3 M aq. HCl (20 mL) at 0 °C, aq. NaNO₂ (1.04 g, 15 mmol) was added dropwise. Upon completion of the addition of NaNO₂, aq. KI (3.32 g, 20 mmol) was then added dropwise at the same temperature. Acetone was added to prevent foaming. The temperature was slowly raised to room temperature and the reaction mixture was stirred for 16 hours. Upon completion of the reaction (monitored by TLC), saturated Na₂S₂O₃ solution (20 mL) was added. The reaction mixture was then extracted with ethyl acetate (3 × 10 mL). The organic layers were combined and dried over Na₂SO₄. The crude product was purified by using an auto-flash column to obtain a brown solid (silica, hexane : EtOAc 2:1 v/v).

The 5-iodoquinoline was dissolved in a mixture of conc. H_2SO_4 and conc. HNO_3 (3:2 v/v) and was stirred at room temperature overnight.¹ The reaction mixture was then neutralized to pH 7 with saturated Na_2CO_3 solution. The aqueous phase was extracted by EtOAc (3×10 mL) and the combined organic layers were dried and purified by liquid chromatography. 5-Iodo-8-nitroisoquinoline was obtained as a yellow solid.

^1H NMR (800 MHz, $\text{DMSO}-d_6$) δ 9.71 (d, $J = 1.8$ Hz, 1H), 8.83 (dd, $J = 6.0, 1.8$ Hz, 1H), 8.62 (dd, $J = 8.0, 1.9$ Hz, 1H), 8.19 (dd, $J = 8.1, 1.9$ Hz, 1H), 8.05 (dd, $J = 5.9, 1.9$ Hz, 1H). ^{13}C NMR (201 MHz, $\text{DMSO}-d_6$) δ 148.90, 146.67, 146.53, 141.08, 137.78, 126.34, 124.44, 120.03, 108.20. HRMS (+)APCI, calculated for: $\text{C}_9\text{H}_6\text{N}_2\text{O}_2\text{I}$ $[\text{M}+\text{H}]^+$ 300.9474, found: 301.0812.

3.2.5 Synthesis of 5,8-Dithiomethylquinoline



Scheme 3.5 Synthesis of 5,8-Dithiomethylquinoline

2,5-Dibromoaniline (1.255 g, 5 mmol) was added in several portions into trifluoromethane sulfonic acid (20 mL) at $125\text{ }^\circ\text{C}$, followed by addition of 3-nitrobenzenesulfonic acid sodium salt (0.788 g, 3.5 mmol) and $\text{FeSO}_4 \cdot 7\text{H}_2\text{O}$ (10 mol%). To the reaction solution, glycerol (~ 3 mL, 15 mmol) was then added dropwise in 3 portions. The temperature was kept at $125\text{ }^\circ\text{C}$ and the reaction mixture was stirred for 12 hours. Afterwards, the mixture was cooled to room temperature and diluted with water. The pH was adjusted to 14 by addition of solid NaOH and the aqueous layer was extracted by Et_2O (3×10 mL). The organic layer was dried and purified via liquid chromatography. The 5,8-dibromoquinoline was obtained as a yellow solid.

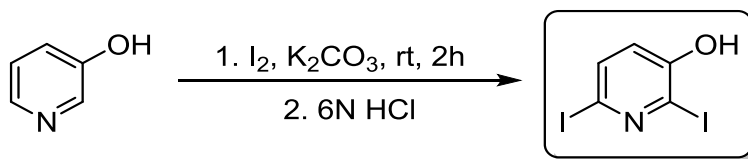
To a solution of 5,8-dibromoquinoline (0.576 g, 2 mmol) in dry DMF, sodium methanethiolate (0.350 g, 5 mmol) was added at $50\text{ }^\circ\text{C}$. After 4 hours of stirring, the reaction

mixture was diluted with water and cooled to 0 °C in an ice bath. Aq. HCl was then added to acidify the mixture.^{2,3} The aqueous layer was extracted with CH₂Cl₂ and the organic layer was dried with Na₂SO₄. Pure 5,8-dithiomethylquinoline was obtained via liquid chromatography as a yellow solid.

¹H NMR (500 MHz, Chloroform-*d*) δ 8.99 (dd, *J* = 4.2, 1.7 Hz, 1H), 8.69 (dd, *J* = 8.5, 1.7 Hz, 1H), 7.58 – 7.52 (m, 2H), 7.38 (d, *J* = 7.8 Hz, 1H), 2.60 (s, 3H), 2.57 (s, 3H). ¹³C NMR (201 MHz, Chloroform-*d*) δ 149.25, 145.62, 138.60, 133.52, 126.74, 122.77, 121.69, 17.54, 14.32. HRMS (+)APCI, calculated for: C₁₁H₁₂N₂S₂ [M+H]⁺ 222.0411, found: 222.0232.

3.3 Synthesis of Substituted Pyridine-based *meta*-Benzyne Precursors

3.3.1 Synthesis of 3-Hydroxy-2,6-diiodopyridine

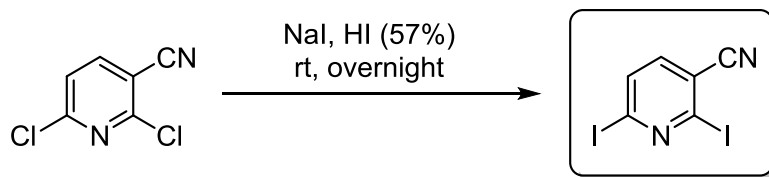


Scheme 3.6 Synthetic route to 3-hydroxy-2,6-diiodopyridine

To a solution of 3-hydroxypyridine (10.0 mmol, 951 mg) in water, I₂ (20.0 mmol, 5.07 g) and K₂CO₃ (30.0 mmol, 4.14 g) were added. The reaction mixture was stirred at room temperature for 2 h. The mixture was then treated with 10 mL 6N aq. HCl solution.⁴ The product, 3-hydroxy-2,6-diiodopyridine, was first purified by using an auto-flash column by using EtOAc : hexanes (2:1 v/v) as the eluent. The obtained eluate solution was subjected to recrystallization in ethanol, filtered and dried to obtain the pure product as a yellow powder (2.18 g, yield 63%).

¹H NMR (800 MHz, Methanol-*d*₄) δ 7.53 (dd, *J* = 8.3, 2.6 Hz, 1H), 6.86 (d, *J* = 8.2 Hz, 1H). ¹³C NMR (201 MHz, Methanol-*d*₄) δ 135.77, 134.48, 128.27, 126.74, 122.96. HRMS (+)APCI, calculated for: C₅H₄NOI₂ [M+H]⁺ 347.8382, found: 347.9027.

3.3.2 Synthesis of 3-Cyano-2,6-diiodopyridine

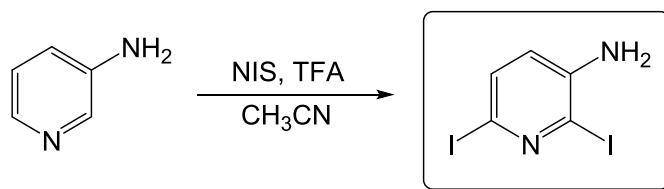


Scheme 3.7 Synthetic route to 3-cyano-2,6-diiodopyridine

To a stirred solution of 2,6-dichloro-3-cyanopyridine (10.0 mmol, 1.73 g) in 57% aq. HI (5 mL), NaI (25.0 mmol, 3.75 g) was added at room temperature. The solution was refluxed overnight.⁵ After this, the solution was neutralized by using Na₂CO₃ and extracted with EtOAc (3 × 50 mL). The combined organic layers were dried using Na₂SO₄ and filtered. The product was purified by an auto-flash column by using EtOAc : hexanes (1:3 v/v) as the eluent to afford 3-cyano-2,6-diiodopyridine as a white powder.

¹H NMR (800 MHz, Chloroform-*d*) δ 7.86 (dd, *J* = 8.0, 1.2 Hz, 1H), 7.38 (dd, *J* = 8.0, 1.2 Hz, 1H). ¹³C NMR (201 MHz, Chloroform-*d*) δ 140.60, 133.95, 120.63, 119.54, 119.25, 117.39. HRMS (+)APCI, calculated for: C₆H₃N₂I₂ [M+H]⁺ 356.8386, found: 356.8033.

3.3.3 Synthesis of 3-Amino-2,6-diiodopyridine



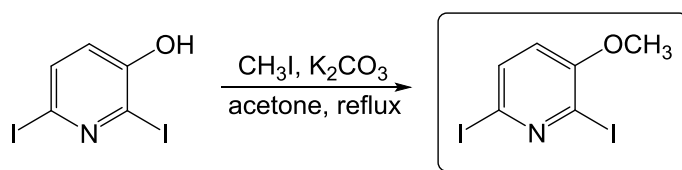
Scheme 3.8 Synthetic route to 3-amino-2,6-diiodopyridine

To a solution of 3-aminopyridine (0.47 g, 5.0 mmol) in acetonitrile (20 mL), N-iodosuccinimide (NIS, 2.70 g, 12.0 mmol) was added, followed by addition of trifluoroacetic acid (TFA, 0.29 g, 2.5 mmol). The mixture was allowed to react at room temperature for 4 h. After this, EtOAc (3 × 20 mL) was used to extract the crude product. The combined organic layers were dried

using Na₂SO₄, concentrated, and purified by liquid chromatography (hexanes : EtOAc 2:1 v/v) to give the product as a brown solid (1.17 g, yield 68%).

¹H NMR (800 MHz, Chloroform-*d*) δ 7.39 (d, *J* = 8.2 Hz, 1H), 6.64 (d, *J* = 8.2 Hz, 1H). ¹³C NMR (201 MHz, Chloroform-*d*) δ 144.43, 134.16, 121.92, 106.92, 99.37. HRMS (+)APCI, calculated for: C₅H₅N₂I₂ [M+H]⁺ 346.8542, found: 346.8257.

3.3.4 Synthesis of 3-Methoxy-2,6-diiodopyridine



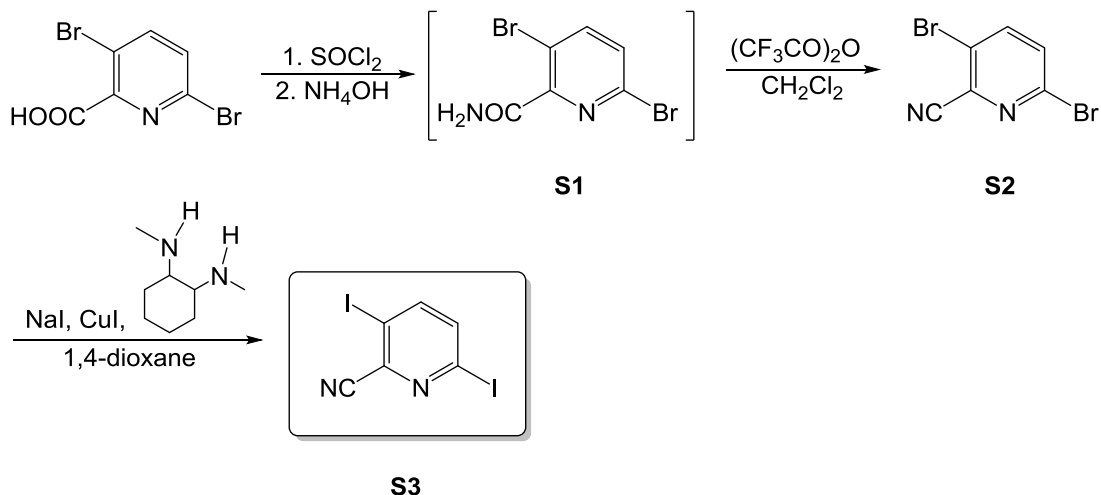
Scheme 3.9 Synthetic route to 3-methoxy-2,6-diiodopyridine

To a solution of 3-hydroxy-2,6-diiodopyridine (0.70 g, 2.0 mmol) in dry acetone, CH₃I (0.37 g, 2.6 mmol) was added slowly. K₂CO₃ (0.41 g, 3.0 mmol) was then added into the mixture. The reaction mixture was heated to a reflux and kept there for 6 h.⁶ After this, the mixture was filtered, extracted with EtOAc (3 × 10 mL), and the organic solution was dried by using Na₂SO₄. The combined organic layers were purified by liquid chromatography (hexanes : EtOAc 3:1 v/v) to give the pure product (0.52 g, yield 72%) as an off-white solid.

¹H NMR (800 MHz, Chloroform-*d*) δ 7.57 (dd, *J* = 8.4, 1.3 Hz, 1H), 6.71 (d, *J* = 8.3 Hz, 1H), 3.90 (s, 3H). ¹³C NMR (201 MHz, Chloroform-*d*) δ 155.89, 134.14, 118.80, 110.51, 103.35, 56.48. HRMS (+)APCI, calculated for: C₆H₅NOI₂ [M+H]⁺ 360.8461, found: 360.8167.

3.4 Synthesis of Cyano-substituted Pyridine-based *para*-Benzyne Precursors

3.4.1 Synthesis of 2-Cyano-3,6-diiodopyridine



Scheme 3.10 Synthetic route to 2-cyano-3,6-diiodopyridine

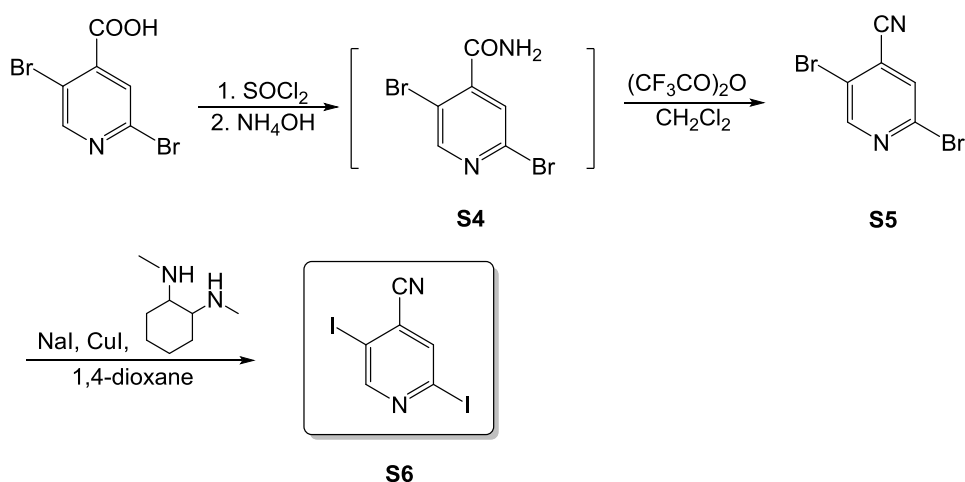
A solution of 3,6-dibromopyridine-2-carboxylic acid (0.3 g, 1 mmol) in thionyl chloride (3 mL) was refluxed for 3 h. The thionyl chloride was evaporated. The solid acid chloride was added in small portions into a concentrated aqueous ammonium hydroxide solution (10 mL) while keeping the reaction mixture at 0–5°C.⁷ The reaction mixture was saturated with potassium carbonate, and the solution was extracted with chloroform (2 × 150 mL). The organic layer was evaporated to dryness to yield crude **S1** (0.2 g), which was used for the next step without further purification.

The crude product was dissolved in 20 mL of CH₂Cl₂ and 0.29 mL pyridine (5 eq). 0.25 mL (2.5 eq) of trifluoroacetic anhydride was slowly added into the mixture at 0 °C.⁸ The mixture was stirred at room temperature for 1 h and it became clear. It was carefully diluted with CH₂Cl₂. The mixture was washed twice with saturated NaHCO₃. The organic layer was dried with Na₂SO₄ and concentrated to give the crude product, which was purified by flash chromatography to give 0.15 g (83%) **S2**. **S2** (0.13 g, 0.496 mmol) was dissolved in 1 mL of anhydrous 1,4-dioxane with these salts in the dioxane solution. NaI (297.7 mg, 1.985 mmol), CuI (9.45 mg, 0.05 mmol) and N1,N2-dimethylcyclohexane-1,2-diamine (14.12 mg, 0.10 mmol) was then added. The mixture was refluxed under argon for 24 h and then quenched with saturated aq. NH₄Cl solution (20 mL). The organic layer was extracted with CH₂Cl₂ (3 × 100 mL), washed with brine, dried with Na₂SO₄

and concentrated. The crude product was purified by using a silica gel column to give **S3** as white crystals.

^1H NMR (800 MHz, Chloroform-*d*) δ 7.83 (d, $J = 8.3$ Hz, 1H), 7.66 (d, $J = 8.4$ Hz, 1H). ^{13}C NMR (201 MHz, Chloroform-*d*) δ 147.43, 139.90, 139.05, 116.45, 116.31, 97.70. HRMS (+)ESI, calculated for: $\text{C}_6\text{H}_3\text{N}_2\text{I}_2$ $[\text{M}+\text{H}]^+$ 356.8386, found: 356.8366.

3.4.2 Synthesis of 4-Cyano-2,5-diiodopyridine



Scheme 3.11 Synthetic route to 4-cyano-2,5-diiodopyridine

A solution of 2,5-dibromoisonicotinic acid (0.3 g, 1 mmol) in thionyl chloride (3 mL) was refluxed for 3 h. The thionyl chloride was evaporated. The solid acid chloride was added in small portions into a concentrated ammonium hydroxide solution (10 mL) while keeping the mixture at $0-5^\circ\text{C}$.⁷ The reaction mixture was saturated with potassium carbonate, and the solution was extracted with chloroform (2×150 mL). Organic layer was evaporated to dryness to yield crude **S4** (0.2 g), which was used for the next step without further purification.

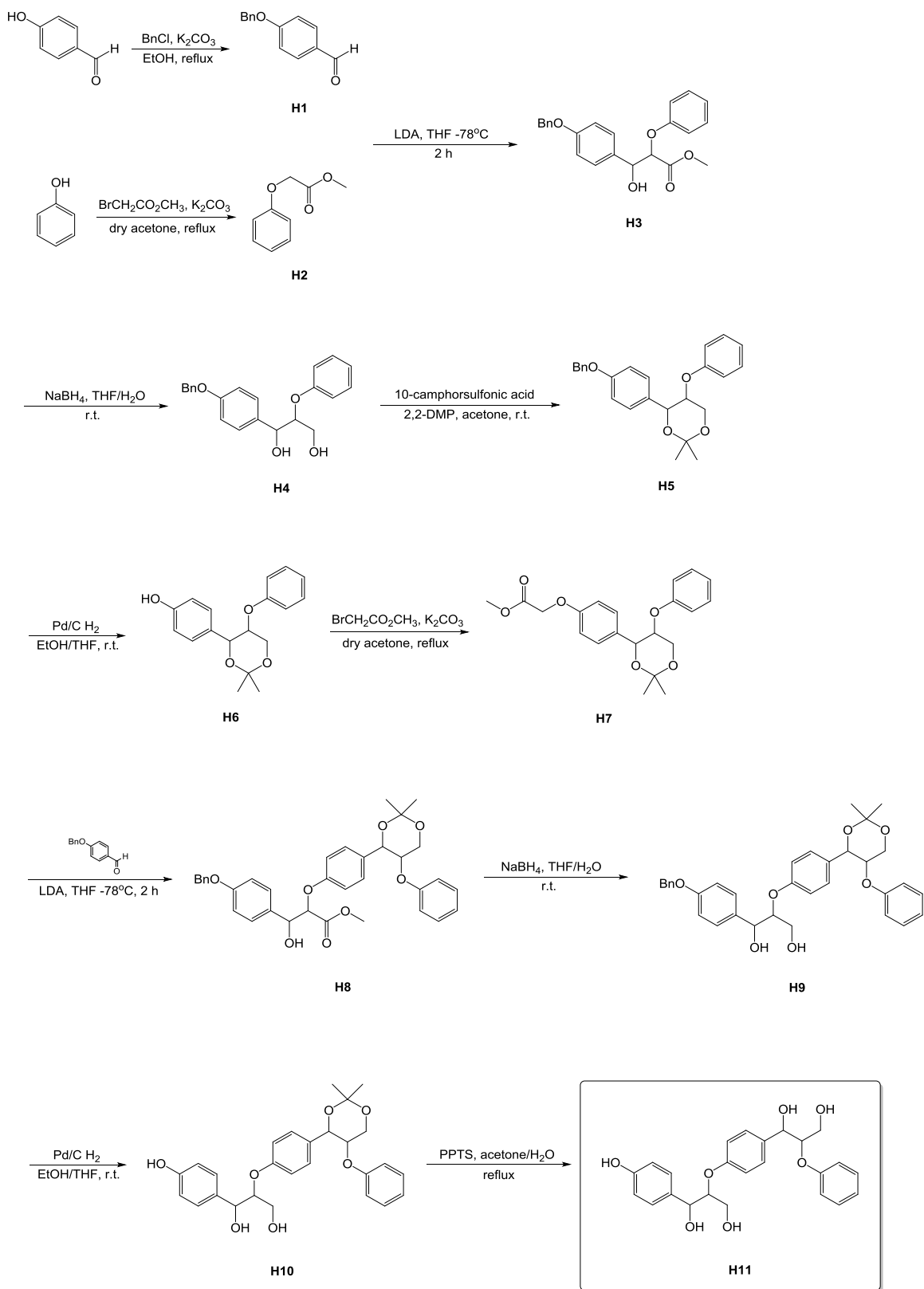
The crude product was dissolved in 20 mL of CH_2Cl_2 and 0.29 mL pyridine (5 eq). 0.25 mL (2.5 eq) of trifluoroacetic anhydride was slowly added into the mixture at 0°C .⁸ The mixture was stirred at room temperature for 1 h and it became clear. It was carefully diluted with CH_2Cl_2 . The mixture was washed twice with saturated NaHCO_3 . The organic layer was dried with Na_2SO_4 and

concentrated to give the crude product, which was purified by flash chromatography to give 0.15 g (83%) **S5**. **S5** (0.13 g, 0.496 mmol) was dissolved in 1 mL of anhydrous 1,4-dioxane. NaI (297.7 mg, 1.985 mmol), CuI (9.45 mg, 0.05 mmol) and N1,N2-dimethylcyclohexane-1,2-diamine (14.12 mg, 0.10 mmol) was then added. The mixture was refluxed under argon for 24 h and then quenched with NH₄Cl solution. The organic layer was extracted with CH₂Cl₂ (3 × 100 mL), washed with brine, dried with Na₂SO₄ and concentrated. The crude product was purified by using a silica gel column to give **S6** as white crystals.

¹H NMR (800 MHz, Chloroform-*d*) δ 8.85 (d, *J* = 1.9 Hz, 1H), 7.92 (d, *J* = 2.0 Hz, 1H). ¹³C NMR (201 MHz, Chloroform-*d*) δ 158.46, 137.82, 129.14, 115.86, 115.53, 95.68. HRMS (+)ESI, calculated for: C₆H₃N₂I₂ [M+H]⁺ 356.8386, found: 356.8377.

3.5 Synthesis of an H-lignin Model Compound

An H-lignin trimer with β-O-4 linkages was synthesized for the first time using a route described below (Scheme 3.12). The route was designed based on literature reports.⁹⁻¹²



Scheme 3.12 Synthetic route to an H-lignin trimer with β -O-4 linkages

Compound **H1**: Benzyl chloride (7.6 g, 60 mmol) was added into a solution of 4-hydroxybenzaldehyde (6.1 g, 50 mmol) in ethanol at room temperature. K_2CO_3 (8.3 g, 60 mmol) was then added into the solution at room temperature. The reaction mixture was refluxed for 4 h. After this (TLC indicated that the reaction had completed), K_2CO_3 was filtered out and the product **H1** was recrystallized from ethanol as a white solid (1.89 g, 8.9 mmol, yield 89%).

1H NMR (800 MHz, Chloroform-*d*) δ 9.90 (s, 1H), 7.90 – 7.78 (m, 2H), 7.53 – 7.33 (m, 5H), 7.10 (d, $J = 8.6$ Hz, 2H), 5.17 (s, 2H). ^{13}C NMR (201 MHz, Chloroform-*d*) δ 190.73, 163.68, 135.90, 131.95, 130.08, 128.69, 128.28, 127.44, 115.10, 70.21. HRMS (+)ESI, calculated for: $C_{14}H_{13}O_2$ $[M+H]^+$ 213.0916, found: 213.0913.

Compound **H2**: Methyl bromoacetate (2.43 g, 15.9 mmol) was added into a solution of phenol (0.96 g, 10.2 mmol) in dry acetone at room temperature. K_2CO_3 (2.07 g, 15.0 mmol) was then added into the mixture at room temperature. The reaction mixture was refluxed for 6 h. After this, K_2CO_3 was filtered out and the mixture was extracted with EtOAc (3×20 mL). The organic layers were combined and dried with Na_2SO_4 . The solvent was removed *in vacuo*. The product was purified by an automatic flash column (hexanes : EtOAc 2:1 v/v) to obtain a colorless oil (1.41 g, 8.5 mmol, yield 83%).

1H NMR (800 MHz, Chloroform-*d*) δ 7.27 (t, $J = 7.9$ Hz, 2H), 7.05 – 6.81 (m, 3H), 4.59 (s, 2H), 3.74 (s, 3H). ^{13}C NMR (201 MHz, Chloroform-*d*) δ 169.31, 157.75, 129.50, 121.64, 114.54, 65.09, 52.00. HRMS (+)ESI, calculated for: $C_9H_{11}O_3$ $[M+H]^+$ 167.0708, found: 167.0690.

Compound **H3**: *n*-Butyllithium (5.0 mL of a 2.5 M solution in hexanes, 12.5 mmol) was added into a solution of diisopropylamine (1.7 mL, 12.1 mmol) in dry THF at 0 °C. The mixture was stirred at 0 °C for 30 min. The mixture was cooled to -78 °C in a dry ice-acetone bath. A solution of **H2** (1.66 g, 10.0 mmol) in dry THF was added dropwise into the mixture at -78 °C and the mixture was stirred for 30 min. After this, a solution of **H1** (2.21 g, 10.4 mmol) in dry THF was added dropwise into the solution at -78 °C. After 2 h of stirring, 30 mL of saturated aq. NH_4Cl was added into the mixture and the mixture was stirred for 20 min. The mixture was then extracted with EtOAc (3×30 mL). The organic layers were combined and dried using Na_2SO_4 . The mixture

was purified via liquid chromatography (hexanes : EtOAc 1:1 v/v) to obtain a yellow wax , which contained two inseparable diastereomeric compounds (2.42 g, yield 64%).

^1H NMR (800 MHz, Chloroform-*d*) δ 7.46 – 7.23 (m, 9H), 7.03 – 6.84 (m, 5H), 5.17 (d, J = 5.9 Hz, 1H), 5.08 (s, 2H), 4.79 (d, J = 6.0 Hz, 1H), 3.67 (s, 3H). ^{13}C NMR (201 MHz, Chloroform-*d*) δ 170.19, 158.76, 157.39, 136.82, 131.48, 129.62, 129.54, 128.53, 127.93, 127.87, 127.42, 122.23, 122.09, 115.38, 115.35, 114.82, 114.71, 81.67, 80.76, 74.39, 73.85, 69.94, 52.28. HRMS (+)ESI, calculated for: $\text{C}_{23}\text{H}_{22}\text{O}_5\text{Na}$ $[\text{M}+\text{Na}]^+$ 401.1365, found: 401.1330.

Compound **H4**: **H3** (2.21 g, 5.8 mmol) was dissolved in 36 mL THF-H₂O (3:1 v/v). NaBH₄ (2.19 g, 58 mmol) was added in several portions over a period of 2.5 h. The mixture was stirred overnight, and 30 mL water was added. The solution was then extracted with EtOAc (3 \times 20 mL) and dried using Na₂SO₄. The combined organic layers were concentrated to give product **H4** (1.81 g, yield 89%) as a yellow syrup/wax, which was used in next step without purification.

^1H NMR (800 MHz, Chloroform-*d*) δ 7.47 – 7.24 (m, 9H), 7.04 – 6.89 (m, 5H), 5.08 (s, 1H), 5.06 (d, J = 12.5 Hz, 2H), 4.41 (dq, J = 9.6, 4.4 Hz, 1H), 3.98 – 3.55 (m, 2H). ^{13}C NMR (201 MHz, Chloroform-*d*) δ 158.44, 157.57, 136.83, 132.68, 129.68, 129.58, 128.54, 128.15, 127.94, 127.47, 127.41, 121.79, 116.56, 116.49, 114.91, 114.82, 81.80, 73.75, 73.51, 69.98, 61.27, 61.01. HRMS (+)ESI, calculated for: $\text{C}_{22}\text{H}_{22}\text{O}_4\text{Na}$ $[\text{M}+\text{Na}]^+$ 373.1416, found: 373.1393.

Compound **H5**: To a solution of **H4** (1.75 g, 5.0 mmol) in dry acetone, 2,2-dimethoxypropane (DMP, 0.72 mL, 29.5 mmol) was added. Camphorsulfonic acid (0.12 g, 0.5 mmol) was then added into the solution and the mixture was stirred overnight. After this, 10 mL of saturated aq. NaHCO₃ was added. The mixture was extracted with EtOAc (3 \times 20 mL) and dried using Na₂SO₄. A yellow syrup **H5** (1.58 g, yield 81%) was isolated via liquid chromatography (hexanes: EtOAc 3:1 v/v) as a pair of diastereomers to be used in next step.

^1H NMR (800 MHz, Chloroform-*d*) δ 7.46 – 7.18 (m, 9H), 6.98 – 6.91 (m, 3H), 6.74 (d, J = 8.4 Hz, 2H), 5.07 (s, 2H), 4.90 (d, J = 9.1 Hz, 1H), 4.35 – 3.94 (m, 2H), 1.65 (s, 6H). ^{13}C NMR (201 MHz, Chloroform-*d*) δ 158.59, 157.42, 136.97, 131.62, 129.44, 128.51, 128.34, 127.87,

127.37, 121.48, 115.94, 114.73, 99.57, 75.06, 74.06, 72.87, 70.00, 69.92, 62.58, 28.25, 19.74. HRMS (+)ESI, calculated for: C₂₅H₂₆O₄Na [M+Na]⁺ 413.1729, found: 413.1718.

Compound **H6**: **H5** (1.95 g, 5.0 mmol) was added into 20 mL EtOH-THF (1:1 v/v) containing 10% Pd/C (0.20 g). The mixture was hydrogenated at atmospheric pressure and room temperature for 4 h. The solution was filtered over Celite and concentrated to give **H6** (1.48 g, yield 99%) as a colorless syrup, which was used in the next step without purification.

¹H NMR (800 MHz, Chloroform-*d*) δ 7.36 (d, *J* = 8.2 Hz, 2H), 7.19 – 7.16 (m, 2H), 6.90 (t, *J* = 7.3 Hz, 1H), 6.78 (d, *J* = 8.3 Hz, 2H), 6.70 (d, *J* = 8.1 Hz, 2H), 4.85 (d, *J* = 9.1 Hz, 1H), 4.29 – 3.90 (m, 3H), 1.64 (s, 3H), 1.53 (s, 3H). ¹³C NMR (201 MHz, Chloroform-*d*) δ 157.48, 155.28, 131.51, 129.42, 128.54, 121.47, 115.90, 115.33, 115.11, 99.54, 75.06, 74.03, 62.55, 28.24, 19.66. HRMS (+)ESI, calculated for: C₂₅H₂₆O₄Na [M+Na]⁺ 323.1259, found: 323.1247. (-)ESI, calculated for: C₁₈H₁₉O₄ [M-H]⁻ 299.1283, found: 299.1288.

Compound **H7**: To a solution of **H6** (1.48 g, 4.9 mmol) in dry acetone, methyl bromoacetate (1.12 g, 7.4 mmol) was added. K₂CO₃ (1.08 g, 7.8 mmol) was then added at room temperature and the mixture was refluxed and stirred overnight. The solution was filtered, extracted with EtOAc (3 × 20 mL), and the solution was dried using Na₂SO₄. **H7** (1.29 g, yield 71%) was obtained as a colorless oil after purification by liquid chromatography (hexanes : EtOAc 2:1 v/v).

¹H NMR (800 MHz, Chloroform-*d*) δ 7.42 (d, *J* = 8.2 Hz, 2H), 7.28 – 7.03 (m, 2H), 7.01 – 6.78 (m, 3H), 6.70 (d, *J* = 8.4 Hz, 2H), 4.88 (d, *J* = 9.1 Hz, 1H), 4.61 (s, 2H), 4.29 – 3.90 (m, 3H), 3.79 (s, 3H), 1.62 (s, 6H). ¹³C NMR (201 MHz, Chloroform-*d*) δ 169.19, 157.23, 132.58, 129.44, 128.39, 121.48, 121.23, 116.50, 115.86, 114.41, 114.16, 99.51, 75.05, 73.84, 72.62, 67.91, 65.23, 62.45, 52.03, 28.16, 19.72. HRMS (+)ESI, calculated for: C₂₁H₂₄O₆Na [M+Na]⁺ 395.1471, found: 395.1445.

Compound **H8**: *n*-Butyllithium (2.4 mL of a 2.5 M solution in hexanes, 6.0 mmol) was added into a solution of diisopropylamine (0.9 mL, 6.3 mmol) in dry THF at 0 °C. The mixture was stirred at 0 °C for 30 min. The mixture was cooled to -78 °C. A solution of **H7** (1.86 g, 5.0 mmol) in dry

THF was added dropwise into the mixture at -78 °C that was stirred for 30 min. A solution of **H1** (1.17 g, 5.5 mmol) in dry THF was added dropwise into the solution at -78 °C. After 2 h stirring, 30 mL of saturated aq. NH₄Cl was added into the mixture and the mixture was stirred for 20 min. The mixture was then extracted with EtOAc (3 × 20 mL). The organic layers were combined and dried using Na₂SO₄. The mixture was purified via liquid chromatography (hexanes : EtOAc 1:1 v/v) to obtain a yellow syrup, which contained two inseparable diastereomeric compounds (2.04 g, yield 70%).

¹H NMR (800 MHz, Chloroform-*d*) δ 7.46 – 7.31 (m, 11H), 7.18 – 7.16 (m, 1H), 6.98 – 6.78 (m, 5H), 6.68 (dd, *J* = 8.0, 4.9 Hz, 1H), 5.07 (d, *J* = 6.3 Hz, 2H), 4.84 (d, *J* = 9.3 Hz, 1H), 4.72 (dd, *J* = 9.0, 6.1 Hz, 1H), 4.27 – 4.14 (m, 2H), 3.91 (ddd, *J* = 12.1, 8.6, 4.6 Hz, 1H), 3.68 (d, *J* = 13.0 Hz, 2H), 3.59 (d, *J* = 13.9 Hz, 1H), 1.52 (s, 3H), 1.30 (s, 3H). ¹³C NMR (201 MHz, Chloroform-*d*) δ 157.26, 136.80, 134.89, 129.41, 128.52, 127.92, 127.42, 126.93, 121.46, 115.82 (d, *J* = 9.4 Hz), 115.29 (d, *J* = 12.0 Hz), 114.81 (d, *J* = 5.8 Hz), 99.54, 80.87, 80.77, 74.92, 74.84, 73.84, 73.78, 69.98, 69.93, 69.90, 62.48, 60.78, 52.26, 43.22, 28.16, 19.68. HRMS (+)ESI, calculated for: C₃₅H₃₆O₈Na [M+Na]⁺ 607.2308, found: 607.2299.

Compound **H9**: **H8** (1.17 g, 2.0 mmol) was dissolved in 16 mL THF-H₂O (3:1 v/v), followed by the addition of NaBH₄ (0.76 g, 20 mmol) in several portions over a period of 3 h. The mixture was stirred overnight, and 20 mL water was added. The solution was then extracted with EtOAc (3 × 20 mL) and the combined organic layers were dried using Na₂SO₄. The combined organic layers were concentrated to give product **H9** (1.09 g, yield 98%) as a colorless syrup, which was used in next step without purification.

¹H NMR (800 MHz, Chloroform-*d*) δ 7.48 – 7.24 (m, 11H), 7.17 – 6.68 (m, 7H), 5.09 – 5.05 (m, 2H), 4.36 (p, *J* = 4.8, 4.3 Hz, 1H), 4.29 – 4.15 (m, 2H), 3.95 – 3.82 (m, 2H), 1.64 (s, 3H), 1.53 (s, 3H). ¹³C NMR (201 MHz, Chloroform-*d*) δ 158.45, 157.29, 136.81, 132.55, 129.40, 128.54, 128.48, 128.12, 127.93, 127.40, 126.90, 121.45, 116.42, 115.81, 114.82, 99.56, 81.92, 74.85, 74.12, 73.66, 69.97, 62.51, 61.20, 50.81, 28.20, 19.67. HRMS (+)ESI, calculated for: C₃₄H₃₆O₇Na [M+Na]⁺ 579.2359, found: 579.2344.

Compound **H10**: **H9** (1.11 g, 2.0 mmol) was added into 20 mL EtOH-THF (1:1 v/v) containing 10% Pd/C (0.11 g). The mixture was hydrogenated at atmospheric pressure and room temperature for 4 h. The solution was filtered over Celite and concentrated to give **H10** (0.93 g, yield 100%) as a colorless syrup, which was used in next step without purification.

^1H NMR (800 MHz, Chloroform-*d*) δ 7.46 – 7.14 (m, 7H), 7.01 – 6.66 (m, 6H), 5.04 – 4.94 (m, 1H), 4.86 (dd, $J = 17.1, 9.1$ Hz, 1H), 4.35 (h, $J = 4.3$ Hz, 1H), 4.30 – 4.15 (m, 2H), 4.07 – 3.66 (m, 3H), 1.64 (d, $J = 6.7$ Hz, 3H), 1.53 (d, $J = 6.4$ Hz, 3H). ^{13}C NMR (201 MHz, Chloroform-*d*) δ 157.30, 155.29, 129.41, 128.57, 128.47, 128.31, 127.60, 122.37, 121.44, 116.45, 116.36, 115.79, 115.38, 115.28, 99.58, 81.85, 74.79, 73.93, 73.71, 73.65, 73.46, 62.50, 61.34, 61.29, 50.83, 28.20, 19.67. HRMS (+)ESI, calculated for: $\text{C}_{27}\text{H}_{30}\text{O}_7\text{Na}$ $[\text{M}+\text{Na}]^+$ 489.1889, found: 489.1871. (-)ESI, calculated for: $\text{C}_{27}\text{H}_{29}\text{O}_7$ $[\text{M}-\text{H}]^-$ 465.1913, found: 465.1920.

Compound **H11**: Pyridinium *p*-toluenesulfonate (PPTS, 0.13 g, 0.5 mmol) was added into a solution in 20 mL acetone- H_2O (1:1, v/v) containing **H10** (0.43 g, 0.9 mmol) at room temperature.¹² The solution was refluxed overnight and concentrated. The residue was purified by chromatography <what type? (CH_2Cl_2 : MeOH 9:1 v/v) to give **H11** (0.22 g, yield 58%) as a yellow syrup.

^1H NMR (800 MHz, DMSO-*d*₆) δ 9.22 (s, 1H), 7.35 – 7.05 (m, 6H), 6.95 – 6.76 (m, 5H), 6.76 – 6.58 (m, 2H), 5.52 – 5.19 (m, 1H), 4.75 – 4.62 (m, 4H), 4.25 (d, $J = 5.4$ Hz, 1H), 3.63 (dd, $J = 11.8, 3.2$ Hz, 1H), 3.59 (dq, $J = 10.7, 6.2$ Hz, 2H). ^{13}C NMR (201 MHz, DMSO-*d*₆) δ 159.14, 158.17, 156.66, 134.69, 133.08, 129.60, 128.42, 128.26, 128.14, 120.82, 116.64, 115.91, 115.68, 114.88, 83.57, 71.67, 60.37, 60.32, 48.99. HRMS (+)ESI, calculated for: $\text{C}_{24}\text{H}_{26}\text{O}_7\text{Na}$ $[\text{M}+\text{Na}]^+$ 449.1576, found: 449.1567. (-)ESI, calculated for: $\text{C}_{27}\text{H}_{29}\text{O}_7$ $[\text{M}-\text{H}]^-$ 425.1600, found: 425.1588.

3.6 NMR Spectra

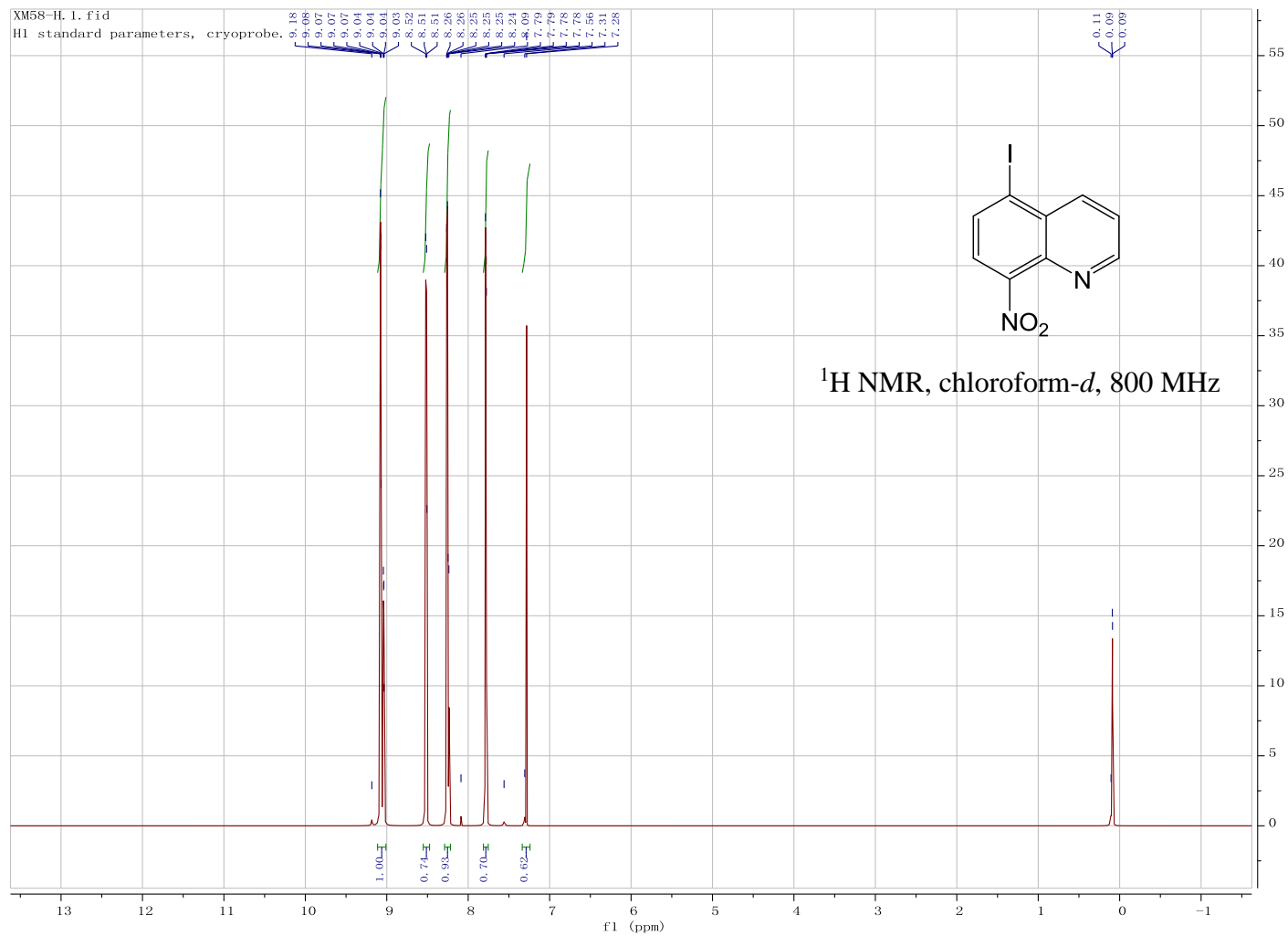


Figure 3.1 ¹H NMR spectrum for 5-iodo-8-nitroquinoline

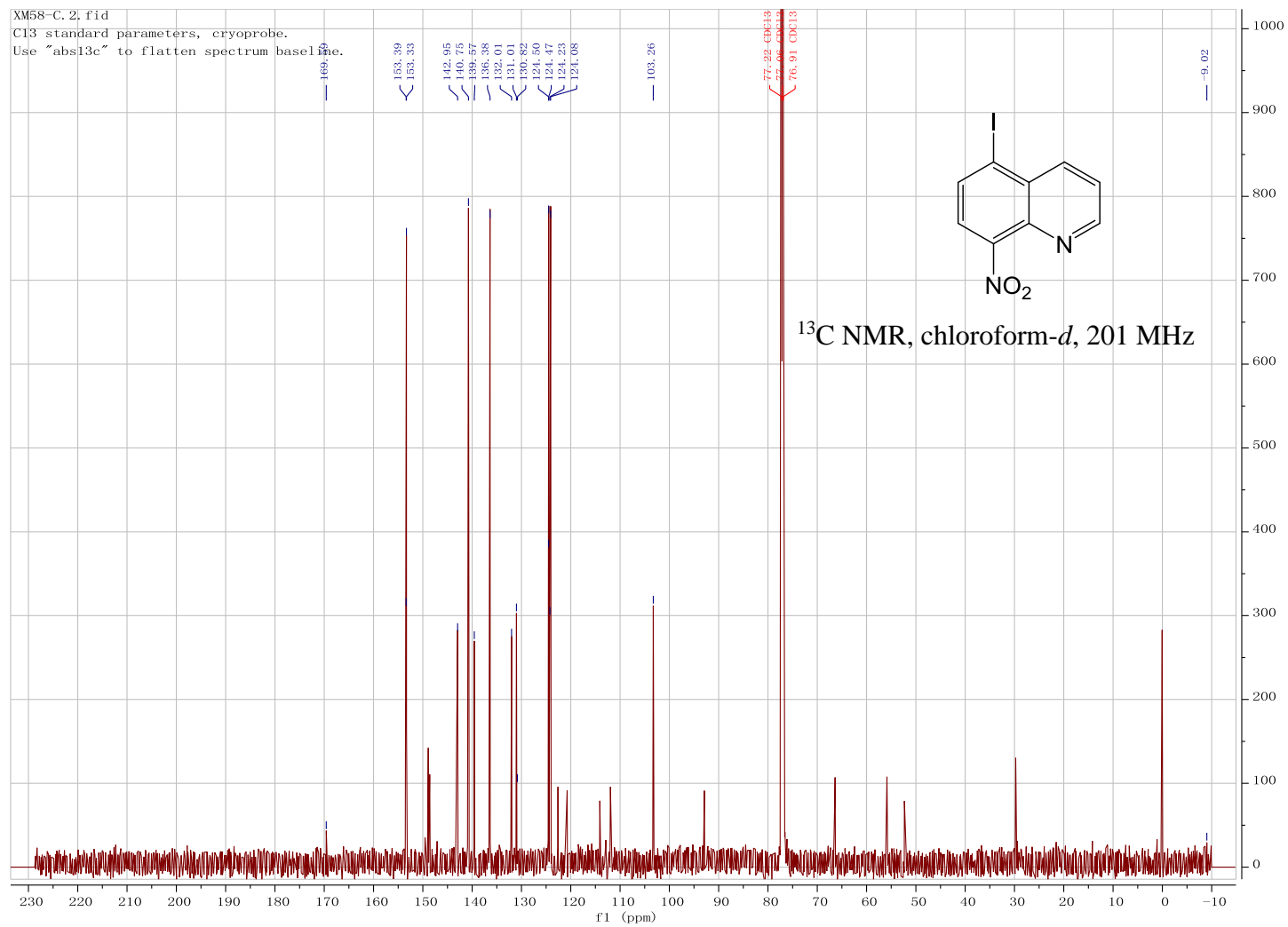


Figure 3.2 ^{13}C NMR spectrum for 5-iodo-8-nitroquinoline

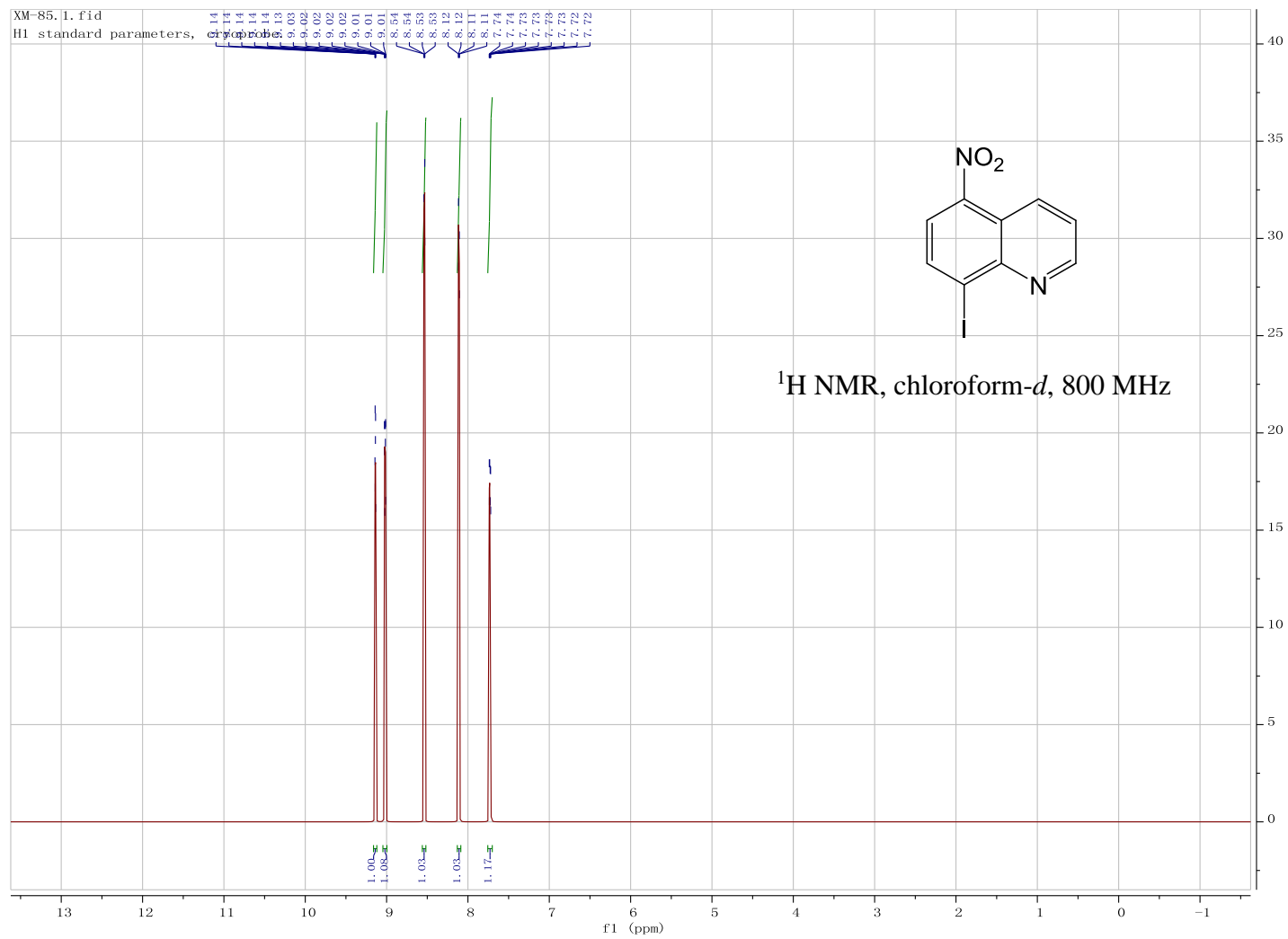


Figure 3.3 $^1\text{H NMR}$ spectrum for 8-iodo-5-nitroquinoline

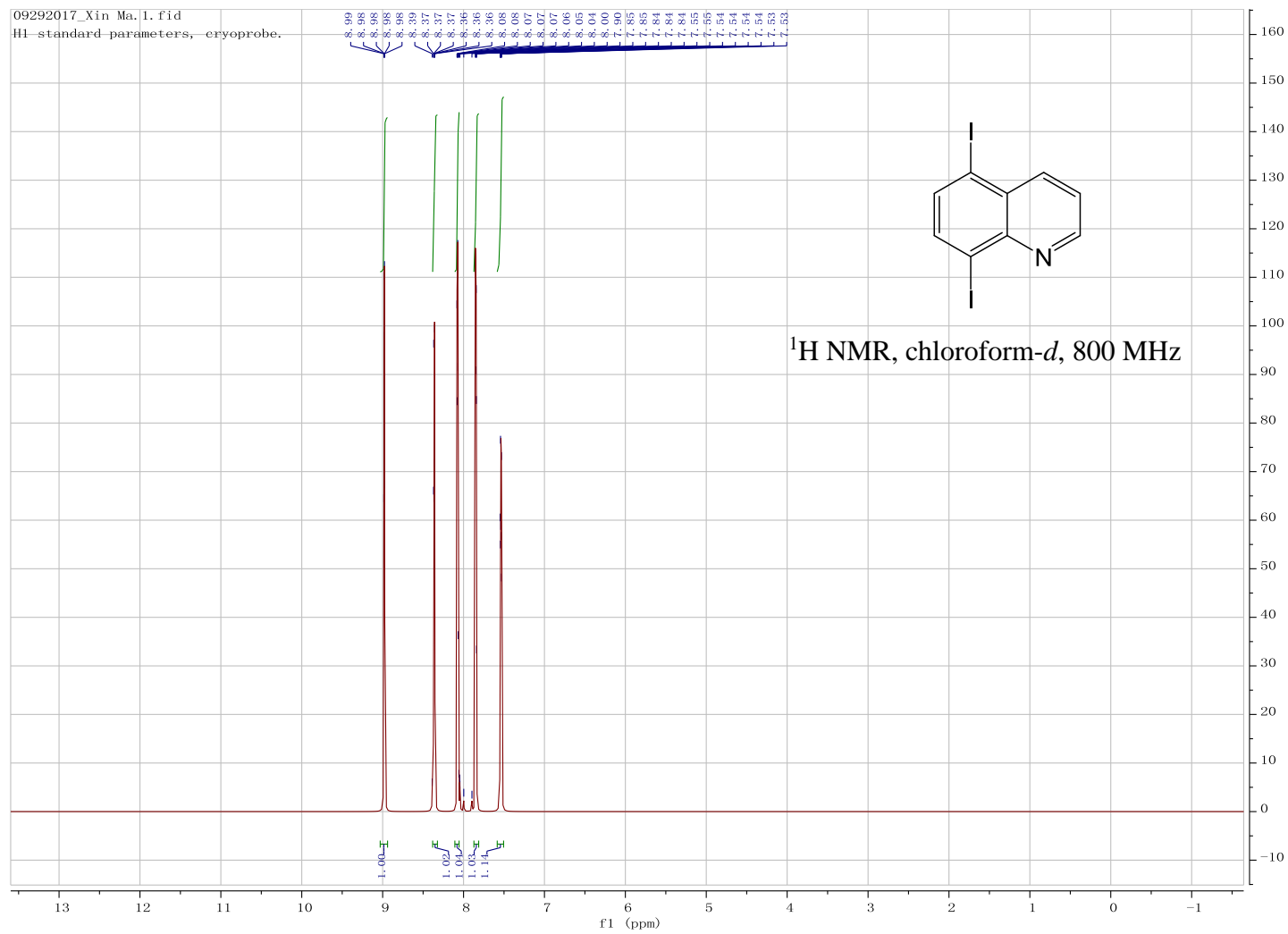


Figure 3.5 ^1H NMR spectrum for 5,8-diiodoquinoline

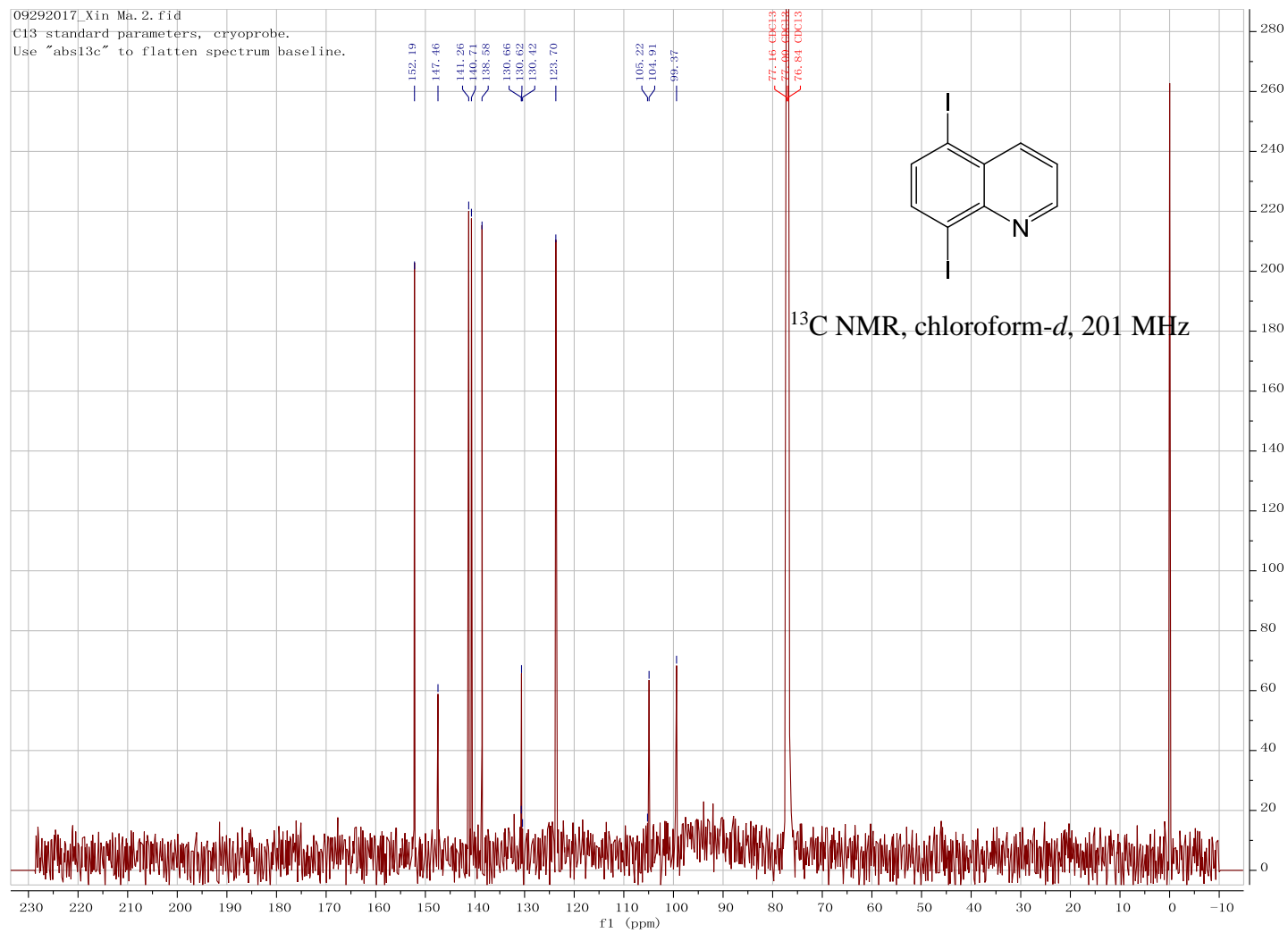


Figure 3.6 ^{13}C NMR spectrum for 5,8-diiodoquinoline

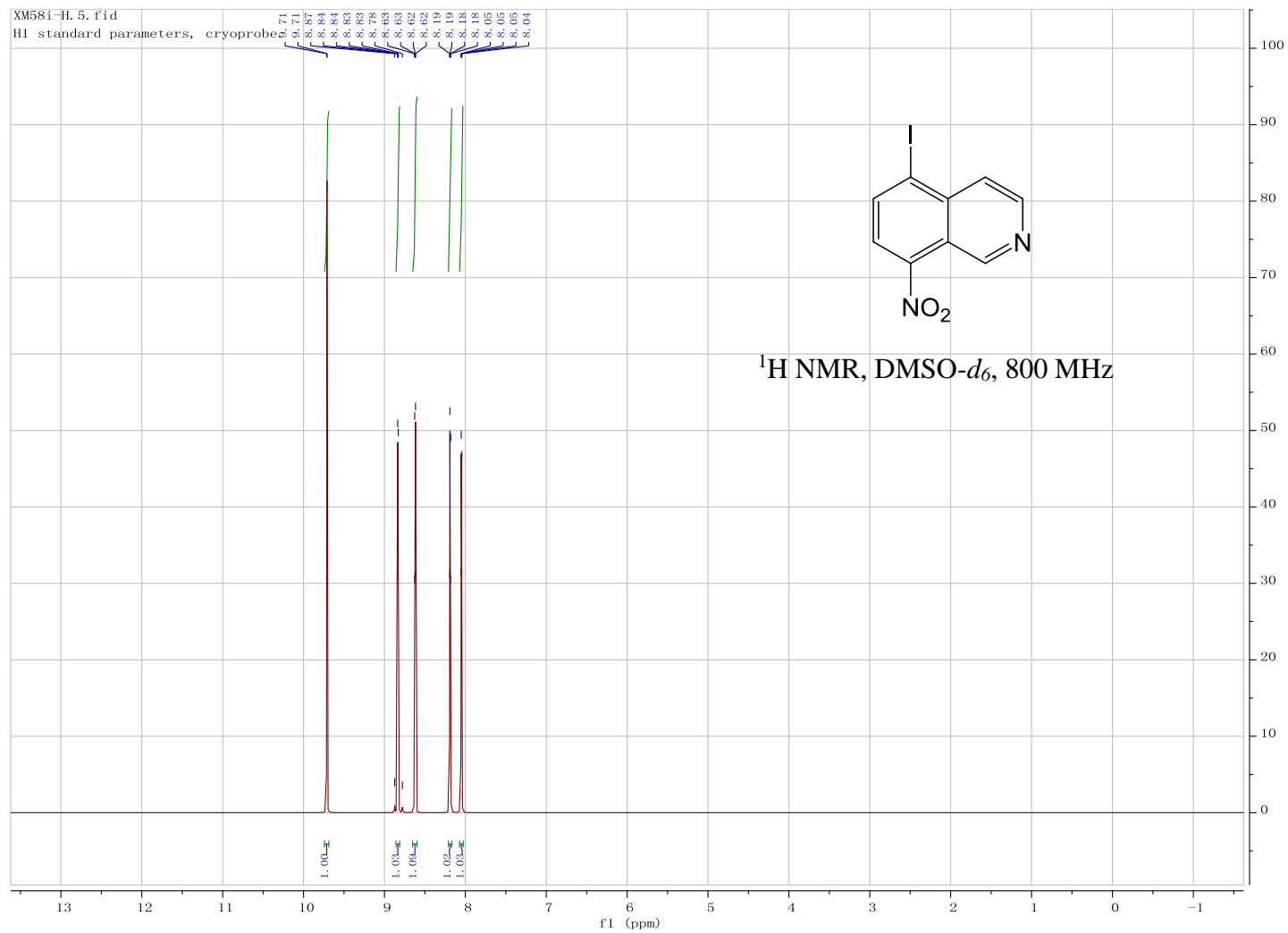


Figure 3.7 ^1H NMR spectrum for 5-iodo-8-nitroisoquinoline

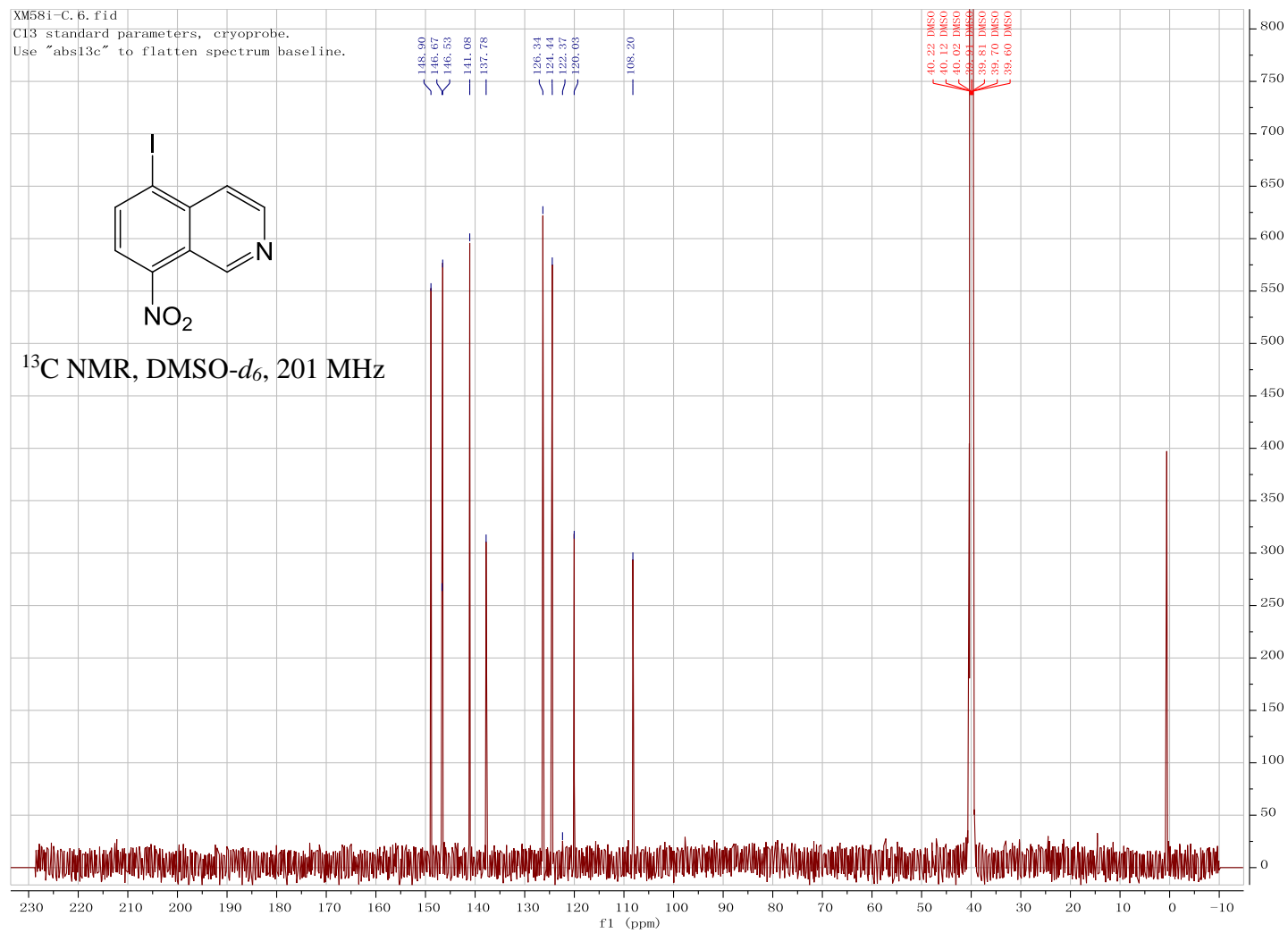


Figure 3.8 ^{13}C NMR spectrum for 5-iodo-8-nitroquinoline

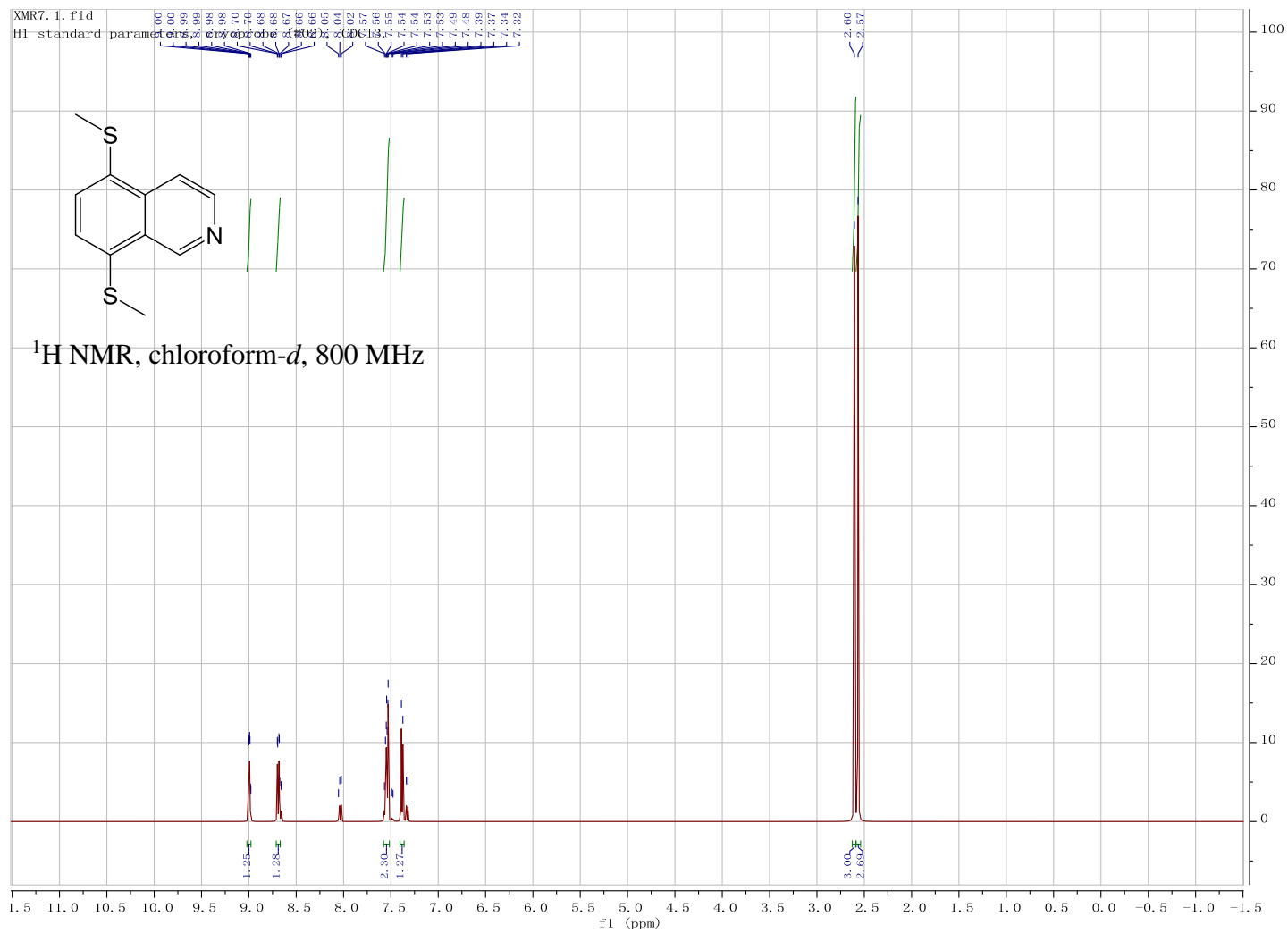


Figure 3.9 ¹H NMR spectrum for 5,8-dithiomethylquinoline

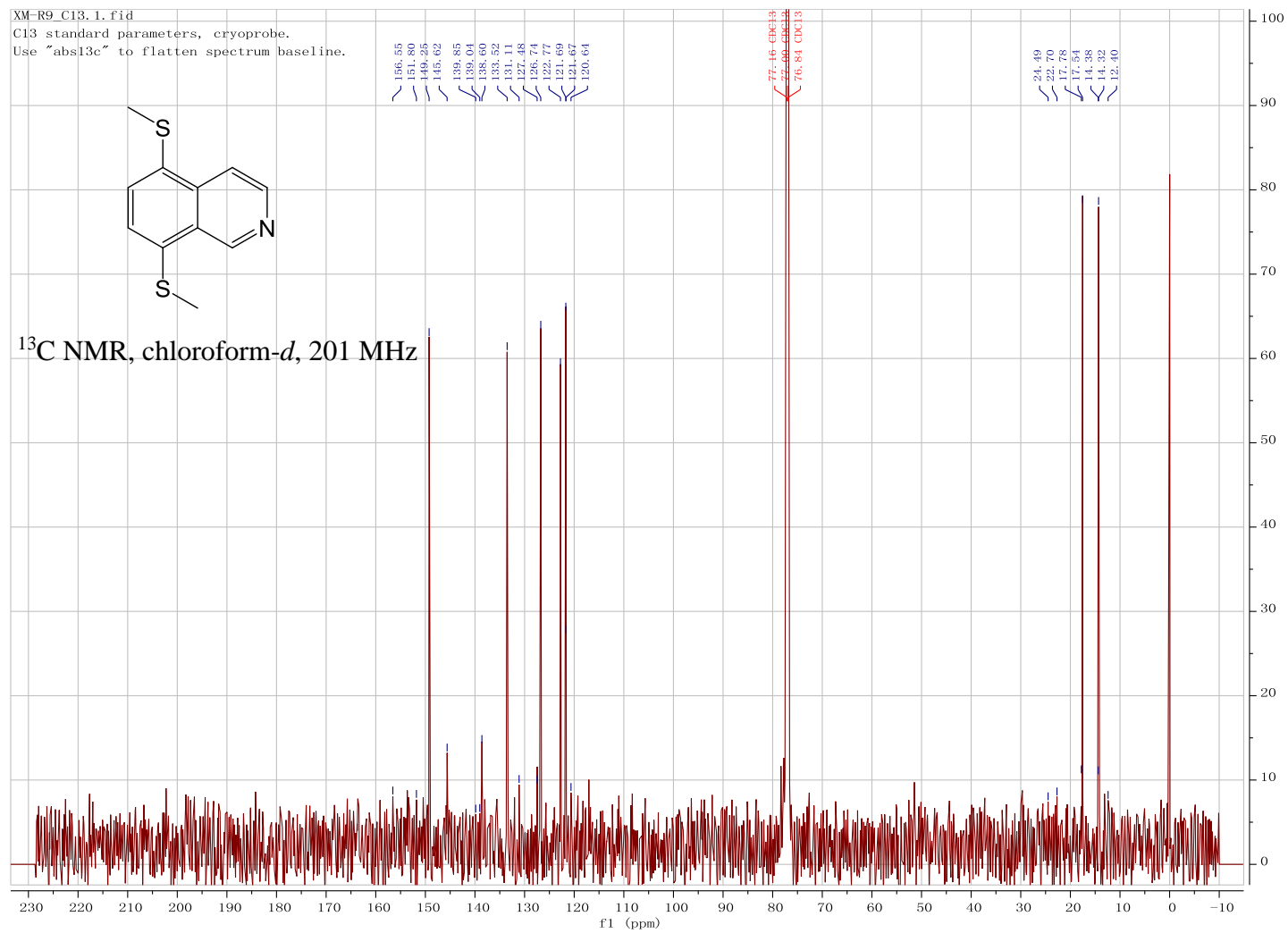


Figure 3.10 ^{13}C NMR spectrum for 5,8-dithiomethylquinoline

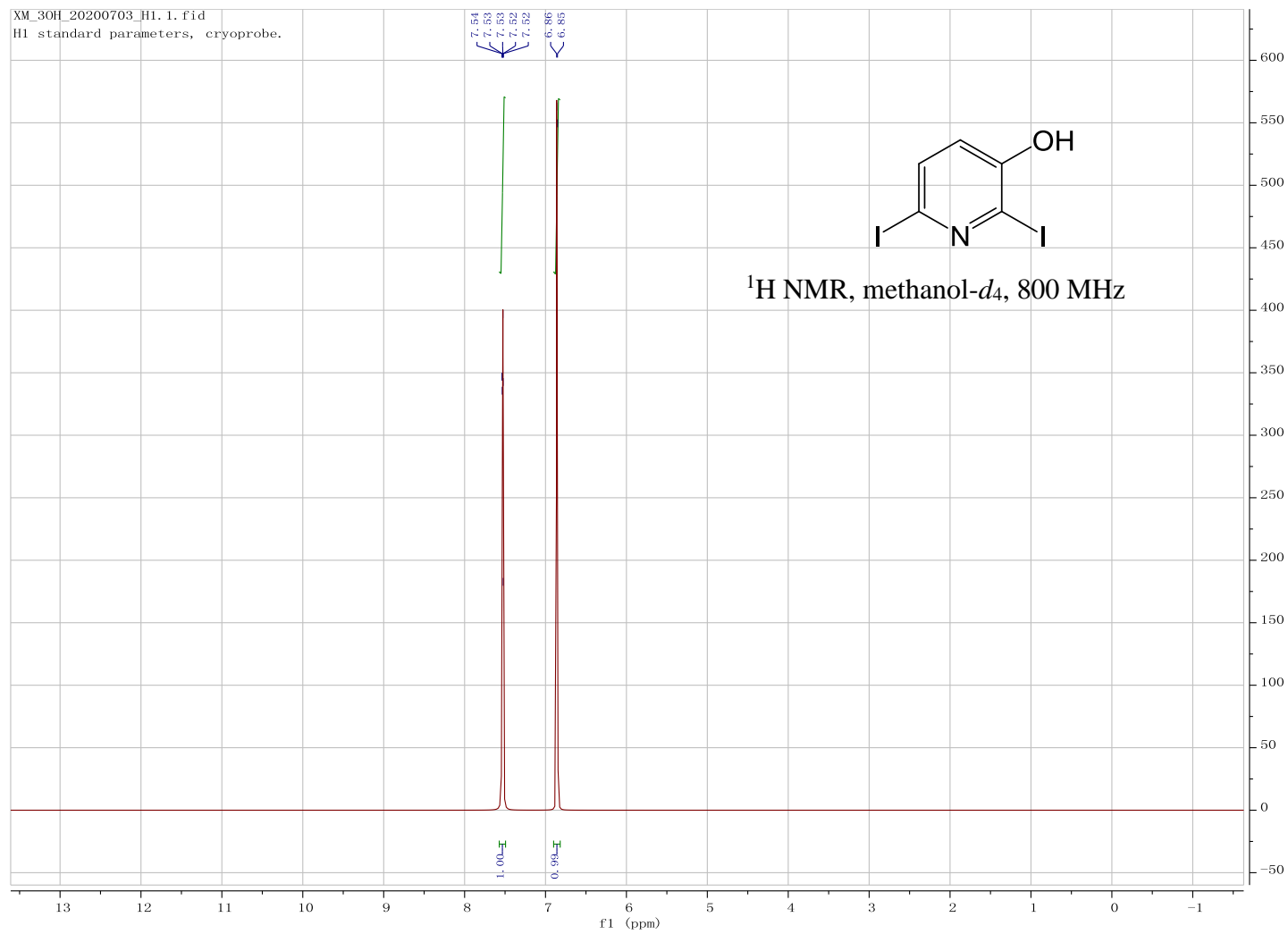


Figure 3.11 ^1H NMR spectrum for 3-hydroxy-2,6-diiodopyridine

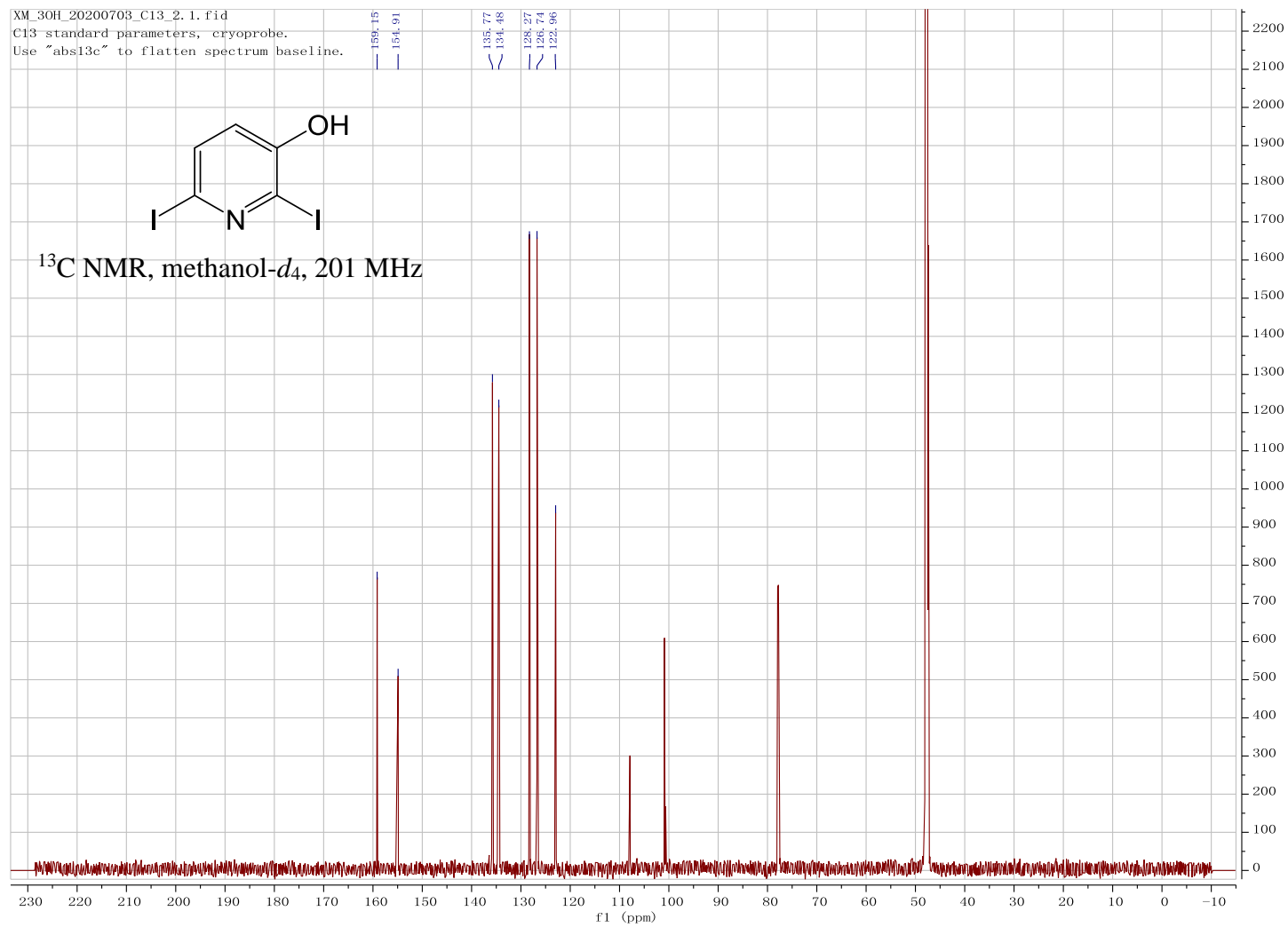


Figure 3.12 ^{13}C NMR spectrum for 3-hydroxy-2,6-diiodopyridine

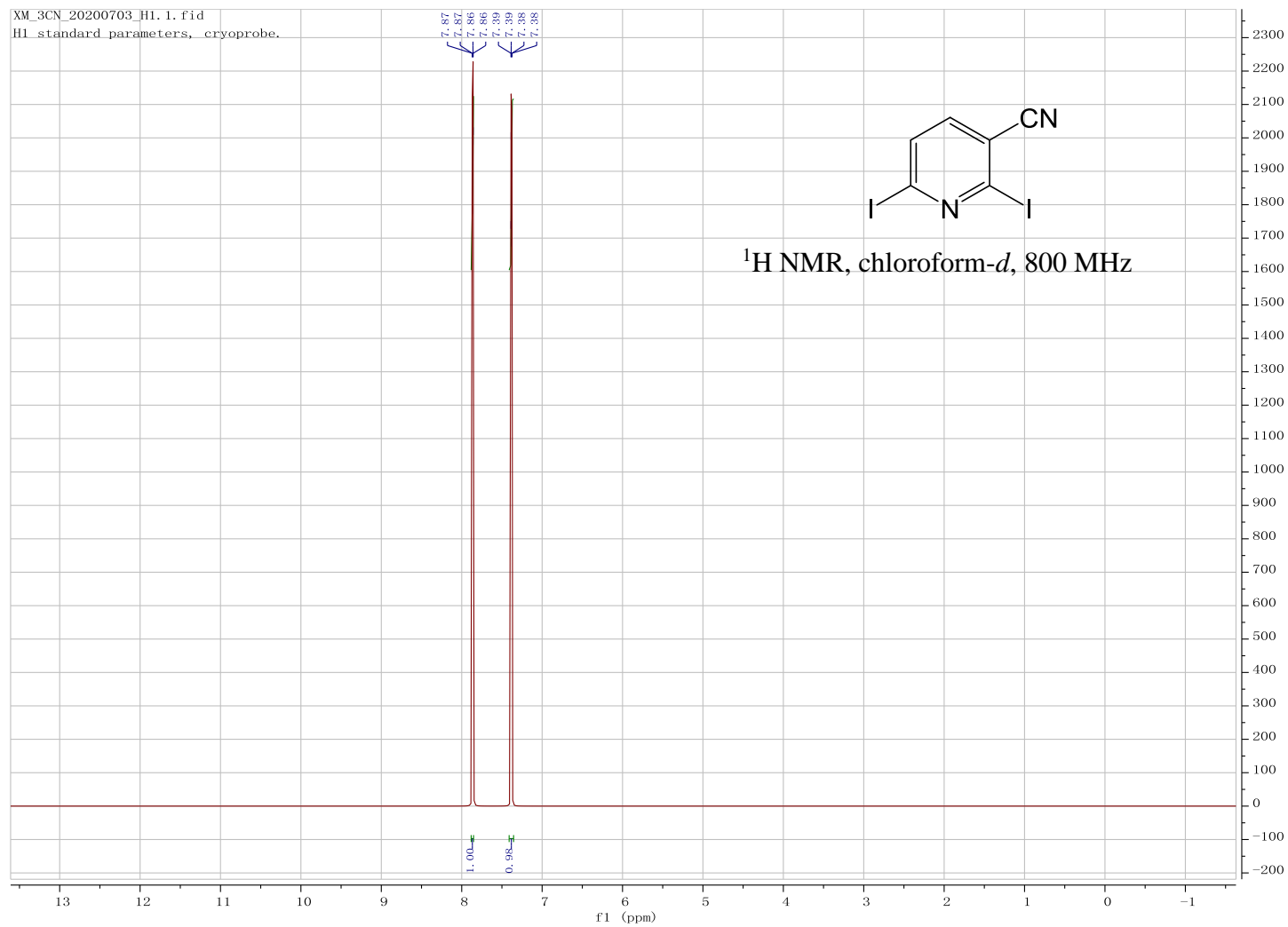


Figure 3.13 ^1H NMR spectrum for 3-cyano-2,6-diiodopyridine

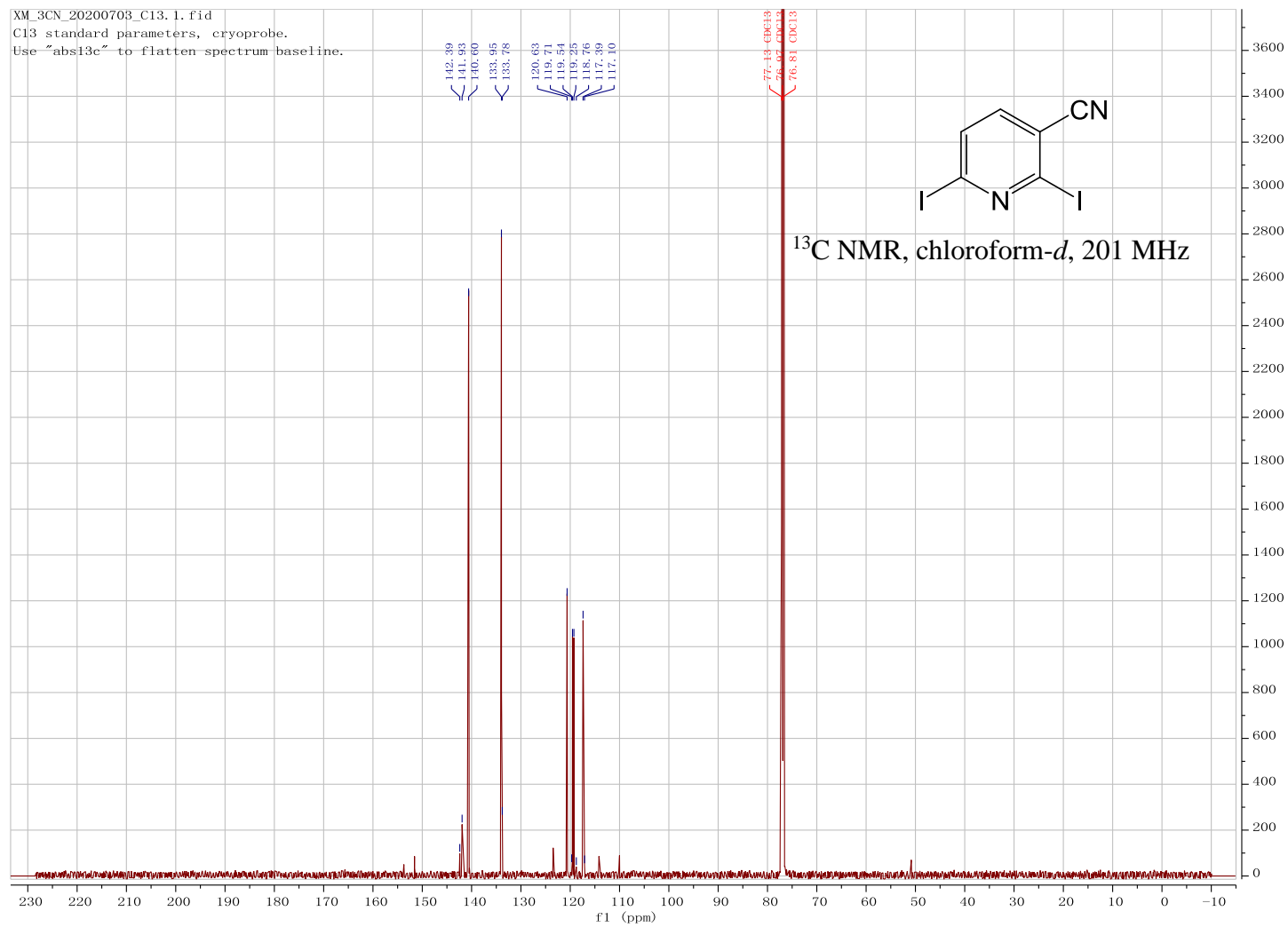


Figure 3.14 ^{13}C NMR spectrum for 3-cyano-2,6-diiodopyridine

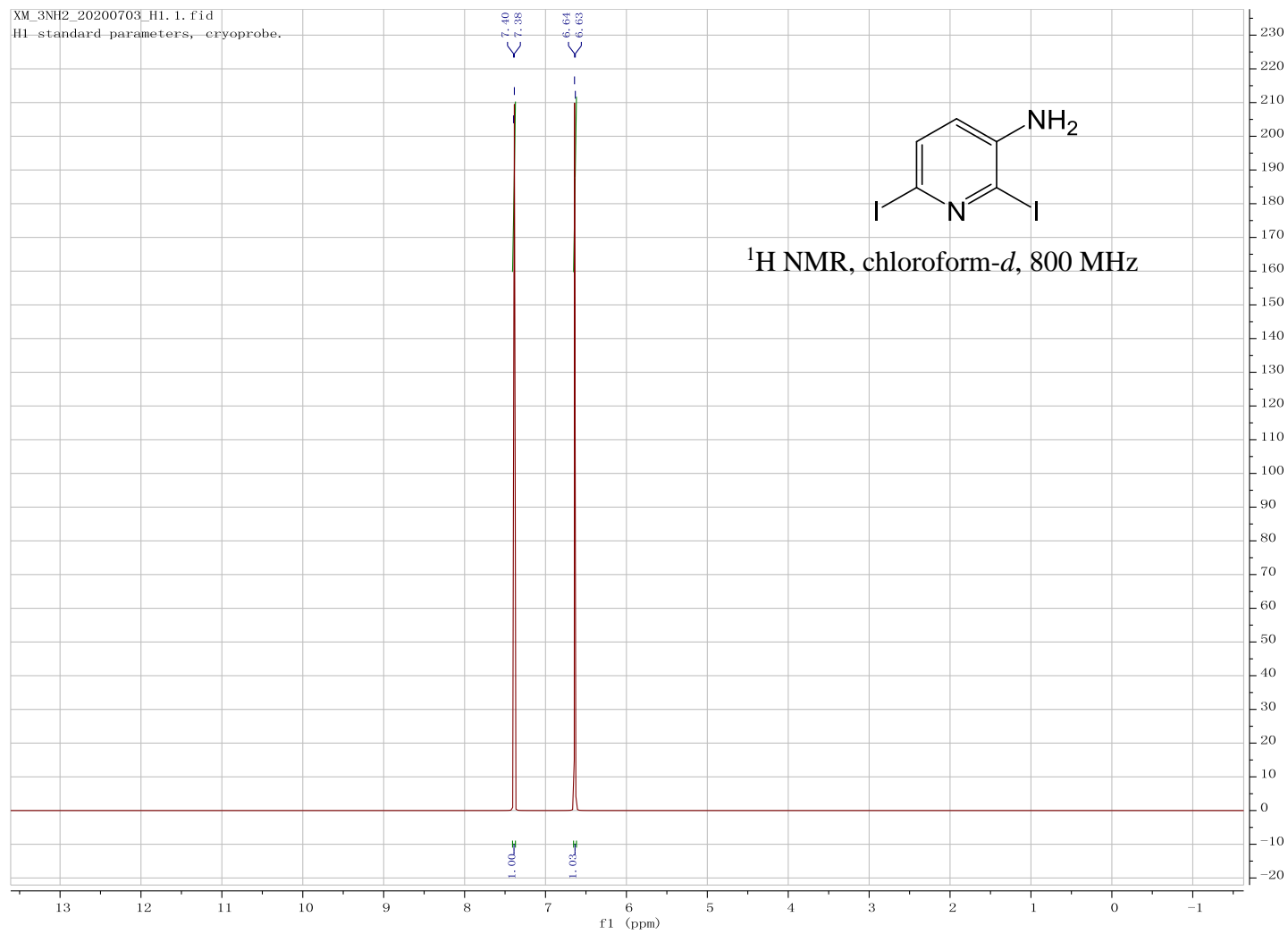


Figure 3.15 ^1H NMR spectrum for 3-amino-2,6-diiodopyridine

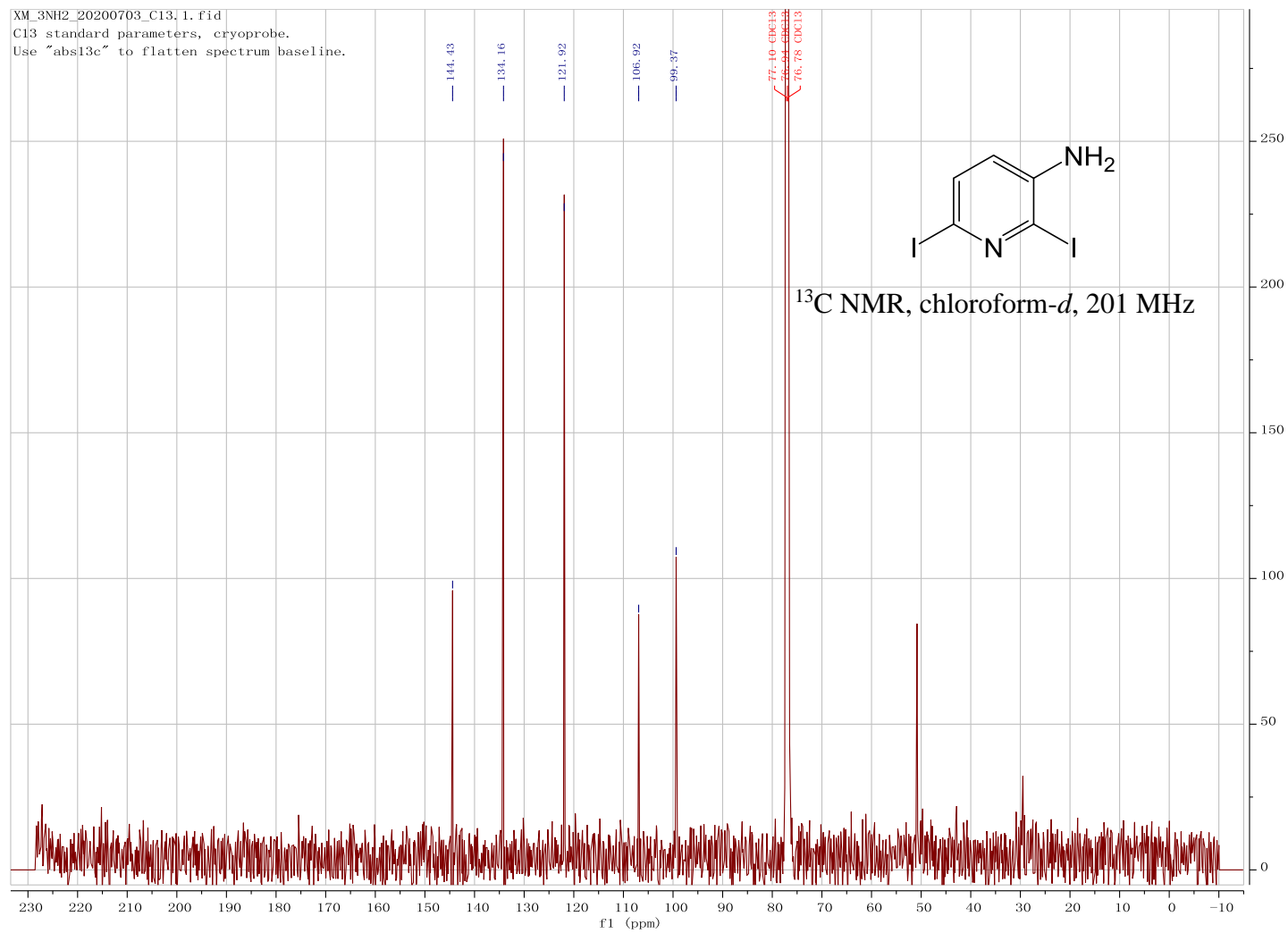


Figure 3.16 ^{13}C NMR spectrum for 3-amino-2,6-diiodopyridine

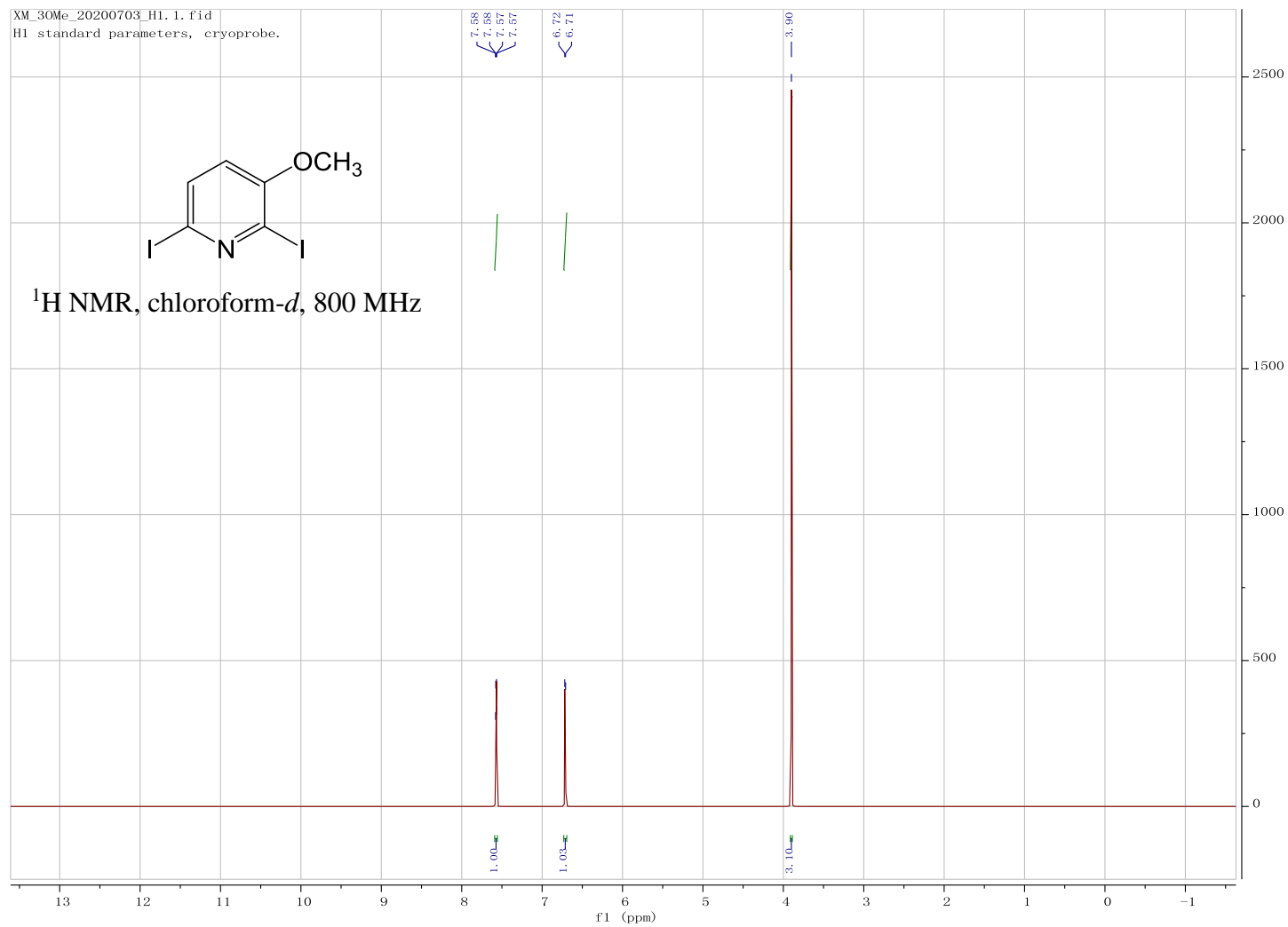


Figure 3.17 ¹H NMR spectrum for 2,6-diiodo-3-methoxypyridine

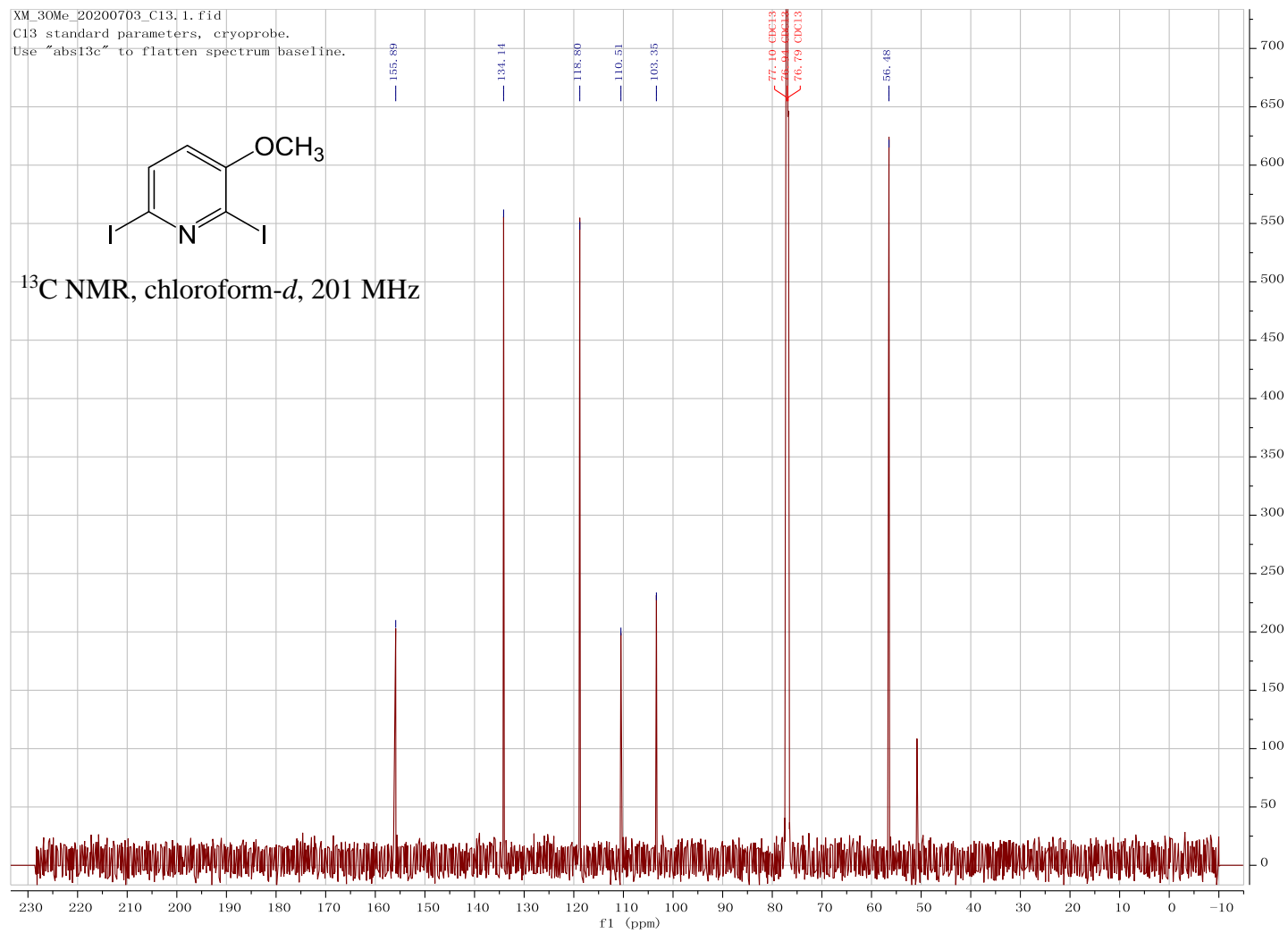


Figure 3.18 ^{13}C NMR spectrum for 2,6-diiodo-3-methoxypyridine

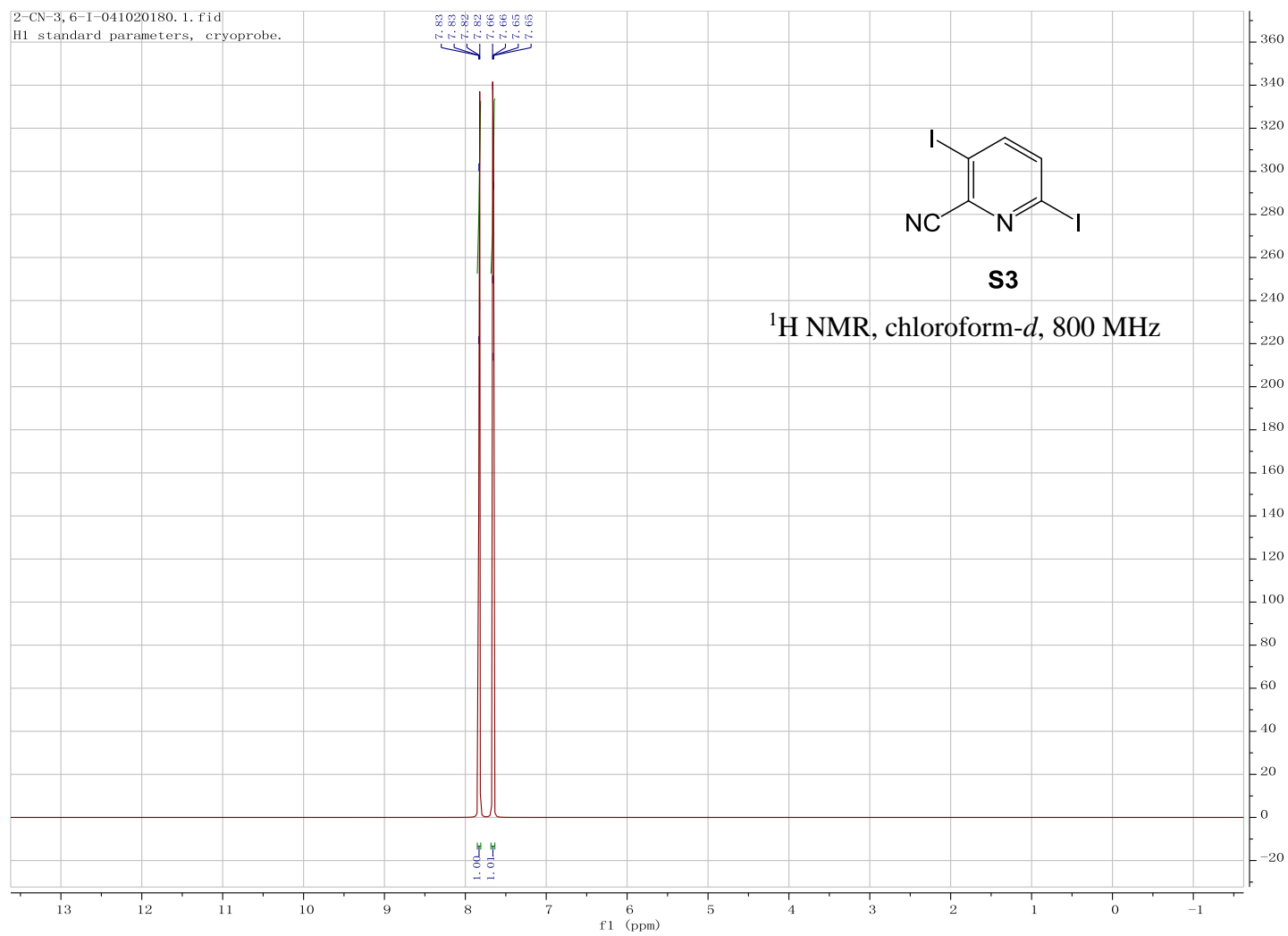


Figure 3.19 ^1H NMR spectrum for 2-cyano-3,6-diiodopyridine

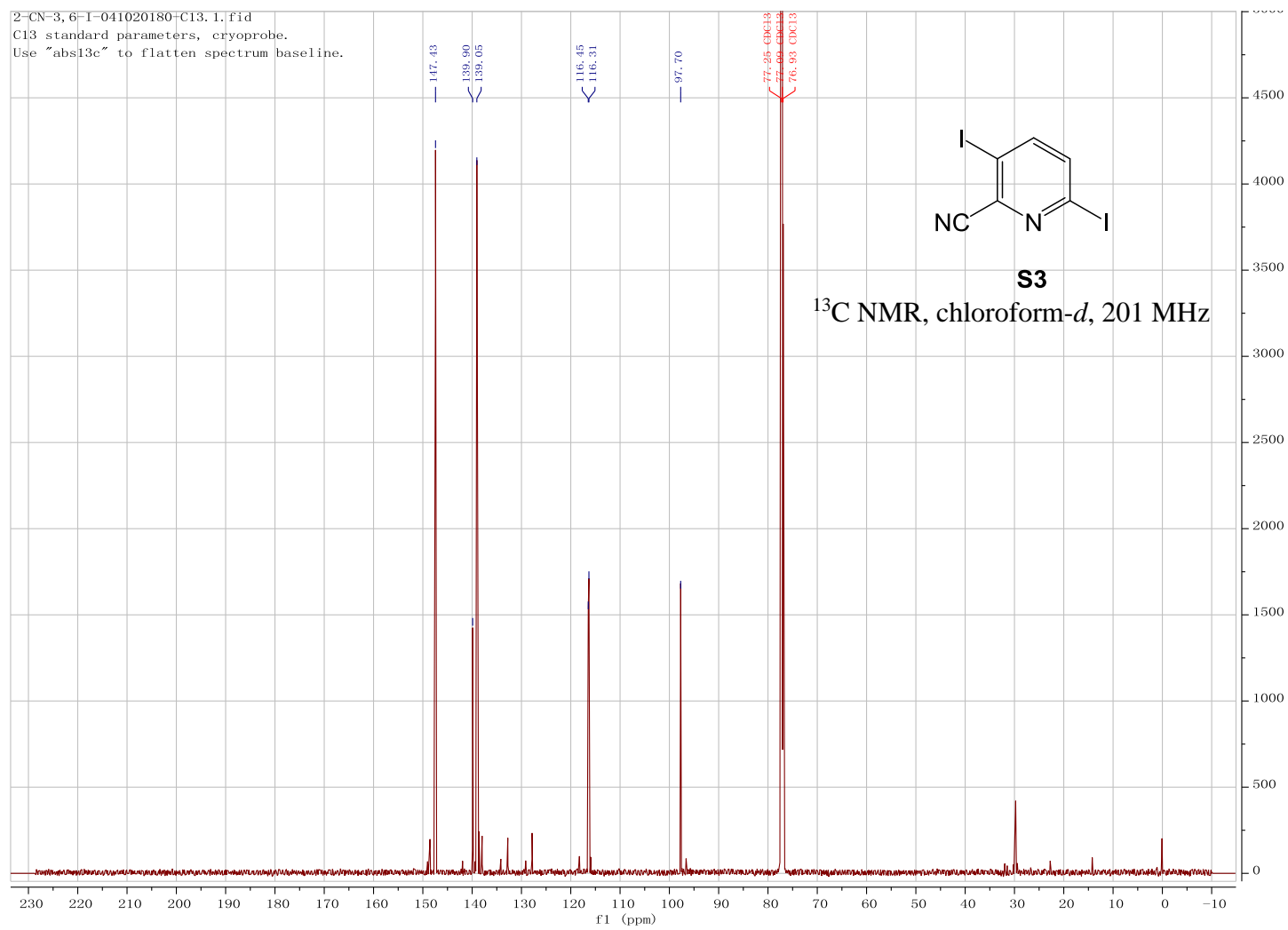


Figure 3.20 ¹³C NMR spectrum for 2-cyano-3,6-diiodopyridine

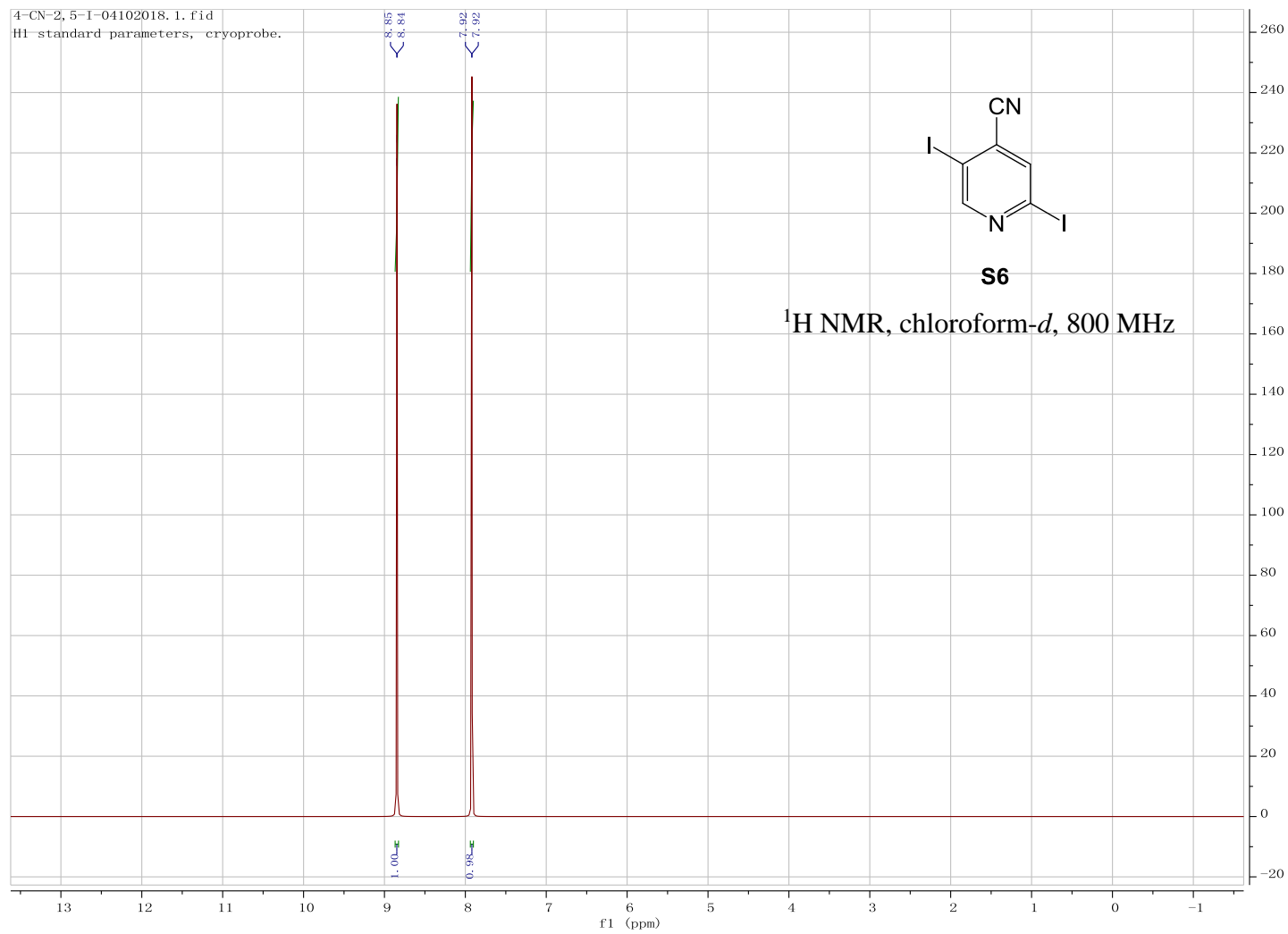


Figure 3.21 ^1H NMR spectrum for 4-cyano-2,5-diiodopyridine

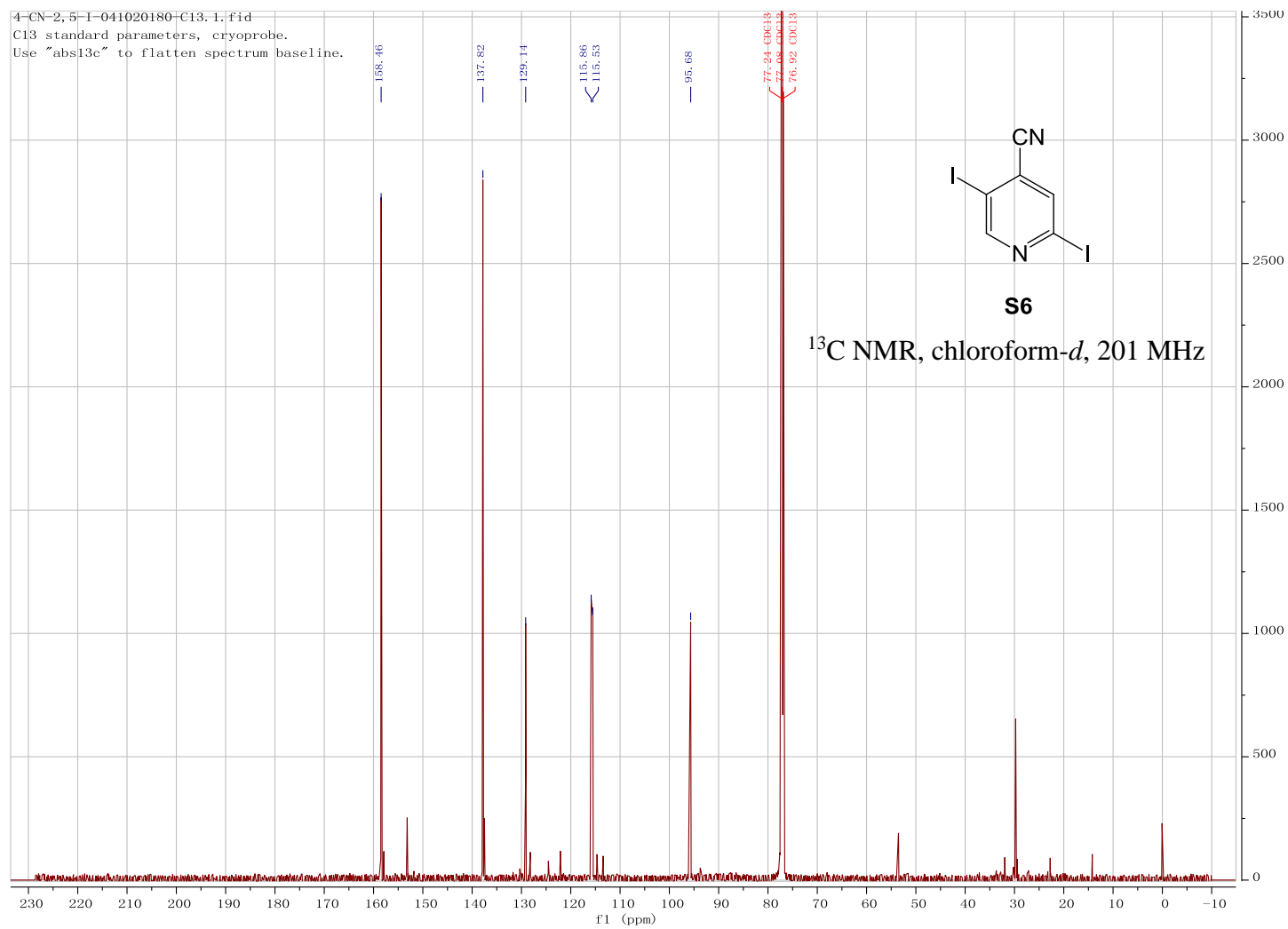


Figure 3.22 ¹³C NMR spectrum for 4-cyano-2,5-diiodopyridine

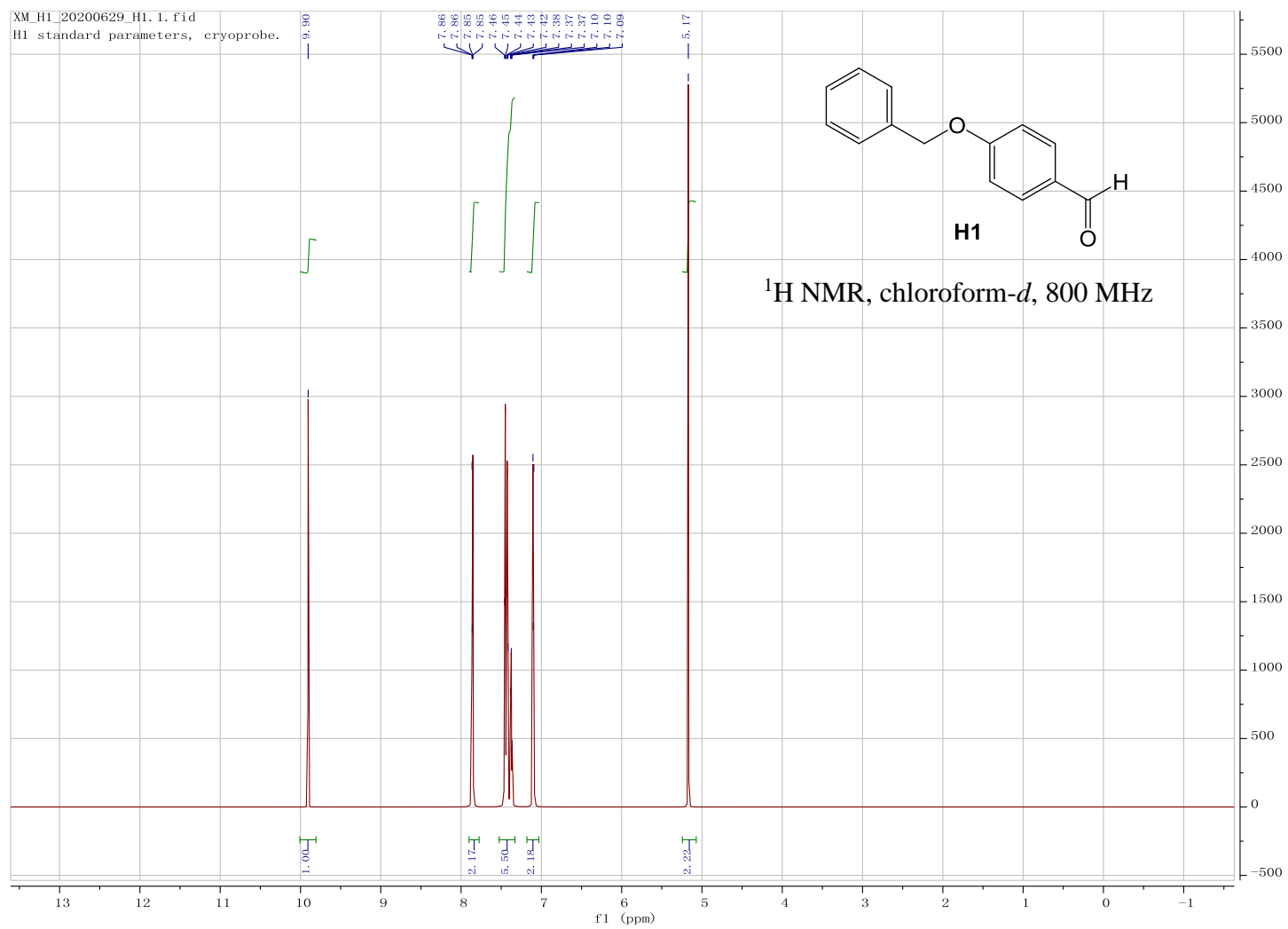


Figure 3.23 ^1H NMR spectrum for 4-(benzyloxy)benzaldehyde

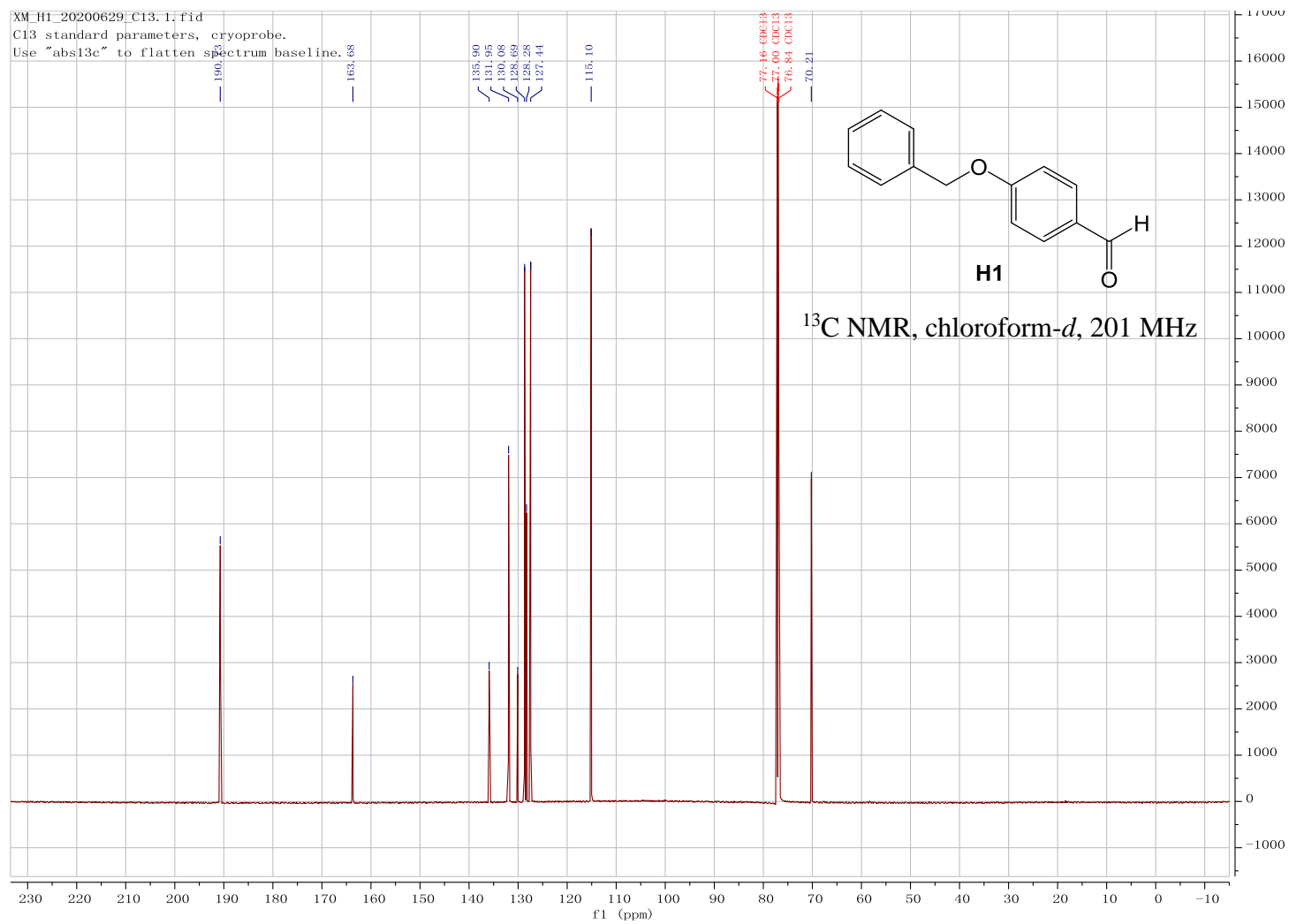


Figure 3.24 ^{13}C NMR spectrum for 4-(benzyloxy)benzaldehyde

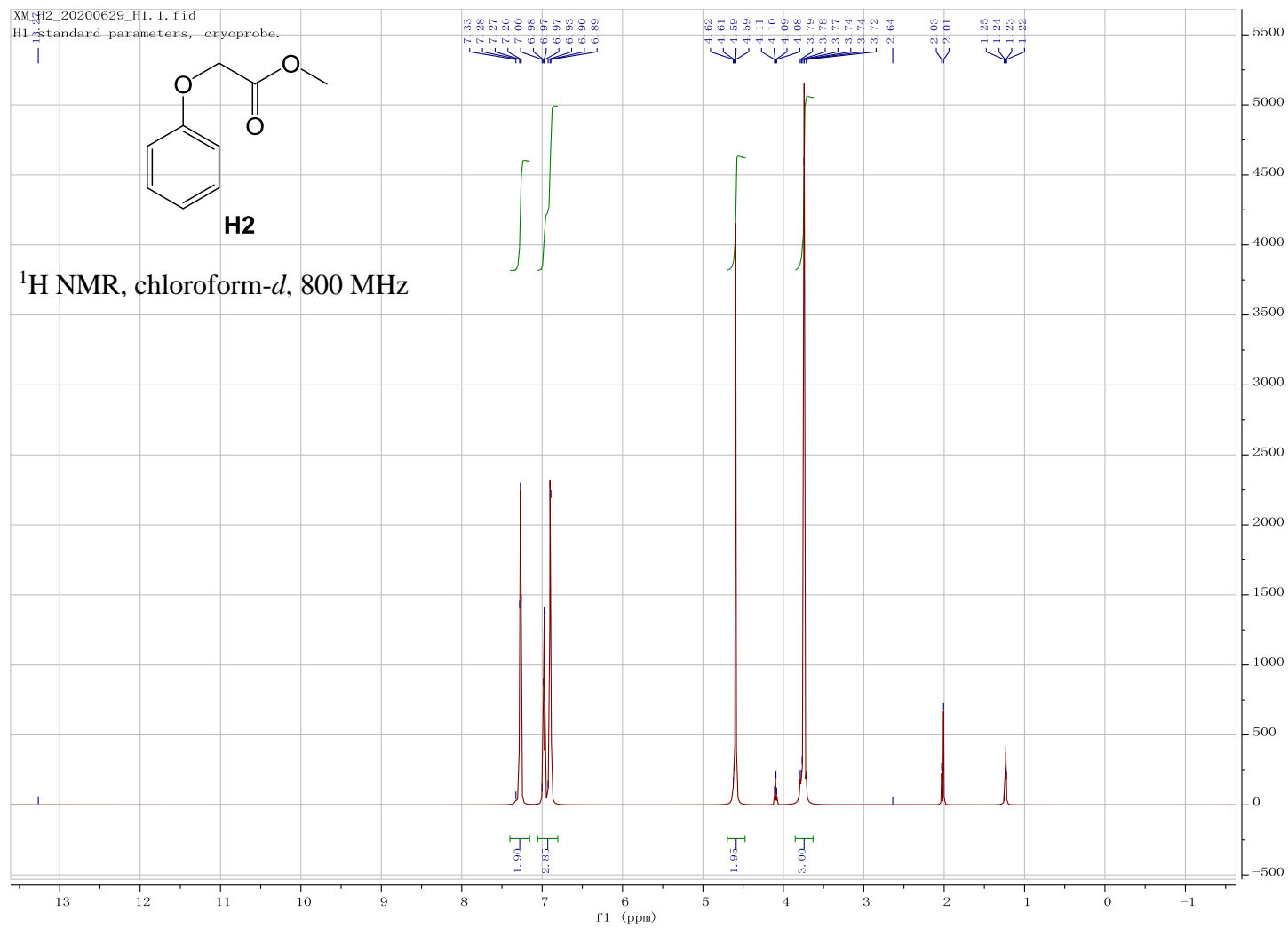


Figure 3.25 ^1H NMR spectrum for methyl 2-phenoxyacetate

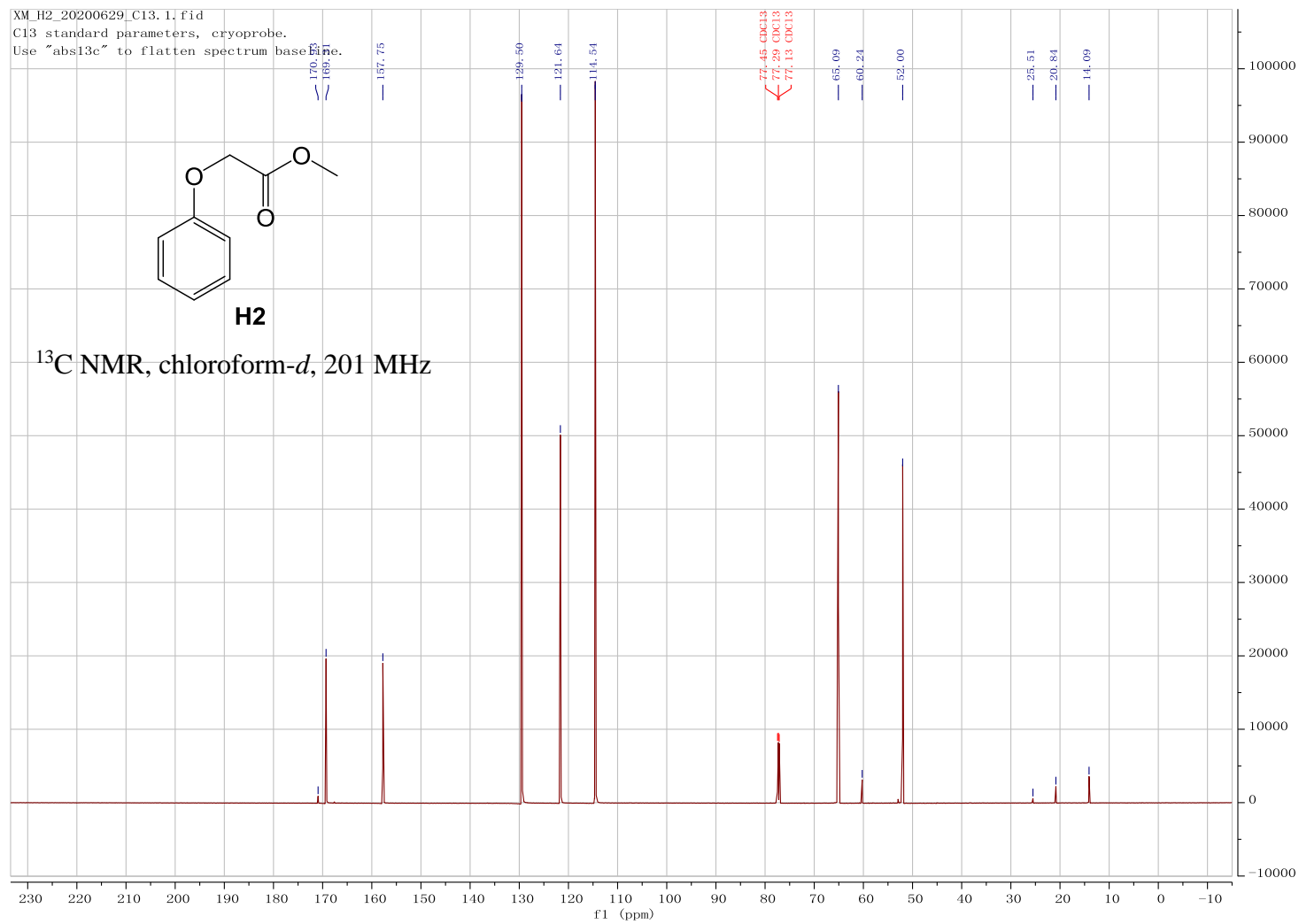


Figure 3.26 ¹³C NMR spectrum for methyl 2-phenoxyacetate

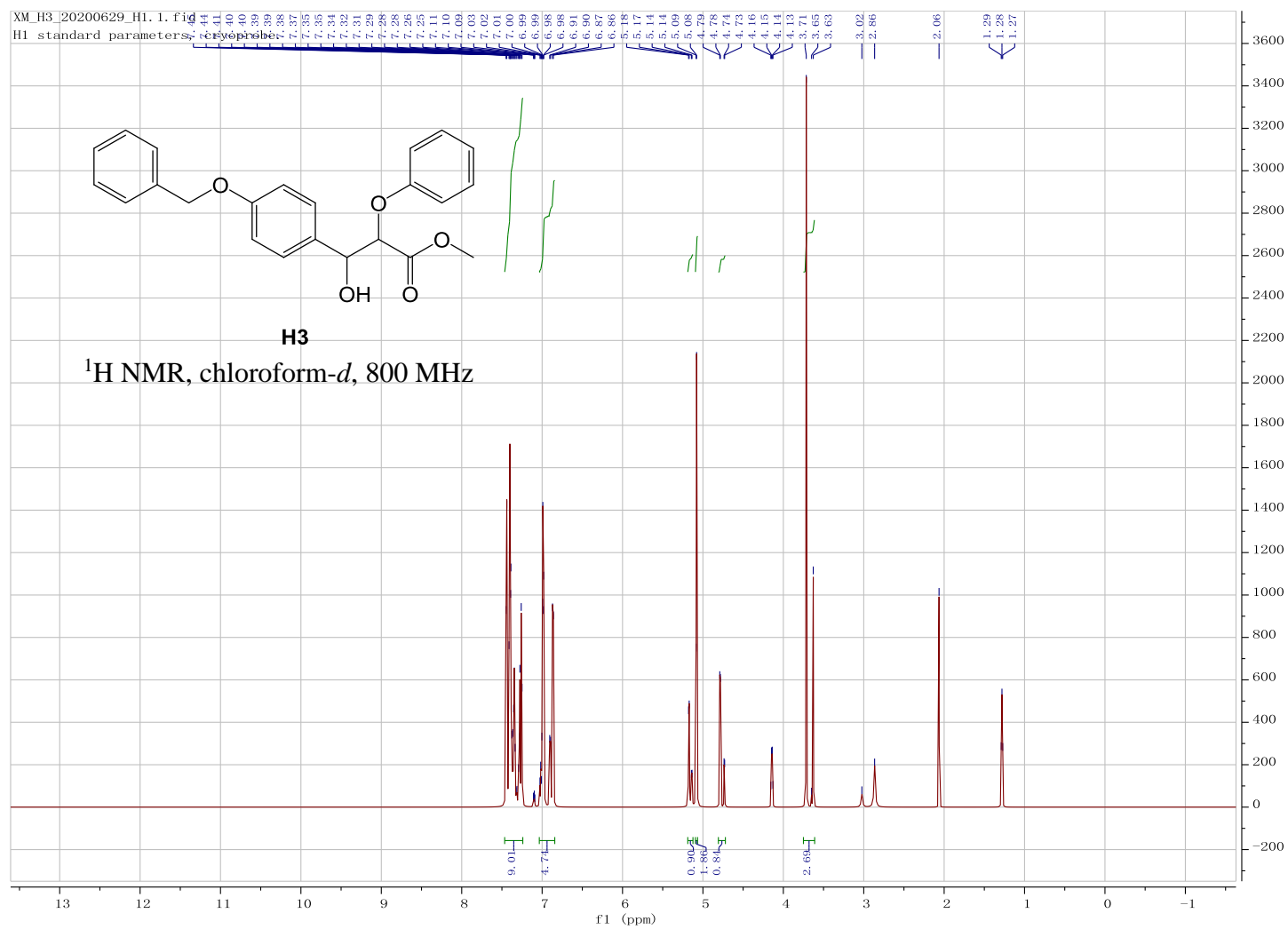


Figure 3.27 ^1H NMR spectrum for methyl 3-(4-(benzyloxy)phenyl)-3-hydroxy-2-phenoxypropanoate

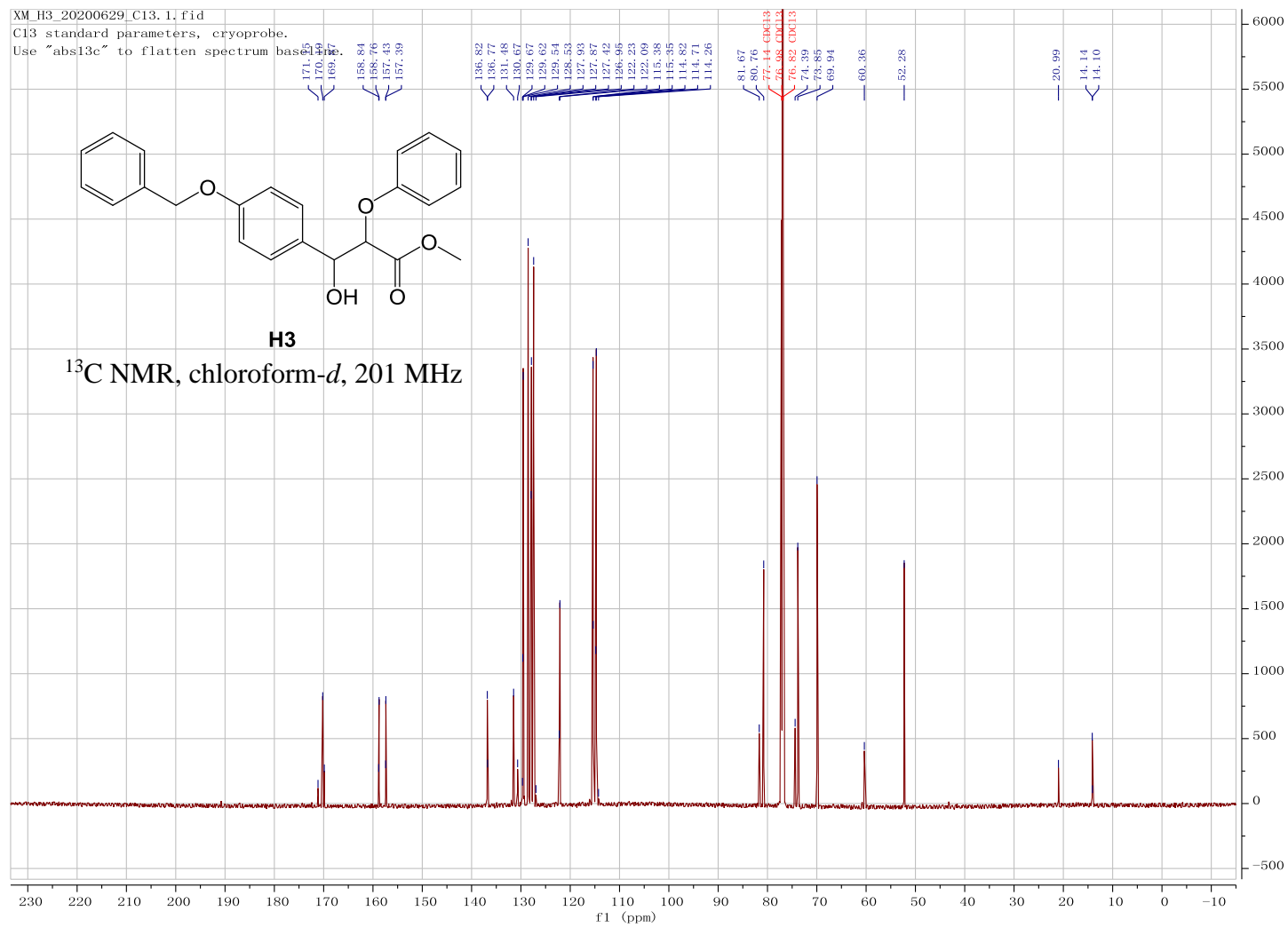


Figure 3.28 ¹³C NMR spectrum for methyl 3-(4-(benzyloxy)phenyl)-3-hydroxy-2-phenoxypropanoate

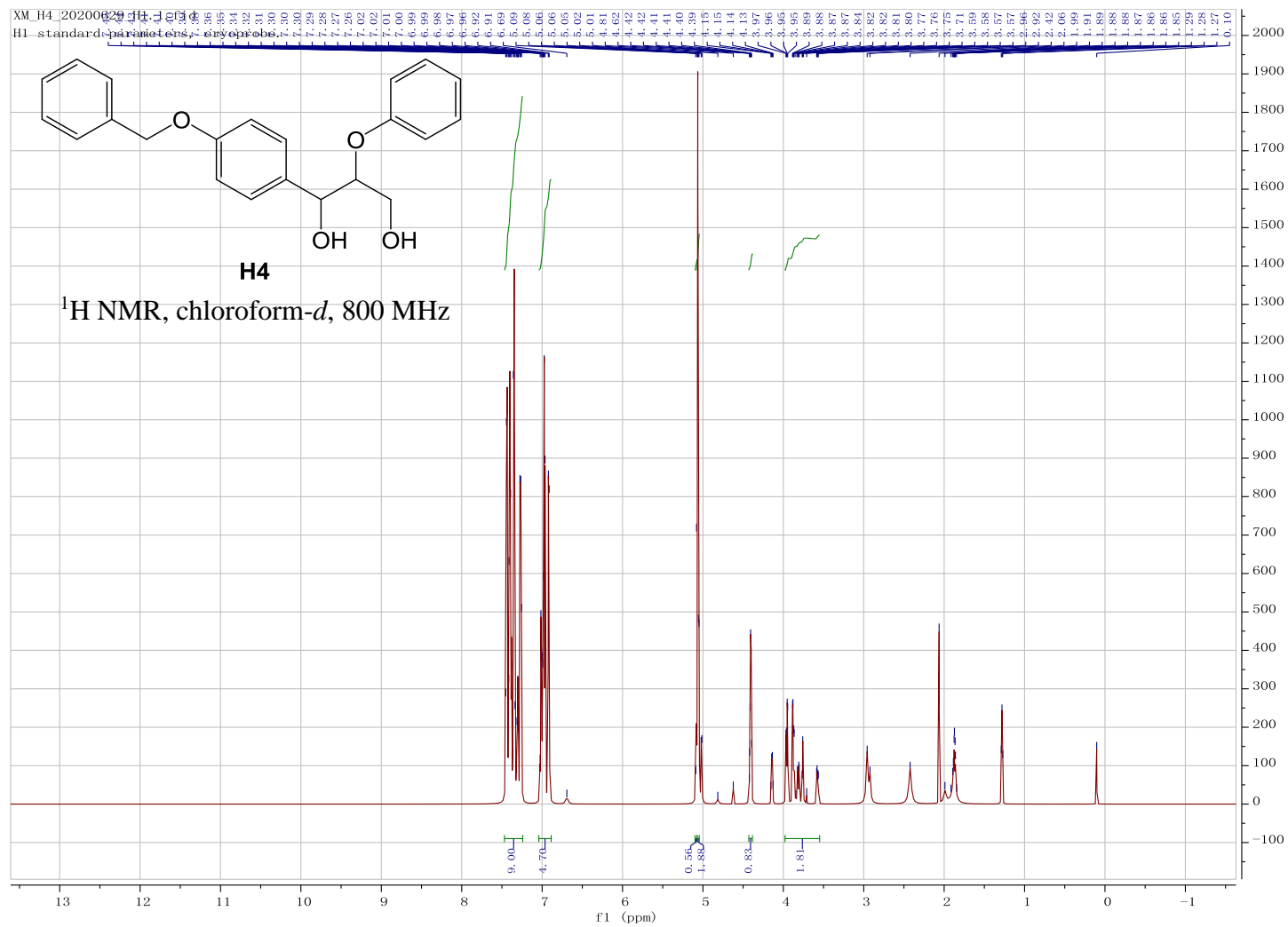


Figure 3.29 ¹H NMR spectrum for 1-(4-(benzyloxy)phenyl)-2-phenoxypropane-1,3-diol

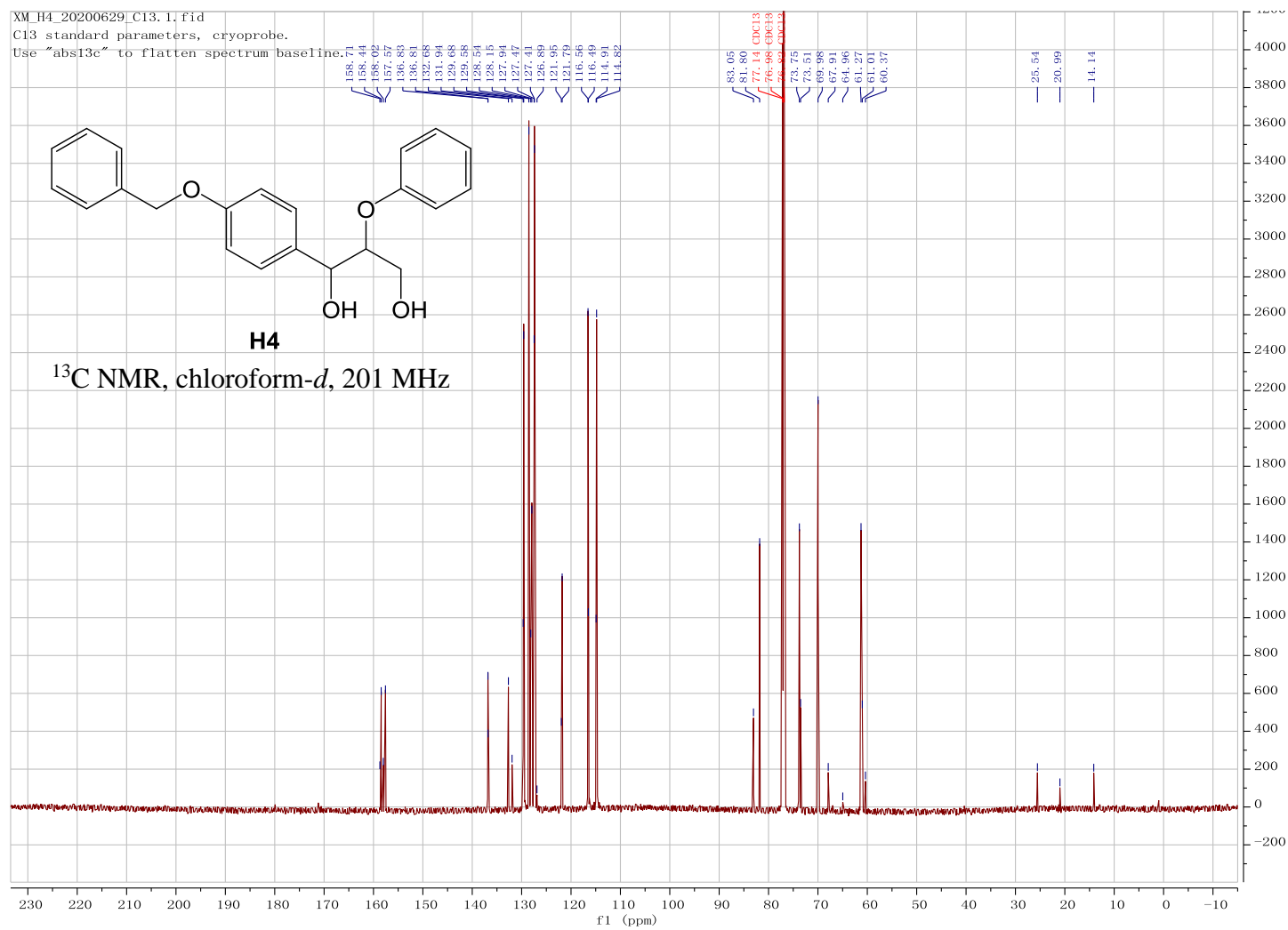


Figure 3.30 ¹³C NMR spectrum for 1-(4-(benzyloxy)phenyl)-2-phenoxypropane-1,3-diol

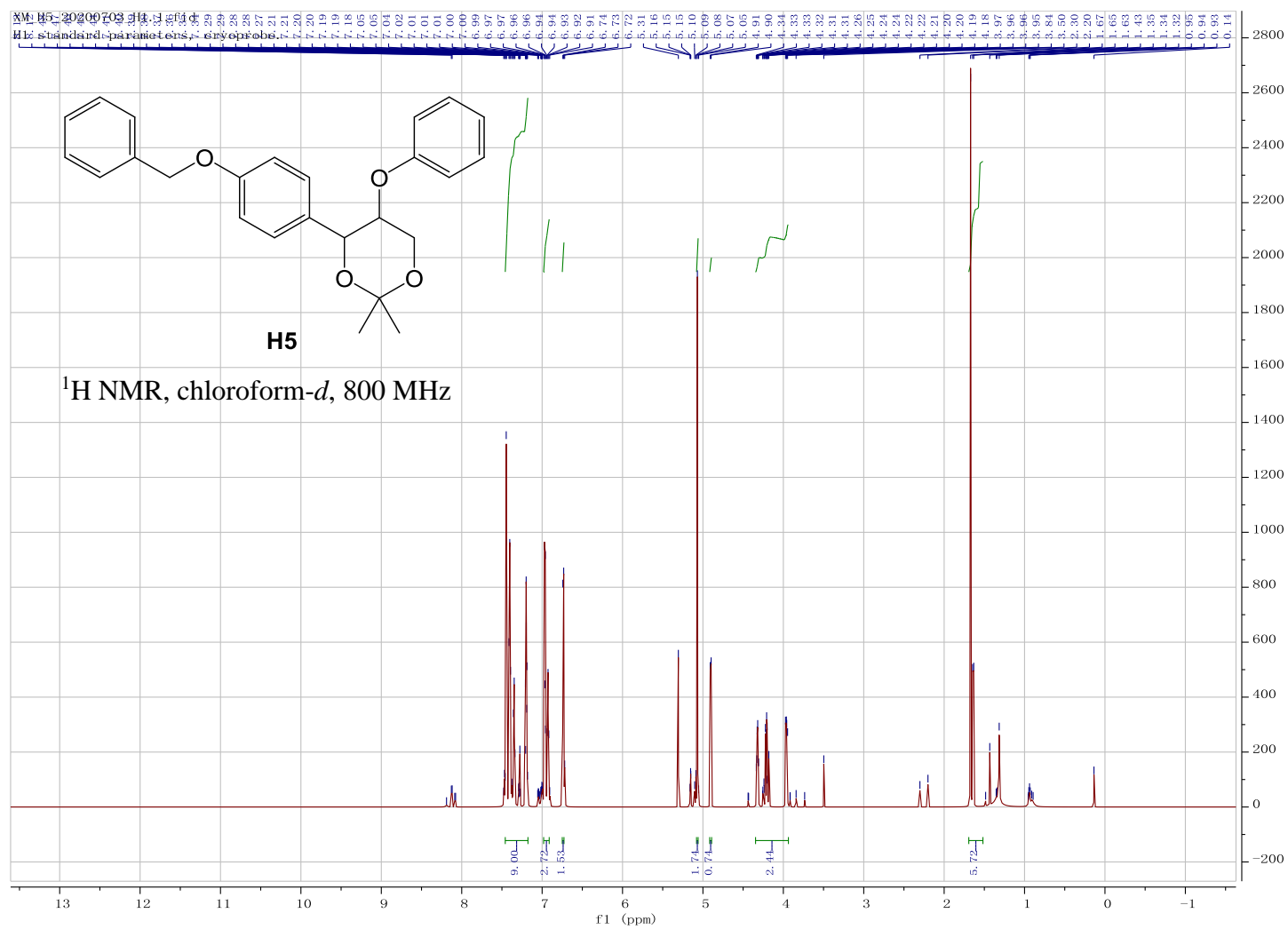


Figure 3.31 ¹H NMR spectrum for 4-(4-(benzyloxy)phenyl)-2,2-dimethyl-5-phenoxy-1,3-dioxane

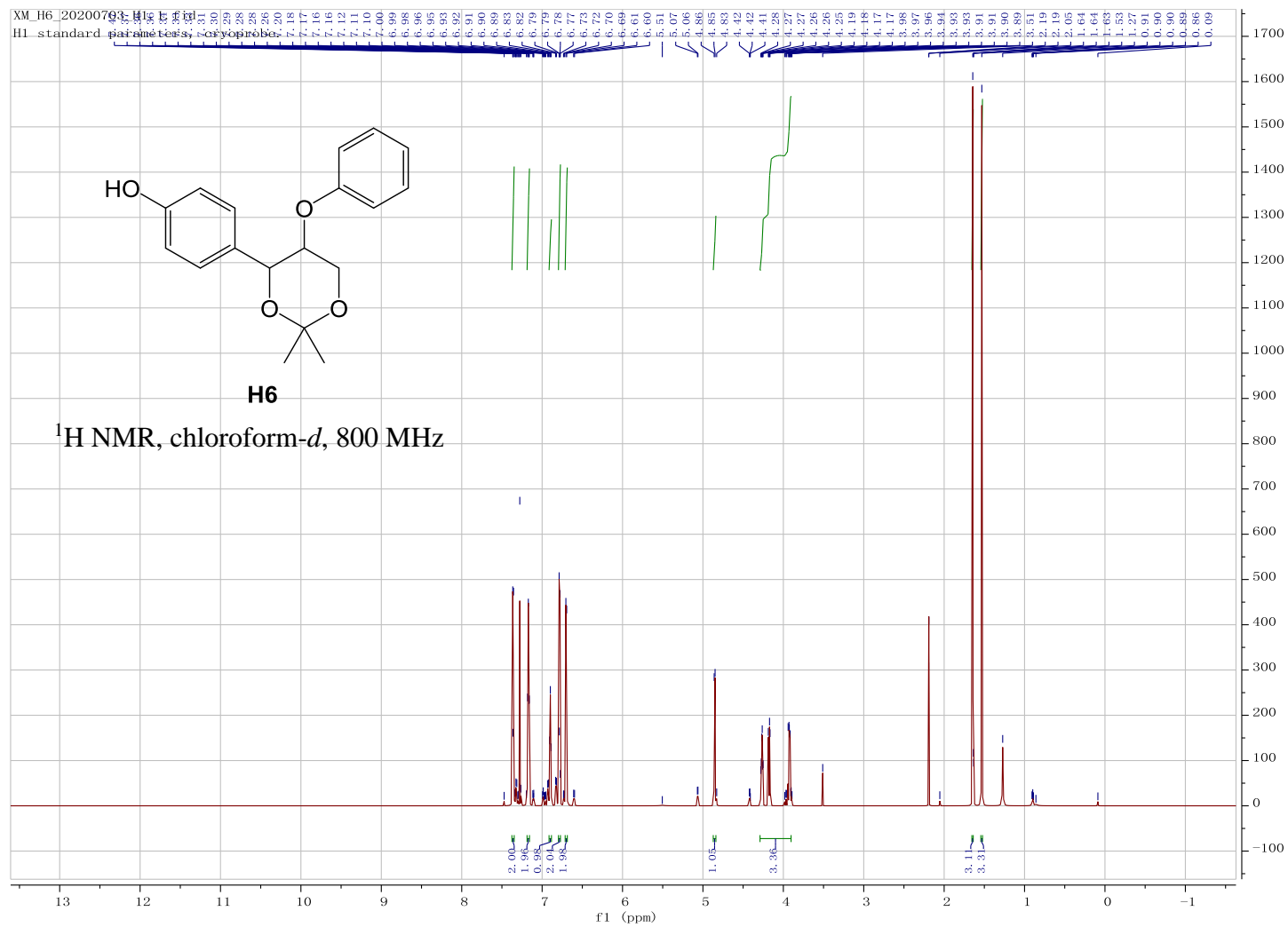


Figure 3.33 ¹H NMR spectrum for 4-(2,2-dimethyl-5-phenoxy-1,3-dioxan-4-yl)phenol

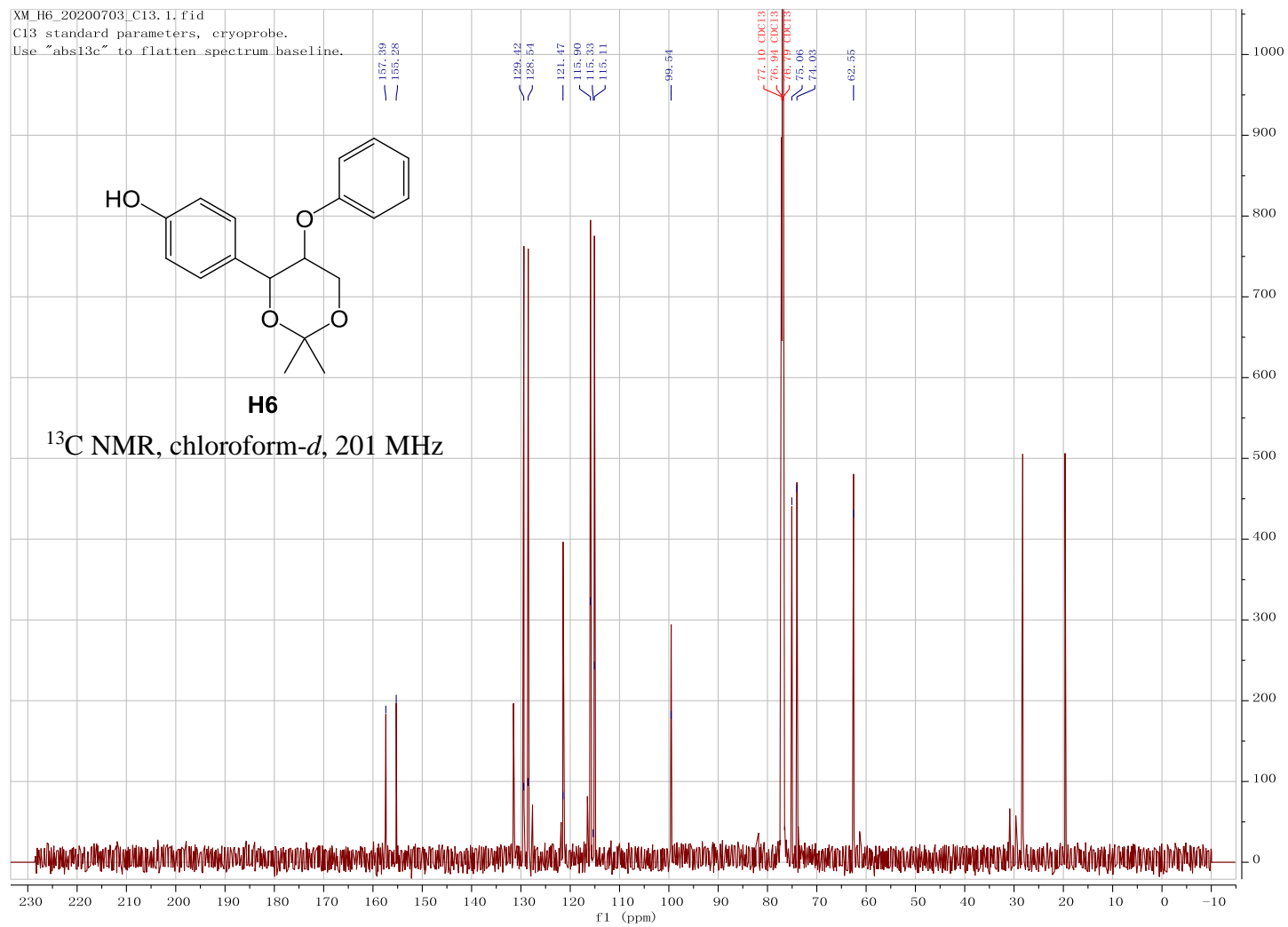


Figure 3.34 ¹³C NMR spectrum for 4-(2,2-dimethyl-5-phenoxy-1,3-dioxan-4-yl)phenol

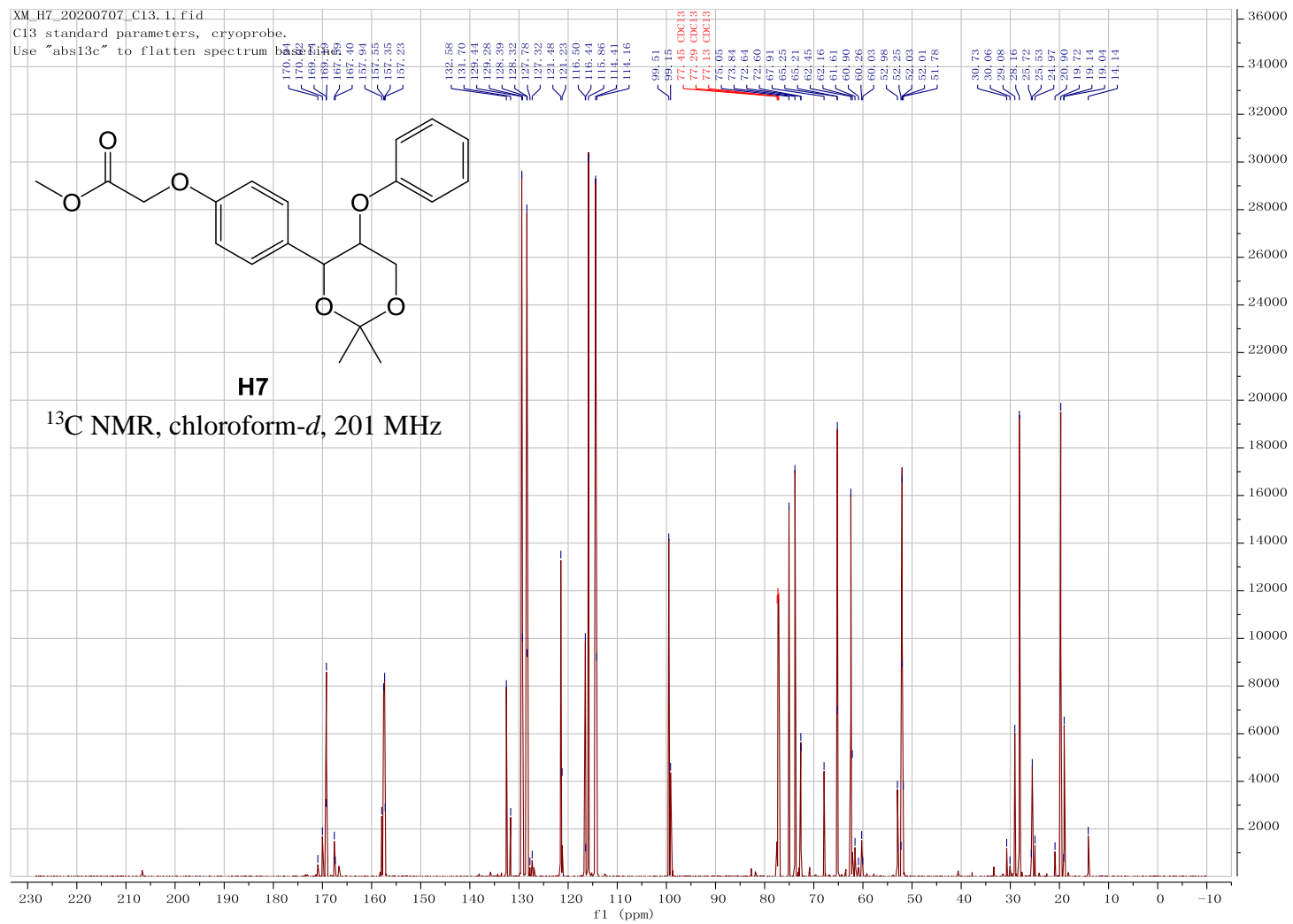


Figure 3.36 ^{13}C NMR spectrum for methyl 2-(4-(2,2-dimethyl-5-phenoxy-1,3-dioxan-4-yl)phenoxy)acetate

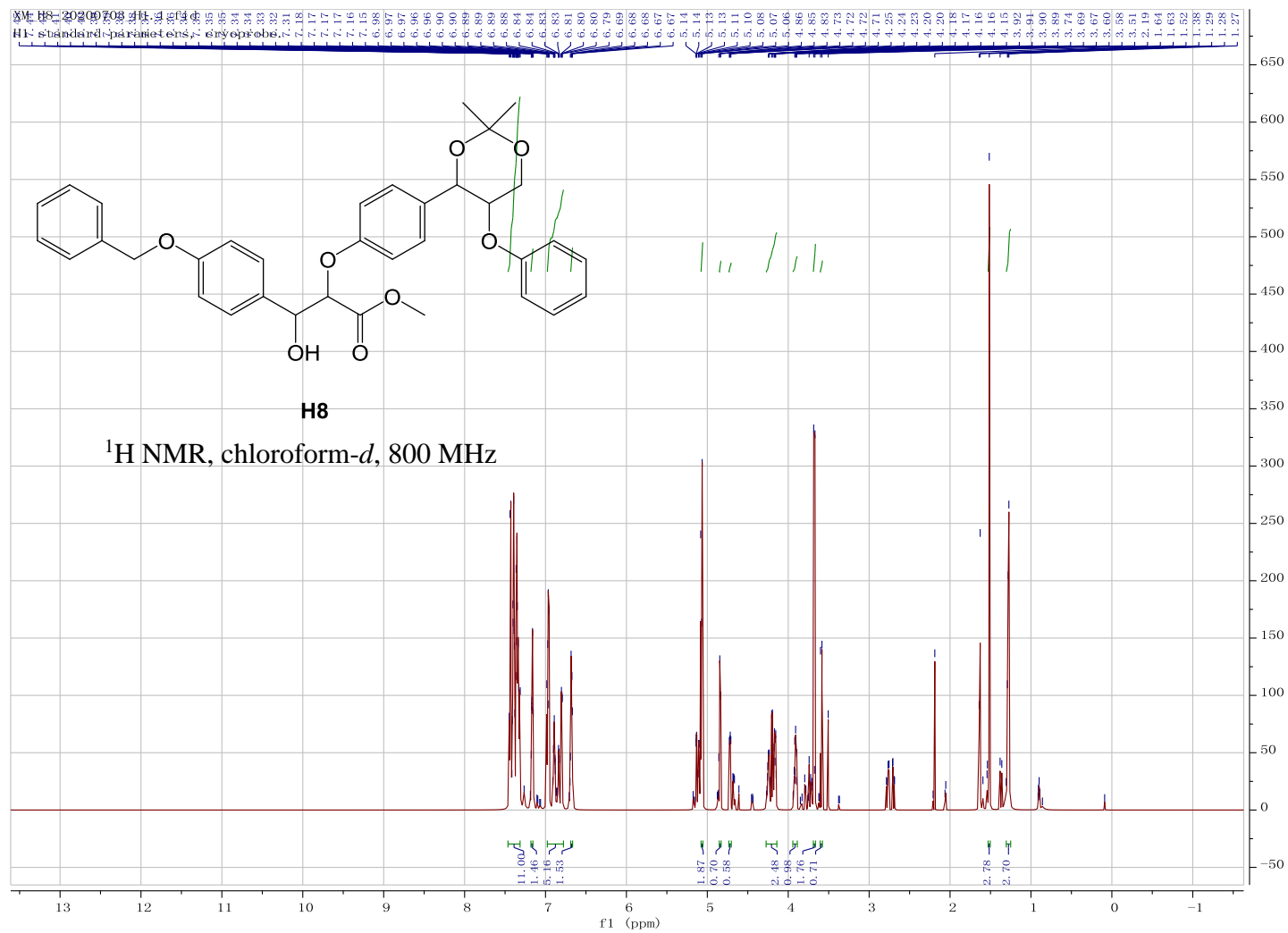


Figure 3.37 ¹H NMR spectrum for methyl 3-(4-(benzyloxy)phenyl)-2-(4-(2,2-dimethyl-5-phenoxy-1,3-dioxan-4-yl)phenoxy)-3-hydroxypropanoate

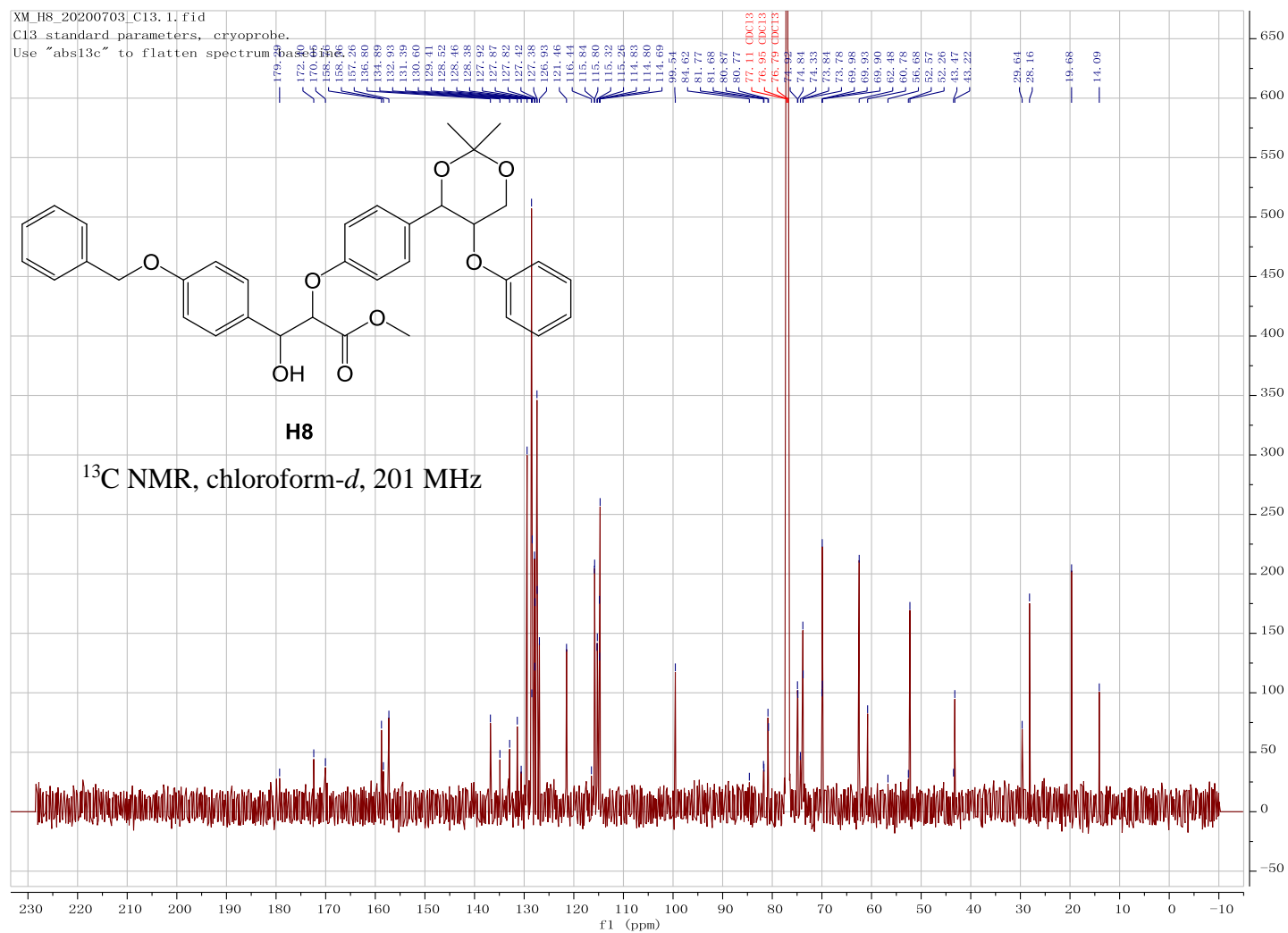


Figure 3.38 ¹³C NMR spectrum for methyl 3-(4-(benzyloxy)phenyl)-2-(4-(2,2-dimethyl-5-phenoxy-1,3-dioxan-4-yl)phenoxy)-3-hydroxypropanoate

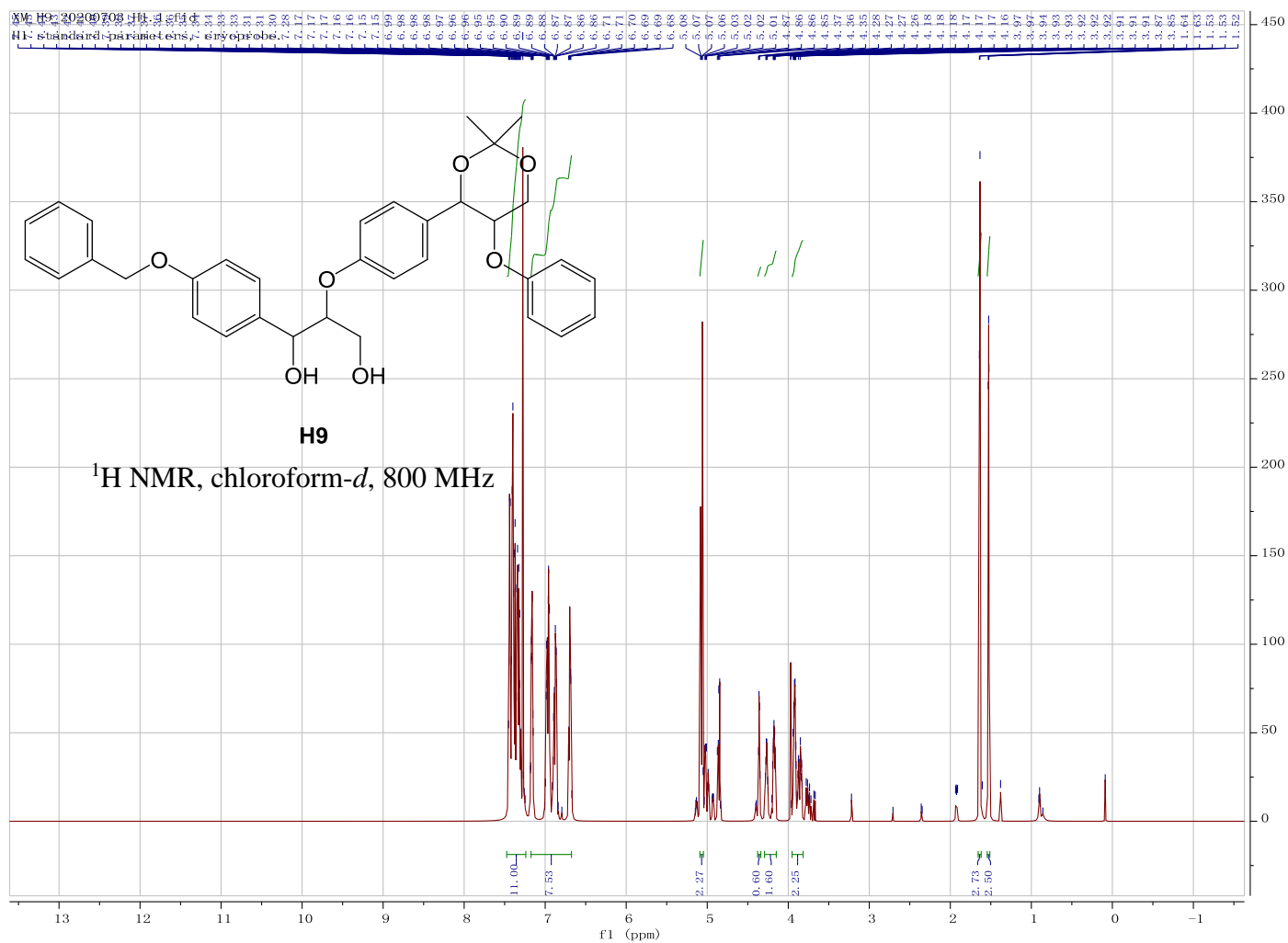


Figure 3.39 ^1H NMR spectrum for 1-(4-(benzyloxy)phenyl)-2-(4-(2,2-dimethyl-5-phenoxy-1,3-dioxan-4-yl)phenoxy)propane-1,3-diol

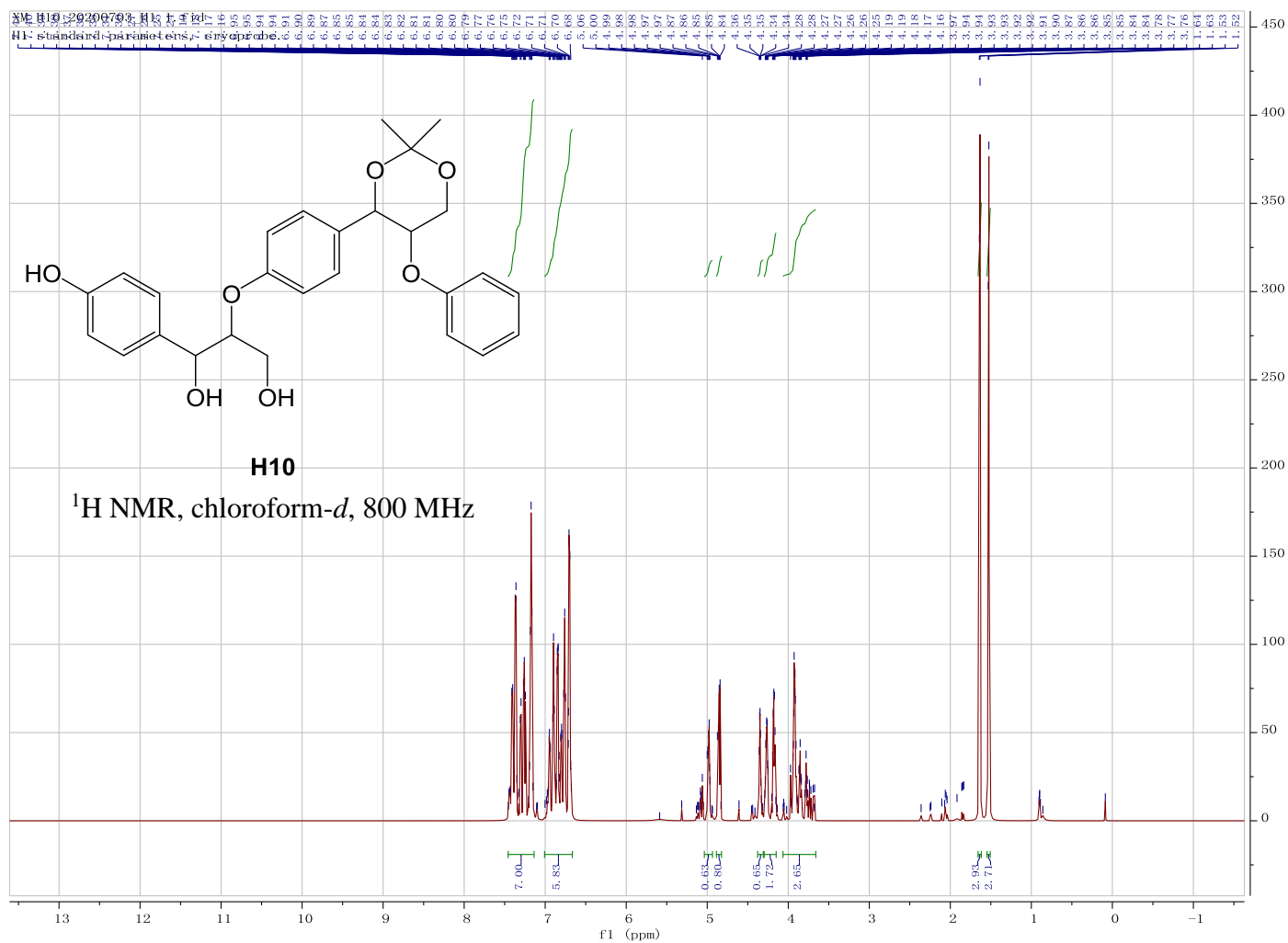


Figure 3.41 ^1H NMR spectrum for 2-(4-(2,2-dimethyl-5-phenoxy-1,3-dioxan-4-yl)phenoxy)-1-(4-hydroxyphenyl)propane-1,3-diol

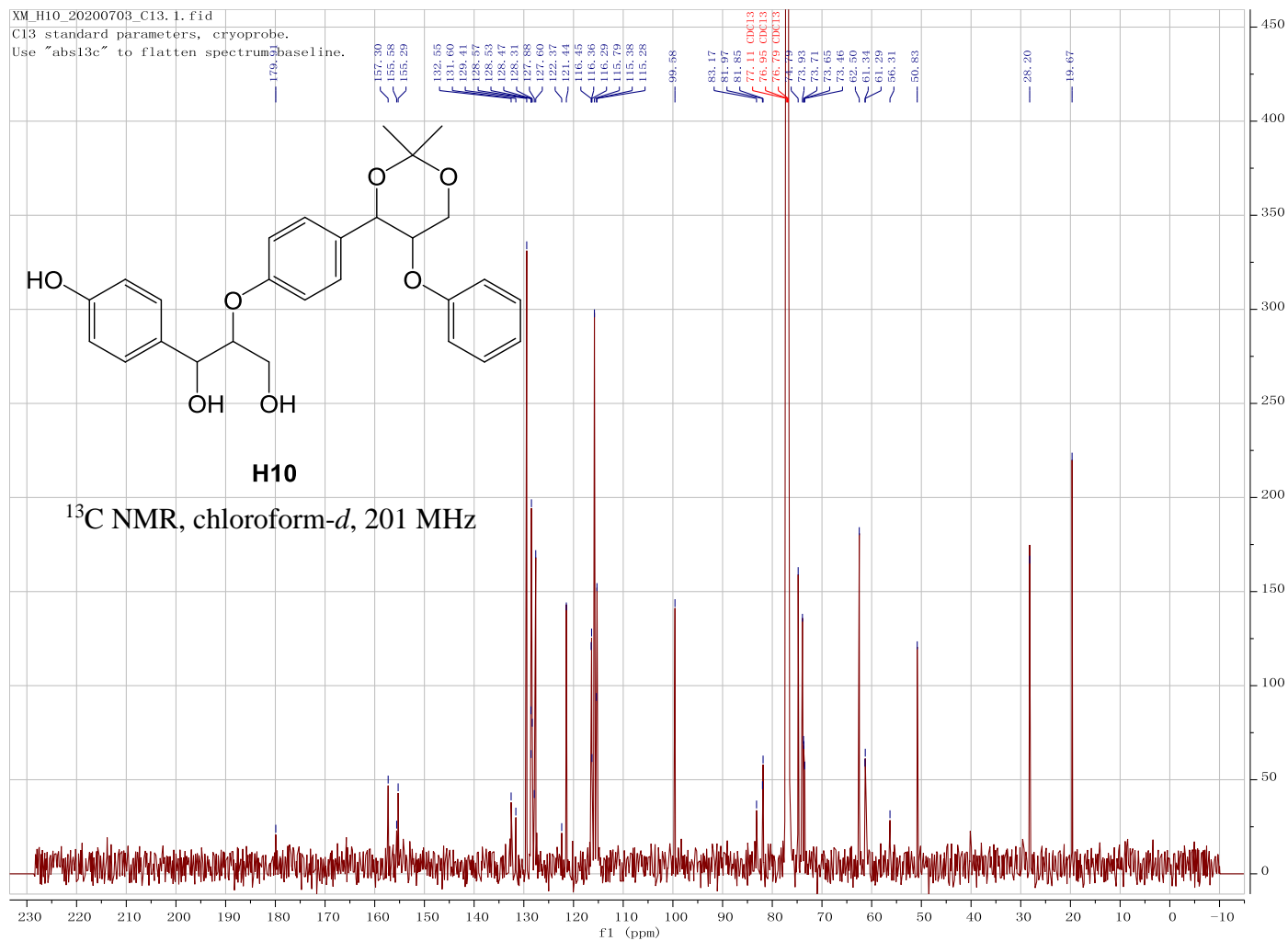


Figure 3.42 ^{13}C NMR spectrum for 2-(4-(2,2-dimethyl-5-phenoxy-1,3-dioxan-4-yl)phenoxy)-1-(4-hydroxyphenyl)propane-1,3-diol

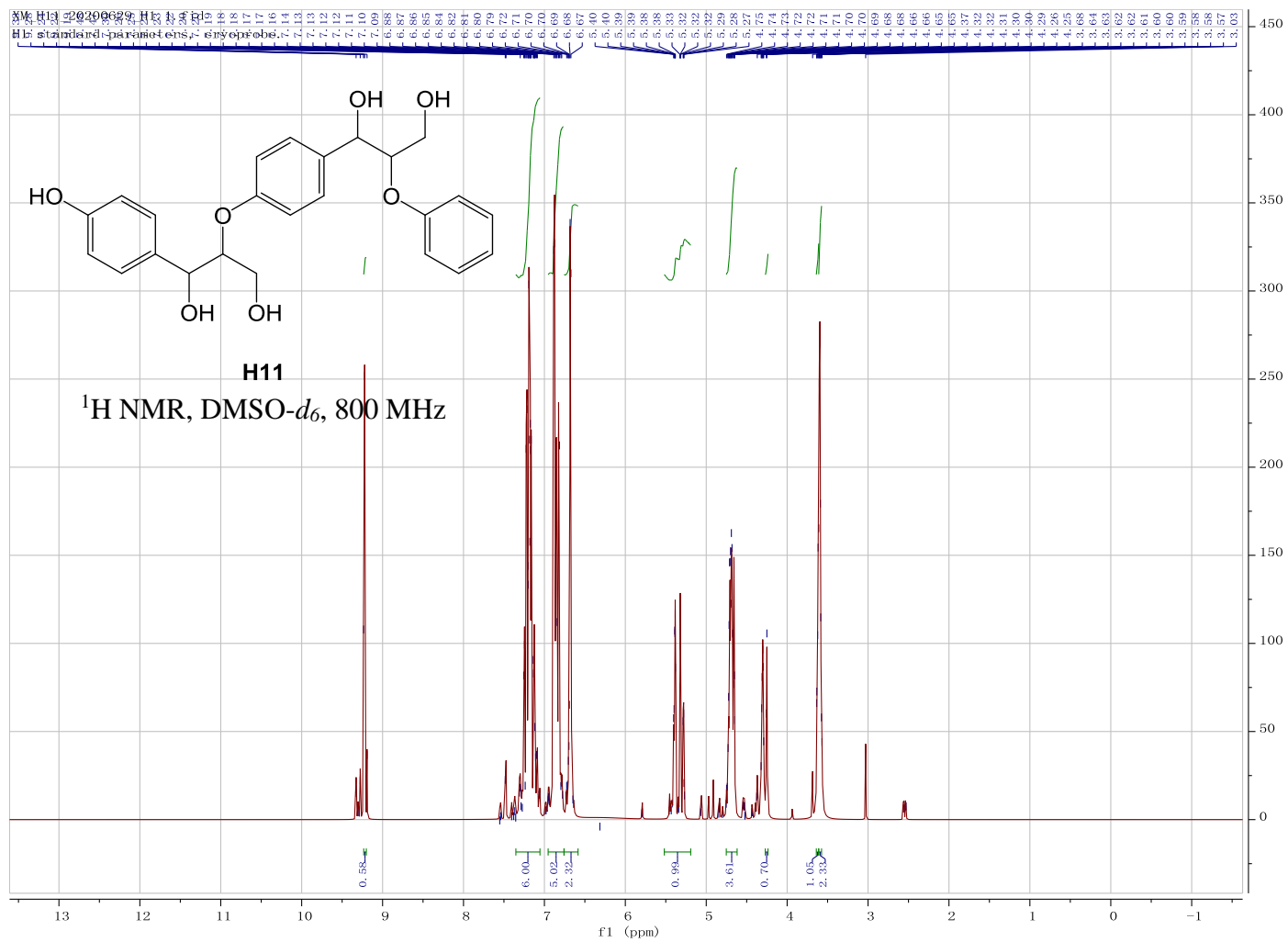


Figure 3.43 ¹H NMR spectrum for 1-(4-((1,3-dihydroxy-1-(4-hydroxyphenyl)propan-2-yl)oxy)phenyl)-2-phenoxypropane-1,3-diol

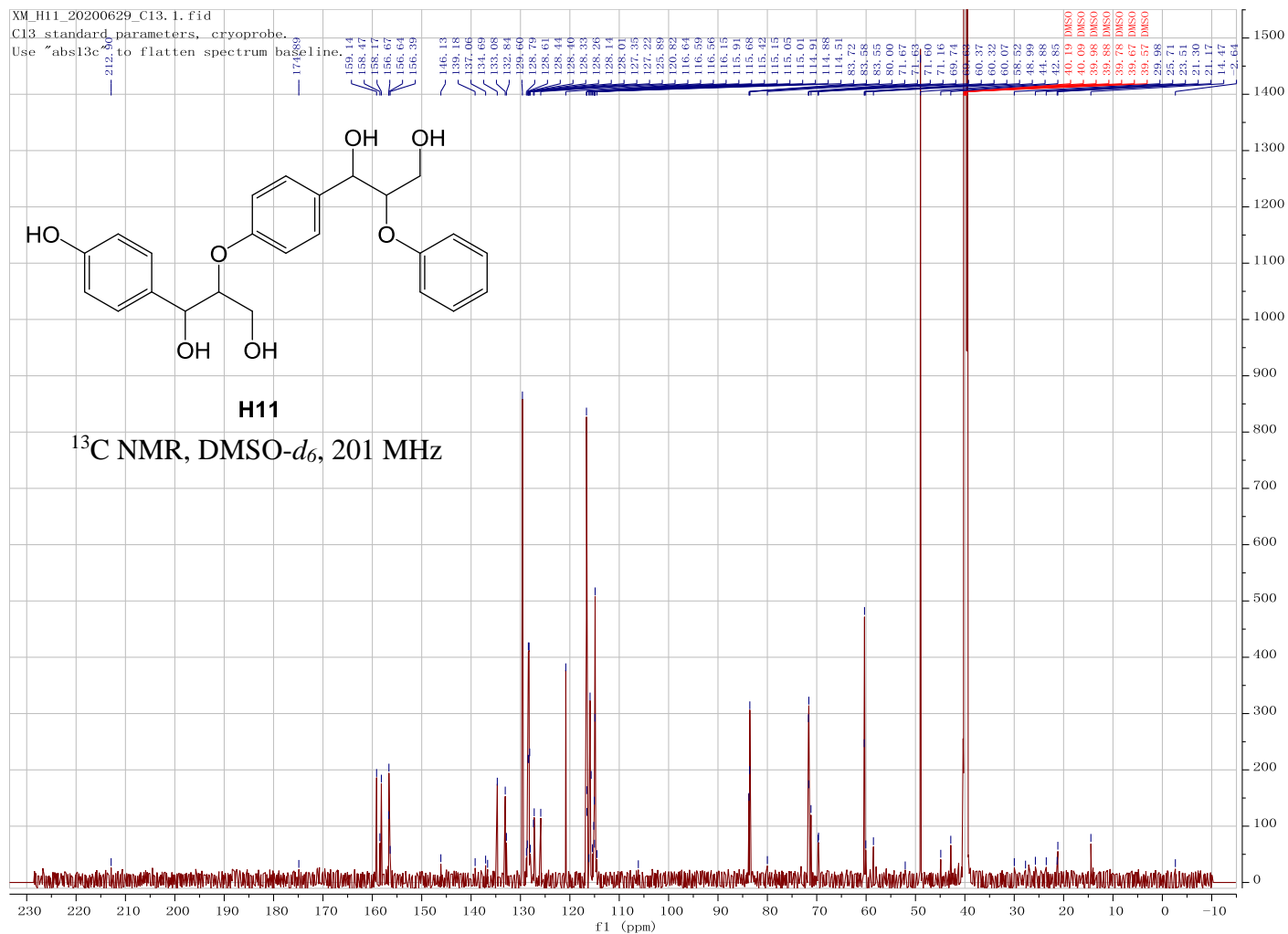


Figure 3.44 ¹³C NMR spectrum for 1-(4-((1,3-dihydroxy-1-(4-hydroxyphenyl)propan-2-yl)oxy)phenyl)-2-phenoxypropane-1,3-diol

3.7 X-ray Crystallography

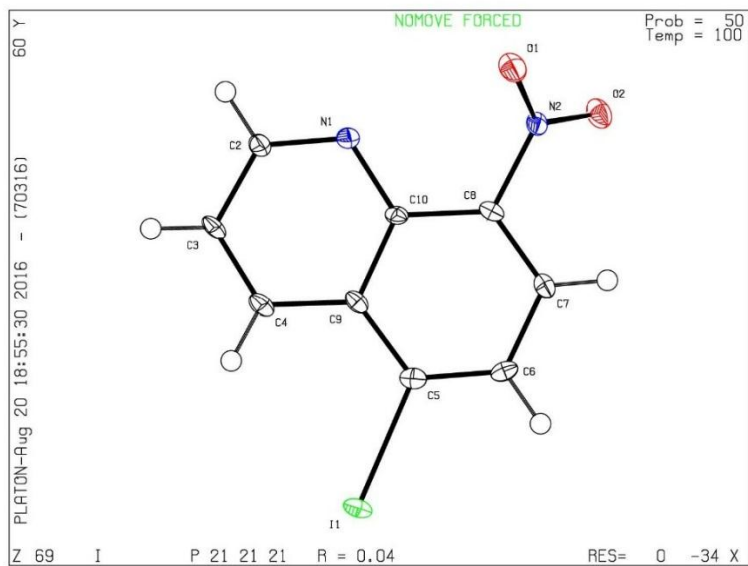


Figure 3.45 5-Iodo-8-nitroquinoline

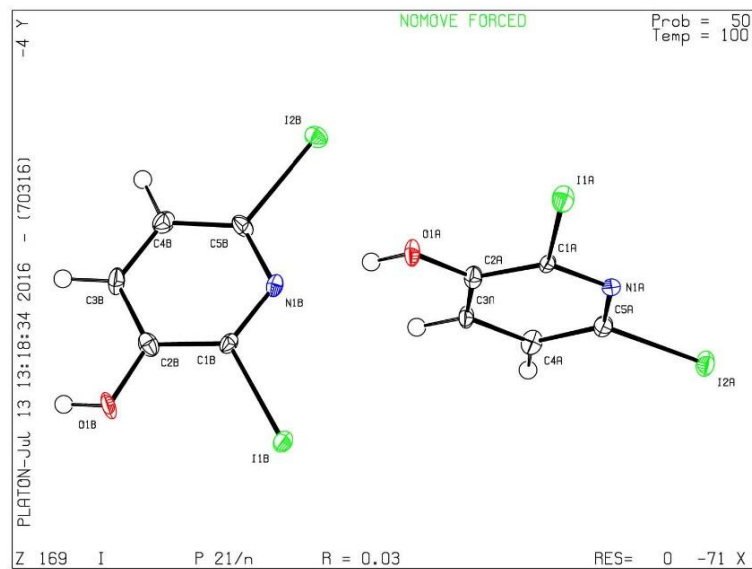


Figure 3.46 3-Hydroxy-2,6-diiodopyridine

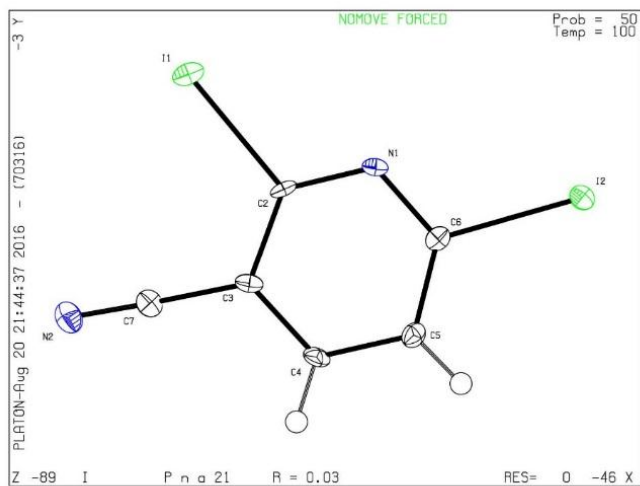


Figure 3.47 3-Cyano-2,6-diiodopyridine

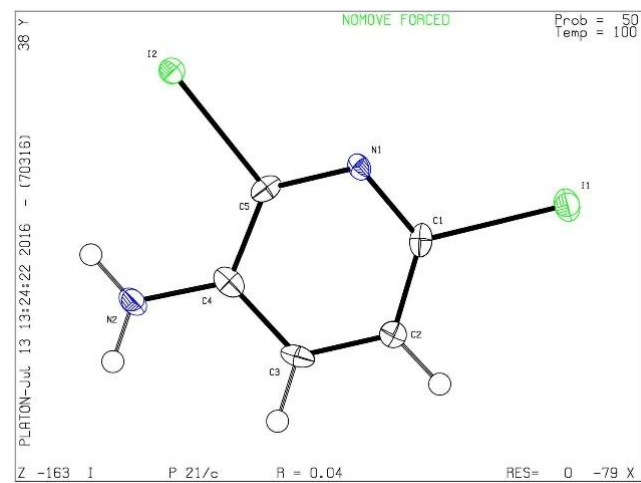


Figure 3.48 3-Amino-2,6-diiodopyridine

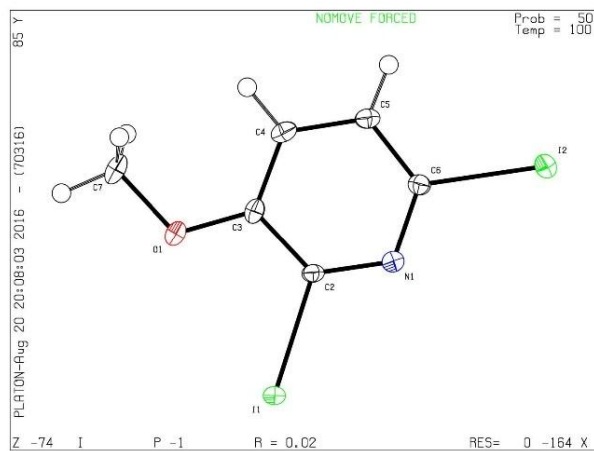


Figure 3.49 2,6-Diiodo-3-methoxy-pyridine

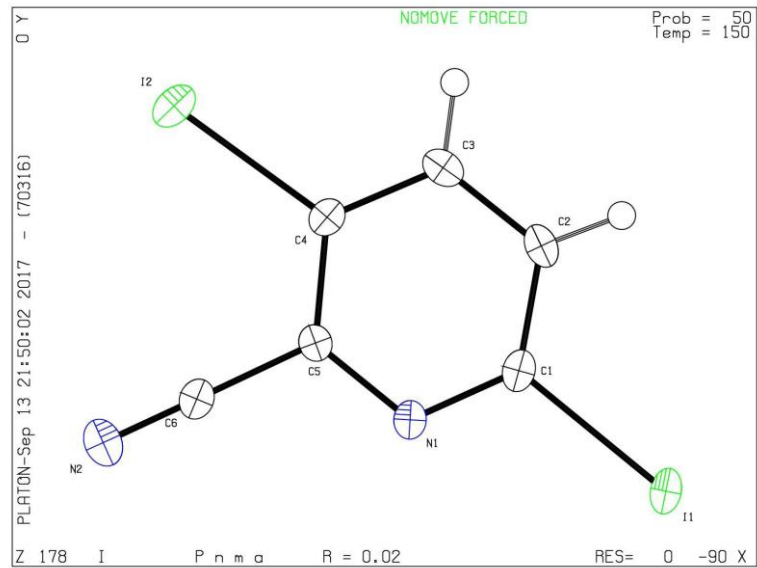


Figure 3.50 2-Cyano-3,6-diiodopyridine

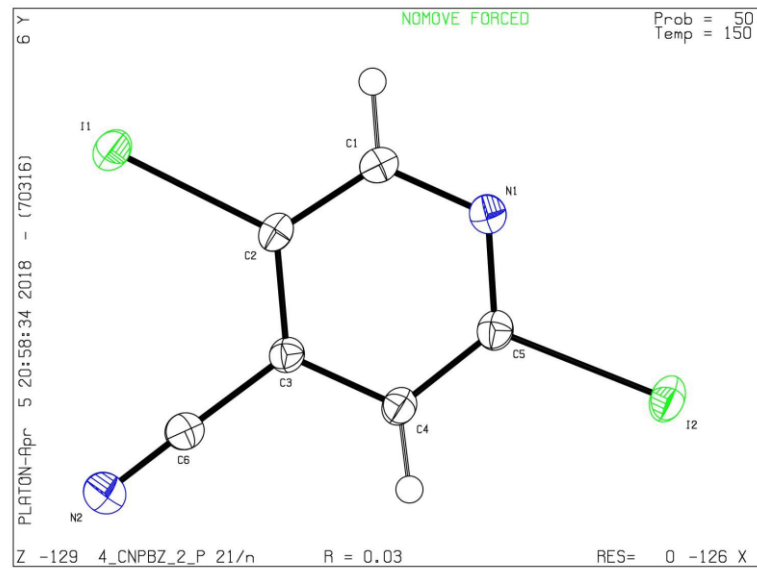


Figure 3.51 4-Cyano-2,5-diiodopyridine

3.8 References

1. Son, J.-H.; Pudenz, M. A.; Hoefelmeyer, J. D. *Dalton Trans.* **2010**, 39, 11081.
2. Palmer, M. H. *J. Chem. Soc.* **1962**, 3645.
3. Maślankiewicz, A.; Marciniec, K.; Pawlowski, M.; Zajdel, P. *Heterocycles* **2007**, 71, 1975.
4. Koch, V.; Schnatterer, S. *Synth.* **1990**, 497.
5. Bucsis, L.; Friedrich, K. *Chem. Ber.* **1976**, 109, 2462.
6. Jankiewicz, B. J. “*Gas-phase Studies on the Reactivity of Charged, Aromatic σ,σ,σ -Triradicals by Using Distonic Ion Approach and Fourier Transform Ion Cyclotron Resonance (FT-ICR) Mass Spectrometry*”, Ph.D. dissertation, Purdue University, **2008**.
7. Kiselev, E.; Agama, K.; Pommier, Y.; Cushman, M. *J. Med. Chem.* **2012**, 55, 1682.
8. PCT Int. Appl. 2009024905.
9. Zhang, H.-Q.; G., F.-H.; Y., J.-Q.; Zhang, C.; Yue, X.-H.; Li, C.-G.; Xu, Y.-G.; Sun, L.-P. *Eur. J. Med. Chem.* **2017**, 125, 245.
10. Mudduluru, H.; Hindupur, R. M.; Dubey, P. K.; Madhavaram, S.; Tatini, L.; Subbaraju, G. V. *Lett. Org. Chem.* **2011**, 8, 234.
11. Cho, D. W.; Latham, J. A.; Park, H. J.; Yoon, U. C.; Langan, P.; Dunaway-Mariano, D. ; Mariano, P. S. *J. Org. Chem.* **2011**, 76, 2840.
12. Sheng, H.; Tang, W.; Gao, J.; Riedeman, J. S.; Li, G.; J., Tiffany M.; Hurt, M. R.; Yang, L.; Murria, P.; Ma, X.; Nash, J. J.; Kenttamaa, H. I. *Anal. Chem.* **2017**, 89, 13089.

CHAPTER 4. GROUND-STATE SINGLET *META*-BENZYLE CATIONS REACT FROM AN EXCITED TRIPLET STATE

4.1 Introduction

meta-Benzyne derivatives have received increasing interest recently¹⁻⁴ as their radical reactivity has been demonstrated to be tunable from nonexistent to predominant by minor structural changes, such as addition of substituents to the system.^{3,4} They are also important intermediates in many organic reactions and bioorganic processes.^{1,5-7} However, examination of the chemical properties of *meta*-benzynes in the condensed phases is challenging due to the difficulty in either generating pure *meta*-benzynes or due to their high reactivities under these conditions. Therefore, many gas-phase reactivity studies have been carried out to explore the reactivity of protonated *meta*-benzyne analogs by using ion trap mass spectrometry.⁸⁻¹¹

All protonated *meta*-benzyne analogs studied thus far have a singlet ground state.^{2,3,12-15} Many of them, such as the 2,4- and 3,5-didehydropyridinium cations and their derivatives, have been calculated to have singlet-triplet (S-T) splittings (ΔE_{S-T} , defined as the energy difference between the lowest-energy singlet state and the lowest-energy excited triplet state) between -36.0 and -16.6 kcal mol⁻¹.^{2,3,12-15} However, one *meta*-benzyne analog, the 2,6-didehydropyridinium cation (**3**, Figure 4.1), was recently reported² to have a calculated ΔE_{S-T} of only -11.0 kcal mol⁻¹, which is the smallest among the charged *meta*-benzyne analogs studied thus far.^{2,3,12-15} Interestingly, this *meta*-benzyne analog has been demonstrated to undergo endothermic proton transfer reactions in the gas phase.² Similar reactivity was not reported for the isomeric 3,5- and 2,4-didehydropyridinium cations (**1** and **2**, Figure 4.1).² The unique reactivity of the 2,6-didehydropyridinium cation was attributed to its capability of undergoing proton transfer reactions from the lowest-energy excited triplet state that was calculated to be substantially more acidic than the singlet state.² This was rationalized by the destabilization of its singlet conjugate base due to three-center four-electron interactions involving the two radical sites and the nitrogen lone pair. In order to examine the scope of such reactivity for *meta*-benzyne analogs, four substituted 2,6-didehydropyridinium cations (**4** – **7**, Figure 4.1), all with small (calculated) ΔE_{S-T} , have been generated in the gas phase in a linear quadrupole ion trap (LQIT) mass spectrometer and their reactions with allyl iodide, tetrahydrofuran, ethanol, and *N*-methylformamide were examined. The

reactivity of one such biradical with 2,6-topology in an expanded π -system, the 1,3-didehydroisoquinolinium cation (**8**), was also studied. Their reactivities were compared to that of the 2,4- and 3,5-didehydropyridinium cations (**1** and **2**). Quantum chemical calculations were utilized to explore the factors that control the reactivity of these biradicals.

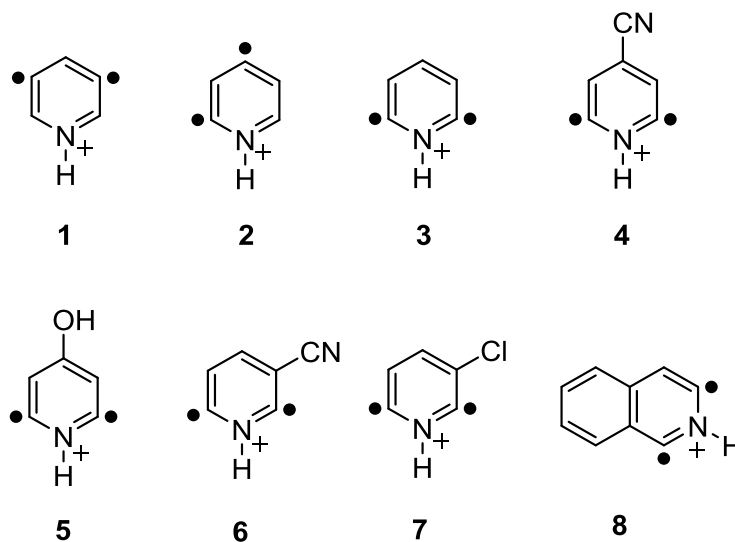


Figure 4.1 Studied biradicals

4.2 Experimental Section

Materials. 3,5-Diiodopyridine (precursor for **1**, purity $\geq 97\%$), 2,4-diiodopyridine (precursor for **2**, purity $\geq 97\%$) and 2,6-diiodopyridine (precursor for **3**, purity $\geq 95\%$), were purchased from Sigma Aldrich (St. Louis, MO). They were used as received. 3-Chloro-2,6-diiodopyridine (precursor for **7**) and 1,3-diiodoisoquinoline (precursor for **8**) were synthesized following procedures described in the literature.¹⁶⁻¹⁹ 4-Cyano-2,6-diiodopyridine (precursor for **4**), 4-hydroxy-2,6-diiodopyridine (precursor for **5**), 3-cyano-2,6-diiodopyridine (precursor for **6**) are new compounds and were synthesized using procedures described in Chapter 3. All the starting materials for synthesis were purchased from Sigma Aldrich (St. Louis, MO) and used as received. Allyl iodide (purity 98%), tetrahydrofuran (anhydrous, purity $\geq 99.9\%$), and N-methylformamide (purity 99%) were purchased from Sigma Aldrich (St. Louis, MO). Ethanol (200 proof, anhydrous) was purchased from Decon Labs. They were used as received.

Ion-molecule reactions. The biradicals **1** – **8** (Figure 4.1) were generated in a Thermo LTQ linear quadrupole ion trap (LQIT) mass spectrometer from the corresponding diiodo-precursors as described previously.¹⁻⁴ The precursors were dissolved in LC-MS methanol (purchased from Thermo Fisher Scientific, used as received), injected into an atmospheric pressure chemical ionization source (APCI) at a flow rate of 15 $\mu\text{L min}^{-1}$, and protonated. The protonated precursors were transferred into the linear quadrupole ion trap and trapped. After isolation and upon subsection to two consecutive collision-activated dissociation (CAD) events with helium buffer gas as the collision gas (collision energy 30 – 50, arbitrary units) to cleave off the two iodine atoms, **1** – **8** were generated, isolated and stored in the ion trap for ion-molecule reactions.

The reagents were introduced into the ion trap via a homebuilt reagent mixing manifold²⁰⁻²² at a flow rate of 5 $\mu\text{L h}^{-1}$. They were vaporized, mixed with the helium buffer gas in the manifold, and transferred into the ion trap. The pressure of the reagents was kept between 0.7×10^{-5} and 0.8×10^{-5} torr (nominal pressure). The helium buffer gas pressure was about 10^{-3} torr and was controlled by a leak valve connected to the manifold. The amount of the reagents in the ion trap was monitored by electron transfer reactions with CS_2 radical cations (generated in the APCI source from CS_2) to ensure that it remained nearly constant as a function of time. The isolated biradicals were allowed to react with allyl iodide, tetrahydrofuran, ethanol and *N*-methylformamide for various time periods (30 – 10000 ms). Based on the measured ion abundances, pseudo-first order reaction rate plots were generated in order to determine the primary and secondary product ions and reaction efficiencies for allyl iodide and tetrahydrofuran. The reaction efficiency is defined as the fraction of the ion-molecule collisions that leads to a reaction, expressed as % $k_{\text{exp}}/k_{\text{coll}}$, where k_{exp} is the experimental rate constant derived from the semilogarithmic rate plot by taking the slope of the rate plot and the concentration of the reagent, and k_{coll} is the collision rate constant determined using a parameterized trajectory theory.²³ Branching ratios for the primary ionic products were determined by taking the ratio of each primary product ion abundance and the total product ion abundances at early reaction times.

Quantum chemical calculations. All the quantum chemical calculations were carried out by Dr. John J. Nash at Department of Chemistry of Purdue University. Molecular geometries for all neutral and protonated (charged) species were optimized at the density functional (DFT) level of

theory by using the correlation-consistent polarized valence-triple- ζ (cc-pVTZ) basis set.²⁴ The DFT calculations used the gradient-corrected exchange functional of Becke,²⁵ which was combined with the gradient-corrected correlation functional of Lee, Yang and Parr²⁶ (B3LYP). All DFT geometries were verified to be local minima by computation of analytic vibrational frequencies, and these (unscaled) frequencies were used to compute zero-point vibrational energies (ZPVE) and 298 K thermal contributions ($H_{298} - E_0$). All DFT calculations for the biradicals employed an unrestricted formalism. For singlet biradicals, the DFT “wave function” was allowed to break spin symmetry by using an unrestricted formalism.²⁷ Total spin expectation values for Slater determinants formed from the optimized Kohn-Sham orbitals in these cases ranged widely between 0.0 and 1.0. For triplet biradicals, total spin expectation values did not exceed 2.02.

Molecular geometries for the neutral and protonated triplet and singlet states of biradicals **1** – **6**, pyridine, and pyridinium cation were also optimized at the coupled-cluster level of theory by using the cc-pVTZ basis set (such calculations for biradicals **7** and **8** were not possible due to their size). For pyridine and pyridinium cation, a restricted formalism was used (RHF-RCCSD(T)/cc-pVTZ). For triplet states of biradicals **1** – **6**, an unrestricted formalism was used (i.e., RHF-UCCSD(T)/cc-pVTZ) by using a single-configuration reference wave function. These calculations included all single and double excitations and a perturbative estimate for triple excitations. For singlet states of biradicals **1** – **6**, a single-configuration wave function was also used, but the reference wave functions were expanded in Brueckner orbitals (i.e., RHF-BCCD(T)/cc-pVTZ). Brueckner orbitals were used for the singlet states of the biradicals in order to avoid potential instabilities associated with contributions from single excitations in the coupled-cluster ansatz. However, note that for those molecules where the geometry of the singlet state was optimized by using both RHF-BCCD(T)/cc-pVTZ and RHF-UCCSD(T)/cc-pVTZ, the computed CASPT2/CASSCF(m,n)/cc-pVTZ energies (see below) using the geometries derived from these two methods were nearly identical.

To improve the molecular orbital calculations, dynamic electron correlation was also accounted for by using multi-reference second-order perturbation theory^{28,29} (CASPT2) for multi-configurational self-consistent field (MCSCF) reference wave functions; these calculations were carried out for the RHF-(U)CCSD(T)/cc-pVTZ (RHF-BCCD(T)/cc-pVTZ for singlet states; see

above) optimized geometries for biradicals **1** – **6** (UB3LYP/cc-pVTZ geometries were used for biradicals **7** and **8**; see above). The MCSCF calculations were of the complete active space (CASSCF) variety³⁰ and included (in the active space) the full π -space for each molecule and, for each of the biradicals, the nonbonding σ orbital(s). For biradicals **4** – **7**, the active space also included the additional electrons present in the π -space due to the substituent (lone pair electrons in the case of **5** and **7**). Thus, CASPT2/CASSCF(6,6) calculations were carried out for pyridine and pyridinium cation, CASPT2/CASSCF(8,8) calculations were carried out for biradicals **1**, **2**, **3** and **8** and CASPT2/CASSCF(10,10) calculations were carried out for biradicals **4** – **7**, isoquinoline and isoquinolinium cation (see below). Some caution must be applied in interpreting the CASPT2 results since this level of theory is known to suffer from a systematic error proportional to the number of unpaired electrons.³¹ Therefore, electronic energies are of the CASPT2/CASSCF(m,n)/cc-pVTZ//RHF-(U)CCSD(T)/cc-pVTZ (or CASPT2/CASSCF(m,n)/cc-pVTZ//RHF-BCCD(T)/cc-pVTZ, for singlet states) variety for biradicals **1** – **6** (where m is the number of active electrons and n is the number of active orbitals), and estimates of the thermodynamic quantities, E_0 and H_{298} , are derived by adding to these electronic energies ZPVE and the sum of ZPVE and ($H_{298} - E_0$), respectively, where the latter are derived from the DFT calculations. For biradicals **7** and **8**, similar CASPT2 calculations were carried out but UB3LYP/cc-pVTZ optimized geometries were used (see above).

Proton affinities (PA) for the conjugate bases of biradicals **1** – **7** were calculated by using an isodesmic reaction involving proton transfer from the charged aromatic biradical to pyridine to produce pyridinium cation and the neutral biradical. The calculated enthalpy change for this isodesmic reaction was then added to the experimentally determined PA for pyridine ($222 \text{ kcal mol}^{-1}$)³⁷ to derive PAs for the conjugate bases of the biradicals. For biradical **8**, PAs for the conjugate bases were calculated in a similar manner using an isodesmic equation involving proton transfer to isoquinoline ($PA^{37} = 227.5 \text{ kcal mol}^{-1}$). As noted above, these calculations were carried out at the CASPT2/CASSCF(m,n)/cc-pVTZ//RHF-(U)CCSD(T)/cc-pVTZ (or CASPT2/CASSCF(m,n)/cc-pVTZ//RHF-BCCD(T)/cc-pVTZ for singlet states of biradicals) level of theory for biradicals **1** – **6**, and the CASPT2/CASSCF(m,n)/cc-pVTZ//UB3LYP/cc-pVTZ level of theory for **7** and **8**. In all cases, the calculated PAs were corrected for zero-point vibrational energy differences at 298 K by using the (U)B3LYP/cc-pVTZ frequencies.

Choice of Molecular Geometries. A comparison of the calculated CASPT2/CASSCF(m,n)/cc-pVTZ energies (E_0) for biradicals **1** – **6** using either the UB3LYP/cc-pVTZ or RHF-UCCSD(T)/cc-pVTZ geometries shows that the energies of the triplet states for both the neutral and protonated biradicals do not depend significantly on the choice of geometry; differences in CASPT2 energies using the two different geometries range from 0.0 to 0.2 kcal mol⁻¹, and the RHF-UCCSD(T)/cc-pVTZ geometry provides the lowest (CASPT2) energy for eight of the twelve triplet biradicals. Similar results were obtained for the singlet states of the protonated biradicals. For these species, differences in CASPT2 energies ranged from 0.0 to 0.8 kcal mol⁻¹, and the RHF-BCCD(T)/cc-pVTZ geometries provided the lowest energies in all cases. The situation is quite different for the singlet states of the neutral biradicals, however. For these molecules, differences in CASPT2 energies ranged from 0.5 (biradical **2**) to 7.6 (biradical **3**) kcal mol⁻¹, and the RHF-BCCD(T)/cc-pVTZ geometries also gave the lowest energies in all cases. Thus, while the (CASPT2) energies of the triplet states of both the neutral and protonated biradicals, as well as the singlet states of the protonated biradicals, are relatively insensitive to the geometry used, the energies of the singlet states of the neutral biradicals can be quite sensitive to the molecular geometry. For these reasons, we have chosen to use coupled-cluster optimized geometries (UB3LYP/cc-pVTZ geometries for **7** and **8** due to their size) to derive values for singlet-triplet splittings and proton affinities for the biradicals.

All CASPT2/CASSCF and DFT calculations were carried out with the MOLCAS 8.0³² and Gaussian 09³³ electronic structure program suites, respectively. Coupled-cluster and conical intersection calculations were carried out with MOLPRO.³⁴

4.3 Results and Discussion

Biradicals **1** – **8**, all except **1** and **2** with the 2,6-biradical topology, were allowed to react with allyl iodide, tetrahydrofuran and ethanol in the linear quadrupole ion trap for variable periods of time (see Tables 4.1 and 4.2, Figures 4.2, 4.3, and 4.4). Reactions of some of the biradicals with *N*-methylformamide were also examined. The reactions with allyl iodide are discussed first, followed by reactions with *N*-methylformamide, ethanol and tetrahydrofuran.

All biradicals with the 2,6-biradical topology, namely **3** – **8**, have (calculated) ΔE_{S-T} values ranging from -8.8 down to -14.2 kcal mol⁻¹, while **1** (with the 3,5-biradical topology) has a substantially greater ΔE_{S-T} value (-21.7 kcal mol⁻¹). The same applies to **2** (with the 2,4-biradical topology; $\Delta E_{S-T} = -24.4$ kcal mol⁻¹). Therefore, only biradicals **3** – **8** have a relatively small ΔE_{S-T} and hence might be expected to display reactivity from their triplet states. The ΔE_{S-T} values of these biradicals are small due to the destabilization of their singlet states relative to the triplet states because the radical sites of the singlet states cannot get as close to each other as in related and isomeric protonated *meta*-benzynes due to the nitrogen atom in the middle. Indeed, their dehydrocarbon atom separations are all about 2.2 Å while those of the related and isomeric ions are typically about 1.5 Å.³

4.3.1 Reactions of Allyl Iodide

Table 4.1 summarizes the observations made for reactions of **1** – **8** with allyl iodide, including reaction efficiencies, primary products and their branching ratios. Upon reactions with allyl iodide, transfer of a proton from the protonated biradicals to the reagent was observed for all biradicals except **1**, **2** and **8** (Table 4.1). For these three biradicals, only radical-type reactions, i.e., abstraction of an allyl radical and/or an iodine atom, were observed (the reasons for the lack of proton transfer is discussed later). In sharp contrast, biradicals **3** (reported² earlier), **4** and **6** were found to undergo predominant proton transfer reactions with allyl iodide (91 – 96% of the products corresponded to proton transfer) instead of the expected¹⁻⁴ I atom or allyl group abstraction observed for **1**, **2** and **8** (Table 4.1). The remaining biradicals, **5** and **7**, showed minor proton transfer products (10% and 40%, respectively, of all products corresponded to proton transfer). In order to determine whether these proton transfer reactions are exo- or endothermic, quantum chemical calculations were carried out.

The proton affinities (PAs) calculated for the conjugate bases of biradicals **1** – **8** in their singlet ground states range from 194.8 up to ~226 kcal mol⁻¹ (Table 4.1). Compared to the PA of allyl iodide (193.4 kcal mol⁻¹),³⁵ proton transfer from all biradicals except two to allyl iodide would be highly endothermic (by at least 16 kcal mol⁻¹) and thus not observable under the experimental conditions used.^{2,9,36} The only exceptions are biradicals **4** and **6**, with PAs 196.9 and 194.8 kcal mol⁻¹, respectively. These biradicals are able to protonate allyl iodide from their singlet ground

states via thermoneutral or slightly endothermic reactions (the errors associated with all calculated PAs is at least 3 kcal mol⁻¹).

The nature of the other observed proton transfer reactions, those that would be highly endothermic for the singlet-state biradicals (i.e., **3**, **5** and **7**; Figure 4.2), were explored by calculating the PAs of the triplet states of their conjugate bases. The calculated PAs are 196.9 (calculated previously), 201.1 and 191.8 kcal mol⁻¹, respectively (Table 4.1). Therefore, **3** and **7** can undergo a nearly thermoneutral or slightly exothermic proton transfer reaction with allyl iodide (PA = 193.4 kcal mol⁻¹) from their triplet states. Their proton transfer efficiencies (branching ratio for proton transfer product × total reaction efficiency) are 0.7% and 0.8%, respectively, similar within experimental error, which likely reflects their similar PAs and ΔE_{S-T} . However, proton transfer from the triplet state of **5** to allyl iodide is more endothermic (by about 8 kcal mol⁻¹ without consideration of the errors in the PA values). Furthermore, the ΔE_{S-T} and the relevant PA value for this biradical are greater than for **7** and **8** (Table 4.1). These considerations explain the very low efficiency of this proton transfer reaction (0.2%)

Table 4.1 Reactions, total reaction efficiencies and branching ratios for primary products of biradicals **1** – **8** for reactions with allyl iodide and the calculated ΔE_{S-T} values (kcal mol⁻¹) and PAs (kcal mol⁻¹) of the conjugate bases of the biradicals in their singlet (S) and triplet (T) states. The experimental PAs of **1** and **2** were obtained previously by bracketing experiments³⁶ and the calculated PA of allyl iodide was obtained from literature.³⁵ Reactions that appear to occur from triplet states are **bolded** and underlined and the relevant PAs are **bolded**.

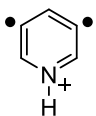
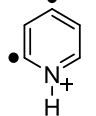
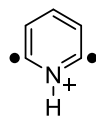
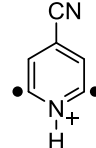
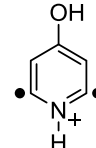
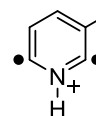
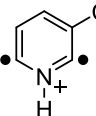
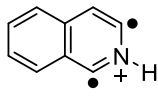
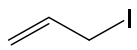
									
	1	2	3	4	5	6	7	8	
ΔE_{S-T} ^a	-21.7	-24.4	-10.3	-11.1	-14.2	-9.4	-8.8	-12.3	
PA ^b	S: 214.3 T: 207.7	S: 207.0 T: 209.3 (Exp ^c 209.6 ± 3.3)	S: 209.7 T: 196.9 (Exp ^c 196.6 ± 3.3)	S: 196.9 T: 185.0	S: 212.3 T: 201.1	S: 194.8 T: 183.5	S: 215.0 T: 191.8	S: ~226 T: 203.7	
	I abs ^e	59%	Allyl abs 62%	H⁺ trn^h 92%	H ⁺ trn 91%	Addition 80%	H ⁺ trn 99%	Allyl abs 48%	Allyl abs 100%
	2° I abs ^f		2° I abs	2° ^f I ⁺ trn ⁱ	2° I ⁺ trn	H⁺ trn 20%	2° I ⁺ trn	2° I abs	2° I abs
	Allyl abs	41%	I abs 38%	Addition 6%	2° allene sub ^k	2° allene sub ^j	2° allene sub	H⁺ trn 40%	
	2° I abs		2° I abs	Allyl abs 2%	Allyl abs 8%		Allyl abs 1%	2° I ⁺ trn	
	PA = 193.4 kcal mol ⁻¹ ^d				2° I abs	I abs 1%		2° allene sub	
Efficiency ^g	7%	Efficiency 8%	Efficiency 15%	Efficiency 17%	Efficiency 1%	Efficiency 24%	Efficiency 2%	Efficiency 2%	
			H ⁺ trn Eff. 14%	H ⁺ trn Eff. 15%	H ⁺ trn Eff. 0.2%	H ⁺ trn Eff. 24%	H ⁺ trn Eff. 0.8%		

Table 4.1 Continued

^a Calculated at the CASPT2/CASSCF(*m,n*)/cc-pVTZ//RHF-(U)CCSD(T)/cc-pVTZ level of theory. ^b For triplet states, calculated at the CASPT2/CASSCF(*m,n*)/cc-pVTZ//RHF-(U)CCSD(T)/cc-pVTZ level of theory, for singlet states, calculated at CASPT2/CASSCF(*m,n*)/cc-pVTZ//RHF-BCCD(T)/cc-pVTZ level of theory. ^c Experimental PA from reference 24. ^d RHF-RCCSD(T)/6-311G(d,p)//B3LYP/6-311(d,p) level of theory; reference 36. ^e abs = abstraction. ^f 2° indicates a secondary product of the above primary product. ^g Reaction efficiency (% of collisions leading to reaction) = $k_{\text{exp}}/k_{\text{coll}} \times 100$; precision $\pm 10\%$; accuracy $\pm 50\%$. ^h trn = transfer. ⁱ The product ion (*m/z* 295) is formed upon substitution of a proton with an iodine atom in protonated allyl iodide (*m/z* 169). ^j sub = substitution; the product ion (*m/z* 81) was formed by substitution of the iodine atom in the protonated allyl iodide (*m/z* 169) with an allene molecule.

While **5** and **7** are likely to react from their triplet states, their proton transfer reactions have substantially lower efficiencies (0.2% and 0.8%, respectively) than those of **3** (14%). These observations suggest that the intersystem crossing rate must be sensitive to substitution in **1** as both **5** and **7** undergo proton transfer substantially less efficiently than **3** in spite of the fact that **7** has a smaller ΔE_{S-T} value (-8.8 kcal mol⁻¹) than **3** ($\Delta E_{S-T} = -10.3$ kcal mol⁻¹; Table 1) and its conjugate base has a smaller triplet-state PA (191.8 kcal mol⁻¹) than **3** (PA = 196.9 kcal mol⁻¹). Based on these two values, **7** would be expected to react faster than **3** but it does not. It should be noted here that the proton transfer efficiencies for the biradicals reacting from their triplet states (0.2%, 0.8% and 14%; see above) are generally lower than those for the biradicals reacting from their singlet states (15% and 25% for **4** and **6**, respectively).

Biradicals **1**, **2** and **8** were mentioned above not to transfer a proton to allyl iodide. Based on above discussions, this finding can now be rationalized based on the high PAs of their conjugate bases in both singlet and triplet states (equal to or greater than 203.7 kcal mol⁻¹). Proton transfer to allyl iodide (PA = 193.4 kcal mol⁻¹) from these biradicals would be endothermic by at least 10 kcal mol⁻¹. In addition, **1** and **2** (without the 2,6-radical topology) also have very large ΔE_{S-T} , which should prevent their access to their triplet states.

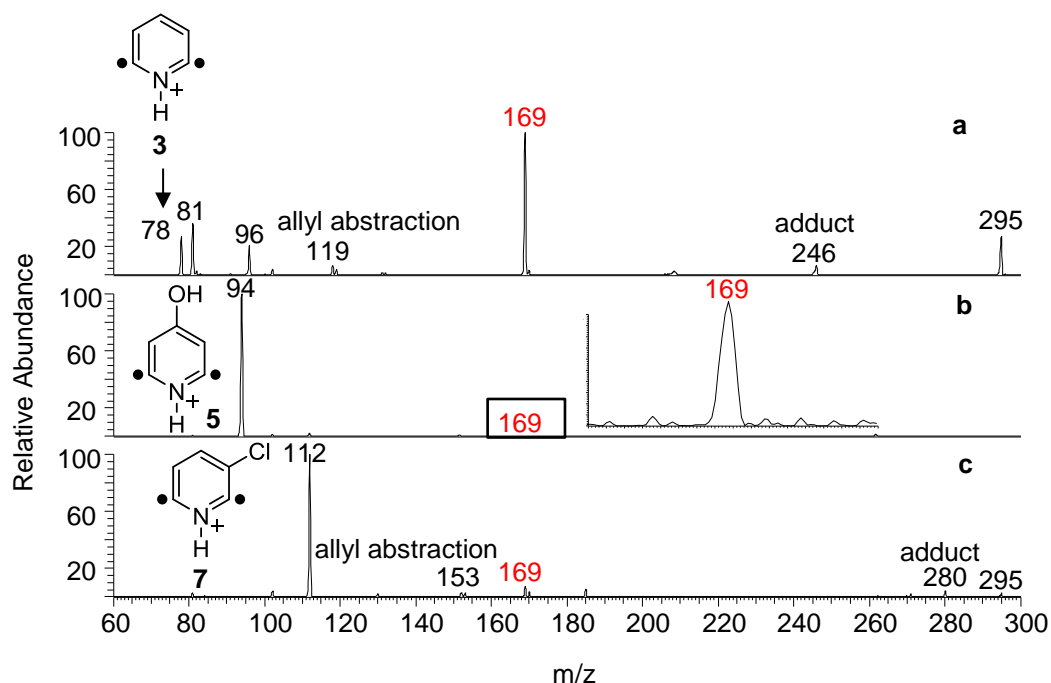


Figure 4.2 Mass spectra measured after 300 ms reactions with allyl iodide for (a) **3**, (b) **5** (zoomed area near m/z 169), and (c) **7**. The proton transfer product ions (m/z 169) are labelled in red. The ions of m/z of 81 and 295 are secondary product ions formed upon reactions of the ions of m/z 169 with allyl iodide (see Table 1 for their identities). The ion of m/z 96 is a water adduct formed from **1** upon reactions with adventitious water in the ion trap.

4.3.2 Reactions of *N*-Methylformamide

Biradical **8** is the only species with the 2,6-biradical topology that did not transfer a proton to allyl iodide ($PA = 193.4 \text{ kcal mol}^{-1}$) due to the large PA of its conjugate base in both the singlet and triplet states (203.7 and $\sim 226 \text{ kcal mol}^{-1}$). Therefore, the ability of this biradical to react from its triplet state was tested using a reagent with a larger PA than allyl iodide, i.e., *N*-methylformamide with a PA of $203.5 \text{ kcal mol}^{-1}$.³⁷ This PA is comparable to that of the conjugate base of **8** in its triplet state but substantially smaller than the PA of the conjugate base in its singlet state (Table 4.1). Therefore, if proton transfer is observed from **8** to *N*-methylformamide, this reaction must occur from the triplet state. This is indeed what was observed (Figure 4.3a). Therefore, **8** can react from its triplet state if the basicity of the reagent is appropriate.

Biradical **1** was also allowed to react with *N*-methylformamide as the PA of its conjugate base in the triplet state ($207.7 \text{ kcal mol}^{-1}$) is closer to that of *N*-methylformamide than allyl iodide. However, no reactions were observed (Figure 4.3b). This finding again suggests that **1** (with ΔE_s

$T = -21.7 \text{ kcal mol}^{-1}$) cannot react from its triplet state. Therefore, among all the *meta*-benzynes studied so far, only those with ΔE_{S-T} smaller than 15 kcal mol^{-1} (all with 2,6-biradical topology) appear to react from their excited triplet states.

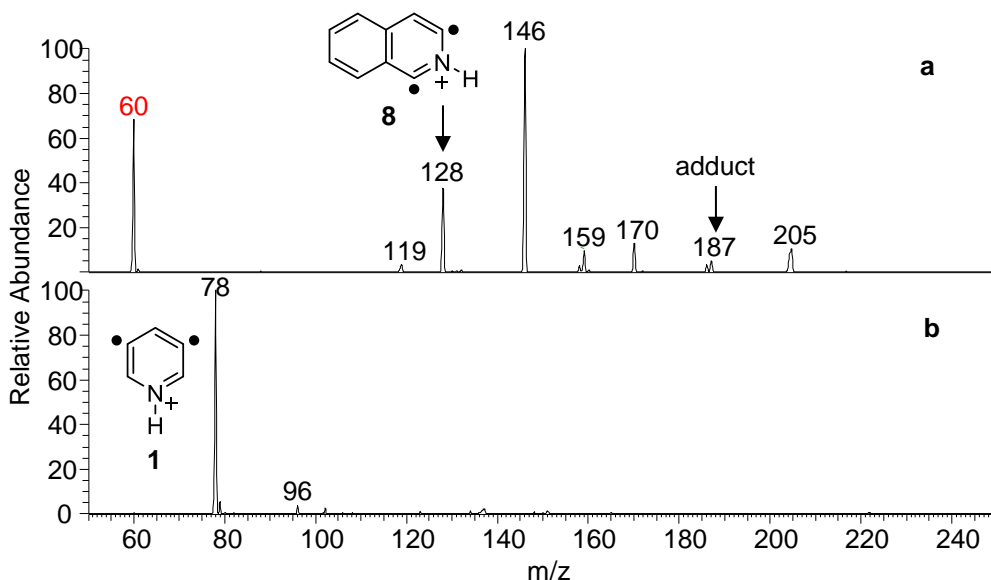


Figure 4.3 (a) Mass spectrum measured after 300 ms of reactions of **8** with *N*-methylformamide. The proton transfer product ion (m/z 60) is labelled in red. The ion of m/z 119 is the protonated *N*-methylformamide dimer generated upon reactions of the ion of m/z 60 with *N*-methylformamide. The ion of m/z 146 is a water adduct formed upon reactions of **8** with adventitious water in the ion trap. The ion of m/z 187 is an adduct of **8** with *N*-methylformamide and the ion of m/z 205 is a water adduct of this ion. The ions of m/z 159 and m/z 170 are fragment ions of the ion of m/z 187 formed via loss of CO and NH_3 , respectively. (b) Mass spectrum measured after 3000 ms reactions of **1** with *N*-methylformamide. The ion of m/z 96 is an adduct formed upon reactions of **1** with adventitious water in the ion trap.

4.3.3 Reactions of Ethanol

In order to learn more about proton transfer reactions occurring from the excited triplet states of biradicals with 2,6-biradical topology, reactions of **3** – **8** were examined with ethanol. Ethanol has a PA of only $185.6 \text{ kcal mol}^{-1}$.³⁷ Therefore, the singlet states of none of these biradicals can transfer a proton to ethanol. However, three of them, namely **4** (triplet-state PA = $185.0 \text{ kcal mol}^{-1}$), **6** (triplet-state PA = $183.5 \text{ kcal mol}^{-1}$), and **7** (triplet-state PA = $191.8 \text{ kcal mol}^{-1}$) should be able to transfer a proton to ethanol from their triplet states if they can access these states. As shown in Figure 4.4, the cyano-substituted biradicals **4** and **6**, which transfer a proton to allyl iodide from their singlet ground states, also transfer a proton to ethanol but from their triplet states. Biradical

7 was also found to transfer a proton to ethanol from its triplet state. However, none of the remaining biradicals (**3**, **5**, and **8**) transferred a proton to ethanol, due to the large triplet-state PAs of their conjugate bases compared to that of ethanol (> 10 kcal mol⁻¹ greater than the PA of ethanol).

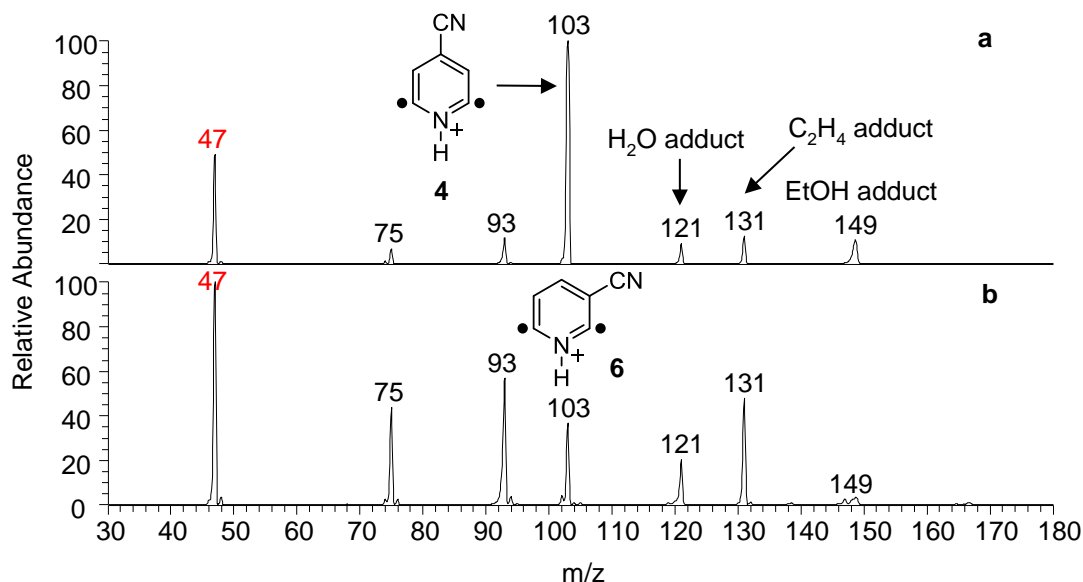


Figure 4.4 Mass spectra measured after 300 ms reactions with ethanol for (a) **4** and (b) **6**. The proton transfer product ions (m/z 47) are labelled in red. The ions of m/z 75 and 93 are secondary product ions formed upon reactions of the ions of m/z 47 with ethanol; the ion of m/z 93 is a protonated ethanol dimer and the ion of m/z 75 is the product formed from the ion of m/z 93 upon elimination of a water molecule. The ions of m/z 121 and 131 are formed upon dissociation of the ethanol adduct (m/z 149) via elimination of ethylene and water, respectively.

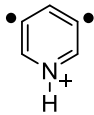
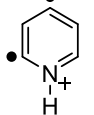
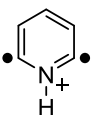
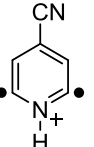
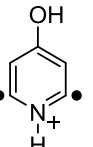
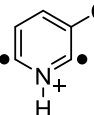
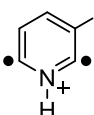
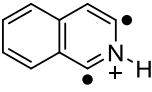
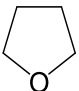
4.3.4 Reactions of Tetrahydrofuran

The reactions of **1** – **8** with tetrahydrofuran were also studied as this reagent³⁷ has a PA (196.5 ± 1.9 kcal mol⁻¹) that is in the middle of the PA range for the reagents discussed above. All biradicals except **1** and **2** (both PAs being too high to transfer a proton to tetrahydrofuran; Table 4.2) were observed to transfer a proton to tetrahydrofuran at varying efficiencies (from 2% up to 94%; Table 4.2). Some of these reactions must take place from a triplet state but other can occur either from a singlet state or an excited triplet state.

Biradicals **3**, **5** and **7** that transfer a proton to allyl iodide from their excited triplet states do that also for tetrahydrofuran but more efficiently (14%, 0.2%, and 0.8%, respectively, vs. 37%,

18%, and 2%, respectively). It is not obvious at this time why **5** transfers a proton to tetrahydrofuran more efficiently than **7**. Finally, biradical **8** that did not transfer a proton to allyl iodide from its triplet state did that quite efficiently (19%) to tetrahydrofuran.

Table 4.2 Reactions, reaction efficiencies and branching ratios for primary products of biradicals **1** – **8** upon interactions with tetrahydrofuran and their calculated ΔE_{S-T} values (kcal mol^{-1}) and the PAs (kcal mol^{-1}) of the conjugate bases of the biradicals in their singlet (S) and triplet (T) electronic states. The experimental PA of tetrahydrofuran was obtained from literature.³⁷ The PA values in **bold** indicate which state is proposed to transfer a proton to tetrahydrofuran.

								
	1	2	3	4	5	6	7	8
ΔE_{S-T} ^a	-21.7	-24.4	-10.3	-11.1	-14.2	-9.4	-8.8	-12.3
PA ^b	S: 214.3 T: 207.7	S: 207.0 T: 209.3 (Exp 209.6 ^c)	S: 209.7 T: 196.9 (Exp 196.6)	S: 196.9 T: 185.0	S: 212.3 T: 201.1	S: 194.8 T: 183.5	S: 215.0 T: 191.8	S: ~226 T: 203.7
	No reactions	CH ₂ O abs ^d 49% 2° addition ^e H ⁺ abs 26% C ₂ H ₄ O abs 25%	H ⁺ trn ^f 99% 2° addition Addition 1%	H ⁺ trn 95% 2° addition Addition 5%	H ⁺ trn 80% 2° addition Addition 19% CH ₂ O abs 1%	H ⁺ trn 98% 2° addition Addition 2%	H ⁺ trn 82% 2° addition Addition 18%	H ⁺ trn 75% 2° addition Addition 25%
PA = 196.5 kcal mol ⁻¹	Efficiency 0%	Efficiency 27%	Efficiency ^f 37% H ⁺ trn Eff. ^h 37%	Efficiency 46% H ⁺ trn Eff. 44%	Efficiency 23% H ⁺ trn Eff. 18%	Efficiency 96% H ⁺ trn Eff. 94%	Efficiency 2% H ⁺ trn Eff. 2%	Efficiency 25% H ⁺ trn Eff. 19%

^a Calculated at the CASPT2/CASSCF(*m,n*)/cc-pVTZ//RHF-(U)CCSD(T)/cc-pVTZ level of theory. ^b For triplet states, calculated at the CASPT2/CASSCF(*m,n*)/cc-pVTZ//RHF-(U)CCSD(T)/cc-pVTZ level of theory, for singlet states, calculated at CASPT2/CASSCF(*m,n*)/cc-pVTZ//RHF-BCCD(T)/cc-pVTZ level of theory. ^c Experimental PA from reference 24. ^d abs = abstraction. ^e 2° indicates a secondary product of the above primary product. ^f trn = transfer. ^g Reaction efficiency (% of collisions leading to reaction) = $k_{\text{exp}}/k_{\text{coll}} \times 100$; precision $\pm 10\%$; accuracy $\pm 50\%$. ^h H⁺ transfer efficiency.

4.3.5 Triplet-state Reactivity

Considering the fact that the calculated singlet-triplet splittings for the biradicals having a 2,6-topology (i.e., **3** – **8**) are relatively large (ranging from ca. -11 to -17 kcal mol⁻¹), it is rather surprising that these species show reactivity (e.g., proton transfer) from their (excited) triplet states. Let us first briefly consider how our experiments are performed. After the precursor ions are introduced into the ion trap, in the presence of helium buffer gas and the chosen reagent (introduced through a manifold), they are accelerated. Activating collisions (CAD) between the precursor ions and the buffer gas (present at a much higher concentration than the reagent) lead to the first C-I bond cleavage (i.e., to generate a protonated monoradical). The monoradical is then allowed to cool via collisions with primarily the buffer gas. Any collisions of the monoradical with the reagent at this time may result in proton transfer to the reagent if its proton affinity is high enough; however, the protonated monoradical is then isolated (by ejecting all other ions from the ion trap) before the subsequent CAD step to generate the biradical. The protonated monoradical ions are accelerated again to cleave the second C-I bond (in the presence of buffer gas and reagent). The resulting biradical is then cooled via collisions with primarily the buffer gas (see above). The protonated biradical is then isolated (by ejecting all other ions from the ion trap) and allowed to react with the reagent.

In order to examine the effects of cooling, an experiment was performed in which a protonated biradical (**3**) was generated in the presence of the buffer gas but in the absence of a neutral reagent. The biradical was cooled for 1 s, and then allyl iodide was temporarily introduced into the ion trap via a pulsed valve. The product distribution (84% proton transfer, 11% allyl abstraction, and 5% addition) was similar to that obtained with allyl iodide initially present in the ion trap (92% proton transfer, 2% allyl abstraction, and 6% addition; Table 4.1). Thus, it appears that the ions are being sufficiently cooled (i.e., they are not “hot” ions), and the extent of proton transfer does not depend on whether or not the neutral reagent is present in the ion trap initially.

For (cooled) biradicals that are formed on the (excited) triplet surface, intersystem crossing is expected to allow the biradicals to cross to the (ground) singlet surface as long as the biradicals have sufficient internal energy to reach an avoided crossing or a conical intersection between these

two states. CASSCF(m,n)/6-311G(2df,p) calculations for biradicals **3** – **8** locate conical intersections for each molecule that are 13.9, 15.2, 24.9, 12.4, 12.9 and 15.1 kcal mol⁻¹, respectively, higher in energy than the minimum energy geometry of the triplet state (the conical intersections are 23.3, 24.9, 37.3, 21.2, 21.6 and 24.9 kcal mol⁻¹ higher in energy than the minimum energy geometries of the (ground) singlet states for **3** – **8**, respectively). Thus, it seems that once the triplet state of the biradical is formed, it lacks sufficient internal energy to reach the conical intersection where intersystem crossing can occur. It is also noteworthy that relatively slow intersystem crossing in biradicals that have a 2,6-topology (such as **3** – **8**) may be a result of the increased rigidity of the (hetero)aromatic ring system about the two dehydrocarbon atoms and the nitrogen atom.

One might also expect that the energy required for the triplet biradical to reach the conical intersection could be supplied by the solvation energy associated with the formation of an ion-molecule complex²⁸ when the chosen reagent is introduced into the ion trap (5 – 20 kcal mol⁻¹). However, for the biradicals studied here, it seems that the rate of proton transfer (between the ion and molecule) is faster than the rate of intersystem crossing.

4.3.6 Theoretical Disquisition

An analysis of the computed CASPT2/CASSCF(m,n)/cc-pVTZ energies using both the UB3LYP/cc-pVTZ optimized geometries, and the RHF-UCCSD(T)/cc-pVTZ (or RHF-BCCD(T)/cc-pVTZ for singlet states) optimized geometries, for biradicals **1** – **6** shows very small differences (less than 0.3 kcal mol⁻¹) for the energies of the triplet states of these molecules, and for four of the six biradicals, the coupled-cluster geometries provide the lowest energies. For the singlet states of **1** – **6**, the differences in computed energies are also quite small (less than 0.9 kcal mol⁻¹; in all cases, the coupled-cluster geometries provide the lowest energies). This is also the case for the triplet states of the (neutral) conjugate bases for **1** – **6**. Differences in the computed energies are less than 0.2 kcal mol⁻¹ (coupled-cluster geometries provide the lowest energies for four of the six biradicals). Thus, for the singlet and triplet states of the protonated biradicals, and the triplet states of their (neutral) conjugate bases, the CASPT2/CASSCF(m,n)/cc-pVTZ computed energies do not depend significantly on the choice of geometry. This is not the case, however, for the singlet states of the (neutral) conjugate bases for **1** – **6**. For these, the differences in computed

energies range from 0.5 kcal mol⁻¹ (biradical **2**) to 7.6 kcal mol⁻¹ (biradical **3**) and, in all cases, the coupled-cluster geometries give lower CASPT2/CASSCF(*m,n*)/cc-pVTZ energies. Moreover, the differences in computed energies are largest for those biradicals that have a 2,6-topology (e.g., 7.6, 7.5, 6.4 and 4.8 kcal mol⁻¹ for **3** – **6**, respectively).

The choice of geometry has little effect on the calculated singlet-triplet splittings (ΔE_{S-T}) for biradicals **1** – **6**. However, it can have a significant effect on the calculated ΔE_{S-T} values for the (neutral) conjugate bases of **1** – **6**. For example, at the CASPT2/CASSCF(*m,n*)/cc-pVTZ level of theory, using the UB3LYP/cc-pVTZ geometries, the calculated ΔE_{S-T} for the conjugate bases of **1** – **6** are: -18.6, -26.5, +3.4, +3.4, -1.1 and +5.0 kcal mol⁻¹, respectively. Using the coupled-cluster geometries, the calculated ΔE_{S-T} for the conjugate bases of **1** – **6** are: -21.4, -26.9, -4.3, -4.0, -7.5 and 0.3 kcal mol⁻¹, respectively. The calculated ΔE_{S-T} values are more negative using the coupled-cluster geometries because the CASPT2/CASSCF(*m,n*)/cc-pVTZ energies of the singlet states are lower than those obtained using the UB3LYP/cc-pVTZ geometries. Thus, the choice of geometry has a significant influence on the computed ΔE_{S-T} values of the neutral biradicals, especially those having a 2,6-topology.

As expected, the calculated proton affinities (using an isodesmic equation involving proton transfer to pyridine; see Computational Methods above) for the singlet (but not the triplet) states for the (neutral) conjugate bases of **1** – **6** can also be quite different at the CASPT2/CASSCF(*m,n*)/cc-pVTZ level of theory when either the UB3LYP/cc-pVTZ or coupled-cluster geometries are used. Such differences are particularly evident for the biradicals that have a 2,6-topology (e.g., **3** – **6**). These differences can again be traced to the singlet state of the neutral biradical (which is a product in the isodesmic equation used to calculate the PA). For **3** – **6**, PAs calculated at the CASPT2/CASSCF(*m,n*)/cc-pVTZ level of theory using the UB3LYP/cc-pVTZ geometries are higher by ca. 4 – 8 kcal mol⁻¹ compared to those calculated using the coupled-cluster geometries.

4.4 Conclusions

All six of the pyridine-based biradicals that have a 2,6-biradical topology and singlet electronic ground states (**3** – **8**) studied here were found to transfer a proton from their excited

triplet states to at least one of the four bases studied. Based on the calculated proton affinities of the conjugate bases of the biradicals, the (excited) triplet states are stronger Brønsted acids than the (ground) singlet states. This is rationalized by the destabilization of the singlet states due to three-center four-electron interactions involving the two radical sites and the nitrogen lone pair. Further, the cations that have the 2,6-biradical topology were calculated to have substantially smaller singlet-triplet (S-T) splittings (ΔE_{S-T} ; ranging from ca. -11 to -17 kcal mol⁻¹) than other related or isomeric *meta*-benzyne analogs (e.g., the calculated ΔE_{S-T} for the didehydropyridinium cations that have either a 2,4- or a 3,5-biradical topology studied here (**1** and **2**) are -23.4 and -24.6 kcal mol⁻¹, respectively). The singlet states of the protonated 2,6-biradicals are destabilized relative to the triplet states because the radical sites of the singlet states cannot get as close to each other as in related and isomeric protonated *meta*-benzynes due to the presence of the nitrogen atom (which makes the (hetero)aromatic ring structure more rigid). A *meta*-benzyne analogous to the 2,6-dehydropyridinium cation but in an expanded π -system, the 1,3-didehydroisoquinolinium cation (singlet ground state), was also found to undergo proton transfer reactions from its lowest-energy excited triplet state. No such proton transfer reactions were observed (or have been reported) for biradicals that have either a 2,4- or a 3,5-biradical topology.

Even though the calculated singlet-triplet splittings for the biradicals having a 2,6-topology (i.e., **3** – **8**) are relatively large (ranging from ca. -11 to -17 kcal mol⁻¹), these species show reactivity (proton transfer) from their (excited) triplet states. Under the experimental conditions used here, the ions are being sufficiently cooled so that highly endothermic reactions (endothermicity greater than ca. 10 kcal mol⁻¹) cannot take place.³⁶ Thus, it seems that once the triplet state of the biradical is formed, it lacks sufficient internal energy to undergo intersystem crossing to the (ground) singlet state. Moreover, even though the solvation energies³⁸ associated with most of the ion-molecule complexes of interest here (5 – 20 kcal mol⁻¹) should provide enough energy for the ion to reach a conical intersection (and undergo intersystem crossing), this does not occur to any great extent because the rate of proton transfer within the ion-molecule complex is too fast.

Finally, the magnitude of the singlet-triplet splitting (ΔE_{S-T}) is known to influence the reactivity of singlet state biradicals due to the need to partially uncouple the electrons in the

transition state. For triplet state biradicals, the nonbonding electrons are not coupled, and the magnitude of ΔE_{S-T} should have little to no influence on reactivity. For the proton transfer reactions described here, the magnitude of ΔE_{S-T} does not appear to have much, if any, effect on the reaction efficiency. Thus, the efficiency of proton transfer appears to be controlled entirely by the proton affinity of the conjugate base of the biradical.

4.5 References

1. Nelson, E. D.; Artau, A.; Price, J. M.; Tichy, S. E.; Jing, L.; Kenttämä, H. I. *J. Phys. Chem. A* **2001**, *105* (44), 10155–10168.
2. Jankiewicz, B. J.; Vinueza, N. R.; Kirkpatrick, L. M.; Gallardo, V. A.; Li, G.; Nash, J. J.; Kenttämä, H. I. *J. Phys. Org. Chem.* **2013**, *26* (9), 707–714.
3. Gao, J.; Jankiewicz, B. J.; Reece, J.; Sheng, H.; Cramer, C. J.; Nash, J. J.; Kenttämä, H. I. *Chem. Sci.* **2014**, *5* (6), 2205–2215.
4. Kotha, R. R.; Yerabolu, R.; Ding, D.; Szalwinski, L.; Ma, X.; Wittrig, A.; Kong, J.; Nash, J. J.; Kenttämä, H. I. *Chem. Eur. J.* **2019**, *25* (17), 4472–4477.
5. Wenk, H. H.; Winkler, M.; Sander, W. *Angew. Chem. Int. Ed.* **2003**, *42* (5), 502–528.
6. Billups, W. E.; Buynak, J. D.; Wolf, D. *J. Org. Chem.* **1979**, *44* (23), 4218–4219.
7. Luo, S.; Kuhn, A. J.; Castano, I.; Castro, C.; Karney, W. L. *J. Org. Chem.* **2018**, *83* (1), 314–322.
8. Gao, J.; Jankiewicz, B. J.; Sheng, H.; Kirkpatrick, L.; Ma, X.; Nash, J. J.; Kenttämä, H. I. *Eur. J. Org. Chem.* **2018**, *2018* (46), 6582–6589.
9. Sheng, H.; Ma, X.; Lei, H.-R.; Milton, J.; Tang, W.; Jin, C.; Gao, J.; Wittrig, A. M.; Archibold, E. F.; Nash, J. J.; Kenttämä, H. I. *ChemPhysChem* **2018**, *19* (21), 2839–2842.
10. Ma, X.; Jin, C.; Wang, D.; Nash, J. J.; Kenttämä, H. I. *Chem. Eur. J.* **2019**, *25* (25), 6355–6361.
11. Max, J. P.; Ma, X.; Kotha, R. R.; Ding, D.; Milton, J.; Nash, J. J.; Kenttämä, H. I. *Int. J. Mass Spectrom.* **2019**, *435*, 280–290.
12. Wenthold, P. G.; Squires, R. R.; Lineberger, W. C. *J. Am. Chem. Soc.* **1998**, *120* (21), 5279–5290.
13. Johnson, W. T. G.; Cramer, C. J. *J. Am. Chem. Soc.* **2001**, *123* (5), 923–928.

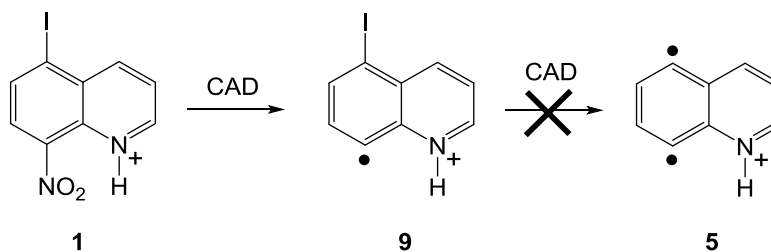
14. Price, J. M.; Nizzi, K. E.; Campbell, J. L.; Kentt ämaa, H. I.; Seierstad, M.; Cramer, C. J. *J. Am. Chem. Soc.* **2003**, *125* (1), 131–140.
15. Nash, J. J.; Nizzi, K. E.; Adeuya, A.; Yurkovich, M. J.; Cramer, C. J.; Kentt ämaa, H. I. *J. Am. Chem. Soc.* **2005**, *127* (16), 5760–5761.
16. Grauert, M.; Bischoff, D.; Dahmann, G.; Kuelzer, R.; Rudolf, K. US Patent 514210200.
17. Dhau, J. S.; Singh, A.; Kasetti, Y.; Bhatia, S.; Bharatam, P. V.; Brand ão, P.; F élix, V.; Singh, K. N. *Tetrahedron* **2013**, *69* (48), 10284–10291.
18. Zhang, Y.; Pavlova, O. A.; Chefer, S. I.; Hall, A. W.; Kurian, V.; Brown, L. L.; Kimes, A. S.; Mukhin, A. G.; Horti, A. G. *J. Med. Chem.* **2004**, *47* (10), 2453–2465.
19. Kadiyala, R. R.; Tilly, D.; Nagaradja, E.; Roisnel, T.; Matulis, V. E.; Ivashkevich, O. A.; Halauko, Y. S.; Chevallerier, F.; Gros, P. C.; Mongin, F. *Chem. Eur. J.* **2013**, *19* (24), 7944–7960.
20. Gronert, S. *J. Am. Soc. Mass Spectrom.* **1998**, *9* (8), 845–848.
21. Gronert, S. *Mass Spectrom. Rev.* **2005**, *24* (1), 100–120.
22. Habicht, S. C.; Vinueza, N. R.; Archibold, E. F.; Duan, P.; Kentt ämaa, H. I. *Anal. Chem.* **2008**, *80* (9), 3416–3421.
23. Su, T.; Chesnavich, W. J. *J. Chem. Phys.* **1982**, *76* (10), 5183–5185.
24. Dunning, T. H. *J. Chem. Phys.* **1989**, *90*, 1007–1023.
25. Becke, A. D. *Phys. Rev. A* **1988**, *38*, 3098–3100.
26. Lee, C. T.; Yang, W. T.; Parr, R. G. *Phys. Rev. B*, **1988**, *37*, 785–789.
27. (a) Polo, V.; Kraka, E.; Cremer, D. *Theor. Chem. Acc.* **2002**, *107*, 291–303. (b) Gr äfenstein, J.; Hjerpe, A. M.; Kraka, E.; Cremer, D. *J. Phys. Chem. A* **2000**, *104*, 1748–1761. (c) Cramer, C. J. *J. Am. Chem. Soc.* **1998**, *120*, 6261–6269. (d) Gr äfenstein, J.; Kraka, E.; Cremer, D. *Chem. Phys. Lett.* **1998**, *288*, 593–602. (e) Crawford, T. D.; Kraka, E.; Stanton, J. F.; Cremer, D. *J. Chem. Phys.* **2001**, *114*, 10638–10650.
28. Andersson, K.; Malmqvist, P.-Å.; Roos, B. O.; Sadlej, A. J.; Wolinski, K. *J. Phys. Chem.* **1990**, *94*, 5483–5488.
29. Andersson, K. *Theor. Chim. Acta* **1995**, *91*, 31–46.
30. Roos, B. O.; Taylor, P. R.; Siegbahn, P. E. M. *Chem. Phys.* **1980**, *48*, 157–173.
31. Andersson, K.; Roos, B. O. *Int. J. Quantum Chem.* **1993**, *45*, 591–607.

32. (a) MOLCAS 7.4: Aquilante, F.; De Vico, L.; Ferré N.; Ghigo, G.; Malmqvist, P.-Å.; Neogrady; Pedersen, T. B.; Pitonak, M.; Reiher, M.; Roos, B. O.; Serrano-Andrés, L.; Urban, M.; Veryazov, V.; Lindh, R. *J. Comp. Chem.* **2010**, *31*, 224–247. (b) Code Development: Veryazov, V.; Widmark, P.-O.; Serrano-Andrés, L.; Lindh, R. Roos, B. O. *Int. J. Quant. Chem.* **2004**, *100*, 626–635. (c) MOLCAS 7: Karlström, G.; Lindh, R.; Malmqvist, P.-Å.; Roos, B. O.; Ryde, U.; Veryazov, V.; Widmark, P.-O.; Cossi, M.; Schimmelpfennig, B.; Neogrady, P.; Seijo, L. *Comp. Mat. Sci.* **2003**, *28*, 222–239.
33. Frisch, M. J.; Trucks, G. W.; Schlegel, H. B.; Scuseria, G. E.; Robb, M. A.; Cheeseman, J. R.; Scalmani, G.; Barone, V.; Mennucci, B.; Petersson, G. A.; Nakatsuji, H.; Caricato, M.; Li, X.; Hratchian, H. P.; Izmaylov, A. F.; Bloino, J.; Zheng, G.; Sonnenberg, J. L.; Hada, M.; Ehara, M.; Toyota, K.; Fukuda, R.; Hasegawa, J.; Ishida, M.; Nakajima, T.; Honda, Y.; Kitao, O.; Nakai, H.; Vreven, T.; Montgomery, Jr., J. A.; Peralta, J. E.; Ogliaro, F.; Bearpark, M.; Heyd, J. J.; Brothers, E.; Kudin, K. N.; Staroverov, V. N.; Keith, T.; Kobayashi, R.; Normand, J.; Raghavachari, K.; Rendell, A.; Burant, J. C.; Iyengar, S. S.; Tomasi, J.; Cossi, M.; Rega, N.; Millam, J. M.; Klene, M.; Knox, J. E.; Cross, J. B.; Bakken, V.; Adamo, C.; Jaramillo, J.; Gomperts, R.; Stratmann, R. E.; Yazyev, O.; Austin, A. J.; Cammi, R.; Pomelli, C.; Ochterski, J. W.; Martin, R. L.; Morokuma, K.; Zakrzewski, V. G.; Voth, G. A.; Salvador, P.; Dannenberg, J. J.; Dapprich, S.; Daniels, A. D.; Farkas, O.; Foresman, J. B.; Ortiz, J. V.; Cioslowski, J.; Fox, D. J. Gaussian, Inc., Wallingford CT, 2013.
34. MOLPRO, version 2008.1, a package of ab initio programs, Werner, H.-J.; Knowles, P. J.; Lindh, R.; Manby, F. R.; Schütz, M.; Celani, P.; Korona, T.; Mitrushenkov, A.; Rauhut, G.; Adler, T. B.; Amos, R. D.; Bernhardsson, A.; Berning, A.; Cooper, D. L.; Deegan, M. J. O.; Dobbyn, A. J.; Eckert, F.; Goll, E.; Hampel, C.; Hetzer, G.; Hrenar, T.; Knizia, G.; Köppl, C.; Liu, Y.; Lloyd, A. W.; Mata, R. A.; May, A. J.; McNicholas, S. J.; Meyer, W.; Mura, M. E.; Nicklass, A.; Palmieri, P.; Pflüger, K.; Pitzer, R.; Reiher, M.; Schumann, U.; Stoll, H.; Stone, A. J.; Tarroni, R.; Thorsteinsson, T.; Wang, M.; Wolf, A., see <http://www.molpro.net>.
35. Kirkpatrick, L. M.; Vinueza, N. R.; Jankiewicz, B. J.; Gallardo, V. A.; Archibold, E. F.; Nash, J. J.; Kenttämaa, H. I. *Chem. Eur. J.* **2013**, *19* (27), 9022–9033.
36. Kumar, R.; Li, G.; Gallardo, V.A.; Milton, J.; Li, A.; Nash, J.J.; Kenttämaa, H. I. *J. Am. Chem. Soc.* 2020, *142*(19), 8679–8687.
37. NIST Chemistry Webbook, SRD 69 (<https://webbook.nist.gov/chemistry/>).
38. Keesee, R. G.; Castleman, A. W. *J. Phys. Chem. Ref. Data* **1986**, *15*, 1011-1071.

CHAPTER 5. POLAR EFFECTS CONTROL THE REACTIVITY OF THREE BIRADICALS WITH A 1,4-TOPOLOGY

5.1 Introduction

Aromatic carbon-centered σ -type biradicals are reaction intermediates that are involved in various biochemical¹⁻³ and chemical processes.⁴ *para*-Benzynes, in particular, have drawn much attention due to their roles as the biologically active intermediates of some enediyne anticancer drugs.⁵⁻⁹ However, understanding of the fundamental chemical properties of *para*-benzynes and the factors that control their reactivity is limited. Therefore, tandem mass spectrometry has been used in the past to generate such biradicals and related species with a chemically inert charge site for mass spectrometric manipulation.¹⁰⁻¹³ Previously studied *para*-benzynes, including the 2,5-didehydropyridinium^{12,13} cation and the 5,8-didehydroisoquinolinium cation,¹³ showed surprisingly low reactivity. To explore this further, generation of the 5,8-didehydroquinolinium cation from the 5-iodo-8-nitroquinolinium cation precursor in two collision-activated dissociation (CAD) steps was attempted in this study (Scheme 5.1). However, an entirely unexpected isomer was generated. The identity of this isomer, the rearrangement mechanism leading to its formation, and a comparison of its reactivity to that of the 5,8-didehydroquinolinium cation (generated from a different precursor) and the 5,8-didehydroisoquinolinium cation are reported herein.



Scheme 5.1 Attempted generation of the 5,8-didehydroisoquinolinium cation.

5.2 Experimental Section

Materials. The biradical precursors, 5-iodo-8-nitroquinoline, 8-iodo-5-nitroquinoline, 5,8-diiodoquinoline, and 5-iodo-8-nitroisoquinoline, as well as 5-iodoquinoline and 8-iodoquinoline used to generate monoradicals, and the model compound 5,8-dithiomethylquinoline were

synthesized via procedures described in Chapter 3 from 5-aminoquinoline, 8-aminoquinoline, 5-aminoisoquinoline, and 2,5-dibromoaniline respectively.¹⁴⁻¹⁶ The starting materials were purchased from Sigma-Aldrich (St. Louis, MO) and used as received. The reagents dimethyl disulfide, allyl iodide and cyclohexane were also purchased from Sigma-Aldrich and used as received.

Ion-molecule reactions. All the gas-phase reactions were studied in a Thermo LTQ linear quadrupole ion trap mass spectrometer (LQIT-MS) coupled with a home-built reagent mixing manifold for reagent introduction. All biradical precursors were dissolved in methanol, injected into the mass spectrometer, and protonated via atmospheric pressure chemical ionization (APCI). Protonated biradicals were generated either by two consecutive collision-activated dissociation (CAD) events in the ion trap (ITCAD, collision energy ranging from 30 to 50, arbitrary units; the monoradical formed in the first ITCAD event was isolated before activating it in the second ITCAD event) and/or in-source CAD (ISCAD, collision energy 60 V), which resulted in homolytic cleavages of the C-I and C-NO₂ bonds. The protonated biradicals were then isolated and allowed to react with dimethyl disulfide, allyl iodide or cyclohexane in the ion trap for variable reaction times¹³ up to 10,000 ms. The monoradical precursors 5-iodoquinoline and quinoline were dissolved in CS₂ and ionized via APCI to generate their molecular ions. The 5-iodoquinoline molecular ion was subjected to ITCAD to generate the 5-dehydroquinoline radical cation. The reactivities of the radical cations were studied toward dimethyl disulfide, allyl iodide, and cyclohexane as described above.

Pseudo-first order reaction rate plots were used to determine the reaction efficiencies (defined as the fraction of collisions that lead to reaction) given as k_{exp}/k_{coll} , where k_{exp} is the experimentally measured rate constant and k_{coll} is the collision rate constant calculated using a parameterized trajectory theory.¹⁷ Primary products' branching ratios were also determined. Many of the observed ionic reaction products were isolated and subjected to further ITCAD to obtain structural information.

Computational methods. All the quantum chemical calculations were performed by Dr. John J. Nash at Department of Chemistry of Purdue University. Molecular geometries for all species

were optimized at the multiconfigurational self-consistent field (MCSCF) and DFT levels of theory by using the correlation-consistent polarized valence-triple- ζ (cc-pVTZ) basis set¹⁸ or the 6-311G(d,p) basis set.¹⁹ The latter basis set was used for calculations in which the chemical species contained at least one iodine atom. The MCSCF calculations were of the complete active space (CASSCF) variety²⁰ and included (in the active space) the full p space for each molecule and, for each of the mono- and biradicals, the nonbonding s orbital(s). The DFT calculations used 1) the gradient-corrected exchange functional of Becke,²¹ which was combined with the gradient-corrected correlation functional of Lee, Yang, and Parr²² (B3LYP), or 2) the M06-2X functional.²³ All DFT geometries were verified to be local minima by computation of analytical vibrational frequencies, and these (unscaled) frequencies were used to compute zero-point vibrational energies (ZPVE) and 298 K thermal contributions ($H_{298} - E_0$) for all species. DFT calculations for the mono- and biradicals employed an unrestricted formalism.

To improve the molecular orbital calculations, dynamic electron correlation was also accounted for by using multireference second order perturbation theory^{24,25} (CASPT2) for multiconfigurational self-consistent field (MCSCF) reference wave functions; these calculations were carried out for the MCSCF optimized geometries. Some caution must be applied in interpreting the CASPT2 results, since this level of theory is known to suffer from a systematic error proportional to the number of unpaired electrons.²⁶ Thus, the electronic energies are of the CASPT2/CASSCF(m,n)/cc-pVTZ//CASSCF(m,n)/cc-pVTZ variety (where m is the number of active electrons and n the number of active orbitals), and estimates of the thermodynamic quantities E_0 and H_{298} were derived by adding to these electronic energies ZPVE and the sum of ZPVE and ($H_{298} - E_0$), respectively, where the latter are derived from the DFT (B3LYP) calculations.

To compute EA_v values for the mono- and biradicals, single-point calculations (CASPT2/CASSCF(m,n)/cc-pVTZ) on the CASSCF(m,n)/cc-pVTZ optimized geometry for each radical, were also carried out for the states that are produced when a single electron is added to the nonbonding s orbital (or one of the two such orbitals) of each molecule.²⁷ Thus, for the monoradicals, (doublet ground states) these calculations were carried out for (zwitterionic) singlet

states, whereas for the biradicals (singlet ground states) calculations were carried out for (zwitterionic) doublet states.²⁸

All CASPT2/MCSCF and DFT calculations were carried out with the MOLCAS 8.0²⁹ and Gaussian 09³⁰ electronic structure program suites, respectively.

5.3 Results and Discussion

5.3.1 Reactivity of the Biradicals Generated upon Ion Trap Collision-activated Dissociation

The charged biradical generated upon two consecutive ITCAD events [i.e., ion-trap CAD (ITCAD)] from **1** (Scheme 5.1) yielded diagnostic product ions that demonstrated the existence of two radical sites.^{31,32} For example, it reacted with dimethyl disulfide predominantly via abstraction of two SCH₃ groups and an HSCH₃ molecule, which is typical for related biradicals.^{33,34} Similarly, it generated the expected reaction products upon interactions with allyl iodide and cyclohexane. However, it displayed unusually high reactivity toward all the reagents studied compared to the reactivity previously reported for the 5,8-didehydroisoquinolinium cation.¹³ As the previous study used ISCAD instead of ITCAD to generate the 5,8-didehydroisoquinolinium cation, this biradical was regenerated here from the 5-iodo-8-nitroprecursor **4** (Figure 5.1) by using ITCAD to make comparison with the unknown biradical more reliable (**6**; Table 5.1). Indeed, the unknown biradical has reaction efficiencies of 19%, 4% and 8% for dimethyl disulfide, cyclohexane, and allyl iodide, while the 5,8-didehydroisoquinolinium cation (**6**) shows much lower efficiencies (1%, 0.1% and 0.2%, respectively; Table 5.1). This finding suggests that the unknown biradical does not have the expected structure.

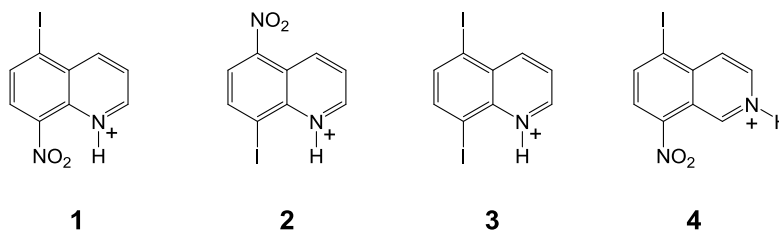


Figure 5.1 Four protonated biradical precursors

In order to explore above issue further, the authentic 5,8-didehydroquinolinium cation was generated from two different precursors, 5-nitro-8-iodo- and 5,8-diiodoquinolinium cations (**2** and **3**, Figure 5.1). Similar reactivity observed for the product ion generated from these two different precursors supports the expectation that authentic 5,8-didehydroquinolinium ion (**5**) had been generated in both cases (Table 5.1). The 5,8-didehydroquinolinium cation showed lower reactivity than the unknown biradical toward dimethyl disulfide (Figure 5.2) but greater reactivity than the 5,8-didehydroisoquinolinium cation (**6**, Table 5.1). These reactivity differences suggest that the unknown biradical does not have the structure **5**.

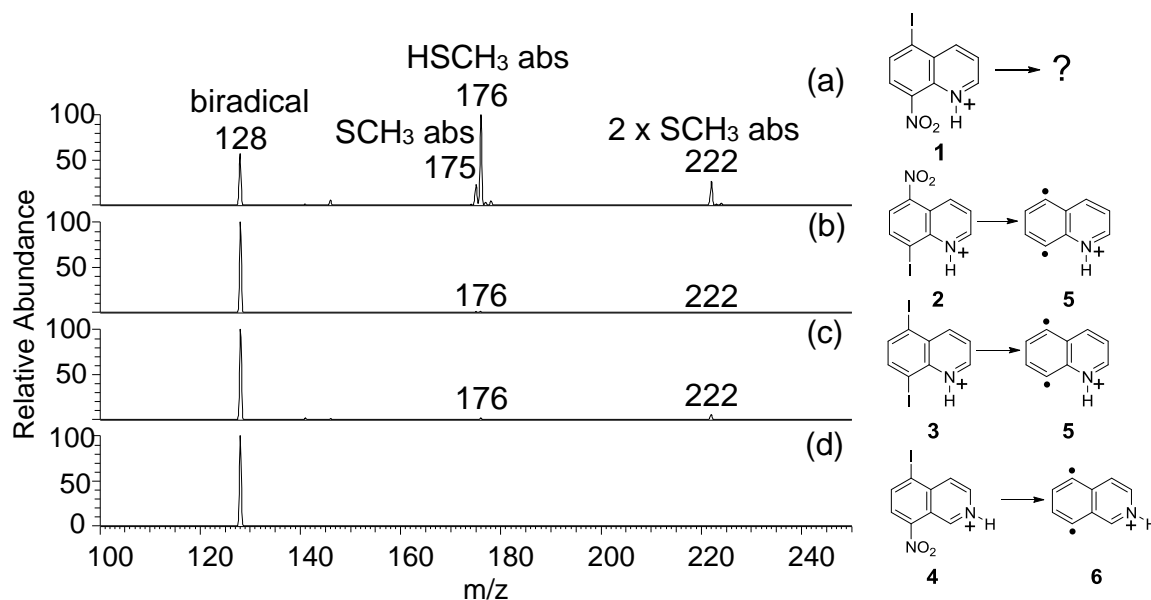


Figure 5.2 Mass spectra measured after 1,000 ms reaction with dimethyl disulfide for the biradicals generated from precursors **1** – **4** (a – d).

Table 5.1 Reactions, their efficiencies and primary product branching ratios for gas-phase reactions of dimethyl disulfide, cyclohexane and allyl iodide with the biradicals generated from **1** – **4** upon ITCAD and their calculated EA_v s and S-T splittings

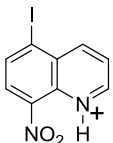
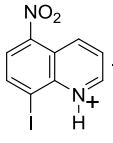
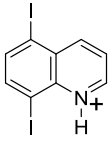
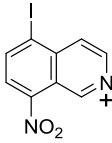
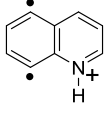
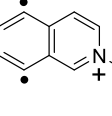
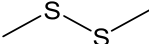
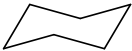
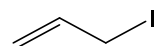
								
	1	2	3	4	5	6		
EA_v (eV) ^a		5.59	5.59	5.32				
S-T splitting (kcal mol ⁻¹) ^b		-3.8	-3.8	-3.7				
	SCH ₃ abs. ^c	68%	SCH ₃ abs.	67%	SCH ₃ abs.	70%	SCH ₃ abs.	58%
	2 °SCH ₃ abs. ^d		2 °SCH ₃ abs.		2 °SCH ₃ abs.		2 °SCH ₃ abs.	
	HSCH ₃ abs.	32%	HSCH ₃ abs.	33%	HSCH ₃ abs.	30%	HSCH ₃ abs.	42%
	17% URI ^e		92% URI		69% URI		70% URI	
	Efficiency = 19%		Efficiency = 4%		Efficiency = 8%		Efficiency = 1%	
	2 × H abs.	60%	2 × H abs.	69%	2 × H abs.	61%	2 × H abs.	55%
	Addition	24%	Addition	21%	Addition	23%	Addition	33%
	H ⁻ abs.	16%	H ⁻ abs.	10%	H ⁻ abs.	16%	H ⁻ abs.	12%
	16% URI		97% URI		47% URI		95% URI	
	Efficiency = 4%		Efficiency = 2%		Efficiency = 1%		Efficiency = 0.1%	

Table 5.1 Continued

Allyl abs.	73%	Allyl abs.	80%	Allyl abs.	81%	Allyl abs.	77%
2 °I abs.		2 °I abs.		2 °I abs.		2 °I abs.	
Allyl-H abs.	26%	Allyl-H abs.	15%	Allyl-H abs.	13%	I abs.	23%
I abs.	1%	I abs.	5%	I abs.	6%	2 °I abs.	
2 °I abs.		2 °I abs.		2 °I abs.			
28% URI		92% URI		93% URI		96% URI	
Efficiency = 8%		Efficiency = 4%		Efficiency = 5%		Efficiency = 0.2%	

^a All EA_{v,s} were calculated at the CASPT2/MCSCF(13,12)/cc-pVTZ//MCSCF(12,12)/cc-pVTZ level of theory. ^b All S-T splittings were calculated at the CASPT2/MCSCF(12,12)/cc-pVTZ//MCSCF(12,12)/cc-pVTZ level of theory. ^c abs. = abstraction. ^d 2 ° indicates a secondary product and it is placed after the primary product that generated it. ^e URI = unreactive isomer.

In order to conclusively demonstrate that the unknown biradical does not have structure **5**, the product formed upon abstraction of two SCH₃ groups from dimethyl disulfide was isolated and subjected to ITCAD. The fragmentation behavior was compared to that of the authentic 5,8-dithiomethylquinolinium ion (*m/z* 222) generated from a synthesized precursor. The fragmentation patterns were found to be distinctly different (Figure 5.3). This finding unambiguously demonstrates that the unknown biradical does not have structure **5**.

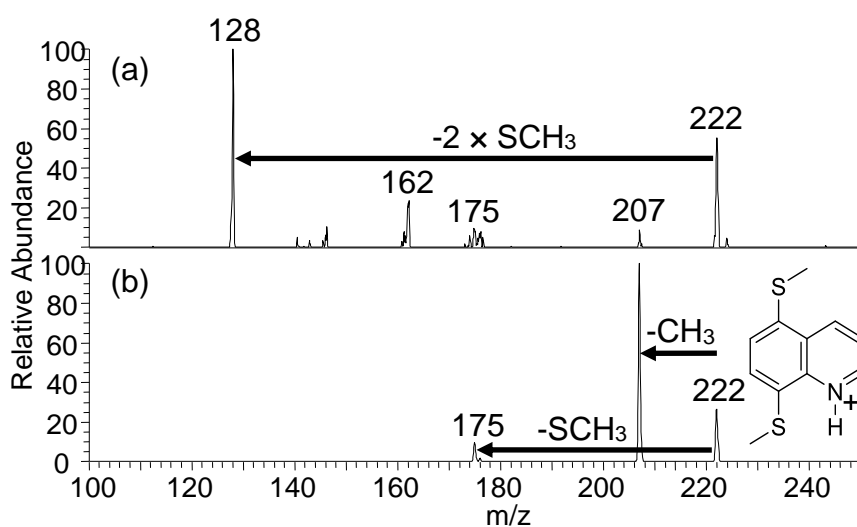


Figure 5.3 ITCAD mass spectra obtained using the same collision energy (20, arbitrary units) for (a) the product ion of *m/z* 222 formed upon abstraction of two SCH₃ groups from dimethyl disulfide by the biradical generated from **1** and (b) the authentic 5,8-dithiomethylquinolinium cation.

5.3.2 Reactivity of Biradicals Generated upon In-source Collision-activated Dissociation

Besides ITCAD, ISCAD was also used to generate the unknown biradical of interest. ISCAD takes place in the medium pressure free-jet expansion region immediately after the MS orifice. In ISCAD, ions are accelerated by an electric field, collide with neutral molecules and fragment.³⁵ This method is more energetic than ITCAD. Indeed, earlier studies on *para*-benzynes and enediynes in the gas phase suggested that ISCAD can be used to homolytically cleave both of the C-I and C-NO₂ bonds nearly simultaneously.³⁶ Therefore, ISCAD was used in this study to test

whether the formation of the highly reactive, unknown biradical requires two steps as in ITCAD or whether it can be generated in one step by using ISCAD. The biradical generated by ISCAD was found to have low reactivity toward dimethyl disulfide, as expected if it had a *para*-benzyne structure (Figure 5.4). Furthermore, its reaction efficiency was similar to that of **5** (7%; 6% measured for the authentic biradical; Table 1). Similar observations were made for cyclohexane and allyl iodide reagents. These findings suggest that the nearly simultaneous cleavage of both C-I and C-NO₂ bonds upon ISCAD of **1** generates the 5,8-didehydroquinolinium cation (**5**) while the two consecutive activation steps utilized in ITCAD yield a rearranged product.

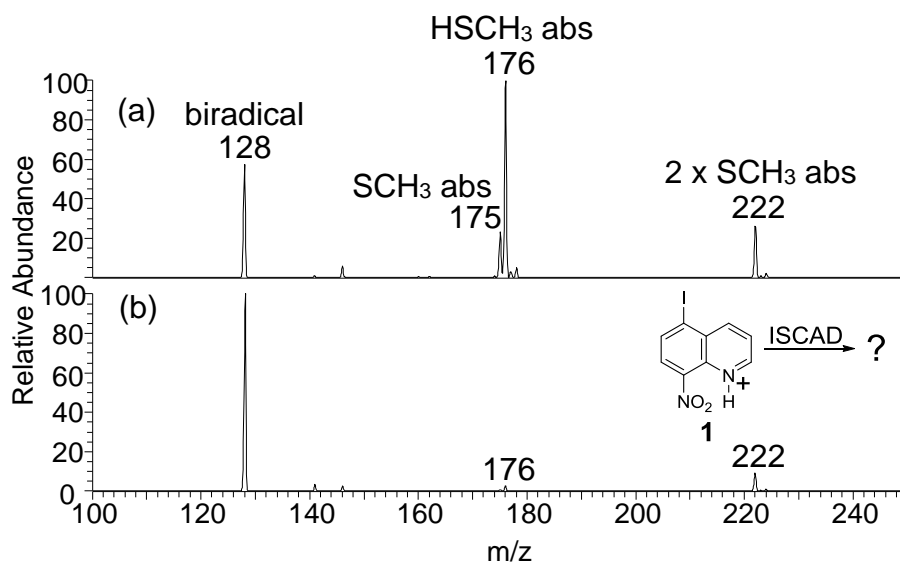


Figure 5.4 Reaction product mass spectra measured for the unknown biradical generated from **1** by using (a) ITCAD and (b) ISCAD after 1,000 ms reaction with dimethyl disulfide.

5.3.3 Structural Elucidation of the Highly Reactive Biradical Generated upon Two Consecutive ITCAD Steps of **1**

The results suggest that the formation of the unknown biradical takes place after the first ITCAD event that generates the 8-dehydro-5-iodoquinolinium cation (**9**) from **1** (Scheme 5.1). To explore whether **9** is the only precursor which generates this reactive biradical, another

monoradical, the 5-dehydro-8-nitroquinolinium cation (**10**) that was also generated upon the first ITCAD event on precursor **1** (Figure 5.5a), was isolated and subjected to a second ITCAD. The reactivity of the biradical generated upon cleavage of the nitro group was found to be substantially lower than that of the unknown biradical generated from **9** (upon elimination of an iodine atom; Figure 5.6), suggesting that it is the 5,8-didehydroquinolinium cation (**5**). Interestingly, when precursor **2** was employed to generate the biradical in yet a different way, by cleavage of a nitro group from 5-nitro-8-dehydroquinolinium cation, no I atom cleavage was observed upon the first ITCAD event on **2** (Figure 5.5b). Therefore, the 5-nitro-8-dehydroquinolinium cation could not be generated.

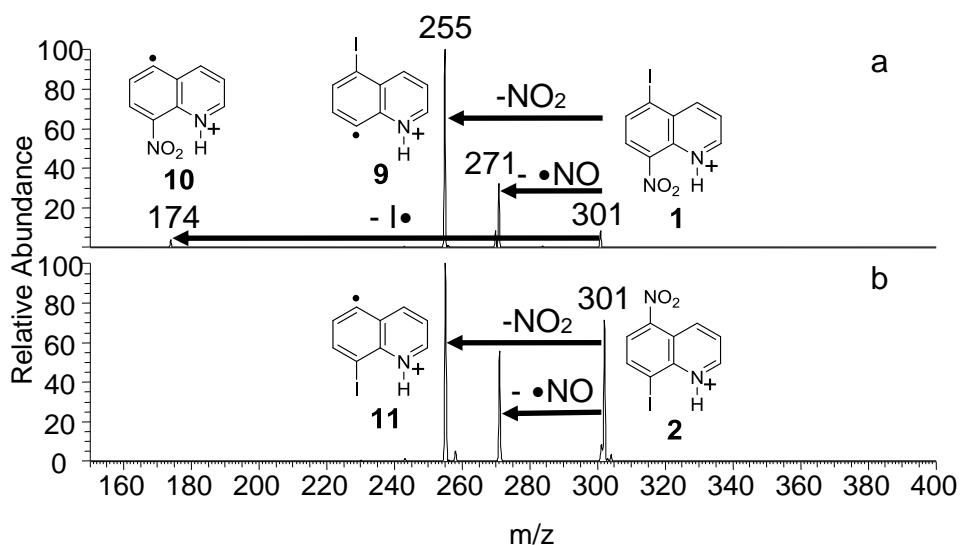


Figure 5.5 ITCAD mass spectra obtained using the same collision energy (40 arbitrary units) for (a) **1** and (b) **2** (ions of m/z 301). **9** has a higher relative abundance than **10** in part a because the C-NO₂ bond is easier to break than the C-I bond in a cation.

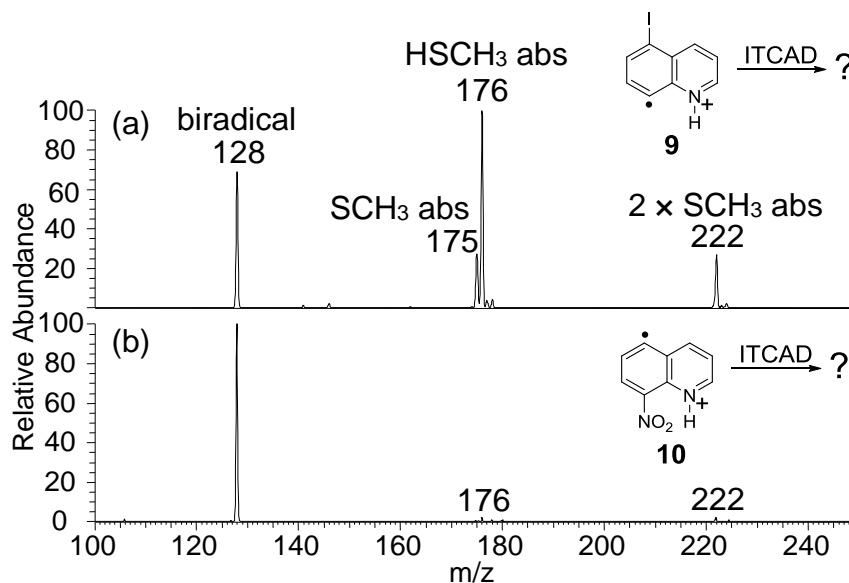
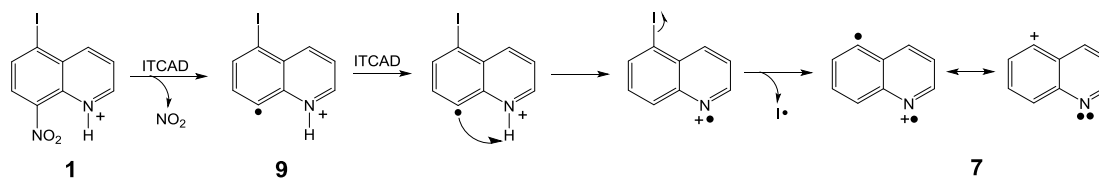


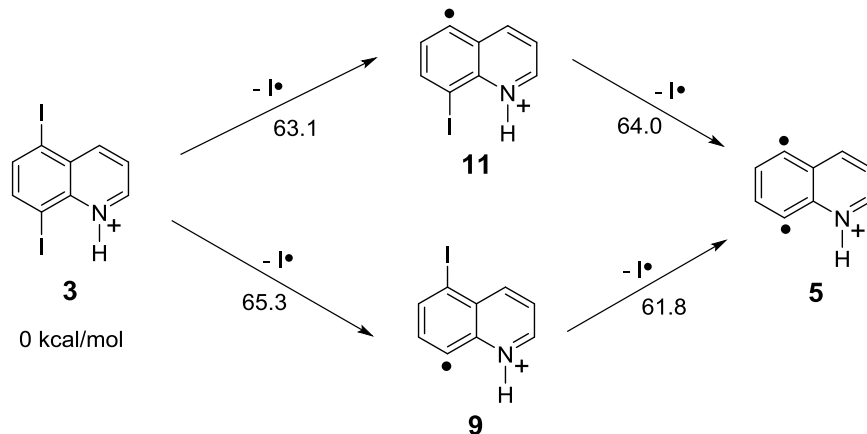
Figure 5.6 The product ion mass spectra measured for (a) the unknown reactive biradical generated from **9** upon ITCAD and (b) the biradical generated from **10** upon ITCAD after reactions with dimethyl disulfide for 1,000 ms.

Based on these findings, monoradical cation **9** is the only precursor for the highly reactive, unknown biradical. This may be rationalized by the vicinity of the radical site on the 8-position and the charge site. The reaction mechanism proposed for the formation of the unknown biradical involves a hydrogen atom shift from the protonated nitrogen atom to the 8-dehydrocarbon atom in **9** to form the 5-iodoquinoline radical cation upon the second ITCAD event (Scheme 5.2). After this rearrangement, the iodine atom is lost to generate biradical **7** (Scheme 5.2).



Scheme 5.2 Proposed mechanism for the formation of **7** from **1** upon ITCAD

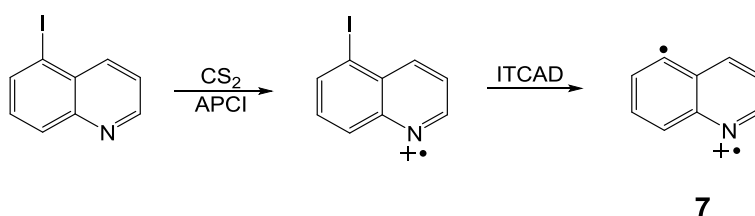
The proposed isomerization pathway was supported by quantum chemical calculations at the M06-2X/6-311G(d,p) level of theory. The activation enthalpy for the rearrangement by hydrogen atom transfer (Scheme 5.2) was calculated to be 54.4 kcal mol⁻¹, 7.4 kcal mol⁻¹ lower than the calculated C-I bond dissociation enthalpy. A similar rearrangement cannot occur for **2** because the iodine atom is not cleaved upon the first ITCAD event (Figure 5.5). On the other hand, the calculated enthalpy changes for homolytic C-I bond cleavages in **3** (Scheme 5.3) suggest that the first bond cleavage occurs at C-5, not at C-8. Therefore, **9** is not generated and rearrangement does not take place.



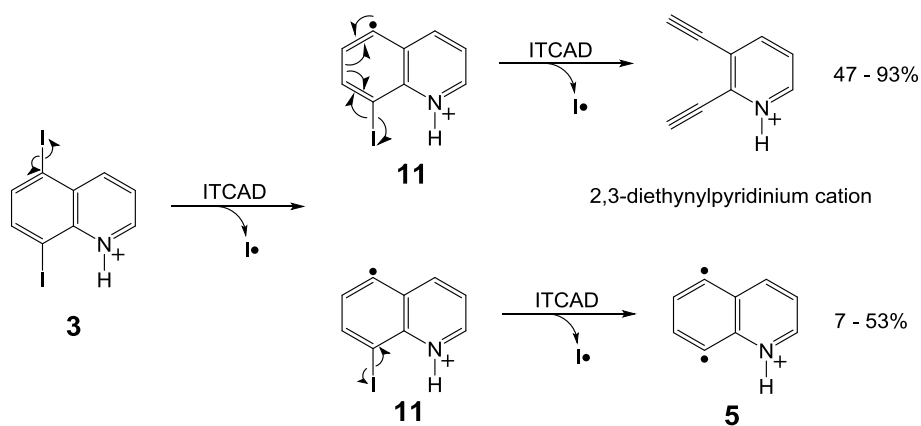
Scheme 5.3 Calculated enthalpy changes for two possible iodine atom loss reactions from **3** to generate **5** (all numbers are in kcal/mol and relative to the protonated radical precursor; M062X-6-311++(d,p) level of theory)

To provide more support for the above reaction mechanism, authentic 5-dehydroquinoline radical cation (**7**) was generated (Scheme 5.4) and its reactivity explored. Comparison of its reactivity to that of the biradical generated from **1** revealed great similarities (Table 5.2). In fact, the only significant difference in reactivity of the unknown biradical and **7** is the observation of 16 – 28% of an unreactive isomer for the former but not for the latter. The unreactive isomer is likely formed on ring opening followed by iodine-atom loss on ITCAD of **9**, as shown in Scheme 5.5 for precursor **11** and previously reported for the isoquinolinium analogue.³⁷ This is not surprising,

since there is only a relatively small energy difference (7.4 kcal mol⁻¹) between the activation enthalpy for rearrangement (Scheme 5.2) and the C-I bond dissociation enthalpy for **9**, and the energy difference between the activation enthalpy for the ring opening and the rearrangement should be even smaller (for the isoquinolinium system, the activation enthalpy for ring opening and the C-I bond dissociation enthalpy have been calculated³⁷ to be 56.8 and 62.2 kcal mol⁻¹, respectively).



Scheme 5.4 Generation of authentic biradical **7**



Scheme 5.5 Two competing reaction pathways after the first ITCAD event of **3**. Top: *retro*-Bergman cyclization; bottom: *para*-benzyne (**5**) formation. The same applies to generation of biradical **6**.

Further, the product ion of m/z 222 formed upon abstraction of two SCH₃ groups from dimethyl disulfide by **7** was subjected to ITCAD and the fragmentation behavior was compared to that of the ion of m/z 222 generated from the unknown biradical generated from **1**. The

fragmentation patterns are similar enough to conclude that the same ion, biradical **7**, produced both of them. This finding conclusively identifies the unknown biradical as **7**.

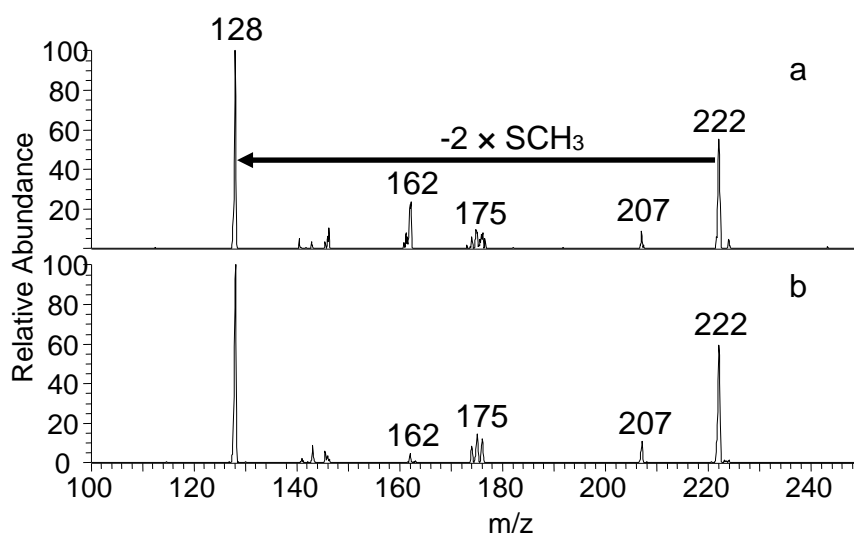
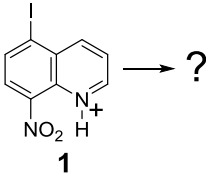
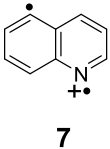
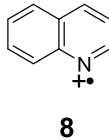
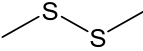
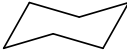
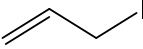


Figure 5.7 ITCAD mass spectra for the product ions of m/z of 222 generated upon abstraction of two SCH_3 groups from dimethyl disulfide by (a) the unknown biradical generated from **1** and (b) biradical **7**.

The reactivity of the quinoline radical cation (**8**) was also studied (Table 5.2). Its reactivity is distinctly different from that of **7**. For example, while **7** predominantly abstracts an allyl group from allyl iodide, **8** predominantly abstracts an iodine atom. This finding, as well as the similarity of the reactivity of **7** to that of the two *para*-benzynes discussed above, suggests that the reactions of **7** are initiated by the 5-radical site rather than the nitrogen-radical cation site.

Table 5.2 Reactions, their efficiencies, and the primary product branching ratios upon reactions with dimethyl disulfide, cyclohexane and allyl iodide for the unknown biradical generated from **1** and for biradicals **7** and **8**, together with their calculated EA_vs and S-T splittings.

	 1	 7	 8	
EA _v (eV)		7.40 ^a	8.40 ^b	
S-T splitting (kcal mol ⁻¹)		-20.3 ^a	–	
		SCH ₃ abs ^c 68% 2 ^{od} SCH ₃ abs HSCH ₃ abs 32% 17% URI ^e Efficiency = 19%	SCH ₃ abs 66% 2 ^o SCH ₃ abs HSCH ₃ abs 34% Efficiency = 21%	e abs 53% H abs 30% SCH ₃ abs 17% Efficiency = 28%
		2 × H abs 60% Addition 24% H ⁻ abs 16% 16% URI Efficiency = 4%	2 × H abs 63% Addition 26% H ⁻ abs 11% Efficiency = 4%	H abs 100% Efficiency = 3%
		Allyl abs 73% 2 ^o I abs Allyl-H abs 26% I abs 1% 2 ^o I abs 28% URI Efficiency = 8%	Allyl abs 80% 2 ^o I abs Allyl-H abs 19% I abs 1% 2 ^o I abs Efficiency = 7%	I abs 97% Allyl abs 3% Efficiency = 19%

^a Calculated at the CASPT2/MCSCF(13,12)/cc-pVTZ//MCSCF(12,12)/cc-pVTZ level of theory. ^b Calculated at the RHF-UCCSD(T)/cc-pVTZ//B3LYP/cc-pVTZ level of theory. ^c abs = abstraction. ^d 2^o indicates a secondary product and it is placed after the primary product that generated it. ^e URI = unreactive isomer

5.3.4 Reactivity-controlling Factors for *para*-Benzynes **5**, **6** and **7**

The different reactivities of **5**, **6** and **7** are next considered. Based on past studies, the extent of spin-spin coupling of the unpaired electrons through bonds or through space is a major factor that controls the reactivity of most singlet biradicals, such as the ones discussed here. This spin-spin coupling is reflected in the biradical's singlet-triplet (S-T) splitting, which is defined as the energy difference between the lowest-energy triplet (excited) electronic state and the singlet (ground) electronic state.^{10,38-40} The greater the (calculated) S-T splitting, the lower the reactivity of the singlet biradical. Another important reactivity-controlling variable is the ability of the biradical to polarize the transition state of its reactions, or polar effects, quantified here using the calculated vertical electron affinity (EA_v) of the radical sites.⁴¹⁻⁴³ The greater the EA_v , the more electrophilic the biradical site, and the more reactive the biradical.¹³

All of the EA_v s and S-T splittings calculated for the biradicals studied here are listed in Tables 5.1 and 5.2. While biradicals **5** and **6** have similar S-T splittings (-3.8 kcal/mol vs. -3.7 kcal/mol), the greater EA_v of **5** (5.59 eV compared to 5.32 eV for **6**) is mainly responsible for the greater reactivity of this biradical. As for biradical **7**, a relatively strong coupling between the odd spins on the nitrogen and the carbon atoms contributes to the large S-T splitting of this biradical (-20.3 eV), which hinders radical reactivity. However, this biradical has a very high EA_v (7.40 eV), which makes it more reactive than the *para*-benzynes **5** and **6**. This is a particularly remarkable example demonstrating that the more important reactivity-controlling factor for biradicals with 1,4-topology is the vertical electron affinity rather than S-T splitting, in agreement with previous studies.¹³

5.4 Conclusions

An unexpected, highly reactive biradical, the 5-dehydroquinoline radical cation, was generated in the gas phase via hydrogen atom transfer in the 8-dehydro-5-iodoquinolinium cation

upon ITCAD followed by a cleavage of the iodine atom in a linear quadrupole ion trap mass spectrometer. The hydrogen atom transfer was found to have a lower transition state energy than the energy required for the homolytic bond dissociation of the iodine atom, which explains the formation of the 5-dehydroquinoline radical cation instead of the 5,8-didehydroquinolinium cation. The 5-dehydroquinoline radical cation showed greater reactivity toward the organic reagents studied than two isomeric *para*-benzynes, the 5,8-didehydroquinolinium and 5,8-didehydroisoquinolinium cations, of which the quinoline-based *para*-benzyne is more reactive. This reactivity ordering is rationalized solely by the vertical electron affinities of the radical sites in these biradicals (EA_v ; 7.40 eV, 5.59, and 5.32 eV, respectively). This finding supports the previous proposal that polar effects predominantly control the reactivities of biradicals with the 1,4-topology,¹³ even when they have substantially different singlet-triplet splittings (-20.3 eV vs. -3.7 and -3.8 kcal mol⁻¹).

5.5 References

1. Wenk, H. H.; Winkler, M.; Sander, W. *Angew. Chem. Int. Ed.* **2003**, *42* (5), 502–528.
2. Biggins, J. B.; Prudent, J. R.; Marshall, D. J.; Ruppen, M.; Thorson, J. S. *Proc. Natl. Acad. Sci.* **2000**, *97* (25), 13537–13542.
3. Plourde, II, G.; El-Shafey, A.; Fouad, F. S.; Purohit, A. S.; Jones, G. B. *Bioorg. Med. Chem. Lett.* **2002**, *12* (20), 2985–2988.
4. Jones, G. B.; Wright, J. M.; Plourde, G.; Purohit, A. D.; Wyatt, J. K.; Hynd, G.; Fouad, F. *J. Am. Chem. Soc.* **2000**, *122* (40), 9872–9873.
5. Nicolaou, K. C.; Dai, W.-M. *Angew. Chem. Int. Ed. Engl.* **1991**, *30* (11), 1387–1416.
6. Nicolaou, K. C.; Smith, A. L. *Acc. Chem. Res.* **1992**, *25* (11), 497–503.
7. Gredičak, M.; Jerić, I. *Acta Pharm.* **2007**, *57* (2).
8. Pratviel, G.; Bernadou, J.; Meunier, B. *Angew. Chem. Int. Ed. Engl.* **1995**, *34* (7), 746–769.
9. Thoen, K. K.; Kentt ämaa, H. I. *J. Am. Chem. Soc.* **1997**, *119* (16), 3832–3833.

10. Williams, P. E.; Jankiewicz, B. J.; Yang, L.; Kenttämaa, H. I. *Chem. Rev.* **2013**, *113* (9), 6949–6985.
11. Gao, J.; Jankiewicz, B. J.; Reece, J.; Sheng, H.; Cramer, C. J.; Nash, J. J.; Kenttämaa, H. I. *Chem Sci* **2014**, *5* (6), 2205–2215.
12. Hoffner, J.; Schottelius, M. J.; Feichtinger, D.; Chen, P. *J. Am. Chem. Soc.* **1998**, *120* (2), 376–385.
13. (a) Sheng, H.; Ma, X.; Lei, H.-R.; Milton, J.; Tang, W.; Jin, C.; Gao, J.; Wittrig, A. M.; Archibold, E. F.; Nash, J. J.; Kenttämaa, H. I. *ChemPhysChem* **2018**, *19* (21), 2839–2842.
(b) Wittrig, A. M.; Archibold, E. F.; Sheng, H.; Nash, J. J.; Kenttämaa, H. I. *Int. J. Mass Spectrom.* **2015**, *377*, 39–43.
14. Son, J.-H.; Pudenz, M. A.; Hoefelmeyer, J. D. *Dalton Trans.* **2010**, *39* (45), 11081.
15. Palmer, M. H. *J. Chem. Soc.* **1962**, *0*, 3645–3652.
16. Maślankiewicz, A.; Marciniec, K.; Pawlowski, M.; Zajdel, P. *Heterocycles* **2007**, *71* (9), 1975.
17. Su, T.; Chesnavich, W. J. *J. Chem. Phys.* **1982**, *76* (10), 5183–5185.
18. T. H. Dunning, *J. Chem. Phys.* **1989**, *90*, 1007–1023.
19. a) R. Krishnan, J. S. Binkley, R. Seeger, J. A. Pople, *J. Chem. Phys.* **1980**, *72*, 650–654; b) M. N. Glukhovstev, A. Pross, M. P. McGrath, L. Radom, *J. Chem. Phys.* **1995**, *103*, 1878–1885.
20. B. O. Roos, P. R. Taylor, P. E. M. Siegbahn, *Chem. Phys.* **1980**, *48*, 157–173.
21. A. D. Becke, *Phys. Rev. A* **1988**, *38*, 3098–3100.
22. C. T. Lee, W. T. Yang, R. G. Parr, *Phys. Rev. B* **1988**, *37*, 785–789.
23. Y. Zhao, D. G. Truhlar, *Theor. Chem. Acc.* **2008**, *120*, 215–241.
24. K. Andersson, P.-a. Malmqvist, B. O. Roos, A. J. Sadlej, K. Wolinski, *J. Phys. Chem.* **1990**, *94*, 5483–5488.
25. K. Andersson, *Theor. Chim. Acta* **1995**, *91*, 31–46.
26. K. Andersson, B. O. Roos, *Int. J. Quantum Chem.* **1993**, *45*, 591–607.

27. Note that, for these calculations, we are computing the electron affinity of the radical site not the electron affinity of the molecule.
28. Because the mono- and biradicals studied here have a formal positive charge on the nitrogen atom, the state that is produced when an electron is added to the nonbonding orbital of any one of these species is formally zwitterionic, and biradicals studied here have a formal positive charge on the nitrogen atom, that is, they contain localized positive (p) and negative (s) charges.
29. a) MOLCAS 7.4: F. Aquilante, L. De Vico, N. Ferré, G. Ghigo, P.-Å. Malmqvist, P. Neogrady, T. B. Pedersen, M. Pitonak, M. Reiher, B. O. Roos, L. Serrano-Andrés, M. Urban, V. Veryazov, R. Lindh, *J. Comput. Chem.* **2010**, *31*, 224–247; b) Code Development : V. Veryazov, P.-O. Widmark, L. Serrano-Andrés, R. Lindh, B. O. Roos, *Int. J. Quantum Chem.* **2004**, *100*, 626–635; c) MOLCAS 7: G. Karlström, R. Lindh, P.-a. Malmqvist, B. O. Roos, U. Ryde, V. Veryazov, P.-O. Widmark, M. Cossi, B. Schimmelpfennig, P. Neogrady, L. Seijo, *Comput. Mater. Sci.* **2003**, *28*, 222–239.
30. Gaussian 09, M. J. Frisch, G. W. Trucks, H. B. Schlegel, G. E. Scuseria, M. A. Robb, J. R. Cheeseman, G. Scalmani, V. Barone, B. Mennucci, G. A. Petersson, H. Nakatsuji, M. Caricato, X. Li, H. P. Hratchian, A. F. Izmaylov, J. Bloino, G. Zheng, J. L. Sonnenberg, M. Hada, M. Ehara, K. Toyota, R. Fukuda, J. Hasegawa, M. Ishida, T. Nakajima, Y. Honda, O. Kitao, H. Nakai, T. Vreven, J. A. Montgomery, Jr., J. E. Peralta, F. Ogliaro, M. Bearpark, J. J. Heyd, E. Brothers, K. N. Kudin, V. N. Staroverov, T. Keith, R. Kobayashi, J. Normand, K. Raghavachari, A. Rendell, J. C. Burant, S. S. Iyengar, J. Tomasi, M. Cossi, N. Rega, J. M. Millam, M. Klene, J. E. Knox, J. B. Cross, V. Bakken, C. Adamo, J. Jaramillo, R. Gomperts, R. E. Stratmann, O. Yazyev, A. J. Austin, R. Cammi, C. Pomelli, J. W. Ochterski, R. L. Martin, K. Morokuma, V. G. Zakrzewski, G. A. Voth, P. Salvador, J. J. Dannenberg, S. Dapprich, A. D. Daniels, O. Farkas, J. B. Foresman, J. V. Ortiz, J. Cioslowski, D. J. Fox, Inc. Gaussian, Wallingford CT, 2013.
31. Jankiewicz, B. J.; Reece, J. N.; Vinueza, N. R.; Nash, J. J.; Kenttämää, H. I. *Angew. Chem. Int. Ed.* **2008**, *47* (51), 9860–9865.
32. Stirk, K. M.; Orlowski, J. C.; Leeck, D. T.; Kenttämää, H. I. *J. Am. Chem. Soc.* **1992**, *114* (22), 8604–8606.
33. Price, J. M.; Kenttämää, H. I. *J. Phys. Chem. A* **2003**, *107* (42), 8985–8995.
34. Jankiewicz, B. J.; Adeuya, A.; Yurkovich, M. J.; Vinueza, N. R.; Gardner, S. J.; Zhou, M.; Nash, J. J.; Kenttämää, H. I. *Angew. Chem. Int. Ed.* **2007**, *46* (48), 9198–9201.

35. Pramanik, B. *Applied Electrospray Mass Spectrometry*; CRC Press: New York, N.Y., 2002.
36. Jankiewicz, B. J.; Vinueza, N. R.; Kirkpatrick, L. M.; Gallardo, V. A.; Li, G.; Nash, J. J.; Kentt ämaa, H. I. *J. Phys. Org. Chem.* **2013**, *26* (9), 707–714.
37. Kirkpatrick, L. M.; Vinueza, N. R.; Jankiewicz, B. J.; Gallardo, V. A.; Archibold, E. F.; Nash, J. J.; Kentt ämaa, H. I. *Chem. - Eur. J.* **2013**, *19* (27), 9022–9033.
38. Schottelius, M. J.; Chen, P. *J. Am. Chem. Soc.* **1996**, *118* (20), 4896–4903.
39. Wenthold, P.; Hu, J.; Squires, R. *J Am Chem Soc* **1996**, *118* (47), 11865–11871.
40. Logan, C. F.; Chen, P. *J. Am. Chem. Soc.* **1996**, *118* (8), 2113–2114.
41. Nash, J. J.; Kentt ämaa, H.; Cramer, C. J. *J Phys Chem A* **2006**, *110*, 10309–10315.
42. Donahue, N. M.; Clarke, J. S.; Anderson, J. G. *J. Phys. Chem. A* **1998**, *102* (22),
43. Clarke, J. S.; Kroll, J. H.; Donahue, N. M.; Anderson, J. G. *J. Phys. Chem. A* **1998**, *102* (48), 9847–9857.

CHAPTER 6. REACTIVITY OF CYANO-SUBSTITUTED PYRIDINIUM-BASED *PARA*-BENZYNES ARE CONTROLLED BY POLAR EFFECTS

6.1 Introduction

para-Benzyne and its analogs have received considerable attention since some *para*-benzyne analogs were reported to act as the biological “warhead” of enediyne natural products (e. g., calicheamicins, esperamicins and dynemicins) that show high antitumor activity.¹⁻⁴ The enediyne unit can undergo Bergman cyclization in vivo to form a highly reactive *para*-benzyne intermediate that can irreversibly cleave double stranded DNA through hydrogen atom abstraction from each DNA strand, ultimately leading to cell apoptosis.¹⁻⁴ Unfortunately, these enediyne natural products are highly toxic and therefore have seen only limited use in cancer treatment.⁵

Better understanding of the fundamental chemical properties of *para*-benzyne analogs may facilitate the design of less toxic synthetic drugs. *para*-Benzyne has been measured to have a singlet-triplet (S-T) splitting of $-3.8 \text{ kcal mol}^{-1}$ and therefore it has a singlet ground state.⁶ The low reactivity of two *para*-benzynes compared to related monoradicals in solution has been suggested to be a result of stabilizing coupling between the two unpaired electrons.⁷ It has been proposed that the two radical sites must partially uncouple in the transition states of radical reactions, which increases the transition state energy.⁸ Accordingly, the larger the magnitude of the S-T splitting, the lower is the reactivity expected to be.^{7,8}

Attaching a charged moiety to a reaction intermediate of interest (the “distonic ion approach”⁹⁻¹³) has been successfully utilized to characterize the gas-phase reactivity of several *meta*-benzynes in mass spectrometers. In a recent study,¹⁴ two *para*-benzyne analogs with different skeletons, the 5,8-didehydroisoquinolinium cation and the 2,5-didehydropyridinium cation (**1**, Figure 6.1), were successfully generated in a dual-linear quadrupole ion trap mass spectrometer¹⁵ and their gas-phase reactivity toward several reagents was studied. The more polar biradical **1** (with the greater calculated vertical electron affinity (EA_v) of the radical sites; 6.76 vs. 5.32 eV, calculated at the RHF/CCD(T)/cc-pVTZ//UB3LYP/cc-pVTZ level of theory) was found to be more reactive, in spite of its greater S-T splitting (-4.6 vs. $-3.7 \text{ kcal mol}^{-1}$, same level of theory).

This preliminary result suggests that EA_v is an important reactivity-controlling parameter for polar *para*-benzynes. In order to further explore this issue, we have studied the gas-phase reactivity of three isomeric *para*-benzyne analogs with the pyridinium skeleton; namely, the three cyano-substituted 2,4-didehydropyridinium cations **2** – **4** (Figure 6.1), and compared their reactivity to that of their unsubstituted analog (**1**, Figure 6.1).

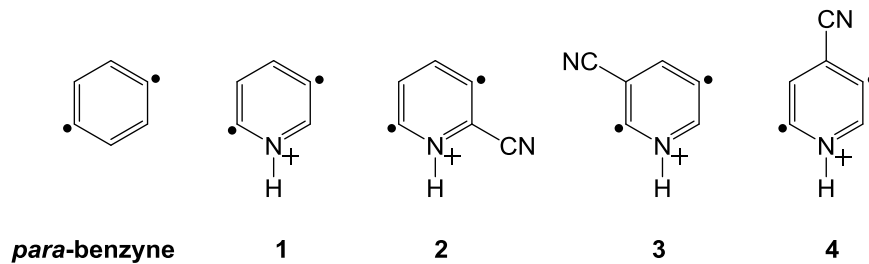


Figure 6.1 *para*-Benzyne analogs studied

This research was helped by several other group members from Kenttämä research group. In addition to Xin Ma's contributions to the synthesis of the precursors and measurements of the reaction efficiencies for the radicals, Dr. Huaming Sheng measured some of the reactivity of the studied *para*-benzynes and carried out some synthesis of the radical precursors. He was also leading the manuscript writing. Hao-Ran Lei helped with the synthesis of radical precursors. This work was also supported by Dr. Weijuan Tang, Dr. Chunfen Jin, and Dr. John J. Nash.

6.2 Experimental Section

Materials. 2,5-Diiodopyridine, all monoradical precursors, cyclohexane and dimethyl disulfide were purchased from Sigma Aldrich (St Louis, MO) and used as received. Two of the cyano-substituted biradical precursors, 2-cyano-3,6-diiodopyridine and 4-cyano-2,5-diiodopyridine were synthesized followed by the steps described in Chapter 3. 3-Cyano-2,5-diiodopyridine was synthesized by Hao-Ran Lei from Kenttämä research group at Purdue University.

Ion-molecule reactions. All gas-phase reactions were carried out in a differentially pumped dual-LQIT tandem mass spectrometer¹⁵ (DLQIT) equipped with a manifold for reagent

introduction designed based on a previously described apparatus.¹⁶ This instrument consists of two differentially pumped Thermo Scientific linear quadrupole ion trap (LQIT) systems that have been connected via an ion transfer octupole encased in a machined manifold. Radical and biradical precursors were introduced into the mass spectrometer and ionized by protonation via atmospheric pressure chemical ionization (APCI). The radical sites were generated by homolytic cleavage of carbon-iodine bonds induced through insource collision-activated dissociation with nitrogen collision gas. The (bi)radicals were transferred into the first linear quadrupole ion trap and allowed to react with each reagent for varying periods of time to determine reaction products and efficiencies. The efficiency of each reaction ($k_{exp}/k_{coll} \times 100 \%$, where k_{exp} is the experimental rate constant determined from a rate plot and k_{coll} is the collision rate constant calculated based on a parameterized trajectory theory¹⁷) corresponds to the fraction of the collisions of the ion and neutral molecule that lead to a reaction. The product branching ratios were determined for only primary products at short reaction times when secondary reactions did not yet take place. Secondary products were confirmed by re-isolating primary products and allowing them to undergo further reactions with the reagent of interest. The measurements were carried out by Xin Ma and Dr. Huaming Sheng.

Computational methods. All the quantum chemical calculations were carried out by Dr John J. Nash at Purdue University. Molecular geometries for all molecules were optimized at the multiconfigurational self-consistent field (MCSCF) and density functional (DFT) levels of theory by using the correlation-consistent polarized valence-triple- ζ (cc-pVTZ) basis set.¹⁸ The MCSCF calculations were of the complete active space (CASSCF) variety¹⁹ and included (in the active space) the full π -space for each molecule and, for each of the mono- and biradicals, the nonbonding σ orbital(s). The DFT calculations used the gradient-corrected exchange functional of Becke, which was combined with the gradient-corrected correlation functional of Lee, Yang and Parr²⁰ (B3LYP). All DFT geometries were verified to be local minima by the computation of analytic vibrational frequencies, and these (unscaled) frequencies were used to compute zero-point vibrational energies (ZPVE) and 298 K thermal contributions ($H_{298} - E_0$) for all species. DFT calculations for the mono- and biradicals employed an unrestricted formalism. To improve the molecular orbital calculations, dynamic electron correlation was also accounted for by using multi-reference second-order perturbation theory^{21,22} (CASPT2) for multi-configurational self-consistent

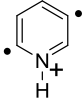
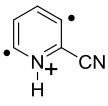
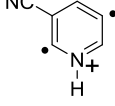
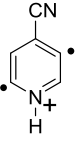
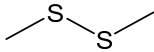
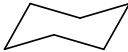
field (MCSCF) reference wave functions; these calculations were carried out for the MCSCF optimized geometries. Some caution must be applied in interpreting the CASPT2 results since this level of theory is known to suffer from a systematic error proportional to the number of unpaired electrons.²³ Thus, the electronic energies are of the CASPT2/CASSCF(m,n)/cc-pVTZ//CASSCF(m,n)/cc-pVTZ variety (where m is the number of active electrons and n is the number of active orbitals), and estimates of the thermodynamic quantities, E_0 and H_{298} , are derived by adding to these electronic energies ZPVE and the sum of ZPVE and $(H_{298} - E_0)$, respectively, where the latter are derived from the DFT calculations. In order to compute vertical electron affinities (EA_v) for the mono- and biradicals, single-point calculations (CASPT2/CASSCF(m,n)/cc-pVTZ), using the CASSCF(m,n)/cc-pVTZ optimized geometry for each radical, were also carried out for the states that are produced when a single electron is added to the nonbonding σ orbital (or one of the two such orbitals) of each molecule.²⁴ Thus, for the monoradicals (doublet ground states), these calculations were carried out for (zwitterionic) singlet states, whereas for the biradicals (singlet ground states), calculations were carried out for (zwitterionic) doublet states.²⁵ Proton affinities (PA) for the biradicals were also computed at the CASPT2/CASSCF(m,n)/cc-pVTZ//CASSCF(m,n)/cc-pVTZ level of theory by using an isodesmic reaction involving proton transfer from the protonated biradical to pyridine to form the pyridinium cation and the neutral (uncharged) biradical. For each biradical, the computed 298 K reaction enthalpy was added to the experimentally determined PA for pyridine ($222 \text{ kcal mol}^{-1}$) to derive the PA of the conjugate base for the biradical. All CASPT2/MCSCF and DFT calculations were carried out with the MOLCAS 8.0²⁶ and Gaussian 09²⁷ electronic structure program suites, respectively.

6.3 Results and Discussion

The reactivity results obtained for **1** – **4** upon interactions with cyclohexane and dimethyl disulfide are shown in Table 6.1. To better understand the observations made for these *para*-benzyne analogs, their reactivities are compared to those of related 2-dehydropyridinium cations with no cyano group (**11**) or a cyano-group at the 2-, 3- or 6-position (**5**, **7** and **9**) and related 3-dehydropyridinium cations with no cyano-group (**12**) or a cyano-group at the 1-, 4- or 5-position (**6**, **8** and **10**; Table 6.2). All monoradicals exclusively abstract a hydrogen atom from cyclohexane and a SCH_3 group from dimethyl disulfide, as expected.²⁸ The monoradicals with the radical site

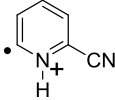
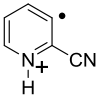
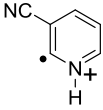
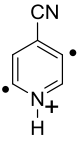
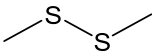
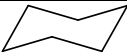
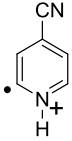
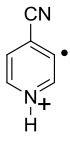
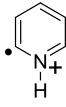
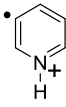
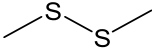
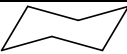
at the 2 position (C-2) are more reactive than those with the radical site at the 3-position (cyclohexane: 46 – 89% vs. 20 – 50%; dimethyl disulfide: 90 – 100% vs. 83 – 90%, respectively; Table 6.2). This can be explained by the differences in their electrophilicities, quantified here by their (calculated) EA_v values of the radical sites. The greater the EA_v , the more polar the transition state, and the lower its energy.¹⁷ Previous calculations suggest that the EA_v of analogous monoradicals with the radical site at the 2-position is larger than for radicals with the radical site at the 3-position,²⁹ thus leading to greater reactivity.¹⁴ The cyano-substituent increases the reactivity of all these radicals when compared to their unsubstituted counterparts by increasing their EA_v (Table 6.2).

Table 6.1 Reaction efficiencies^a and product branching ratios for reactions of biradicals **1** – **4**^b with dimethyl disulfide and cyclohexane, and their calculated^c vertical electron affinities (EA_v) and S-T splittings (ΔE_{S-T}), as well as the proton affinities (PA) of their conjugate bases.

								
	1	2	3	4				
EA _v (eV)	6.65	7.25	7.39	7.26				
ΔE _{S-T} (kcal mol ⁻¹)	-5.3	-4.8	-4.5	-4.2				
PA (kcal mol ⁻¹)	198.9	185.6	185.5	187.3				
 PA ^d = 194.9 kcal mol ⁻¹	SCH ₃ abs ^e	40%	H ⁺ trn	96%	H ⁺ trn	62%	SCH ₃ abs	47%
	2 ^o f SCH ₃ abs		2 ^o add.–CH ₃ SH		2 ^o add.–CH ₃ SH		2 ^o SCH ₃ abs	
	HSCH ₃ abs	34%	SCH ₃ abs	2%	SCH ₃ abs	33%	H ⁺ trn	43%
	e abs	14%	2 ^o SCH ₃ abs		2 ^o SCH ₃ abs		2 ^o add.–CH ₃ SH	
	SCH ₂ abs	7%	HSCH ₃ abs	1%	HSCH ₃ abs	2%	SSCH ₃ abs	5%
	SSCH ₃ abs	5%	e abs	1%	SSCH ₃ abs	2%	HSCH ₃ abs	4%
	2 ^o SCH ₃ abs		SSCH ₃ abs	trace	e abs	1%	e abs	1%
	Efficiency = 0.8%		2 ^o SCH ₃ abs		2 ^o SCH ₃ abs		2 ^o SCH ₃ abs	
		Efficiency = 55%		Efficiency = 55%		Efficiency = 41%		
 PA ^d = 164.2 kcal mol ⁻¹	H abs, e trn ^g	52%	H abs, e trn	46%	H abs, e trn	48%	2 × H abs	66%
	2 × H abs	47%	2 × H abs	45%	2 × H abs	42%	H abs, e trn	18%
	H abs, add. ^h	1%	H abs, add.	9%	H abs, add.	10%	H abs, add.	16%
	Efficiency = 0.1%		Efficiency = 2%		Efficiency = 1%		Efficiency = 1%	

^a Reaction efficiency (% of collisions leading to reaction) = $k_{\text{reaction}}/k_{\text{collision}} \times 100$; precision ± 10 %; accuracy ± 50 % . ^b Experimental data for **1** taken from ref. 14. ^c All values calculated at the CASPT2/CASSCF(m,n)/cc-pVTZ//CASSCF(m,n)/cc-pVTZ level of theory. Singlet–triplet splittings and proton affinities corrected to 298 K by using the (unscaled) UB3LYP/cc-pVTZ frequencies. Proton affinities calculated by using an isodesmic reaction involving proton transfer to pyridine. ^d Experimental value from ref. 19. ^e abs = abstraction. ^f Secondary products are listed below the primary product that produced them and indicated by 2^o. ^g trn = transfer. ^h add. = addition.

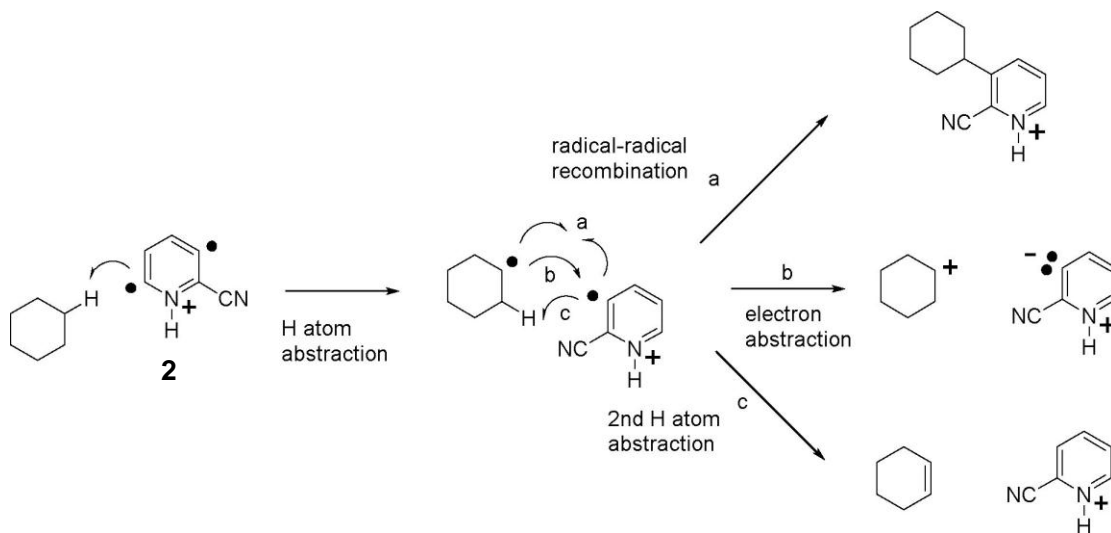
Table 6.2 Reaction efficiencies^a and product branching ratios for reactions of monoradicals **5** – **12**^b with dimethyl disulfide and cyclohexane and their calculated^c vertical electron affinities (EA_v).

				
	5	6	7	8
EA _v (eV)	7.18	6.73	7.33	6.64
	SCH ₃ abs ^d 100% Efficiency = 100%	SCH ₃ abs 100% Efficiency = 90%	SCH ₃ abs 100% Efficiency = 95%	SCH ₃ abs 100% Efficiency = 88%
	H abs 100% Efficiency = 89%	H abs 100% Efficiency = 50%	H abs 100% Efficiency = 77%	H abs 100% Efficiency = 45%
				
	9	10	11	12
EA _v (eV)	7.19	6.75	6.59	6.03
	SCH ₃ abs ^e 100% Efficiency = 93%	SCH ₃ abs 100% Efficiency = 86%	SCH ₃ abs 95% e abs 2% H abs 2% SSCH ₃ abs 1% Efficiency = 90%	SCH ₃ abs 98% H abs 2% Efficiency = 83%
	H abs 100% Efficiency = 67%	H abs 100% Efficiency = 43%	H abs 100% Efficiency = 46%	H abs 100% Efficiency = 20%

^a Reaction efficiency (% of collisions leading to reaction) = $k_{\text{reaction}}/k_{\text{collision}} \times 100$; precision $\pm 10\%$; accuracy $\pm 50\%$. ^b Experimental data for **11** and **12** taken from ref. 14. ^c Values calculated at the CASPT2/CASSCF(m,n)/cc-pVTZ//CASSCF(m,n)/cc-pVTZ level of theory. ^d abs. = abstraction.

All cyano-substituted *para*-benzyne analogs are substantially less reactive than the analogous monoradicals. This finding is in agreement with their singlet ground states hindering radical reactivity.^{7,8} The reactivity observed for *para*-benzyne analogs **1** – **4** shows similarities but also differences when compared to the analogous monoradicals. For example, instead of a single hydrogen atom abstraction from cyclohexane, the biradicals abstract two hydrogen atoms from

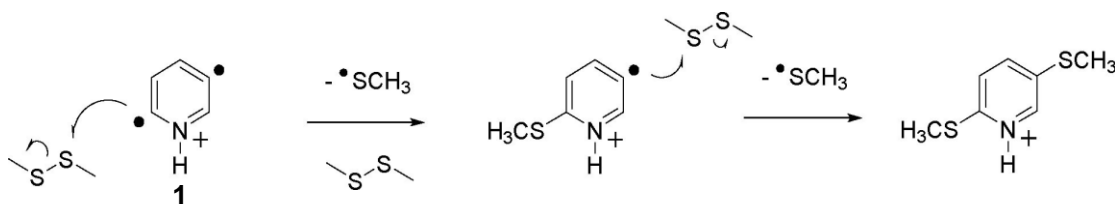
one cyclohexane molecule (Table 6.1). The first hydrogen atom abstraction can also be accompanied by electron transfer (Table 6.1),³⁰ resulting in a product that appears to arise from hydride abstraction. In addition to hydrogen atom abstraction and electron transfer, the first hydrogen atom abstraction can be followed by radical-radical recombination, yielding a stable adduct as the final product. Proposed mechanisms for these reactions are shown in Scheme 6.1. Observation of two hydrogen atom abstractions is consistent with *para*-benzynes containing two radical sites (i. e., they have not undergone *retro*-Bergman ring-opening). This reaction has been calculated (at the RHF-BCCD(T)/cc-pVTZ//UB3LYP/cc-pVTZ level of theory) to be highly exothermic for **1** (-84 kcal mol⁻¹).¹⁴



Scheme 6.1 Proposed mechanisms for two H atom abstractions,¹⁴ H atom abstraction followed by electron transfer,³⁰ and H atom abstraction followed by radical-radical recombination for biradical **2** upon reactions with cyclohexane.

The lowest reactivity was observed for the unsubstituted analog **1**. This biradical has a S-T splitting that is similar to that of the cyano-substituted biradical **2** (-5.3 vs. -4.8 kcal mol⁻¹, respectively; Table 6.1). However, **2** reacts 20 times faster with cyclohexane than **1** (Table 6.1). This finding indicates that the critical rate-controlling parameter here is not the S-T splitting, as has been suggested.^{7,8} On the other hand, the EA_v values of **1** and **2** are significantly different (6.65 eV and 7.25 eV, respectively; Table 6.1). Thus, the greater EA_v likely explains the greater reactivity of **2**. Further support for this hypothesis is provided by the observation of essentially identical reaction efficiencies for **2** – **4** (1–2 %; Table 6.1), all with a similar EA_v. The cyano-

substituted biradicals are also more reactive toward dimethyl disulfide than the unsubstituted biradical (Table 6.1), as expected based on above discussion. Two consecutive abstractions of a SCH₃ group from two dimethyl disulfide molecules were observed for all four biradicals (for likely mechanisms, see Scheme 6.2). The primary abstraction likely occurs at the more reactive radical site (C-2; see discussion above), and the secondary reaction quenches the remaining radical site at C-5. This reaction sequence dominates or is among the two dominant reactions for **1**, **3** and **4** but not for **2** (Table 6.1). The reasons for this behavior are not clear at this time.

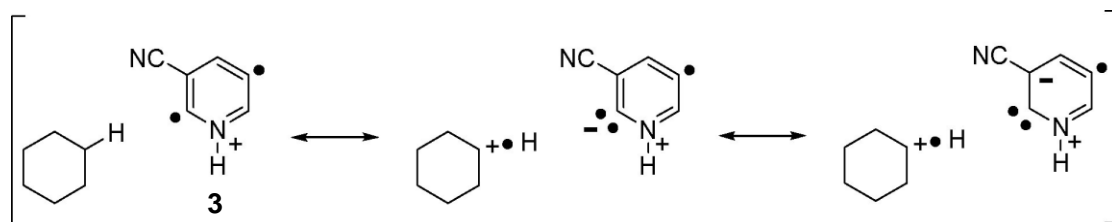


Scheme 6.2 Proposed mechanisms for two SCH₃ abstractions by biradical **1** upon reaction with two dimethyl disulfide molecules.

Large amounts of proton transfer products were observed for the three cyano-substituted biradicals when allowed to react with dimethyl disulfide. This reactivity reflects the low (calculated) proton affinities (PA) of their conjugate bases (<188 kcal mol⁻¹; Table 6.1) relative to that of dimethyl disulfide³¹ (PA = 194.9 kcal mol⁻¹). On the other hand, the unsubstituted biradical **1** shows no proton transfer, as expected, since this reaction would be endothermic (PA(**1**) = 198.9 kcal mol⁻¹; Table 6.1). The same is true for the cyano-substituted monoradicals; for example, the (calculated) PA of the conjugate base of the 3- cyano-2-dehydropyridinium cation is 197.1 kcal mol⁻¹ (same level of theory as described in Table 6.1). Endothermic bimolecular reactions do not generally occur under the conditions employed here. The experimental results demonstrate that exothermic proton transfer can dominate over fast radical reactions for protonated *para*-benzynes, which is not surprising because the proton transfer reactions are likely to be barrierless while the radical reactions are not.

Comparison of the reactivities of the unsubstituted (**1**) and cyano-substituted biradicals (**2** – **4**) toward dimethyl disulfide is complicated by the fact that most of the substituted species undergo predominant proton transfer and not radical reactions. However, biradical **4** shows equally fast SCH₃ group abstraction and proton transfer. Therefore, one may consider approximately half of

the reaction efficiency (41%) to correspond to the radical reaction. This is still about 26 times greater efficiency than that measured for **1**, again supporting the hypothesis that EA_v is the reactivity-controlling factor for these *para*-benzynes.



Scheme 6.3 Proposed zwitterionic resonance structures for the transition state of the H atom abstraction reaction by biradical **3**.

6.4 Conclusions

In conclusion, the reactivity of a *para*-benzyne analog (**1**) and its three cyano-substituted derivatives (**2** – **4**) toward cyclohexane and dimethyl disulfide was studied in a modified dual-linear quadrupole ion trap. The presence of two radical sites in all biradicals was confirmed through observation of two atom or group abstraction reactions. All cyano-substituted biradicals react substantially faster than the unsubstituted analog, which is rationalized by their greater (calculated) EA_v rather than by differences in their S-T splittings. The greater EA_v is likely to lead to a more stable transition state due to stabilization of a dritterionic resonance structure (charge transfer resonance structure; for example, see Scheme 6.3), just like for polar monoradicals.^{29,32}

Fast proton transfer to dimethyl disulfide was observed for the cyano-substituted biradicals, which demonstrates that exothermic proton transfer can compete with fast radical reactions for acidic *para*-benzyne cations. Finally, the reactivity of all the biradicals is substantially lower than that of the related monoradicals. This finding is consistent with the hypothesis that singlet ground states of biradicals hinder radical reactions.^{7,8}

6.5 References

1. Nicolaou, K. C.; Dai, W. M. *Angew. Chem. Int. Ed.* **1991**, *30*, 1387–1416; *Angew. Chem.* **1991**, *103*, 1453–1481.

2. Nicolaou, K. C.; Smith, A. L. *Acc. Chem. Res.* **1992**, *25*, 497–503.
3. Wenk, H. H.; Winkler, M.; Sander, W. *Angew. Chem. Int. Ed.* **2003**, *42*, 502–528.
4. Gredicak, M.; Jeric, I. *Acta Pharm.* **2007**, *57*, 133–150.
5. Liu, W.; Christenson, S. D.; Standage, S.; Shen, B. *Science* **2002**, *297*, 1170–1173.
6. Wenthold, P. G.; Hu, J.; Squires, R. R. *J. Am. Chem. Soc.* **1996**, *118*, 11865–11871.
7. Hoffner, J.; Schottelius, M. J.; Feichtinger, D.; Chen, P. *J. Am. Chem. Soc.* **1998**, *120*, 376–385.
8. Logan, C. F.; Chen, P. J. *J. Am. Chem. Soc.* **1996**, *118*, 2113–2114.
9. Jankiewicz, B. J.; Vinueza, N. R.; Kirkpatrick, L. M.; Gallardo, V. A.; Li, G.; Nash, J. J.; Kenttämaa, H. I. *J. Phys. Org. Chem.* **2013**, *26*, 707–714.
10. Thoen, K. K.; Kenttämaa, H. I. *J. Am. Chem. Soc.* **1997**, *119*, 3832–3833.
11. Price, J. M.; Kenttämaa, H. I. *J. Phys. Chem. A* **2003**, *107*, 8985–8995.
12. Gao, J.; Jankiewicz, B. J.; Reece, J.; Sheng, H.; Cramer, C. J.; Nash, J. J.; Kenttämaa, H. I. *Chem. Sci.* **2014**, *5*, 2205–2215.
13. Kirkpatrick, L. M.; Vinueza, N. R.; Jankiewicz, B. J.; Gallardo, V. A.; Archibold, E. A.; Nash, J. J.; Kenttämaa, H. I. *Chem. Eur. J.* **2013**, *19*, 9022–9033.
14. Wittrig, A. M.; Archibold, E. F.; Sheng, H.; Nash, J. J.; Kenttämaa, H. I. *Int. J. Mass Spectrom.* **2015**, *377*, 39–43.
15. Owen, B. C.; Jarrell, T. M.; Schwartz, J. C.; Oglesbee, R.; Carlsen, M.; Archibold, E. A.; Kenttämaa, H. I. *Anal. Chem.* **2013**, *85*, 11284–11290.
16. Gronert, S. *J. Am. Soc. Mass Spectrom.* **1998**, *9*, 845–848.
17. Su, T.; Chesnavich, W. J. *J. Chem. Phys.* **1982**, *76* (10), 5183–5185.
18. T. H. Dunning, *J. Chem. Phys.* **1989**, *90*, 1007–1023.
19. B. O. Roos, P. R. Taylor, P. E. M. Siegbahn, *Chem. Phys.* **1980**, *48*, 157–173.
20. C. T. Lee, W. T. Yang, R. G. Parr, *Phys. Rev. B* **1988**, *37*, 785–789.
21. K. Andersson, P.-a. Malmqvist, B. O. Roos, A. J. Sadlej, K. Wolinski, *J. Phys. Chem.* **1990**, *94*, 5483–5488.
22. K. Andersson, *Theor. Chim. Acta* **1995**, *91*, 31–46.

23. K. Andersson, B. O. Roos, *Int. J. Quantum Chem.* **1993**, *45*, 591–607.
24. Note that, for these calculations, we are computing the electron affinity of the radical site(s) and not the electron affinity of the molecule.
25. Because the mono- and biradicals studied here have a formal positive charge on the nitrogen atom, the state that is produced when an electron is added to the nonbonding orbital of any one of these species is formally zwitterionic, and biradicals studied here have a formal positive charge on the nitrogen atom, that is, they contain localized positive (p) and negative (s) charges.
26. a) MOLCAS 7.4: F. Aquilante, L. De Vico, N. Ferré, G. Ghigo, P.-Å. Malmqvist, P. Neogrady, T. B. Pedersen, M. Pitonak, M. Reiher, B. O. Roos, L. Serrano-Andrés, M. Urban, V. Veryazov, R. Lindh, *J. Comput. Chem.* **2010**, *31*, 224–247. b) Code Development : V. Veryazov, P.-O. Widmark, L. Serrano-Andrés, R. Lindh, B. O. Roos, *Int. J. Quantum Chem.* **2004**, *100*, 626–635. c) MOLCAS 7: G. Karlström, R. Lindh, P.-a. Malmqvist, B. O. Roos, U. Ryde, V. Veryazov, P.-O. Widmark, M. Cossi, B. Schimmelpfennig, P. Neogrady, L. Seijo, *Comput. Mater. Sci.* **2003**, *28*, 222–239.
27. Gaussian 09, M. J. Frisch, G. W. Trucks, H. B. Schlegel, G. E. Scuseria, M. A. Robb, J. R. Cheeseman, G. Scalmani, V. Barone, B. Mennucci, G. A. Petersson, H. Nakatsuji, M. Caricato, X. Li, H. P. Hratchian, A. F. Izmaylov, J. Bloino, G. Zheng, J. L. Sonnenberg, M. Hada, M. Ehara, K. Toyota, R. Fukuda, J. Hasegawa, M. Ishida, T. Nakajima, Y. Honda, O. Kitao, H. Nakai, T. Vreven, J. A. Montgomery, Jr., J. E. Peralta, F. Ogliaro, M. Bearpark, J. J. Heyd, E. Brothers, K. N. Kudin, V. N. Staroverov, T. Keith, R. Kobayashi, J. Normand, K. Raghavachari, A. Rendell, J. C. Burant, S. S. Iyengar, J. Tomasi, M. Cossi, N. Rega, J. M. Millam, M. Klene, J. E. Knox, J. B. Cross, V. Bakken, C. Adamo, J. Jaramillo, R. Gomperts, R. E. Stratmann, O. Yazyev, A. J. Austin, R. Cammi, C. Pomelli, J. W. Ochterski, R. L. Martin, K. Morokuma, V. G. Zakrzewski, G. A. Voth, P. Salvador, J. J. Dannenberg, S. Dapprich, A. D. Daniels, O. Farkas, J. B. Foresman, J. V. Ortiz, J. Cioslowski, D. J. Fox, Inc. Gaussian, Wallingford CT, 2013.
28. Jankiewicz, B. J.; Reece, J. N.; Vinueza, N. R.; Nash, J. J.; Kenttämä, H. I. *Angew. Chem. Int. Ed.* **2008**, *47*, 9860–9865.
29. Jing, L.; Nash, J. J.; Kenttämä, H. I. *J. Am. Chem. Soc.* **2008**, *130*, 17697–17709.
30. Milton, J. R.; Sheng, H.; Ma, X.; Nash, J. J.; Kenttämä, H. I. Proceedings, 65th Conference on Mass Spectrometry and Allied Topics organized by the American Society for Mass Spectrometry, Indianapolis, IN, June 3–8, 2017.
31. Hunter, E. P.; Lias, S. G.; *J. Phys. Chem. Ref. Data* **1998**, *27*, 413–656.
32. Donahue, N. M.; Clarke, J. S.; Anderson, J. G. *J. Phys. Chem. A* **1998**, *102*, 3923–3933.

CHAPTER 7. GENERATION AND REACTIVITY STUDIES OF QUINOLINE-BASED OXENIUM CATIONS IN A LINEAR QUADRUPOLE ION TRAP MASS SPECTROMETER

7.1 Introduction

Oxenium ions are important reaction intermediates involved in many organic reactions, such as various types of oxidation reactions.¹⁻⁴ They have also been proved to be important intermediates in some biochemical processes.⁵ As ions with a hypovalent oxygen atom and a formal positive charge on the oxygen atom, oxenium ions exhibit interesting reactivity and electronic configurations.⁶⁻¹¹ However, although attempts on generation of some oxenium ions have been made, and experimental investigations have been carried out on some of the generated oxenium ions,⁷⁻¹⁰ the knowledge about them remains limited. Efforts by using high-level computational approaches have also been made for structural characterization and electronic states and energies estimation for several oxenium ions.^{6,11} The difficulty of generating oxenium ions in condensed phase mainly result from the lack of proper precursors and the high reactivity of the ions as strong electrophiles.¹²

Mass spectrometry is a powerful and versatile analytical tool, which allows the generation, observation, and investigation of highly reactive reaction intermediates in the gas phase. For instance, different types of organic mono- and polyradical ions have been successfully studied in a linear quadrupole ion trap (LQIT) mass spectrometer.¹³⁻¹⁵ The radical ions were generated in the ion trap by fragmentation reactions, e.g. collision-activated dissociation (CAD), of the ionized radical precursors; thus, a variety of precursors can be used to generate different types of radical ions. The obtained radical ions can be further trapped and manipulated in the ion trap, which allows the reactivity studies of these ions. Therefore, based on the same considerations, four quinoline-based precursors were chosen to generate four isomeric oxenium ions in the LQIT for the first time (Figure 7.1), and their reactivity toward several organic molecules in the gas phase was studied. To help verify the structures of the generated oxenium ions, quantum chemical calculations were carried out. In addition, the oxenium ions' vertical electron affinities (EA_v) and singlet-triplet splittings (ΔE_{S-T} , defined as the energy difference between the lowest-energy singlet state and the lowest-energy excited triplet state) were also calculated to explain the reactivity of the ions. The

presence of the nitrogen atom in the oxenium ions contributed to some unique reactions of the ions toward some reagents, and also influenced the reactivity of the oxenium ions, as two of the oxenium ions studied can be viewed as a mixture of an oxenium ion and a nitrenium ion.

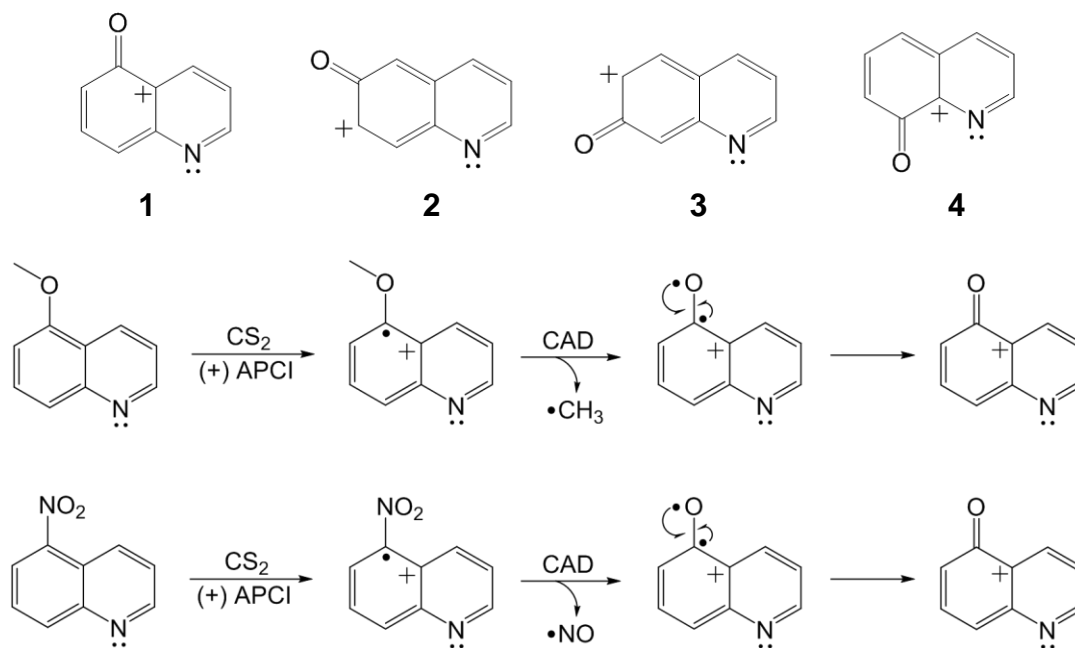


Figure 7.1 Generation of the studied oxenium ions in LQIT and studied oxenium ions

7.2 Experimental Section

Chemicals. All the radical precursors, 5- and 8-nitroquinoline, 6- and 7-methoxyquinoline were purchased from Sigma Aldrich (St Louis, MO) and 1Click Chemistry and used as received. Neutral reagents dimethyl disulfide, allyl iodide, cyclohexane, methanol and acetonitrile were purchased from Sigma Aldrich (St Louis, MO) and used as received. The precursor for the naphthalene-based oxenium ion was synthesized followed by a modified procedure based on procedures as described in literature.⁸ The starting materials for the synthesis were purchased from (St Louis, MO) and used as received.

Ion-molecule reactions. All radical precursors were dissolved in CS_2 and ionized via an atmosphere pressure chemical ionization (APCI) source to generate the molecular ions. The molecular ions were then transferred and trapped in the ion trap of a Thermo LTQ linear quadrupole ion trap (LQIT) mass spectrometer. Upon one collision-activated dissociation (CAD)

step in the ion trap, the oxenium ions were obtained via loss of a NO molecule or a CH₃ radical (Figure 7.1). The neutral reagents were introduced via a homebuilt reagent mixing manifold at a flow rate of 5 μL h⁻¹. The detailed description of the reagent mixing manifold can be found in Chapter 2. Pseudo-first order reaction rate plots were plotted based on the collected reactant ion abundances as a function of time. The reaction efficiency is calculated as the percentage of the collisions that lead to a reaction, and described as %Efficiency = $k_{\text{exp}}/k_{\text{coll}} \times 100$, where k_{exp} is the experimental rate constant calculated using the slope of the rate plot and the reagent concentration, and k_{coll} is the collision rate constant calculated based on a parameterized trajectory theory.¹⁶ Detailed description of the principles of the kinetics studies can be found in Chapter 2. Branching ratios for the primary products were calculated by taking the ratios of the abundances of each primary product and the total abundances of all products at early reaction times.

Computational methods. All the quantum chemical calculations were conducted by Dr. John J. Nash at Department of Chemistry at Purdue University.

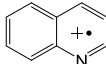
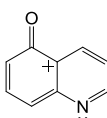
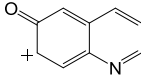
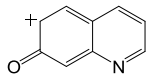
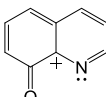
7.3 Results and Discussion

7.3.1 Generation and Structure Characterization of the Oxenium Ions

Ions **1** – **4** (Figure 7.1) generated in the ion trap were proposed to be oxenium ions instead of σ,π -type biradicals, with one radical site localized on nitrogen (σ) whereas the other radical delocalized throughout the π -system, whose orbital is orthogonal to that of the σ -radical. In order to verify the proposed structures, quantum chemical calculations were carried out. To figure out the ground-state spin multiplicities of the ions, relative enthalpies at their closed and open-shell singlet states and two lowest-energy excited triplet states were calculated. As shown in Table 7.1, for all four ions studied, the $1^3A''$ state, one of the triplet states was set to have an enthalpy of 0 kcal mol⁻¹, and the enthalpies of the other states were calculated as relative values to the enthalpy of the $1^3A''$ state. It is obvious that all four biradicals have low-lying singlet ground states ($1^1A'$), and they are all closed-shell singlets, suggesting the two unpaired electrons are not likely to be in two orthogonal orbitals. The vertical electron affinities (EA_v) for each spin state were also calculated and listed in Table 7.1, as EA_v is another important reactivity-controlling factor for radicals and cations.¹⁷ The EA_v of the quinoline radical cation is also listed in the table. Similarly,

a π -electron was abstracted from neutral quinoline molecule while transferring an electron to the CS₂ molecular ion in the APCI source.

Table 7.1 Calculated relative enthalpies (H_{rel} , kcal mol⁻¹) for **1** – **4** at their 1³A^{''}, 1³A['], 1¹A['] and 1¹A^{''} states, and their corresponding vertical electron affinities (EA_v, eV), and the vertical electron affinity for quinoline radical cation

					
	π -radical	1	2	3	4
H_{rel} (1 ³ A ^{''} state) ^a		0.0	0.0	0.0	0.0
H_{rel} (1 ³ A ['] state)		4.6	-3.2	-3.5	7.2
H_{rel} (1 ¹ A ['] state) ^b		-27.5	-29.9	-26.5	-28.0
H_{rel} (2 ¹ A ['] state) ^c		18.4	8.9	9.9	20.7
H_{rel} (1 ¹ A ^{''} state)		0.9	-0.7	3.8	-1.9
EA _v (2 ¹ A ['] state)	8.40	6.82 ^d	7.35 ^e	7.21 ^d	6.88 ^e
EA _v (2 ¹ A ^{''} state)		8.72 ^d	8.78 ^e	8.82 ^d	8.61 ^e
EA _v (2 ¹ A ^{''} state from 1 ¹ A ['])		7.89 ^f	7.87 ^f	7.98 ^f	7.74 ^f

^a Calculated at the CASPT2/CASSCF(12,12)/cc-pVTZ//CASSCF(12,12)/cc-pVTZ level of theory; corrected for zero-point vibrational energies and 298K thermal energies by using the (unscaled) CASSCF(12,12)/cc-pVTZ frequencies. Electron affinity for quinoline radical cation calculated at the CASPT2/CASSCF(12,11)/cc-pVTZ//CASSCF(11,11)/cc-pVTZ level of theory; all other electron affinities calculated at the CASPT2/CASSCF(13,12)/cc-pVTZ//CASSCF(12,12)/cc-pVTZ level of theory. ^bNote that the electron configuration for this state corresponds to an n (where $n = 5, 6, 7, 8$)-oxenium quinoline. ^c Estimated; first A['] excited state; single-point calculation using the 3A['] optimized geometry; zero-point and thermal corrections not applied. ^d For the 1³A^{''} triplet state. ^e For the 1¹A^{''} singlet state. ^f For the 1¹A['] singlet state.

As proposed, **1** – **4** are oxenium ions with several interesting resonance structures (Figure 7.2). Besides oxenium ions, **2** and **4** have a number of carbocation resonance structures, whereas **1** and **3** possess a relatively unstable nitrenium ion resonance structure in addition to all the carbocation resonance structures. In order to further examine the reactivity of **1** – **4**, and to prove that they are indeed oxenium ions instead of biradicals experimentally, the reactions of **1** – **4** with several reagents were studied, including reagents that show diagnostic radical-type reactions¹⁸⁻²⁰ and some nucleophiles.

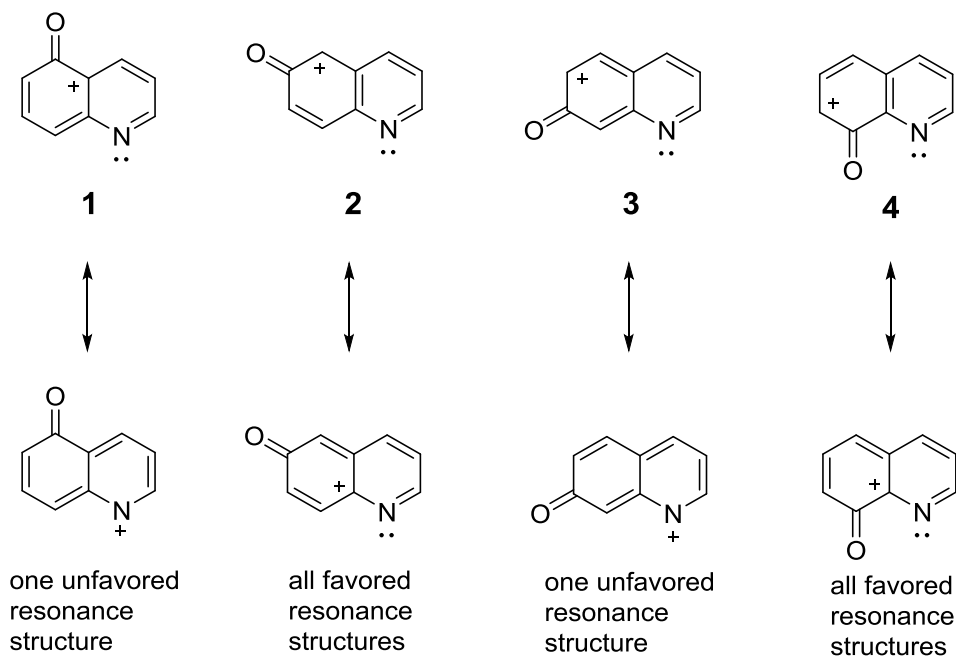


Figure 7.2 Important resonance structures of **1** – **4**

7.3.2 Reactions with Dimethyl Disulfide, Allyl Iodide, and Cyclohexane

The reactions of **1** – **4** with dimethyl disulfide, allyl iodide, and cyclohexane were first studied. The reagents were chosen as the some of the products upon reactions with these reagents are closely related to the number of radical sites in the ions. For instance, abstraction of an SCH_3 radical from dimethyl disulfide, abstraction of an iodine atom from allyl iodide, and abstraction of a hydrogen atom from cyclohexane are diagnostic reactions to “count” the number of radicals in an ion.¹⁸⁻²⁰ As expected, none of the diagnostic reactions were observed for any of the ions **1** – **4**, as shown in Figures 7.3, 7.5, and 7.6. The results again indicated that **1** – **4** are indeed not biradicals.

The products, the reaction efficiencies and primary products' branching ratios for reactions of **1** – **4** with dimethyl disulfide, allyl iodide and cyclohexane are summarized in Table 7.2.

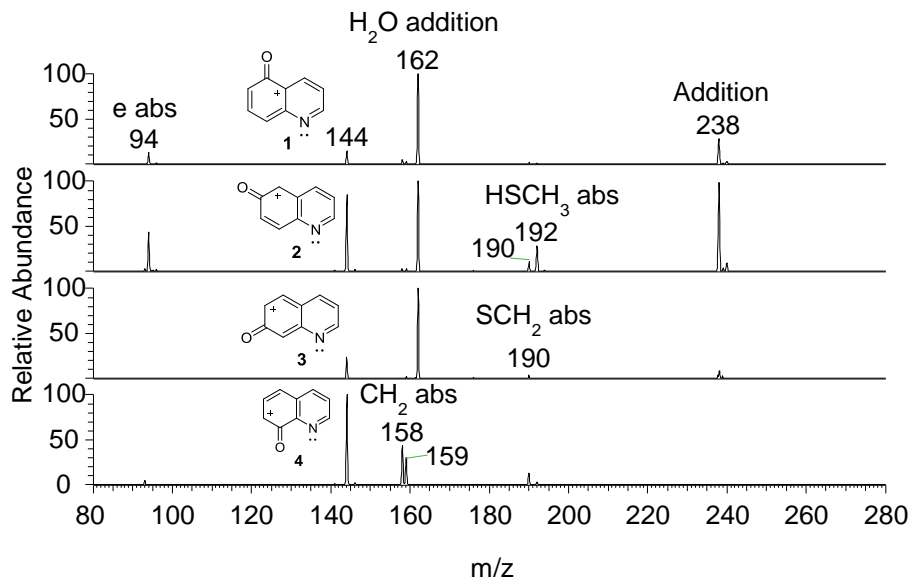


Figure 7.3 Mass spectra measured after 100 ms reactions with dimethyl disulfide for **1** – **4**, the ion of m/z 162 is an adduct formed upon reactions with adventitious water in the ion trap.

For the reactions with dimethyl disulfide (Figure 7.3), an adduct (m/z 238) was observed after short reaction time (< 100 ms). However, even at the shortest reaction time in the the LQIT (0.03 ms), abstraction of one SCH_3 radical was not observed. This suggests the adduct cannot be a secondary product generated upon consecutive abstractions of two SCH_3 radicals from dimethyl disulfide, i.e. it cannot confirm two radical sites are present in the ions. Further collision-activated dissociation (CAD) experiments reinforced the hypothesis. The ion of m/z 238 generated upon reactions of **1** – **3** with dimethyl disulfide were isolated in the ion trap, respectively, and subjected to CAD. As Figure 7.4 illustrates, no fragment ions corresponding to loss of one SCH_3 radical (m/z 191) was observed in the spectrum, unlike the CAD spectrum of the dimethyl disulfide adduct to a biradical cation¹⁵, regardless of the collision energy applied to induce the fragmentation. It apparently illustrates that the addition reaction with dimethyl disulfide is not a radical-type reaction. For reactions with **4**, no adduct was observed, its unique reactivity toward dimethyl disulfide will be discussed later.

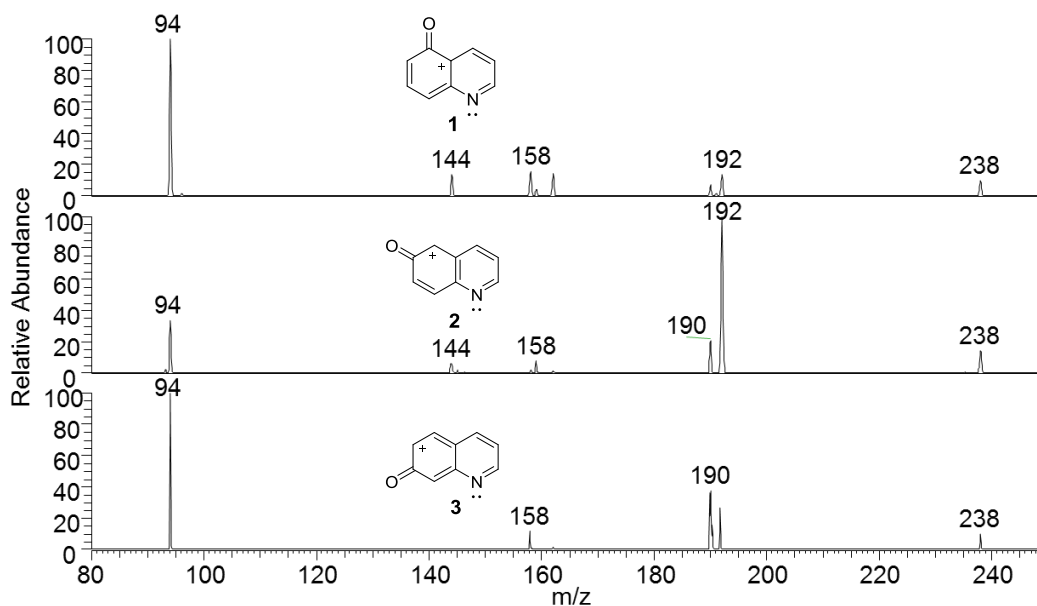
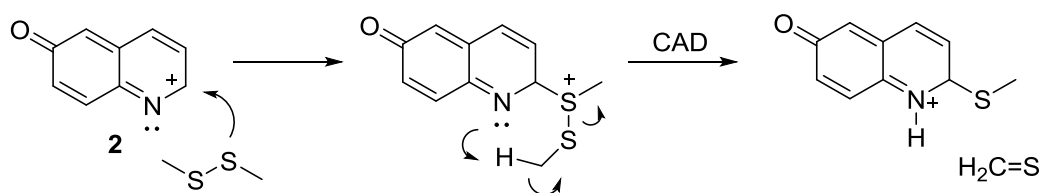


Figure 7.4 CAD mass spectra of the adduct ions (m/z 238) formed upon reactions of **1** – **3** with dimethyl disulfide (collision energy 15, arbitrary unit).

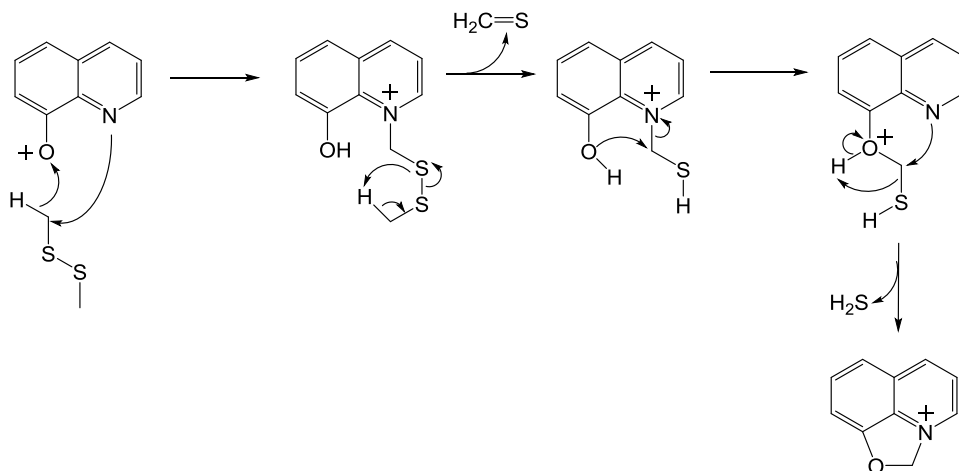
As shown in Figure 7.4, for **1** and **3**, the dominant fragment ion upon CAD of the dimethyl disulfide adduct was the ion of m/z 94, the molecular ion of dimethyl disulfide. Whereas for **2**, the ion of m/z 192 is dominant. This may be due to the participation of the nitrogen atom during the fragmentation reaction. A possible fragmentation mechanism for generation of the ion of m/z 192 is proposed in Scheme 7.1.



Scheme 7.1 Possible addition and fragmentation mechanism for reactions of **2** and dimethyl disulfide

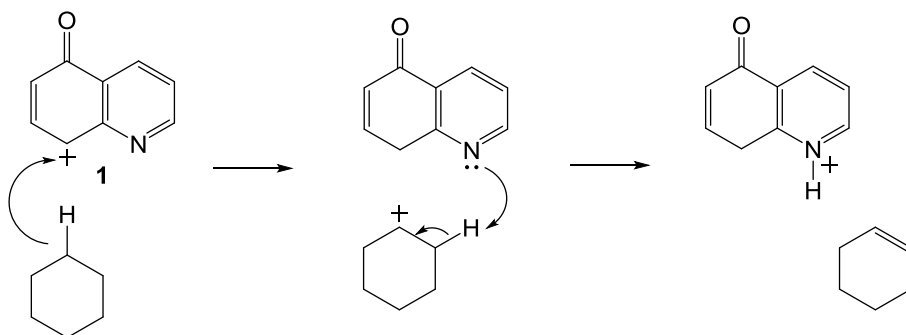
Ion **4** reacted with dimethyl disulfide differently from the other three biradicals. For **4**, abstraction of CH_2 group from dimethyl disulfide was dominant, whereas for **1** – **3**, addition reactions were the predominant reactions with dimethyl disulfide. The proposed reaction mechanism for CH_2 abstraction by **4** is shown in Scheme 7.2. The oxygen atom in **4** is closer to

the nitrogen atom than in **1 – 3** , so that a five-member ring can be formed in the final product. However, it is not possible to form such five-membered ring structures for **1 – 3**.



Scheme 7.2 Proposed mechanism for CH₂ abstraction (*m/z* 158) by **4** from dimethyl disulfide

Similarly, for the reactions with allyl iodide (Figure 7.5), neither abstraction of one iodine atom nor abstraction of two iodine atoms was observed. For the reactions with cyclohexane (Figure 7.6), although the ion of *m/z* 146 was observed in the spectra, which seemed to be a product formed by abstraction of two hydrogen atoms from cyclohexane, no clue for the ions to abstract a single hydrogen atom. In fact, the abstraction of two hydrogen atoms can be accomplished via a hydride abstraction by the cation, followed by a proton transfer, thus a formal two hydrogen atom abstraction reaction was observed. A possible mechanism for the reactions of **1** with cyclohexane is proposed in Scheme 7.3.



Scheme 7.3 Proposed mechanism for the formation of the ion of *m/z* 146 (“2 × H abstraction”) upon reactions of **1** with cyclohexane

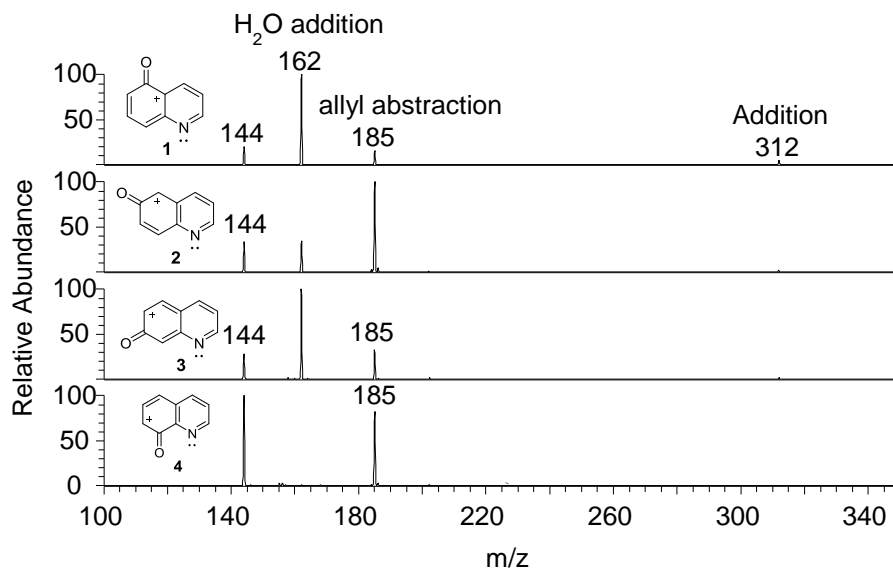


Figure 7.5 Mass spectra measured after 100 ms reactions with allyl iodide for **1** – **4**, the ion of m/z 162 is an adduct formed upon reactions with adventitious water in the ion trap.

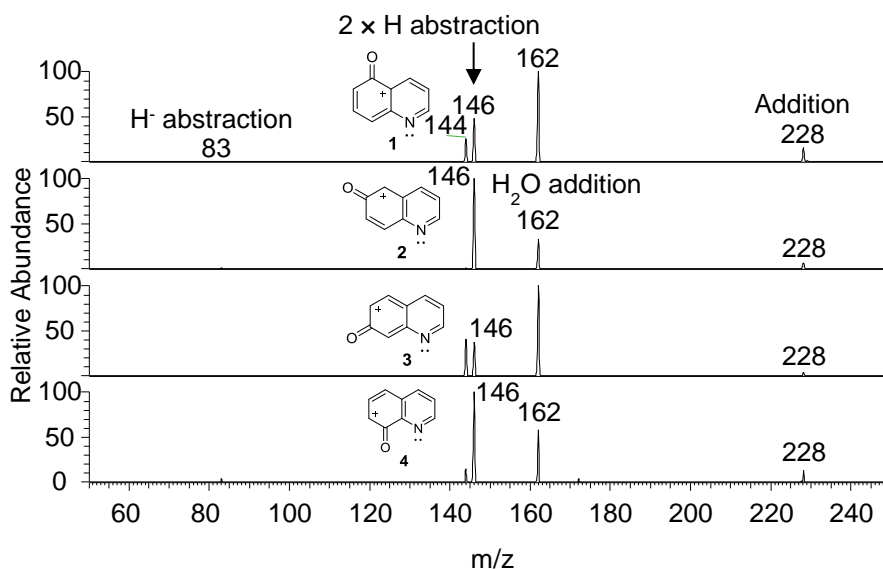
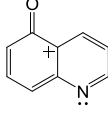
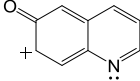
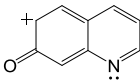
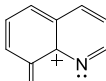
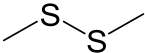
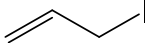
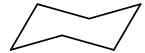


Figure 7.6 Mass spectra measured after 1000 ms reactions with cyclohexane for **1** – **4**, the ion of m/z 162 is an adduct formed upon reactions with adventitious water in the ion trap.

The reaction efficiencies of **1** – **4** upon reactions with dimethyl disulfide, allyl iodide and cyclohexane were also calculated and listed in Table 7.2. As shown in the table, the reaction efficiencies for **2** and **4** are substantially higher than for **1** and **3** (69% and 81% vs. 39% and 31% for reactions with dimethyl disulfide; 60% and 55% vs. 38% and 26% for reactions with allyl

iodide; 20% and 13% vs. 2% and 1% for reactions with cyclohexane). This may be due to the fact that under the same experimental condition, **1** and **3** are more reactive toward adventitious water in the ion trap (Figures 7.3 and 7.6) than **2** and **4**. As a competing reaction, the reactions with water are viewed as “background reactions” and were subtracted from the total reactions of the ions. Therefore, for **1** and **3**, the reactivity toward dimethyl disulfide, allyl iodide, and cyclohexane are lower compared to **2** and **4**. The reactivity of **1** – **4** toward water will be discussed in the following section, and a possible explanation for such reactivity difference toward water will also be discussed. Note that the calculated EA_v values for **1** – **4** are similar for their oxenium ion resonance structures (7.89, 7.87, 7.98 and 7.74 eV, respectively). Therefore, it is unlikely that the reactivity of **1** – **4** toward dimethyl disulfide, allyl iodide, and cyclohexane are controlled by polar effects.

Table 7.2 Reactions, total reaction efficiencies and branching ratios for primary products of biradicals **1** – **4** for reactions with dimethyl disulfide, allyl iodide and cyclohexane, and their calculated $EA_{v,s}$ ^a (eV) and ΔE_{S-T} ^b values (kcal mol⁻¹)

				
	1	2	3	4
EA_v (eV)	7.89	7.87	7.98	7.74
ΔE_{S-T} (kcal mol ⁻¹)	-27.5	-29.9	-26.5	-28.0
	2×SCH ₃ abs ^c 68% e abs 25% CH ₂ abs 5% Add. ^d -HSCH ₃ 2%	2×SCH ₃ abs 57% e abs 21% HSCH ₃ abs 17% Add. -HSCH ₃ 5%	2×SCH ₃ abs 59% HSCH ₃ abs 23% e abs 14% Add.-HSCH ₃ 4%	CH ₂ abs 44% CH ₃ abs 31% Add.-HSCH ₃ 14% e abs 4% 2° ^e SCH ₃ abs H abs 4% HSCH ₃ abs 3% Efficiency 81%
	Allyl abs 73% Addition 27% Efficiency 38%	Allyl abs 98% Addition 2% Efficiency 60%	Allyl abs 97% Addition 3% Efficiency 26%	Allyl abs 100% Efficiency 55%
	2×H abs 78% Addition 21% H abs 1% Efficiency 2%	2×H abs 92% Addition 7% H abs 1% Efficiency 20%	2×H abs 91% Addition 8% H abs 1% Efficiency 1%	2×H abs 93% Addition 7% Efficiency 13%

^a calculated at the CASPT2/CASSCF(12,12)/cc-pVTZ//CASSCF(12,12)/cc-pVTZ level of theory; corrected for zero-point vibrational energies and 298K thermal energies by using the (unscaled) CASSCF(12,12)/cc-pVTZ frequencies;

^b calculated at the CASPT2/CASSCF(13,12)/cc-pVTZ//CASSCF(12,12)/cc-pVTZ level of theory; ^c abs. = abstraction;

^d add. = addition; ^e 2° indicates a secondary product.

7.3.3 Reactions with Water, Methanol and Acetonitrile

As mentioned above, besides the reagents intentionally injected into the ion trap, **1** – **4** showed some reactivity toward adventitious water in the ion trap. Taking the fact that no radical-type reactions was observed for **1** – **4**, and they are indeed oxenium ions with several carbocation resonance structures, they should show considerable reactivity toward nucleophiles. The reactions with adventitious water in the ion trap proved the hypothesis. In fact, previous studies on phenyl oxenium ions also suggested that these ions are good electrophiles that can react with some weak nucleophiles.⁸ Therefore, three weak nucleophiles, water, methanol and acetonitrile were introduced into the ion trap to react with **1** – **4**.

As shown in Figures 7.7, 7.8, and 7.9, **1** – **4** formed stable adducts with all three reagents tested. Besides, it is obvious that for the reactions with these nucleophiles, in contrast to the reactions with dimethyl disulfide, allyl iodide and cyclohexane, **1** and **3** were more reactive than **2** and **4**, under the same reaction conditions (See Table 7.3). This finding can be rationalized that **1** and **3** can react from the nitrenium ion resonance structures (Figure 7.2), that are more electrophilic compared to all the other carbocation resonance structures. Moreover, the adducts formed are not likely to be noncovalent adducts, as large amount of collision energy was required to cause fragmentations of the adduct ions (> 50 normalized collision energy in the ion trap, arbitrary unit, ~ 20 eV of collision energy, after conversion^{21,22}).

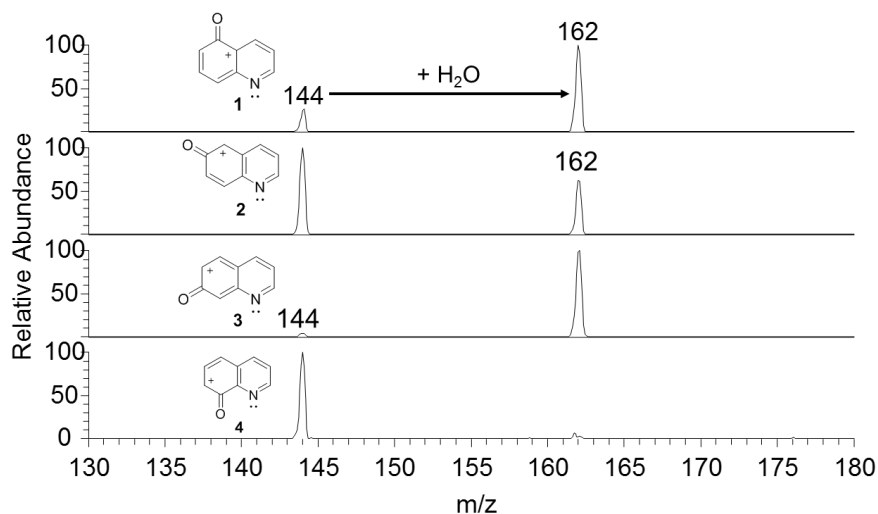


Figure 7.7 Mass spectra measured after 100 ms reactions with water for **1** – **4**

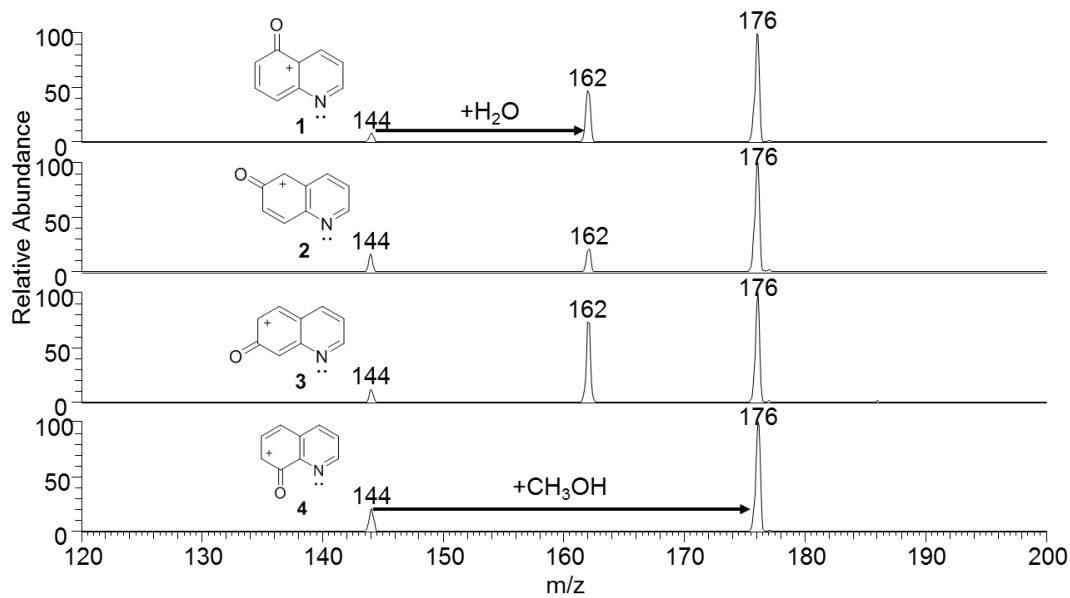


Figure 7.8 Mass spectra measured after 100 ms reactions with methanol for **1 – 4**, the ion of m/z 162 is an adduct formed upon reactions with adventitious water in the ion trap.

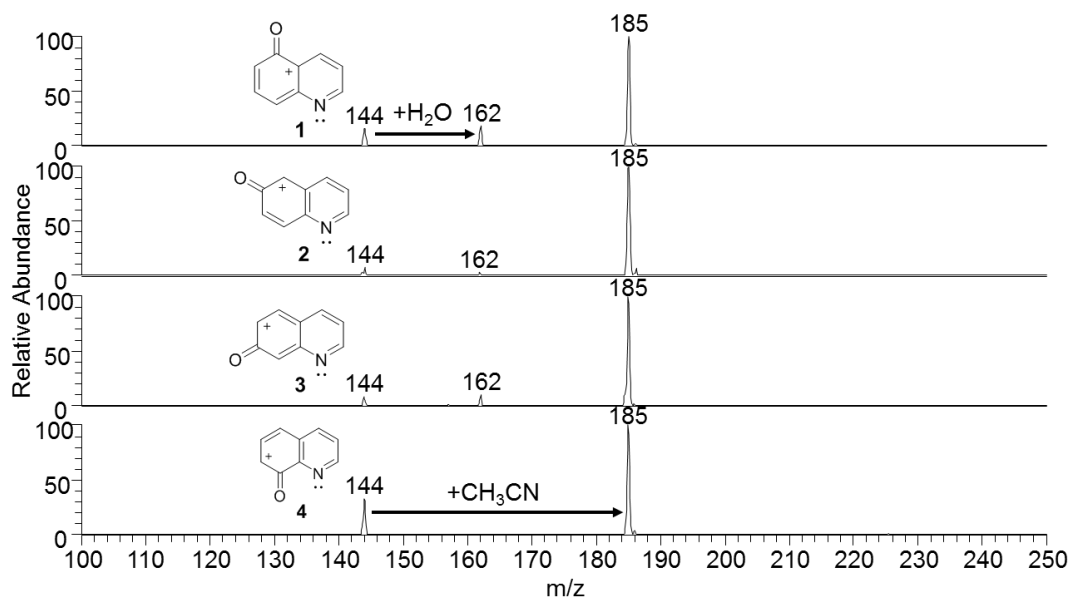
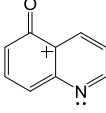
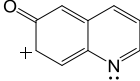
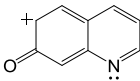
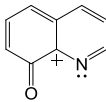


Figure 7.9 Mass spectra measured after 100 ms reactions with acetonitrile for **1 – 4**, the ion of m/z 162 is an adduct formed upon reactions with adventitious water in the ion trap.

Table 7.3 Reactions, total reaction efficiencies and branching ratios for primary products of biradicals **1** – **4** for reactions with dimethyl disulfide, allyl iodide and cyclohexane, and their calculated $EA_{v,s}$ ^a (eV) and ΔE_{S-T} ^b values (kcal mol⁻¹)

								
	1	2	3	4				
EA_v (eV)	7.89	7.87	7.98	7.74				
ΔE_{S-T} (kcal mol ⁻¹)	-27.5	-29.9	-26.5	-28.0				
H₂O	Addition	100%	Addition	100%	Addition	100%	Addition	100%
	Efficiency	78%	Efficiency	22%	Efficiency	100%	Efficiency	0.2%
CH₃OH	Addition	100%	Addition	100%	Addition	100%	Addition	100%
	Efficiency	80%	Efficiency	71%	Efficiency	100%	Efficiency	74%
CH₃CN	Addition	100%	Addition	100%	Addition	100%	Addition	100%
	Efficiency	95%	Efficiency	66%	Efficiency	100%	Efficiency	27%

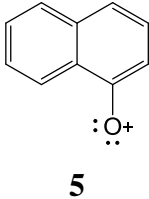
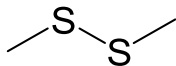
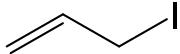
^a calculated at the CASPT2/CASSCF(12,12)/cc-pVTZ//CASSCF(12,12)/cc-pVTZ level of theory; corrected for zero-point vibrational energies and 298K thermal energies by using the (unscaled) CASSCF(12,12)/cc-pVTZ frequencies;

^b calculated at the CASPT2/CASSCF(13,12)/cc-pVTZ//CASSCF(12,12)/cc-pVTZ level of theory.

7.3.4 Comparison to a Naphthalene-based Oxenium Ion

As illustrated in Figure 7.2, one of the important resonance structures of **1** – **4** is an oxenium ion, where a formal positively charged oxygen exists in the systems. Therefore, their reactivity was compared to that of an analogous oxenium ion **5**. **5** was generated from the fragmentation of a precursor ion synthesized using a modified method described in literature.⁸ The reactivity of **5** toward dimethyl disulfide and allyl iodide is summarized in Table 7.4. As the table suggests, **5** exhibited similar chemical properties to **1** – **4**, where addition was the exclusive reaction observed for dimethyl disulfide, and allyl abstraction being the only primary product upon reactions with allyl iodide. No reactions were observed for cyclohexane. No radical-type reactions were tracked. Therefore, the results further confirmed that **1** – **4** behave as electrophiles and the oxenium ion is one of the essential resonance structures responsible for their electrophilicity.

Table 7.4 Reactions, total reaction efficiencies and branching ratios for primary products of biradicals **5** for reactions with dimethyl disulfide and allyl iodide

 5		
	Addition Efficiency	100% 57%
	Allyl abs 2° I abs Efficiency	100% 5%

7.4 Conclusions

The reactivity of four isomeric oxenium ions were studied in a linear quadrupole ion trap mass spectrometer; their structures and electronic configurations were proposed and confirmed via quantum chemical calculations. Instead of being σ, π -type biradicals, the four ions generated via (+)APCI/CS₂ are oxenium ions with low-lying closed-shell singlet ground states. Besides, these ions are resonance-stabilized by several carbocation structures. As a result, no diagnostic radical-type reactions, i.e. SCH₃ radical abstraction from dimethyl disulfide, iodine atom abstraction from allyl iodide, and hydrogen atom abstraction from cyclohexane, was observed upon reactions with the oxenium ions. Further, as strong electrophiles, the ions studied were found to react efficiently with weak nucleophiles such as water, methanol and acetonitrile. Based on the reaction efficiencies calculated, in comparison to oxenium ions **2** and **4**, **1** and **3** showed lower reactivity toward dimethyl disulfide, allyl iodide and cyclohexane, however, higher reactivity toward water, methanol and acetonitrile. The difference in reactivity can be explained by the nitrenium ion resonance structures in **1** and **3**, being more electrophilic than all the other carbocation resonance

structures. As reactive intermediates that are hard to generate and study in condensed phase, this work enriched the understanding of the properties of oxenium ions in the gas phase. With the help of mass spectrometry, more oxenium ions can be stabilized and studied in the gas phase.

7.5 Future Work

Quantum chemical calculations need to be carried out for the verifications of the proposed mechanisms.

7.6 References

1. Williams, L. L.; Webster, R. D. *J. Am. Chem. Soc.* **2004**, *126*(39), 12441–12450.
2. Sabot, C.; Commare, B.; Duceppe, M.-A.; Nahi, S.; Guerard, K. C.; Canesi, S. *Synlett*, **2008**, (20), 3226–3230.
3. Guerard, K. C.; Chapelle, C.; Giroux, M.-A.; Sabot, C.; Beaulieu, M.-A.; Achache, N.; Canesi, S. *Org. Lett.* **2009**, *11*(20), 4756–4759.
4. Wenderski, T. A.; Huang, S.; Pettus, T. R. R. *J. Org. Chem.* **2009**, *74*(11), 4104–4109.
5. Osborne, R. L.; Coggins, M. K.; Raner, G. M.; Walla, M.; Dawson, J. H. *Biochemistry*, **2009**, *48*(20), 4231–4238.
6. Hanway, P. J.; Winter, A. H. *J. Phys. Chem. A* **2012**, *116*(37), 9398–9403.
7. Li, M.-D.; Hanway, P. J.; Albright, T. R.; Winter, A. H.; Phillips, D. L. *J. Am. Chem. Soc.* **2014**, *136*(35), 12364–12370.
8. Du, L.; Qiu, Y.; Lan, X.; Zhu, R.; Phillips, D. L.; Li, M.-D.; Dutton, A. S.; Winter, A. H. *J. Am. Chem. Soc.* **2017**, *139*(42), 15054–15059.
9. Wang, Y.-T.; Wang, J.; Platz, M. S.; Novak, M. *J. Am. Chem. Soc.* **2007**, *129*(47), 14566–14567.
10. Wang, Y.-T.; Jin, K. J.; Leopold, S. H.; Wang, J.; Peng, H.-L.; Platz, M. S.; Xue, J.; Phillips, D. L.; Glover, S. A.; Novak, M. *J. Am. Chem. Soc.* **2008**, *130*(47), 16021–16030.
11. Yang, Y.; Fang, W.; Chen, X. *Phys. Chem. Chem. Phys.* **2018**, *20*(4), 2220–2229.
12. Qiu, Y.; Winter, A. H. *Org. Biomol. Chem.* **2017**, *15*(13), 2666–2671.
13. Sheng, H.; Ma, X.; Lei, H.-R.; Milton, J.; Tang, W.; Jin, C.; Gao, J.; Wittrig, A. M.; Archibold, E. F.; Nash, J. J.; Kentt ämaa, H. I. *ChemPhysChem*, **2018**, *19*(21), 2839–2842.

14. Max, J. P.; Ma, X.; Kotha, R. R.; Ding, D.; Milton, J.; Nash, J. J.; Kentt ämaa, Hilikka I. *Int. J. Mass Spectrom.* **2019**, *435*, 280 – 290.
15. Ma, X.; Jin, C.; Wang, D.; Nash, J. J.; Kentt ämaa, H. I. *Chem. Eur. J.* **2019**, *25*(25), 6355–6361.
16. Su, T.; Chesnavich, W. J. *J. Chem. Phys.* **1982**, *76*, 5183–5185.
17. Jing, L.; Nash, J. J.; Kentt ämaa, H. I. *J. Am. Chem. Soc.* **2008**, *130*(52), 17697–17709.
18. Stirk, K. M.; Orłowski, J. C.; Leeck, D. T.; Kentt ämaa, H. I. *J. Am. Chem. Soc.* **1992**, *114*(22), 8604–8606.
19. Smith, R. L.; Kentt ämaa, H. I. *J. Am. Chem. Soc.* **1995**, *117*(4), 1393–1396.
20. Gao, J.; Jankiewicz, B. J.; Reece, J.; Sheng, H.; Cramer, C. J.; Nash, J. J.; Kentt ämaa, H. I. *Chem. Sci.* **2014**, *5*(6), 2205–2215.
21. Ha, J.; Cho, E.; Kim, S. *Energy Fuels*, **2017**, *31*(7), 6960–6967.
22. Lopez, L. L.; Tiller, P. R.; Senko, M. W.; Schwartz, J. C. *Rapid Commun. Mass Spectrom.* **1999**, *13*(8), 663–668.

CHAPTER 8. REACTIONS OF ELECTROPHILIC ANIONS $[B_{12}X_{11}]^-$ ($X = Cl, Br$) WITH HYDROCARBON MOLECULES: A SYSTEMATIC STUDY

8.1 Introduction

Reagents that are able to react spontaneously with saturated hydrocarbons, alkanes, are rare. Conversion of saturated hydrocarbons is of high economic and environmental significance¹⁻⁴ but is challenging due to the high strength and low polarity of the C-H bonds. While many catalytic processes for selective conversion of alkanes have been investigated,⁵⁻¹⁰ the direct functionalization of unreactive alkanes is only possible for exceptionally reactive molecules.¹¹ Free radicals may react with alkanes by cleaving or forming chemical bonds homolytically,¹² but such reactions tend to be difficult to control. An alternative approach is the use of highly reactive closed-shell molecules, which provide access to a different kind of chemistry.¹³

A special class of highly reactive even electron reagents are $[B_{12}X_{11}]^-$ anions (X =halogen, CN).^{13,14} These anions are generated by heterolytic B-X bond cleavage of stable *closo*-dodecaborate dianions $[B_{12}X_{12}]^{2-}$. The $[B_{12}X_{11}]^-$ anions show “superelectrophilic reactivity”, and even bind N_2 and noble gases (Ar, Kr & Xe) spontaneously at room temperature – a reactivity so far observed only for the most electrophilic cations.¹³ This exceptional anion reactivity can be rationalized by a strong positive partial charge on the vacant boron atom, which is embedded into an overall anionic framework (Figure 8.1).

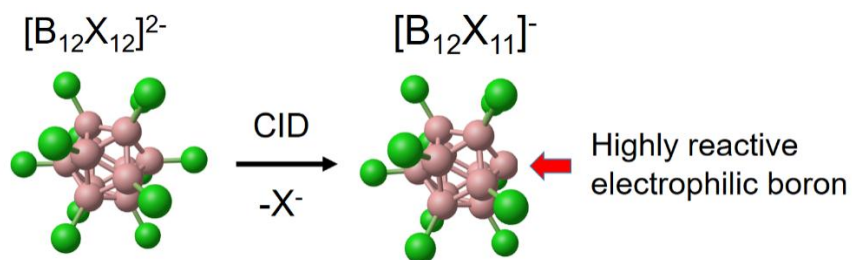
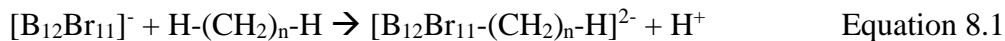


Figure 8.1 Illustration of the electrophilic $[B_{12}X_{11}]^-$ anion

Recently the reactivity of gaseous $[B_{12}X_{11}]^-$ anions toward methane and hexane were reported.¹⁵ In this reaction, heterolytic cleavage of a C-H bonds takes place via a concerted

machanism. $[\text{B}_{12}\text{X}_{11}]^-$ binds to the $[\text{C}_n\text{H}_{2n+1}]^-$ moiety and forms a doubly charged adduct with a B-C bond. The cleaved proton stays Coulomb bound to the dianion in the gas phase.



Herein, a systematic study on the binding of electrophilic anions $[\text{B}_{12}\text{X}_{11}]^-$ ($\text{X}=\text{Cl}, \text{Br}$) towards linear, branched and cyclic alkanes is reported. With the aid of ion-molecule reactions, collision-activated dissociation (CAD) and computational investigations the reactions of electrophilic anions with different C_6 -hydrocarbons have been in-depth analyzed. Signal patterns observed upon CAD of the adduct $[\text{B}_{12}\text{Br}_{11}+\text{C}_n\text{H}_{2n+2}]^-$ were found to be highly dependent on the hydrocarbon structure. These results provide new insights into the exceptional chemistry of electrophilic anions and may open alternative approaches for the analysis of nonpolar hydrocarbons, which are notoriously hard to ionize without causing extensive fragmentations using common ionization methods, such as electron impact (EI) or field ionization(FI) /field desorption (FD).¹⁶⁻¹⁹

8.2 Experimental Section

Chemicals. $[(\text{NEt})_4]_2[\text{B}_{12}\text{X}_{12}]$ ($\text{X} = \text{Cl}$ and Br) was synthesized followed by the procedures as described in literature,^{20,21} the starting materials for synthesis were and hydrocarbon model compounds *n*-hexane, 2-methylpentane, 3-methylpentane, 2,3-dimethylbutane, 2,2-dimethylbutane, *n*-pentane, *n*-heptane, *n*-octane, 2,2,4-trimethylpentane, 1-hexene, *trans*-3-hexene, 3-methyl-2-petene, 2,3-dimethylbutene, cyclohexane, cyclohexene, 1,3-cyclohexadiene, benzene, toluene, ethylbenzene, styrene, and Sigma-Aldrich were purchased from commercial sources and used as received. $[(n\text{-C}_6\text{H}_{13})_4\text{N}][\text{B}_{12}\text{Br}_{11}\text{H}]$ was made by mixing solutions containing $[(n\text{-C}_6\text{H}_{13})_4\text{N}]\text{Br}$ and $[(\text{NEt})_4][\text{B}_{12}\text{Br}_{11}\text{H}]$. $[\text{N}(n\text{-C}_6\text{H}_{13})_4]\text{Br}$ was purchased from Sigma-Aldrich and used as received. Cyclohexane-*d*₁₂ was purchased from Cambridge Isotope and used as received.

Ion-molecule reactions. $[(\text{NEt})_4]_2[\text{B}_{12}\text{X}_{12}]$ was dissolved in methanol and sprayed into a Thermo linear quadrupole ion trap (LQIT) mass spectrometer via an electrospray ionization (ESI) source operated at negative ion mode. The $[\text{B}_{12}\text{X}_{12}]^{2-}$ ions were trapped in the ion trap and subject to one collision-activation dissociation (CAD) step. Upon heterolytic cleavage of the C-X bond, X^- was eliminated and the reactant ion $[\text{B}_{12}\text{X}_{11}]^-$ was generated. The neutral hydrocarbon

molecules were introduced via a homebuilt reagent mixing manifold using helium as a buffer gas. The detailed description of the manifold setup can be found in Chapter 2. The $[\text{B}_{12}\text{X}_{11}]^-$ ions were allowed to react with the hydrocarbon molecules for various reaction times and the reaction mass spectra were collected. The reaction product ions were then isolated and subject to further CAD steps for more detailed structural elucidation and mechanistic studies. A mixture containing more than one hydrocarbon molecules were also injected into the ion trap for observation of the reaction patterns of different hydrocarbon classes.

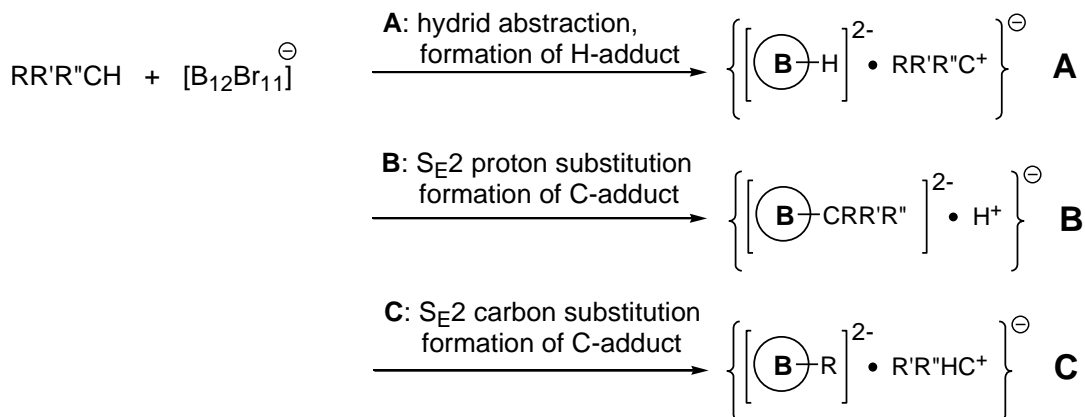
$[\text{N}(\text{n-C}_6\text{H}_{13})_4][\text{B}_{12}\text{Br}_{11}\text{H}]$ was sprayed via ESI into the ion trap and subject to CAD to generate $[\text{n-C}_6\text{H}_{13}][\text{B}_{12}\text{Br}_{11}\text{H}]^-$ ion. This ion was used as a model to verify the proposed structure of the product ion upon reactions of $[\text{B}_{12}\text{Br}_{11}]^-$ and *n*-hexane. the resulting ions were allowed to react with adventitious water in the ion trap and the experimental results were compared to those of the reactions of $[\text{B}_{12}\text{Br}_{11}]^-$ and *n*-hexane.

Computational methods. Quantum chemical calculations were applied in this study to help understand and verify all the proposed addition products and their fragmentation patterns. All calculations were carried out by Marcus Rohdenburg from Universität Leipzig in Germany.

8.3 Results and Discussion

8.3.1 Reactions with Acyclic Alkanes

Isolation of $[\text{B}_{12}\text{Br}_{11}]^-$ in an ion trap in the presence of an alkane resulted in the formation of a strongly bound adduct which did not (or only in negligible amounts) dissociates into the reagents upon collisional excitation. The formation of a strongly bound adduct between $[\text{B}_{12}\text{Br}_{11}]^-$ and a saturated alkane requires breaking of either a C-H or a C-C bond so that a B-H or B-C bond can be formed. A radical mechanism (homolytic bond cleavage) is not expected since the even electron anion $[\text{B}_{12}\text{Br}_{11}]^-$ has a large singlet-triplet gap of around 130 kJ/mol. We distinguish three heterolytic bond cleavages for the alkane (A, B and C, Scheme 8.1), which formally result in cationic and anionic alkane fragments. The anionic alkane fragment is bound to the vacant electrophilic boron atom of $[\text{B}_{12}\text{Br}_{11}]^-$ resulting in a formal dianion and the cationic fragment is Coulomb-stabilized by this dianion.



Scheme 8.1 Three possible elementary mechanisms for the reaction between the electrophilic $[\text{B}_{12}\text{Br}_{11}]^-$ anion and alkane molecule

The different binding motifs of the reactions A, B and C result in different fragmentation patterns upon activation of the products. In our experiments, all isomers of hexane (C_6H_{14}) have been subjected to the reactions with $[\text{B}_{12}\text{Br}_{11}]^-$. Figure 8.2a shows the mass spectra, obtained after isolation of $[\text{B}_{12}\text{Br}_{11}]^-$ (m/z 1009, width 1) and subsequent reaction with the six hexane derivatives for 30 ms. For all hexane isomers, the adduct with molecular formula $[\text{B}_{12}\text{Br}_{11}\text{C}_6\text{H}_{14}]^-$ was subsequently isolated in the ion trap and fragmented using CAD (Figure 8.2b). Note that a fraction of the product $[\text{B}_{12}\text{Br}_{11}\text{C}_6\text{H}_{14}]^-$ is prone to spontaneous fragmentation, likely due to the vibrational energy gained upon the reaction between $[\text{B}_{12}\text{Br}_{11}]^-$ and the alkane. Therefore, fragments generated by CAD (Figure 8.2b) are already observed in Figure 8.2a. The color code marks ions in strong relation and helps to distinguish different reaction/fragmentation pathways.

Green denotes the signals of ions formed by binding of molecules present in the atmosphere of the mass spectrometer. $[\text{B}_{12}\text{Br}_{11}+\text{H}_2\text{O}]^-$ (m/z 1027) and $[\text{B}_{12}\text{Br}_{11}+\text{N}_2]^-$ (m/z 1037) are formed by reactions with water and nitrogen traces in the ion trap. The hexane adduct $[\text{B}_{12}\text{Br}_{11}+\text{C}_6\text{H}_{14}]^-$ is observed at m/z 1095 and an additional water adduct to this ion $[\text{B}_{12}\text{Br}_{11}+\text{C}_6\text{H}_{14}+\text{H}_2\text{O}]^-$ is found at m/z 1113. *Blue* marks the signals of common fragments observed in all five spectra, namely $[\text{B}_{12}\text{Br}_{11}\text{CH}_2]^-$ (m/z 1023) and its water adduct $[\text{B}_{12}\text{Br}_{11}\text{CH}_2 + \text{H}_2\text{O}]^-$ (m/z 1041). Isolation of m/z 1023 and reaction with the background gas for 30 ms resulted in an intense signal at m/z 1041. *Yellow* designates the signal of the fragment ion $[\text{B}_{12}\text{Br}_{11}\text{C}_2\text{H}_4]^-$ at m/z 1037, which has the same nominal mass as the N_2 adduct (in green). Experiments with deuterated hexane allow to unambiguously distinguish between these two ions. Assignment in Figure 8.2 is based on the ratio

of m/z 1027 and 1037. Without the addition of any hydrocarbon, the N_2 adduct intensity is around 45% of the H_2O -adduct intensity. Therefore, if the intensity ratio of signals at m/z 1037 to 1027 > 0.45 is observed, this is attributed to the formation of $[B_{12}Br_{11}C_2H_4]^-$. Orange marks signals of homologous ions with additional CH_2 units ($[B_{12}Br_{11}C_nH_{2n}]^-$, $n>2$). These ions are only observed in small intensities upon fragmentation of the n -hexane adduct. Purple denotes a reaction product with the molecular formula $[B_{12}Br_{11}H_2]^-$. This ion is observed in considerable intensity for 2-methylpentane, 3-methylpentane and 2,2-dimethylbutane but has negligible or no intensity in spectra of n -hexane and *neo*-hexane. Red marks signals of $[B_{12}Br_{11}CH_4]^-$ (m/z 1025) and its water addition product $[B_{12}Br_{11}CH_4+H_2O]^-$, which are exclusively observed in the case of *neo*-hexane.

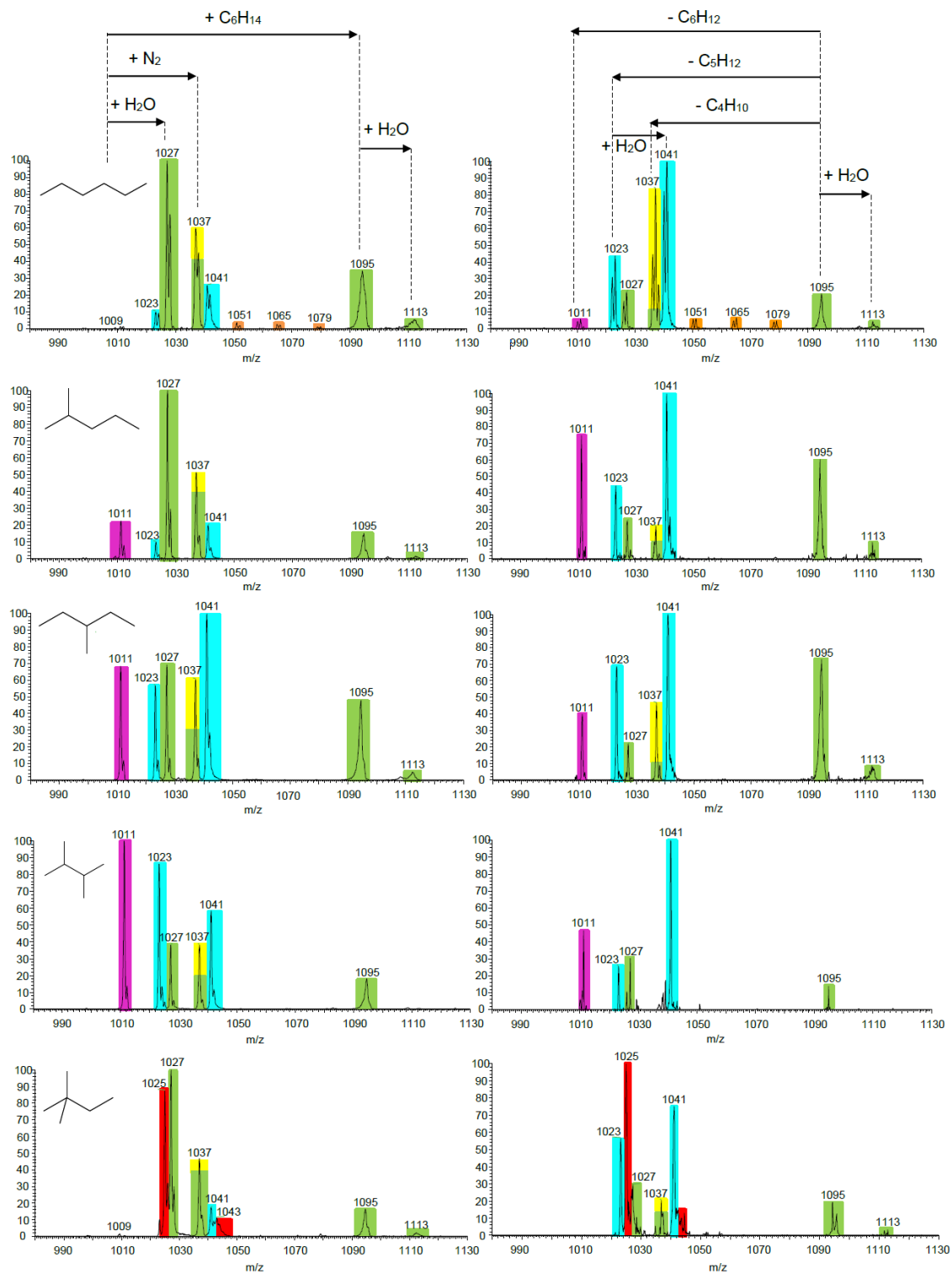
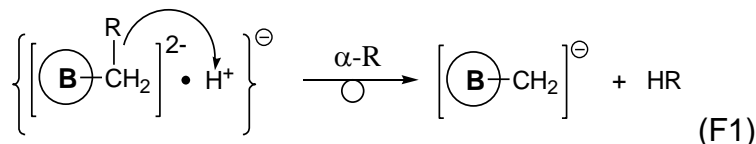


Figure 8.2 CAD Fragmentation spectra of the $[B_{12}Br_{11}]^-$ adducts with five different isomers of C_6H_{14} . The color code is explained in the text.

The formation of the adduct $[\text{B}_{12}\text{Br}_{11}+\text{C}_6\text{H}_{14}]^-$ using *n*-hexane has been thoroughly investigated using CAD, computational investigations and gas phase IR spectroscopy. It has been shown that reaction B (Scheme 8.1) is the dominant reaction pathway, while no evidence for reactions A or C has been found. The $[\text{C}_6\text{H}_{13}]^-$ carbanion is bound to $[\text{B}_{12}\text{Br}_{11}]^-$, and the H^+ is Coulomb-stabilized by the resulting fully saturated dianion. The $[\text{B}_{12}\text{Br}_{11}\text{C}_6\text{H}_{13}]^{2-}\text{H}^+$ ion pair acts as a strong acid. Water from the background of the mass spectrometer is protonated resulting in $[\text{H}_3\text{O}]^+$ which remains Coulomb-bound to the dianion, affording the signal at m/z 1113. Note that only products of reaction B contain a Coulomb-bound proton which is responsible for the subsequent water addition. The signal at m/z 1113 could be observed in all cases after isolation of the adduct m/z 1095. This indicates that reaction B plays a role for all hexane derivatives. After binding hexane following reaction B (Scheme 8.1), the fragmentation reaction F1 (blue) in Scheme 8.2 is assumed to be responsible for the formation of the fragment $[\text{B}_{12}\text{Br}_{11}\text{CH}_2]^-$ (m/z 1023).

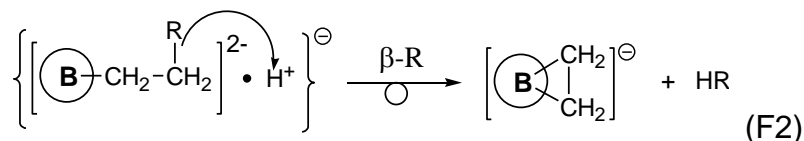


Scheme 8.2 Fragmentation reaction leading to the $[\text{B}_{12}\text{Br}_{11}\text{CH}_2]^-$ adduct (blue-marked signals in Figure 8.2). $\alpha\text{-R}$ denotes fragmentation of the C-C bond next to the α -carbon of the alkyl residue.

The dominant cleavage of the α C-C bond can be rationalized by its spatial proximity to the Coulomb-stabilized proton. We assume that this results in an energetically low-lying transition state for the reaction. The reaction demands an energy of 64 kJ/mol. Competing channels are energetically more demanding (e.g. dissociation into reagents: 81 kJ/mol). Note that reaction F1 can only be formulated if $[\text{B}_{12}\text{Br}_{11}]^-$ reacts with a terminal CH_3 group. The pronounced water addition signal to $[\text{B}_{12}\text{Br}_{11}\text{CH}_2]^-$ is rationalized by the large water attachment enthalpy.

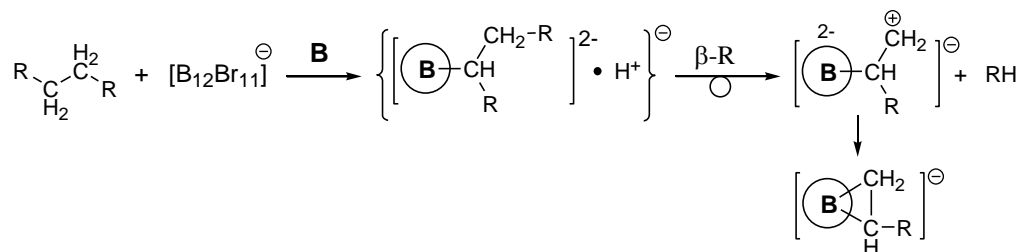
Formation of the fragment $[\text{B}_{12}\text{Br}_{11}\text{C}_2\text{H}_4]^-$ (m/z 1037, *yellow*) can be explained by a similar reaction, which results in cleaving the $\text{C}_2\text{-C}_3$ bond, see F2 in Scheme 8.3. This fragmentation is energetically favorable due to the high stability of $[\text{B}_{12}\text{Br}_{11}\text{C}_2\text{H}_4]^-$, in which the ethylene group binds via the π -bond to the electrophilic boron. Attachment of ethylene to $[\text{B}_{12}\text{Br}_{11}]^-$ was calculated to be favorable by 220 kJ/mol. The observation of stable alkane adducts and the similar product

yields for the endothermic reaction F1 in the case of *n*-hexane indicate that a substantial barrier for the spontaneous fragmentation F2 is present.



Scheme 8.3 Fragmentation reaction leading to the $[\text{B}_{12}\text{Br}_{11}\text{C}_2\text{H}_4]^-$ adduct (yellow-marked signals in Figure 8.2). $\beta\text{-R}$ denotes fragmentation of the C-C bond next to the β -carbon of the alkyl residue.

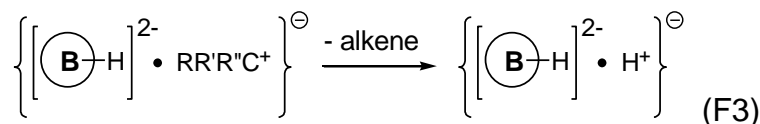
The proposed mechanism for F2 requires $[\text{B}_{12}\text{Br}_{11}]^-$ bound to a $\text{CH}_2\text{-CH}_2\text{-R}$ structural element. Therefore, this fragmentation channel can be expected to be less pronounced in spectra of branched alkanes containing $\text{CH}_3\text{-CHR}'\text{R}''$ groups. Indeed *n*-hexane and 3-methylpentane with two ethyl groups show the product of F2 (yellow) in higher relative intensities than the other isomers. Formation of homologous ions with several CH_2 units $[\text{B}_{12}\text{Br}_{11}\text{C}_n\text{H}_{2n}]^-$ ($n = 3\text{--}5$) is observed in trace amount only for *n*-hexane and can be explained by an addition to the secondary carbons of its alkyl chain followed by the fragmentation most likely according to F2 mechanism (Scheme 8.4). However, addition to a secondary carbon is overall less favorable than to a primary carbon, explaining the observed difference.



Scheme 8.4 Possible mechanism for the formation of homologous ions with a variable number of CH_2 units $[\text{B}_{12}\text{Br}_{11}\text{C}_n\text{H}_{2n}]^-$ ($n = 3\text{--}5$, yellow-marked signals in Figure 8.2) in the case of *n*-hexane. $\beta\text{-R}$ denotes fragmentation of the C-C bond next to the β -carbon of the alkyl residue.

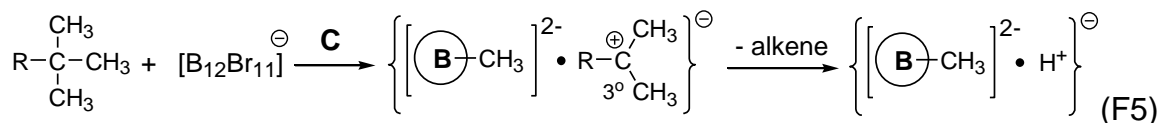
While F1 and F2 are indicative of reaction B in scheme 8.1, we consider $\{[\text{B}_{12}\text{Br}_{11}\text{H}]^{2-} \text{H}^+\}$ (m/z 1011, purple) as a marker for reaction A: hydride abstraction by the electrophilic anion (Scheme 8.1). The product contains the dianion $[\text{B}_{12}\text{Br}_{11}\text{H}]^{2-}$ and an alkyl carbocation. Fragmentation results in a proton transfer from the carbocation by neutral loss of an alkene (F3,

scheme 8.5). The fragment $[B_{12}Br_{11}H]^2-H^+$ is only observed in significant intensity, if the alkane contains tertiary carbons. This can be rationalized by the comparatively high stability and ease of formation of tertiary carbocations, which then dissociate forming an alkene and a electrostatically-bound proton.



Scheme 8.5 Fragmentation reaction leading to the $[B_{12}Br_{11}H_2]^-$ adduct (purple-marked signals in Figure 8.2).

The fragment $[B_{12}Br_{11}CH_3]^2-H^+$ (m/z 1025, red), observed only in the case of *neo*-hexane, is considered to be indicative for reaction C in Scheme 8.1: carbon-carbon bond cleavage. Driving force for the reaction is the formation of a stable tertiary carbocation. Subsequent loss of an alkene (F5, scheme 8.6) results in $[B_{12}Br_{11}CH_3]^2-H^+$. The Coulomb-stabilized proton is responsible for the observed water addition (m/z 1043).



Scheme 8.6 Reaction of an alkene with a quaternary center with $[B_{12}Br_{11}]^-$, leading to $[B_{12}Br_{11}CH_3]^-$ adduct (red-marked signals in Figure 8.2) upon the fragmentation of the reaction intermediate.

The observed differences in CAD spectra demonstrate that fragmentation of adducts between electrophilic anions and alkanes are highly sensitive to the alkane structure. The competition between the reaction pathways A, B and C is strongly dominated by the stability of carbocations. Only if a tertiary carbocation can be formed, hydride abstraction from the alkane (reaction A) or carbanion abstraction (reaction C) is observed in competition to proton substitution (reaction B). Fragment ions, which originate from carbocation-containing products (purple and red), showed higher relative abundance in Figure 8.2a than in Figure 8.2b in comparison to fragments originating from products formed by reaction B (yellow and blue). This implies that the reaction products which contain carbocations are considerably less stable against fragmentation and show

a higher degree of fragmentation in the isolation step, Figure 8.2a. This deplete the products of pathway A and C for the following fragmentation step in Figure 8.2b.

8.3.2 Reactions with Cyclic Hydrocarbons

For the reactions of $[B_{12}X_{11}]^-$ with cyclic hydrocarbons, stable adduct ions generated. No water adducts were observed on top of the hydrocarbon adducts (Figure 8.3). It is worth pointing out that instead of the reactant ion $[B_{12}Br_{11}]^-$, an ion of m/z 1011 was obtained for all the reactions with cyclic hydrocarbons; this ion was believed to be $[Br_{11}B_{11}BH]^{2-H^+}$, indicating a B-H bond was formed during the addition. Based on the observations, a possible addition mechanism was proposed for the reactions of $[B_{12}Br_{11}]^-$ with cyclohexane in terms of the formation of the ions of m/z 1011: abstraction of a hydride from cyclohexane, followed by a proton transfer to the nearby halogen atom. After elimination of a cyclohexene molecule, the ion of m/z 1011 was formed. The reaction mechanisms for unsaturated hydrocarbons is under investigation.

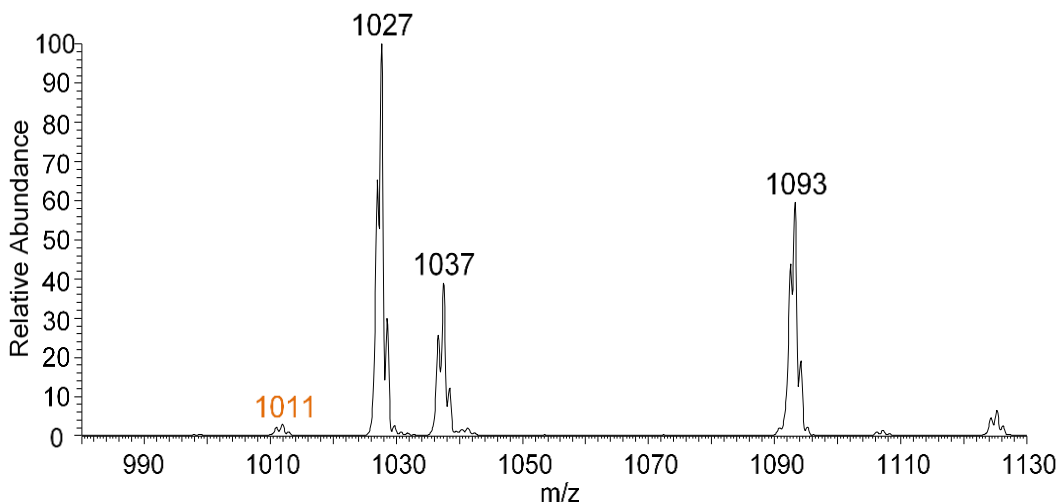


Figure 8.3 Reaction mass spectrum of $[B_{12}Br_{11}]^-$ with cyclohexane after 30 ms of reaction.

CAD was applied to the adducts. The CAD mass spectrum of the adduct ion formed by cyclohexane yielded almost solely the fragment ion of m/z 1037 (Figure 8.4a). Unlike CAD spectra for the adducts with linear alkanes, the ions of m/z 1027 and m/z 1037 were always present at the same time, with the ion of m/z 1027 much more abundant than the ion of m/z 1037. This observation indicated $[B_{12}Br_{11}]^-$ was regenerated upon CAD of the adduct, and it reacted with

adventitious water and N₂ immediately. [B₁₂Br₁₁]⁻ tends to bind to water more efficiently so that the ion of *m/z* 1027 was almost always more abundant. However, the ion of *m/z* 1027 was not observed in Figure 8.4a. This finding suggested the ion of *m/z* 1037 may not be [B₁₂Br₁₁]⁻[N₂]. To clarify that, cyclohexane-*d*₁₂ was used to illustrate the possible structure of the ion of *m/z* 1037. Further, the possible fragmentation pathway will be discussed.

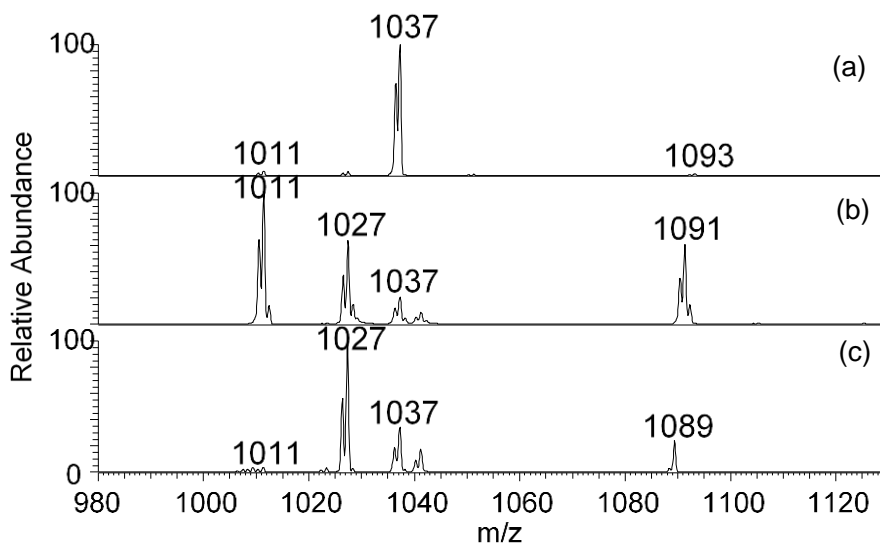


Figure 8.4 CAD mass spectra of the adduct ions upon the reactions of [B₁₂Br₁₁]⁻ with (a) cyclohexane (*m/z* 1093), (b) cyclohexene (*m/z* 1091), and (c) 1,3-cyclohexadiene (*m/z* 1089) (Collision energies 25, 30, and 30, arbitrary units, respectively).

The CAD mass spectra for the adducts formed upon reactions with cyclohexene and 1,3-cyclohexadiene indicated they must have fragmented in a somewhat different way than the cyclohexane adduct fragmented, because more of the ion of *m/z* 1027 was observed in the spectra, suggesting these adducts may yield [B₁₂Br₁₁]⁻[N₂] upon fragmentation and further reactions with adventitious nitrogen.

As shown in Figure 8.5, the adduct formed upon reaction of [B₁₂Br₁₁]⁻ with cyclohexane-*d*₁₂ was subject to CAD, and an ion of *m/z* 1041 was generated. Compared to the ion of *m/z* 1037 upon reaction with cyclohexane, the mass shift of 4 Da implied four of the hydrogen atoms were replaced with deuterium atoms. Meanwhile, the ion of *m/z* 1037 almost disappeared in the CAD spectrum, meaning no [B₁₂Br₁₁]⁻[N₂] generated. Furthermore, it also verified that the

fragmentation pathway for the adduct with cyclohexane cannot be simple dissociation (regeneration of reactant ions).

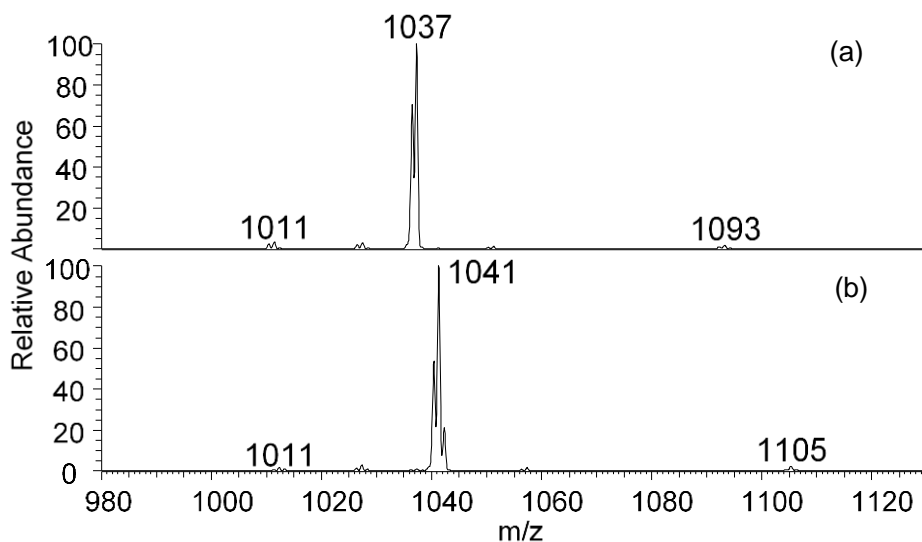


Figure 8.5 CAD mass spectra of the adduct ions upon the reactions of $[B_{12}Br_{11}]^-$ with (a) cyclohexane (m/z 1093), and (b) cyclohexane- d_{12} (m/z 1105).

As discussed previously, the ion of m/z 1011 was observed for all the CAD spectra of the adduct ions. This ion possesses a structure of $[B_{12}Br_{11}H]^2-H^+$, i.e. B-H bond formation was one possible addition pathway for cyclic hydrocarbons, no matter they are saturated or not.

Unlike the addition reactions with saturated cyclic alkanes, based on the product mass spectra obtained for reactions with unsaturated cyclic hydrocarbons, a second possible addition mechanism was proposed. Since the abundance of the ion of m/z 1027 is substantially larger than that of the ion of m/z 1037, a similar addition mechanism to the linear alkane reactions was proposed. Unlike abstracting a hydride directly from the terminal carbon of the linear alkanes, C=C double bonds acted as the nucleophile upon reactions with unsaturated cyclic hydrocarbons. As shown in Scheme 8.7a, the proposed addition mechanism also explained the absence of the water adduct to the hydrocarbon adduct, as no Coulomb-bound protons are available for the protonation of water from the background of the ion trap.

8.3.3 Reactions with Alkenes

Unlike additions to linear alkanes, $[B_{12}X_{11}]^-$ added to acyclic alkenes via a different possible mechanism. As shown in Figure 8.6, when $[B_{12}Br_{11}]^-$ reacted with 1-hexene, the adduct ion (m/z 1093) did not add adventitious water spontaneously, indicating this ion did not contain Coulomb-bound proton for the protonation of water. Moreover, even for linear alkenes, no fragment ions related to sequential C_2H_4 (a series of ions with 14 Da mass difference) losses was observed, suggesting the alkenes did not add to $[B_{12}Br_{11}]^-$ in the same manner as alkanes did. Moreover, the observation of the ion of m/z 1011 indicated the formation of a B-H bond in the adduct. This may be due to the abstraction of the hydride from the allylic position of the alkene led to the formation of a stable allyl carbocation (Scheme 8.7b). Upon elimination of a conjugated diene, the ion of m/z 1011 was obtained.

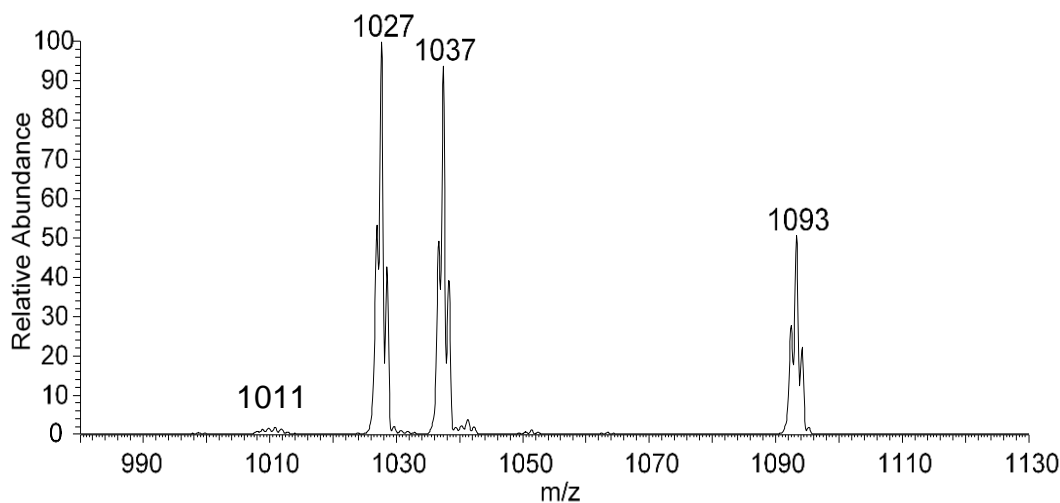


Figure 8.6 Reaction mass spectrum of $[B_{12}Br_{11}]^-$ with 1-hexene after 30 ms of reaction.

To verify the proposed mechanism, ITCAD was applied to the adduct ion formed upon the reaction with 1-hexene. Upon CAD, the ion of m/z 1037 was the only fragment ion generated upon CAD. For all the other examined alkene adduct ions (linear or branched), same fragmentation pattern was observed, namely, the position of the double bond in the alkene or alkyl side chains has no influence on the addition and fragmentation process. Lack of the ion of m/z 1027 in the CAD mass spectra indicated this ion of m/z 1037 could also be identified as $[B_{12}Br_{11}]^- [C_2H_4]$,

which as in agreement with our previous assumptions and observations as C=C double bond also exists and act as a nucleophile upon addition reactions with acyclic alkenes.

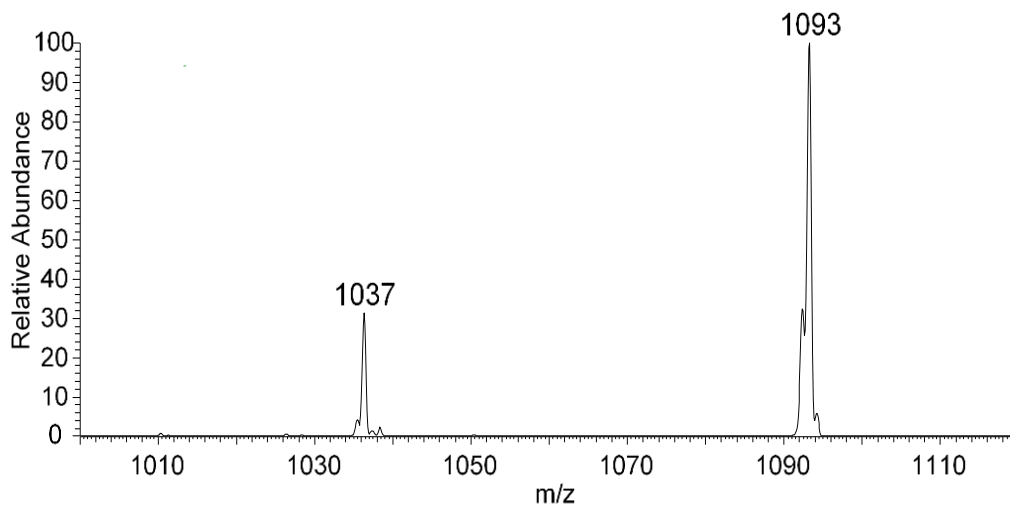
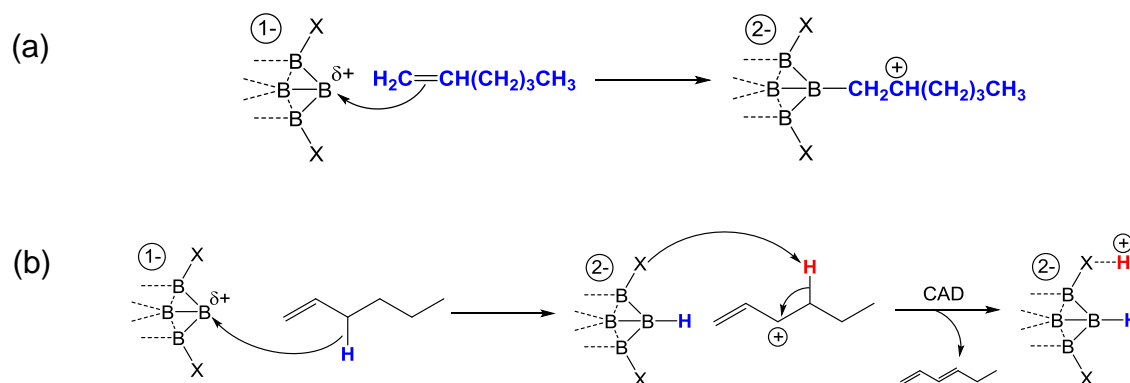


Figure 8.7 CAD mass spectrum of the adduct ion formed upon the reaction of $[B_{12}Br_{11}]^-$ with 1-hexene (m/z 1093).



Scheme 8.7 Proposed addition mechanism of $[B_{12}Br_{11}]^-$ to alkenes (a) and proposed mechanism for the formation of the ion of m/z 1011 upon reactions of $[B_{12}Br_{11}]^-$ and alkenes.

8.3.4 Reactions with Aromatic Hydrocarbons

For the reactions with benzene, CAD of the adduct ion $[B_{12}Br_{11}]^- [C_6H_6]$ regenerated the reactant ion $[B_{12}Br_{11}]^-$, and it spontaneously added to water and N_2 in the ion trap (Figure 8.8a). As benzene can only use one pair of its π electrons to undergo nucleophilic attack, the adduct ion tends to fragment at the B-C bond and release the π electrons to regain aromaticity. The other

aromatic compounds exhibited reactivity toward $[B_{12}Br_{11}]^-$ from not only the phenyl moiety but the side alkyl chain as well. Therefore, upon CAD, the adduct ions showed fragmentation patterns for both aromatic and aliphatic hydrocarbons discussed previously in the text (Figures 8.8b and 8.8c). It is worth mentioning that the fragmentation of the adduct ion formed upon reaction with styrene showed high similarity to that of the benzene adduct. It may be due to the reaction with the side chain of styrene also broke the conjugate system of the molecule. Therefore, it favored the fragmentation pattern that yielded the original reactant ion, $[B_{12}Br_{11}]^-$, to reclaim its stable conjugate structure.

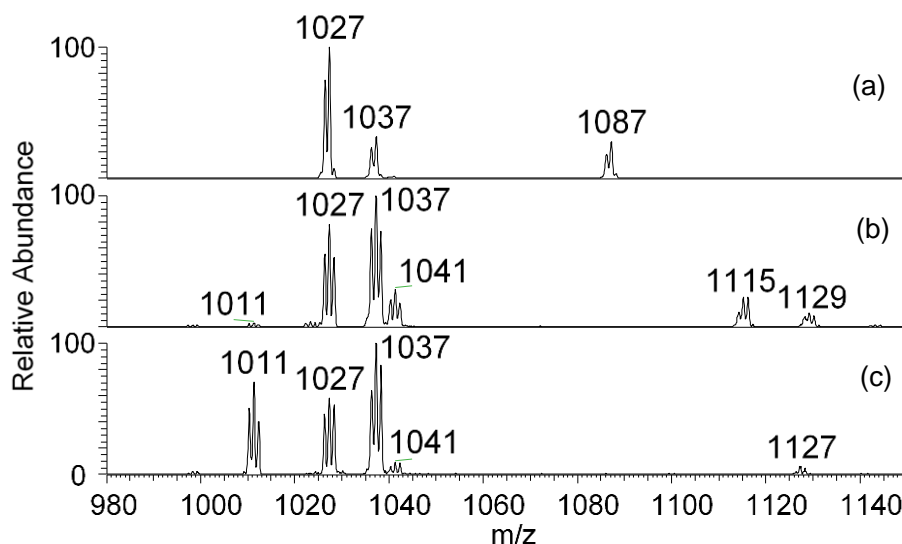
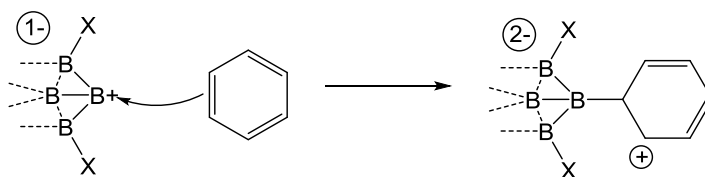


Figure 8.8 CAD mass spectra of the adduct ions formed upon reactions of $[B_{12}Br_{11}]^-$ with (a) benzene (m/z 1087), (b) styrene (m/z 1115), and (c) *trans*- β -Methylstyrene (m/z 1127). (Collision energy 30, arbitrary units, the ion of m/z 1129: unidentified peak)

As discussed above, an addition mechanism to benzene or the aromatic moieties of other aromatic compound derivatives was proposed in Scheme 8.8.



Scheme 8.8 Proposed addition mechanism of $[B_{12}Br_{11}]^-$ to benzene.

8.4 Conclusions

Chlorinated or brominated *closo*-borate anions activate C-H bonds of all the hydrocarbon model compounds studied in the gas phase in a very efficient manner (reaction time 30 ms). The adduct ions were proved to be stable covalent adducts formed via several different pathways. For all the acyclic saturated hydrocarbons, the addition reaction proceeded via the formation of a B-C bond. Computational methods verified that the proposed reaction pathway was more feasible than the formation of a B-H bond upon addition. Furthermore, the adduct ion formed was so acidic that it protonated water in the gas phase, which proved the formation of the B-C bond. Upon collision-activated dissociation (CAD), a series fragment ion related to the water adduct were observed. For all the acyclic unsaturated hydrocarbons studied, the addition was achieved via electrophilic addition to the C=C bond. No evidence of further water addition was observed. Upon CAD, simple dissociation of the adduct ion as well as the formation of $[B_{12}X_{11}]^{-}[C_2H_4]$ were observed, indicating the activation of the C=C bond. The reactions with cyclic hydrocarbons advanced via either one of the previously proposed mechanisms. If a C=C bond presents, the addition will take place at the C=C bond, otherwise the addition will proceed via B-C bond formation. The presence of $[B_{12}X_{11}]^{-}[C_2H_4]$ upon CAD suggested the ring-opening of the adduct ions. Additions to aromatic hydrocarbons took place in a mixed manner if a side chain is attached to the aromatic ring. Based on CAD spectra of the adduct ions, characteristic fragment ions responsible for both addition mechanisms were observed. Therefore, *closo*-borate anions were versatile to activate various types of C-H bonds of hydrocarbon molecules as a metal-free means to build more complex functionalized molecules. Meanwhile, the reactivity toward molecules with different functional groups verified their capability of construct more complex molecules. Moreover, the formation of stable adduct ions without fragmentations in the gas phase provided a promising analytical method for hydrocarbon mixture analysis.

8.5 Future Work

Quantum chemical calculations will be carried out for all the proposed reaction mechanisms.

8.6 References

1. Arndtsen, B. A.; Bergman, R. G.; Mobley, T. A.; Peterson, T. H. *Acc. Chem. Res.* **1995**, *28* (3), 154–162.
2. Yi, H.; Zhang, G.; Wang, H.; Huang, Z.; Wang, J.; Singh, A. K.; Lei, A. *Chem. Rev.* **2017**, *117* (13), 9016–9085.
3. Segawa, Y.; Maekawa, T.; Itami, K. *Angew. Chem. Int. Ed.* **2015**, *54* (1), 66–81.
4. Yamaguchi, J.; Yamaguchi, A. D.; Itami, K. *Angew. Chem. Int. Ed.* **2012**, *51* (36), 8960–9009.
5. He, J.; Wasa, M.; Chan, K. S. L.; Shao, Q.; Yu, J.-Q. *Chem. Rev.* **2017**, *117* (13), 8754–8786.
6. Daugulis, O.; Do, H.-Q.; Shabashov, D. *Acc. Chem. Res.* **2009**, *42* (8), 1074–1086.
7. Labinger, J. A. *Chem. Rev.* **2017**, *117* (13), 8483–8496.
8. Lou, M.; Deng, Z.; Mao, X.; Fu, Y.; Yang, Q.; Peng, Y. *Org. Biomol. Chem.* **2018**, *16* (11), 1851–1859.
9. Shang, R.; Ilies, L.; Nakamura, E. *Chem. Rev.* **2017**, *117* (13), 9086–9139.
10. Ritleng, V.; Sirlin, C.; Pfeffer, M. *Chem. Rev.* **2002**, *102* (5), 1731–1770.
11. Montoro, R.; Wirth, T. *Synthesis*, **2005**, *9*, 1473–1478.
12. Tian, Y.; Ling, A.; Fang, R.; Tan, R. X.; Liu, Z.-Q. *Green Chem.* **2018**, *20*(15), 3432–3435.
13. Rohdenburg, M.; Mayer, M.; Grellmann, M.; Jenne, C.; Borrmann, T.; Kleemiss, F.; Azov, V. A.; Asmis, K. R.; Grabowsky, S.; Warneke, J. *Angew. Chem. Int. Ed.* **2017**, *56*(27), 7980–7985.
14. Mayer, M.; Rohdenburg, M.; van Lessen, V.; Nierstenhoefer, M. C.; Apra, E.; Grabowsky, S.; Asmis, K. R.; Jenne, C.; Warneke, J. *Chem. Comm.* **2020**, *56*(33), 4591–4594.
15. Warneke, J.; Mayer, M.†; Rohdenburg, M.; Ma, X.; Liu, J. K.-Y. Grellmann, M.; Azov, V. A.; Apra, E.; Asmis, K. R.; Jenne, C.; Johnson, G. E.; Kentt ämaa H. I.; Laskin, J. *Proc. Natl. Acad. Sci. U. S. A.*, doi: 10.1073/pnas.2004432117.
16. Saetre, R.; Somogyvari, A.; Yamashita, G. *Abstr. Pap. Am. Chem. Soc.* **1989**, *197*, 40-PETR.
17. Qian, K.; Dechert, G. J. *Anal. Chem.* **2002**, *74*, 3977–3983.

18. Liang, Z.; Hsu, C. S. *Energy Fuels* **1998**, *12*, 637–643.
19. Sarpal, A. S.; Kapur, G. S.; Mukherjee, S.; Jain, S. K. *Fuel* **1997**, *76*, 931–937.
20. Geis, V.; Guttsche, K.; Knapp, C.; Scherer, H.; Uzun, R. *Dalton Trans.* **2009**, *15*, 2687–2694.
21. Tiritiris, I.; Schleid, T. *Z. Anorg. Allg. Chem.* **2004**, *630*, 1555–1563.

VITA

Xin Ma was born on May 2nd, 1991 in Lanzhou City, Gansu Province, China. He joined Professor Hilkka Kenttämäa's research group at Purdue University in 2014 to pursue his Ph.D. degree, after obtaining his Bachelor of Science with a major in chemistry in 2013. In Professor Kenttämäa's group, his research interests include gas-phase reactivity of organic carbon- and boron-centered bi- and polyradicals toward small organic molecules and biomolecules as well as gas-phase C–H bond activation in hydrocarbons by using halogenated *closo*-borate anions. His research also focuses on the synthesis of lignin model compounds for the exploration of the mechanisms of their fast pyrolysis reactions by using tandem mass spectrometry and the development of mass spectrometry methods for the identification of functionalities in drug metabolites via ion–molecule reactions. He successfully defended his Ph.D. degree on September 23rd, 2020.

PUBLICATIONS

1. Zhang, Y.; Jing, L.; He, X.; Li, Y.; **Ma, X.** Sorption Enhancement of TBBPA from Water by Fly Ash-supported Nanostructured γ -MnO₂, *J. Ind. Eng. Chem.* **2015**, *21*, 610-619.
2. Sheng, H.; Tang, W.; Gao, J.; Riedeman, J.; Li, G.; Jarrell, T.; Hurt, M.; Yang, L.; Murria, P.; **Ma, X.**; Nash, J. J.; Kenttämä, H. I. (-)ESI/CAD MSⁿ Procedure for Sequencing Lignin Oligomers Based on a Study of Synthetic Model Compounds with β -O-4 and 5-5 Linkages, *Anal. Chem.* **2017**, *89* (24), 13089–13096.
3. Zhu, H.; **Ma, X.**; Kong, J.; Zhang, M.; Kenttämä, H. I. Identification of Carboxylate, Phosphate, and Phenoxide Functionalities in Deprotonated Molecules Related to Drug Metabolites via Ion-molecule Reactions with Water and Diethylhydroxyborane, *J. Am. Soc. Mass Spectrom.* **2017**, *28* (10), 2189-2200.
4. Kong, J.; Yu, Z.; Easton, M.; Niyonsaba, E.; **Ma, X.**; Yerabolu, R.; Sheng, H.; Jarrell, T.; Zhang, Z.; Ghosh, A.; Kenttämä, H. I. Differentiating Isomeric Deprotonated Glucuronide Drug Metabolites via Ion/Molecule Reactions in Tandem Mass Spectrometry, *Anal. Chem.* **2018**, *90* (15), 9426-9433.
5. Sheng, H.; **Ma, X.**; Lei, H.-R.; Milton, J.; Tang, W.; Jin, C.; Gao, J.; Wittrig, A. M.; Archibold, E. F.; Nash, J. J.; Kenttämä, H. I. Polar Effects Control the Gas-phase Reactivity of *para*-Benzyne Analogs, *ChemPhysChem.* **2018**, *19* (21), 2839-2842.
6. Gao, J.; Jankiewicz, B.; Sheng, H.; Kirkpatrick, L.; **Ma, X.**; Nash, J. J.; Kenttämä, H. I. Substituent Effects on the Reactivity of the 2,4,6-Tridehydropyridinium Cation, an Aromatic σ,σ,σ -Triradical, *Eur. J. Org. Chem.* **2018**, *2018* (46), 6582-6589.
7. Max, J.; **Ma, X.**; Kotha, R.; Ding, D.; Milton, J.; Nash, J. J.; Kenttämä, H. I. Reactivity of Organic $\sigma,\sigma,\sigma,\sigma,\sigma$ -Pentaradicals, *Int. J. Mass Spectrom.* **2019**, *435*, 280-290.
8. Warneke, J.; Rohdenburg, M. Liu, J. K.-Y.; Johnson, E.; **Ma, X.**; Kumar, R.; Su, P.; Apra, E.; Wang, X.-B.; Jenne, C.; Finze, M.; Kenttämä, H. I.; Laskin, J. Gas Phase Fragmentation of Adducts between Dioxygen and *closo*-Borate Radical Anions, *Int. J. Mass Spectrom.* **2019**, *436*, 71-78.
9. Kotha, R.; Yerabolu, R.; Ding, D.; Szalwinsky, L.; **Ma, X.**; Wittrig, A.; Kong, J.; Nash, J. J.; Kenttämä, H. I. Spin-spin Coupling Between Two *meta*-Benzyne Moieties in a Quinolinium Tetraradical Cation Increases Their Reactivities, *Chem. Eur. J.* **2019**, *25* (17), 4272-4277.
10. **Ma, X.**; Jin, C.; Wang, D.; Nash, J. J.; Kenttämä, H. I. Relative Reactivities of Three Isomeric Aromatic Biradicals with a 1,4-Biradical Topology Are Controlled by Polar Effects, *Chem. Eur. J.* **2019**, *25* (25), 6355-6361.

11. **Ma, X.**; Zhang, Y.; Lei, H.-R.; Kenttämaa, H. I. Laser-induced Acoustic Desorption, *MRS Bulletin*, **2019**, *44* (5), 372-381.
12. Ding, D.; Jiang, H.; **Ma, X.**; Nash, J. J.; Kenttämaa, H. I. Effects of the Distance Between Radical Sites on the Reactivities of Aromatic Biradicals, *J. Org. Chem.* **2020**, *85*, 8415-8428.
13. Warneke, J.; Mayer, M.[‡]; Rohdenburg, M.[‡]; **Ma, X.**[‡] (‡equal contribution); Liu, J. K.-Y.; Grellmann, M.; Azov, V. A.; Apra, E.; Asmis, K. R.; Jenne, C.; Johnson, G. E.; Kenttämaa H. I.; Laskin, J. Direct functionalization of C-H bonds by electrophilic anions, *Proc. Natl. Acad. Sci. U. S. A.* **2020**, *117*(38), 23374-23379.
14. Fine, J.; Liu, J. K.-Y.; Beck, A.; Alzarini, K. Z.; **Ma, X.**; Boulos, V.; Kenttämaa, H. I.; Chopra, G. Graph-based Machine Learning Interprets Diagnostic Isomer-Selective Ion-Molecule Reactions in Tandem Mass Spectrometry, *Chem. Sci.* **2020**, DOI: [10.1039/D0SC02530E](https://doi.org/10.1039/D0SC02530E).
15. **Ma, X.**[‡]; Feng, E.[‡] (‡equal contribution); Jiang, H.; Boulos, V. M.; Gao, J.; Nash, J. J.; Kenttämaa, H. I. Ground-state Singlet *meta*-Benzyne Cations React from an Excited Triplet State, *submitted*.
16. **Ma, X.**; Feng, E.; Johnson, E.; Nash, J. J.; Kenttämaa, H. I. Generation and Reactivity Studies of Isomeric Quinoline-based Oxenium Cations in a Linear Quadrupole Ion Trap Mass Spectrometer, *manuscript in preparation*.
17. **Ma, X.**; Rohdenburg, M.; Liu, J. K.-Y.; Azov, V. A.; Laskin, J.; Jenne, C.; Kenttämaa, H. I.; Warneke, J. Reactions of Electrophilic Anions [B₁₂X₁₁]⁻ (X=Cl, Br) with Hydrocarbons: a Systematic Mechanistic Study, *manuscript in preparation*.